

Heat transfer modeling at an interface between a porous medium and a free region

Aliénor d'Hueppe

► To cite this version:

Aliénor d'Hueppe. Heat transfer modeling at an interface between a porous medium and a free region. Other. Ecole Centrale Paris, 2011. English. NNT : 2011ECAP0049 . tel-00711470

HAL Id: tel-00711470

<https://tel.archives-ouvertes.fr/tel-00711470>

Submitted on 25 Jun 2012

HAL is a multi-disciplinary open access archive for the deposit and dissemination of scientific research documents, whether they are published or not. The documents may come from teaching and research institutions in France or abroad, or from public or private research centers.

L'archive ouverte pluridisciplinaire **HAL**, est destinée au dépôt et à la diffusion de documents scientifiques de niveau recherche, publiés ou non, émanant des établissements d'enseignement et de recherche français ou étrangers, des laboratoires publics ou privés.

THÈSE DE DOCTORAT DE L'ÉCOLE CENTRALE PARIS

Spécialité
Mécanique et Energie

Présentée par
Alienor D'HUEPPE

pour obtenir le grade de
DOCTEUR DE L'ÉCOLE CENTRALE PARIS

Laboratoire d'accueil:

Commissariat à l'Energie Atomique
Direction de l'Energie Nucléaire
Département d'Etude des Réacteurs
Service de Simulation en Thermo-Hydraulique
Laboratoire de Modélisation et de Développement de Logiciels

HEAT TRANSFER MODELING AT AN INTERFACE BETWEEN A POROUS MEDIUM AND A FREE REGION

Thèse soutenue le 17 novembre 2011 devant le jury composé de :

M. Dominique GOBIN	FAST	Examineur
M. Olivier GREGOIRE	CEA STXN	Examineur
M. Marion CHANDESRIS	CEA Grenoble	Encadrant
M. Didier JAMET	CEA Grenoble	Encadrant
M. Christian MOYNE	INPL-Nancy	Rapporteur
M. Michel QUINTARD	IMF-Toulouse	Rapporteur
M. Benoît GOYEAU	Ecole Centrale Paris	Directeur de thèse
M. Wim-Paul BREUGEM	Delft Uni. Tech.	Invité

Table des matières

1	Introduction	9
1.1	Modeling of turbulent transfers in porous media	9
1.2	Modeling of transfers at a free-porous interface	11
1.3	Contents	14
2	Heat transfer modeling in homogeneous porous media	17
2.1	Porous medium modeling	17
2.1.1	Context	17
2.1.2	The volume averaging formalism	18
2.2	One-temperature model	24
2.2.1	Closure of the macroscopic equation	25
2.2.2	Determination of the effective thermal conductivity tensor	26
2.3	Two-temperature models: literature review	28
2.3.1	The heuristic approach	29
2.3.2	The mixed approach	29
2.3.3	The volume averaging approach	30
2.3.4	Discussion	34
2.4	Two-temperature modeling: another interpretation	36
2.4.1	Active dispersion	36
2.4.2	The two-temperature model	37
2.5	Conclusion	48
3	Free-porous interface modeling for laminar heat transfer at local thermal equilibrium	51
3.1	Introduction	51
3.2	Article 1: Boundary conditions at a fluid-porous interface for a convective heat transfer problem: Analysis of the jump relations	53
3.3	Introduction	53
3.4	First up-scaling step	55
3.4.1	Microscopic model	55
3.4.2	Mesosopic model	55
3.4.3	Determination of the effective thermal conductivity tensor	58
3.5	Second up-scaling step	60
3.5.1	Generic analysis	60
3.5.2	Method of matched asymptotic expansions	62
3.6	Determination of the apparent interface	64
3.6.1	Procedure	64
3.6.2	Illustration	66
3.7	Conclusion	69
3.8	Appendix	69
3.8.1	Appendix1: The matched asymptotic expansion method	69

3.9	Conclusion	73
4	Free-porous interface modeling for laminar heat transfer at local thermal non-equilibrium	75
4.1	Introduction	75
4.2	Article 2: Coupling a two-temperature model and a one-temperature model at a fluid-porous interface	77
4.3	Introduction	77
4.4	The first up-scaling step	78
4.4.1	Microscopic equations	78
4.4.2	Mesososcopic model	80
4.4.3	Determination of the effective transfer coefficients	82
4.5	The second up-scaling step	84
4.5.1	The generic analysis	86
4.5.2	The method of the matched asymptotic expansion	88
4.5.3	Illustration	90
4.6	Conclusion	91
4.7	Appendix	95
4.7.1	Appendix A: Closed mesoscopic model	95
4.7.2	Appendix B: The method of the matched asymptotic expansion	96
4.8	Apparent interface	101
4.8.1	Determination of an apparent interface	101
4.8.2	Heat transfer driven by a heat source in the solid	104
4.8.3	Variable heat source	105
4.8.4	Industrial nuclear codes	107
4.9	Conclusion	108
5	Direct numerical simulation of a turbulent heat flow in a partially porous domain	111
5.1	Introduction	111
5.2	Problem description and numerical method	113
5.2.1	Geometry	113
5.2.2	Boundary conditions	114
5.2.3	Study parameters	116
5.2.4	Numerical method	116
5.3	Governing equations	117
5.3.1	General equations	117
5.3.2	Simplified equations	119
5.4	Results	120
5.4.1	Statistics of the velocity field	121
5.4.2	Turbulent viscosity profile	125
5.4.3	Statistics of the temperature field	126
5.5	Conclusion	138
6	Turbulent heat transfer at the free-porous interface for a Poiseuille flow	139
6.1	Introduction	139
6.2	First up-scaling step	141
6.2.1	Governing equations at the microscopic scale	141
6.2.2	Governing equations at the mesoscopic scale	143
6.2.3	Closed mesoscopic equations	148
6.2.4	1D problem	150

TABLE DES MATIÈRES

6.3	Second up-scaling step	152
6.3.1	Jump conditions for the velocity and the turbulent quantities	152
6.3.2	Jump conditions for the heat transfer	154
6.4	Results	155
6.4.1	Results for the momentum transfer	155
6.4.2	Results for heat transfer	157
6.5	Conclusion	163
7	Conclusion	167
7.1	Main conclusions	167
7.2	Discussion and outlooks	169
A	Boundary conditions of pseudo-periodicity	171
A.1	The variable change	171
A.2	Determination of the source term	172
A.3	Implementation in Trio-U	173
	Bibliography	175

Nomenclature

Letters

A_{fs}	fluid-solid interface	-
a_V	interfacial area per unit volume	m^{-1}
\mathbf{b}_{wu}	vector field that maps $\nabla \langle T_u \rangle^u$ on to \tilde{T}_w ($w, u = s, f$)	m
\mathbf{b}_w	one-temperature model vector field that maps $\nabla \langle T \rangle$ on to \tilde{T}_w	m
c_p	heat capacity	$J.kg^{-1}.K^{-1}$
D_a	Darcy number	-
d_p	distance between solid cubes	m
\mathbf{d}_w	transport coefficient associated to $(\langle T_u \rangle^u - \langle T_w \rangle^w)$ ($w, u = s, f$)	$W.m^{-2}.K^{-1}$
d_i^w	component of transport coefficient associated of the w-phase	$W.m^{-2}.K^{-1}$
\mathbf{D}_a	active dispersive vector of the fluid phase	$W.m^{-1}.K^{-1}$
$\overline{\overline{D}}_p^w$	passive dispersive tensor of the w-phase	$W.m^{-1}.K^{-1}$
$\overline{\overline{D}}_p$	total passive dispersive tensor = $\overline{\overline{D}}_p^w + \overline{\overline{D}}_p^u$	$W.m^{-1}.K^{-1}$
\mathcal{F}	Forchheimer's term	?
f_t^i	component of the drag vector	N
h	film heat transfer coefficient	$W.m^{-1}.s^{-1}$
h_w	film heat transfer coefficient of the w-phase	$W.m^{-1}.s^{-1}$
k	turbulent kinetic energy	$m^2.s^{-2}$
k_e	one-temperature model equivalent conductivity	$W.m^{-1}.K^{-1}$
k_w	thermal conductivity of the w-phase	$W.m^{-1}.K^{-1}$
\mathcal{K}	permeability	m^2
$\overline{\overline{K}}$	one-equation model effective thermal conductivity tensor of the w-phase	$W.m^{-1}.K^{-1}$
$\overline{\overline{K}}_w$	two-equation model effective thermal conductivity tensor of the w-phase	$W.m^{-1}.K^{-1}$
$\overline{\overline{K}}_{wu}$	two-equation model effective thermal conductivity tensor of the w-phase associated with $\nabla \langle T_u \rangle^u$ in the w-phase equation	$W.m^{-1}.K^{-1}$
K_{ij}	component of the tensor $\overline{\overline{K}}$	$W.m^{-1}.K^{-1}$
K_{ij}^w	component of the tensor $\overline{\overline{K}}_w$	$W.m^{-1}.K^{-1}$
$\overline{\overline{K}}_{dis}$	one-temperature model dispersive tensor	$W.m^{-1}.K^{-1}$
K_{ij}^{dis}	component of the tensor $\overline{\overline{K}}_{dis}$	$W.m^{-1}.K^{-1}$
$\overline{\overline{K}}_{tor}$	one-temperature model tortuosity tensor	$W.m^{-1}.K^{-1}$
$\overline{\overline{K}}_{tor}^{wu}$	tortuosity tensor associated with $\nabla \langle T_u \rangle^u$ in the w-phase equation	$W.m^{-1}.K^{-1}$
$\overline{\overline{K}}_{tor}^w$	tortuosity tensor of the w-phase	$W.m^{-1}.K^{-1}$
$K_{ij}^{tor,w}$	component of tortuosity tensor of the w-phase equation	$W.m^{-1}.K^{-1}$
\mathbf{K}_{tor}^a	tortuosity vector associated with $(\langle T_s \rangle^s - \langle T_f \rangle^f)$ in the fluid-phase equation	$W.m^{-1}.K^{-1}$
l_c	length scale of the microscopic variations	m

L_M	length scale of the macroscopic variations	m
m_p	weighting function	-
p	pressure	$N.m^2$
\mathcal{P}	wall heat flux	$W.m^{-3}$
Pe	Péclet number = $v_f d_p \rho c_p / k_f$	-
Pr	Prandtl number = $\nu \rho c_p / k_f$	-
Pr_t	turbulent Prandtl number	-
P_k	sub-filter production term of the kinetic energy $\langle k \rangle$	$m^2.s^{-3}$
Q	q criterion = $\frac{1}{2} \left[\left(\frac{\partial u}{\partial x} \right)^2 + \left(\frac{\partial v}{\partial y} \right)^2 + \frac{\partial u}{\partial y} \frac{\partial v}{\partial x} \right]$	s^{-2}
q_w	wall heat flux	$W.m^{-2}$
Re	Reynolds number = $v_f d_p / \nu$	-
Re_b	Reynolds number based on the bulk velocity U_b	-
\mathbf{r}	position vector	m
r_o	radius of the averaging volume	m
S_m	Solid source at the macroscopic scale	$W.m^{-3}$
S_s	Solid source at the local scale	$W.m^{-3}$
s_w	scalar field that maps $(\langle T_u \rangle^u - \langle T_w \rangle^w)$ on to \tilde{T}_w ($w, u = s, f$)	-
S_ϵ	sub-filter production term of the dissipation rate $\langle \epsilon \rangle$	$m^2.s^{-4}$
t	time	s
T_{or}	term of tortuosity	$W.m^{-3}$
T_w	temperature of the fluid phase	K
U_b	bulk velocity	$m.s^{-1}$
u_τ^t	friction velocity at the upper wall	$m.s^{-1}$
u_τ^p	friction velocity at the porous wall $y = 0$	$m.s^{-1}$
\mathbf{u}_{wu}	transport coefficient associated with $\nabla \langle T_u \rangle^u$ in the w-phase equation	$W.m^2.K^{-1}$
\mathbf{u}	total transport coefficient = $\mathbf{u}_{wu} + \mathbf{u}_{ww}$	$W.m^2.K^{-1}$
\mathbf{u}_i^f	compent of the total transport coefficien	$W.m^2.K^{-1}$
V	REV volume	m^3
\mathbf{v}_f	fluid velocity vector	$m.s^{-1}$
\mathbf{v}_m	superficial macroscopic velocity vector	$m.s^{-1}$
u, v, w	velocity component of \mathbf{v}_f	$m.s^{-1}$
y_m	interface location	m
y_ψ	center of gravity of the quantity ψ	m

Nomenclature

Greek symbols

α	thermal diffusivity	$m^2.s^{-1}$
α_t	turbulent diffusivity	$m^2.s^{-1}$
$\alpha_{t\phi}$	mesoscopic turbulent diffusivity	$m^2.s^{-1}$
α_{tm}	macroscopic turbulent diffusivity	$m^2.s^{-1}$
α_{tor}	diffusivity of the tortuosity	$m^2.s^{-1}$
δ	length of the transition zone	m
ε	small parameter of the method of matched asymptotic expansions	-
ϵ	kinetic energy dissipation rate	$m^2.s^{-3}$
ϕ_w	volume fraction of the w-phase	-
θ	transformed temperature	K
ν	fluid kinematic viscosity	$m^2.s^{-1}$
ν_t	turbulent viscosity	$m^2.s^{-1}$
$\nu_{t\phi}$	mesoscopic turbulent viscosity	$m^2.s^{-1}$
ν_{tm}	macroscopic turbulent viscosity	$m^2.s^{-1}$
ρ	fluid density	$kg.m^{-3}$
σ	$1/\sqrt{D_a}$	-
$\sigma_k, \sigma_\epsilon$	Prandtl numbers	-
$\widetilde{\sigma}_k, \widetilde{\sigma}_\epsilon$	macroscopic Prandtl numbers	-
τ_u^{ij}	component of the momentum dispersion tensor	s^{-1}
τ_{vT}	thermal dispersion vector	$W.m^{-2}$
τ_{uT}^i	component of the thermal dispersion vector	$W.m^{-2}$
τ_ϵ^i	component of the sub-filter dispersion vector of $\langle \epsilon \rangle$	$m.s^{-3}$
τ_k^i	component of the sub-filter dispersion vector of $\langle k \rangle$	$m.s^{-2}$

Superscripts

ψ^+	normalize quantity
ψ^{ex}	excess value
ψ_{rms}	roots mean square fluctuations

Special symbols

$\overline{\psi}$	time average of ψ
ψ'	time fluctuation
$\langle \psi \rangle$	spatial average of ψ
$\langle \psi_w \rangle$	phase average of ψ for the w-phase
$\langle \psi_w \rangle^w$	intrinsic phase average of ψ for the w-phase
$\widetilde{\psi}_w$	spatial deviation of ψ in the w-phase
$\widehat{\psi}$	<i>inner</i> quantity

Abbreviations

DNS	Direct numerical simulation
LES	Large Eddy Simulation
RANS	Reynolds Averaged Navier Stokes equations
VANS	Volume Averaged Navier Stokes equations
REV	Representative Elementary Volume

Résumé

Ce travail porte sur l'étude des transferts thermiques à une interface entre un milieu poreux et un milieu libre en utilisant une approche multi-échelles. L'utilisation d'une approche multi-échelles permet de passer d'une description fine du milieu poreux et de l'interface à une échelle de description macroscopique. A l'échelle macroscopique, le domaine est constitué d'une région poreuse homogène et d'une région libre séparée par une interface de discontinuité. L'enjeu d'une telle description réside dans la détermination des conditions de saut à imposer à l'interface. Quelle est la forme des conditions de saut à imposer? Les grandeurs physiques sont-elles continues ou discontinues? Quelle est la valeur des paramètres de saut associés à ces conditions de saut? Ces paramètres de saut sont-ils des grandeurs intrinsèques? Afin d'aborder ces questions, nous avons choisi d'utiliser une méthodologie basée sur l'utilisation de trois niveaux de description de l'interface et deux étapes de changement d'échelle.

Le premier changement d'échelle correspond au passage de la description microscopique à la description mésoscopique grâce à l'opérateur de prise de moyenne volumique. A l'échelle mésoscopique, l'interface est diffuse et le domaine est séparé en trois parties: une région poreuse homogène, une zone de transition et une région libre. L'objectif de ce changement d'échelle est de caractériser les transferts thermiques grâce à un modèle dont les coefficients effectifs sont constants dans les régions homogènes et varient de façon continue dans la zone de transition.

Le second changement d'échelle correspond au passage de la description mésoscopique à la description macroscopique. L'enjeu de cette étape est de remplacer la description continue de l'interface par des conditions de sauts équivalentes. Pour cela, deux méthodes sont utilisées: l'analyse générique et la méthode des développements asymptotiques raccordés.

L'*analyse générique* est une méthode basée sur la conservation de l'énergie entre les échelles mésoscopiques et macroscopique. Elle permet d'obtenir des conditions de saut sous forme de valeur en excès de grandeur physiques. Cependant ces valeurs en excès impliquent des grandeurs mésoscopiques qui ne sont pas connues à l'échelle macroscopique.

La méthode des *développements asymptotiques raccordés* est un outil mathématique utilisé pour résoudre les équations différentielles partielles dont les coefficients varient en fonction d'un petit paramètre ε . Appliquée à une interface libre-poreux, cette méthode donne des solutions approchées à différent ordres des équations mésoscopiques en fonction de ε , où ε correspond à la longueur de la zone interfaciale sur la longueur du domaine. Les solutions d'ordre 0 correspondent à la résolution du modèle macroscopique avec des conditions limites de continuité à l'interface libre-poreux. Ces solutions ne capturent pas l'ensemble des transferts thermiques et dépendent de la position de l'interface. Il faut donc augmenter l'ordre de la résolution. Pour les solutions d'ordre 1, des conditions de sauts à l'interface libre-poreux apparaissent. Ces conditions de sauts impliquent des grandeurs macroscopiques d'ordre 0 et des valeurs en excès de coefficients effectifs. Sous cette forme, les conditions de saut sont fermées et les solutions ainsi obtenues ne dépendent pas de la position de l'interface. La pertinence de cette méthode est illustrée sur des exemples d'application.

Nous notons cependant que l'évaluation de ces solutions nécessite une résolution en deux temps. Dans un premier temps, le modèle macroscopique d'ordre 0 doit être calculé pour déterminer les grandeurs

d'ordre 0 présentes dans les relations de saut d'ordre 1, puis le modèle macroscopique d'ordre 1 peut être calculé.

Pour s'affranchir de la résolution en deux temps, nous étudions la notion d'interface apparente. Cette notion consiste à déterminer la position de l'interface où les conditions de continuité sont suffisantes pour fermer le problème à l'échelle macroscopique et obtenir les champs souhaités dans les milieux homogènes. Plusieurs questions se posent: est-elle unique? Dépend-elle uniquement de grandeurs intrinsèques de l'interface? Si la réponse à ces questions est positive, la connaissance de l'interface apparente permet de simplifier considérablement la résolution du modèle macroscopique. Dans ce cas, la détermination des solutions d'ordre 1 en deux temps peut être évitée. Seule la détermination des coefficients effectifs et une unique résolution sont nécessaires. On montrera que les solutions d'ordre 1 obtenues grâce à cette approche multi-échelles permettent d'étudier analytiquement la notion d'interface apparente.

Dans ce mémoire, nous allons appliquer cette approche multi-échelles et discuter l'existence de l'interface apparente pour les problèmes de transferts de chaleur (i) à l'équilibre thermique local et (ii) dans le cas du déséquilibre thermique local pour un écoulement normal à l'interface libre-poreux, et enfin (ii) pour un écoulement turbulent tangent à l'interface libre-poreux. Afin de modéliser les transferts dans la zone de transition libre-poreux, nous avons dû développer une méthode alternative. Pour cela nous nous sommes appuyés sur les méthodes classiques des milieux poreux homogènes.

Le chapitre 2 présente les connaissances théoriques de la modélisation des transferts thermiques dans un milieu poreux homogène. Trois méthodes sont exposées.

La méthode *heuristique*, basée sur des modèles empiriques et dont les coefficients effectifs sont déterminés à partir d'expériences. La méthode *de prise de moyenne volumique*, qui dérive un système d'équations à l'échelle macroscopique via un filtre spatial. Ce processus fait apparaître des termes caractéristiques de l'échelle locale qui doivent être fermés. Des analyses d'ordre de grandeurs et la résolution de problème de fermeture permettent de déterminer ces termes. La dernière méthode est la méthode *mixte*. Elle dérive la forme ouverte des équations macroscopique en utilisant l'opérateur de prise de moyenne, mais postule la forme fermée des équations sans la prouver formellement comme pour la méthode de prise de moyenne volumique.

À l'équilibre thermique, les trois approches convergent vers un modèle à une température identique. Dans le chapitre 3, nous étendons la méthode *mixte* pour caractériser les transferts thermiques à l'interface libre-poreux.

Dans le cas du déséquilibre thermique, les méthodes présentent des différences que nous discutons. Par ailleurs aucune de ces méthodes ne peut être directement utilisée pour caractériser les transferts à l'interface libre-poreux. Pour pallier à ce manque, nous proposons une méthode alternative basée sur les méthodes déjà existantes. Une fois validée pour un milieu poreux homogène, cette méthode à l'avantage de pouvoir être facilement étendue à l'étude des transferts dans une zone interfaciale. Elle sera utilisée dans les chapitres 4 et 6.

Le chapitre 3 étudie les transferts à l'équilibre thermique local pour un écoulement normal à l'interface libre-poreux. Cette étude permet de présenter l'approche multi-échelles de façon didactique. Le premier changement d'échelle abouti à une équation continue de la température. La détermination du tenseur de conductivité thermique effectif dans l'ensemble du domaine incluant la zone de transition permet de fermer le problème à l'échelle mésoscopique. Le second changement d'échelle donne les conditions de saut à imposer à l'interface libre-poreux pour la température et le flux de chaleur total. En s'appuyant sur les résultats obtenus par la méthode des développements asymptotiques raccordés nous montrons de façon analytique que l'interface apparente existe et qu'elle est facilement localisable une fois le profil du tenseur de conductivité thermique effectif connu dans la zone de transition.

Le chapitre 4 étudie les transferts dans le cas du déséquilibre thermique local pour un écoulement normal à l'interface libre-poreux. Cette étude est plus complexe que la précédente du fait du nombre de coefficients effectifs impliqués dans le modèle à deux températures. Une fois le problème fermé à l'échelle mésoscopique grâce à la détermination des coefficients effectifs, le second changement d'échelle est étudié. A cette étape, une nouvelle difficulté apparaît: coupler le modèle à deux températures dans le milieu poreux homogène avec un modèle à une température dans la région libre. Ce problème est résolu en introduisant une écriture équivalente pour rétablir le même nombre d'équations dans chaque région homogène. De cette façon, l'analyse générique et la méthode des développements asymptotiques raccordés peuvent être utilisées. Ainsi nous obtenons des conditions de saut sur la température et le flux de chaleur total pour la phase fluide et une condition de saut sur le flux total pour la phase solide. Comme pour le cas de l'équilibre thermique local, nous déterminons de façon analytique la relation donnant la position de l'interface apparente. Cette relation fait intervenir les gradients des flux transverses des phases fluide et solide, et la source solide volumique. Si un des ces phénomènes est dominant devant les autres, la position de l'interface apparente peut être déterminée a priori. Dans le cas contraire l'interface apparente n'est pas intrinsèque et la résolution du problème macroscopique à l'ordre 1 est nécessaire.

Le chapitre 5 étudie les transferts thermiques pour un écoulement turbulent tangent à l'interface. La physique des transferts thermiques turbulents pour une telle configuration est très complexe et n'a encore jamais été étudiée. Pour pallier à ce manque d'information, une simulation numérique directe des transferts est réalisée. A partir de la géométrie utilisée par [Breugem and Boersma \(2005\)](#) pour les écoulements turbulents au dessus d'un milieu poreux, nous calculons le champ de température pour trois conditions aux limites différentes. Les résultats obtenus pour le champ vitesse sont comparés à ceux de Breugem afin de valider la DNS pour le transfert des moments. Pour les transferts thermiques, seule la couche limite thermique à la paroi solide supérieure est comparée aux résultats existant dans la littérature. Les champs obtenus permettent de comprendre plus clairement l'impact de l'interface libre-poreux sur les transferts thermiques. Pour le nombre de Péclet étudié, nous montrons que la diffusivité turbulente et la diffusivité moléculaire sont toutes les deux présentes dans la région libre, tandis que dans le milieu poreux, la diffusivité turbulente disparaît au profit de la diffusivité moléculaire. De plus cette DNS donne les informations nécessaires à la modélisation de la turbulence (viscosité turbulente, énergie cinétique turbulente, taux de dissipation et diffusivité thermique turbulente...).

Le chapitre 6 étudie la modélisation des transferts thermiques pour un écoulement turbulent tangent à l'interface. L'objectif de ce chapitre est de coupler un modèle macroscopique de type $k-\epsilon$ avec un modèle de Prandtl turbulent dans le milieu poreux homogène avec un modèle standard $k-\epsilon$ avec un modèle Prandtl turbulent standard dans la région libre. Pour le transfert des moments, [Chandesris and Jamet \(2009b\)](#) déterminent une position de l'interface où les conditions limites de continuité sont suffisantes pour capturer correctement les profils des différentes grandeurs physiques (vitesse, énergie cinétique turbulente et taux de dissipation). Pour le transfert thermique, une équation de la conservation de l'énergie avec un modèle de Prandtl turbulent moyenné est dérivée à l'échelle mésoscopique avec l'opérateur de prise de moyenne volumique. Puis l'analyse générique est appliquée donnant la forme des conditions de saut. A partir de la connaissance acquise lors des études laminaires, nous sommes capable de faire les simplifications appropriées afin de fermer les conditions de saut pour le transfert thermique. Après cette étape, la difficulté principale de cette étude réside dans la modélisation du transfert thermique turbulent. En effet, le modèle de Prandtl turbulent moyenné ne permet pas de capturer les bons transferts thermiques dans le milieu poreux. Nous proposons donc un autre modèle de turbulence capable de retrouver le profil de diffusivité thermique turbulent et les bons flux de chaleur en comparaison avec les résultats de référence donné par la DNS.

Chapter 1

Introduction

The issue of this study is to propose physical models to characterize heat transfer problems at an interface between a porous medium and a free medium. Such problems are encountered in many industrial applications, and especially in the nuclear industry, for which an important application is related to thermal-hydraulic characteristics of the nuclear vessel. In this context, the transfers considered are turbulent and the physics involved are very complex. It involves porous modeling, turbulent transfers, turbulence modeling and free-porous interface problematic. However these physical phenomena can be studied in fundamental configurations, for which analytical developments are possible. This introduction presents the issues related to these subjects.

1.1 Modeling of turbulent transfers in porous media

The use of numerical simulations in fluid mechanics has increased during the last thirty years. Today, numerical simulation is used as a tool to study transfers in many industrial domains such as aeronautics, nuclear industry, car industry etc.

The constant increase of the computing power makes possible the direct numerical simulation (DNS) of physical problems increasingly complex. In a DNS, the Navier-Stokes and energy equations are solved directly without any modeling. Furthermore it gives access to instantaneous local quantities of the overall transfers. Thus, a DNS corresponds to a *numerical experiment* allowing a better understanding of the physical phenomena involved in the transfer. Even though the available computing power is significant, the use of DNS is limited by the mesh size and the computation time required to study complex problems. The study of turbulent transfers or transfers in porous media are particularly concerned by this limitation.

The numerical simulation of turbulent flows requires a cubic mesh with a cell number proportional to Reynolds numbers of $Re^{9/4}$, while the computing capacity and the computation time limit the meshes to $[10^8-10^9]$ cells. This is why DNS is not used to study industrial configurations with high Reynolds numbers ($Re \approx 10^6$). To reduce the computation cost, turbulence models are developed allowing the simulation of turbulent transfers for higher Reynolds numbers.

The Reynolds Averaged Navier-Stokes (RANS) approach is based on a statistical average of the equations. This process creates turbulent correlation terms that are modeled as a function of averaged characteristics of the transfers. The closure models reduce the number of degrees of freedom, and therefore the computation cost. However, the ability to reproduce the transfers depends on the closure models used that depend themselves on the studied configurations. Thus, this approach often suffers from a lack of universality.

Another approach is the Large Eddy Simulation (LES), which is an intermediate between the DNS and the RANS approach. The turbulent structures of the transfers, whose size is larger than a cut-off

scale are explicitly computed as for a DNS. The impact of the smallest structures on the larger scales are modeled with sub-filter models. The asset of this approach relies on the generality of the sub-filter modeling. Furthermore, as for a DNS, this approach captures the unsteady characteristics of the transfers. Nevertheless, the computation cost associated is important and limits its use to industrial applications to moderate Reynolds numbers ($Re \approx 10^4 - 10^5$).

In the context of porous media, the direct numerical simulation of the transfers relies on the fine meshing of the porous matrix to compute precisely the transfers at the local scale, also called the *microscopic scale*. However a porous medium is often composed by a very large number of solid grains, whose size is small compared to the size of the system studied. The description of such geometries requires an important amount of mesh cells that limits the use of the DNS. To overcome this difficulty, the fine representation of the fluid and solid phases of the porous medium is substituted by an equivalent continuous description at the system scale called the *macroscopic scale*. This description can be reached using different formalisms. The issue is to derive a description at the macroscopic scale from the governing equations at the microscopic scale. Different up-scaling formalisms exist in the literature.

The probabilistic approaches (Renard and de Marsily, 1997; Matheron, 1967) are often used to study natural porous media. For such problems, the porous medium is very irregular and can be considered as random. Thus, the quantities at the local scale are random variables and the up-scaling step to reach the macroscopic description is realized using expected values.

The homogenization approach (Sanchez-Palencia, 1974; Allaire, 1989; Mikelic, 2000) is based on the introduction of independent length variables: a quick variable ψ^* and a slow variable $\tilde{\psi}^* = \psi^*/\epsilon$, where ϵ is supposed to be very small. The quantities are decomposed following an asymptotic expansion in ϵ . Then, the separation by orders of magnitude as a function of ϵ leads to different problems. This approach is mathematically accurate and gives information on the shape and regularity of the solutions, but does not take an interest in the evaluation of the macroscopic properties of the porous medium.

The volume averaging approach (Whitaker, 1967) consists in integrating the local governing equations on a representative elementary volume (REV) to derive a system of equations at the macroscopic scale. It combines a phase indicator function to discriminate the fluid and solid phases and a volume averaging operator to smooth spatially. Thus, the fluid and the solid phases are substituted by an equivalent continuous medium and the equations of each phase are valid in the whole domain. The process of spatial smoothing creates at the macroscopic scale unclosed terms involving local quantities. These terms must be closed and the determination of closure models constitutes the main difficulty of this approach. This volume averaging approach is used with success for a large range of transfers and gives informations on the effective properties of the porous medium at the macroscopic scale. Furthermore, this approach is able to combine the turbulence modeling and the porous description by the application of successive averaging (Antohe and Lage, 1997; Nakayama and Kuwahara, 1999; Getachew et al., 2000; de Lemos and Pedras, 2001b,a; Chandris and Jamet, 2009b; Pinson et al., 2007; Drouin et al., 2010).

In a nuclear reactor, the geometry of the core is very complex and involves many solid structures as presented in Fig 1.1. The reactor core contains a fuel zone where the assemblies are located. For a pressurized water reactor (PWR), the fuel zone is made of about 150 assemblies made of 389 rods. Thus, the complexity of the geometry and the number of mesh cells required for a fine description prevents the use of DNS in the entire fuel zone. To perform the computation of the transfers in such a domain, modeling is required that combine the porous and turbulent models.

Thus, the fuel zone is described with less details using a porous modeling approach. The fine structure is substituted by an equivalent continuous medium with effective properties at the macroscopic scale. Since the fuel zone is composed of a large amount of identical elements, the equivalent continuous medium is homogeneous.

Introducing the turbulent problematic in the homogeneous porous medium, the issue is to get information on the characteristics of the turbulent transfers at the macroscopic scale. The modeling of turbulence in

a porous medium relies on the choice of two methods: one to model the turbulence and another to model the porous medium, both having to be compatible. A first approach is to introduce in LES-type modeling additional terms related to the friction created by the solid structures in the porous medium (Shaw and Schumann, 1992; Finnigan, 2000; Watanabe, 2004). However this approach is not relevant for a homogeneous porous medium for which the size of the pore is larger than the size of the turbulent structures. The second approach consists in combining the RANS modeling with the volume averaging method (Antohe and Lage, 1997; Nakayama and Kuwahara, 1999; Getachew et al., 2000; de Lemos and Pedras, 2001b,a). In the context of transfers in a nuclear core, this approach is more relevant and has been validated in different studies (Chandesris and Jamet, 2009b; Pinson et al., 2007; Drouin et al., 2010).

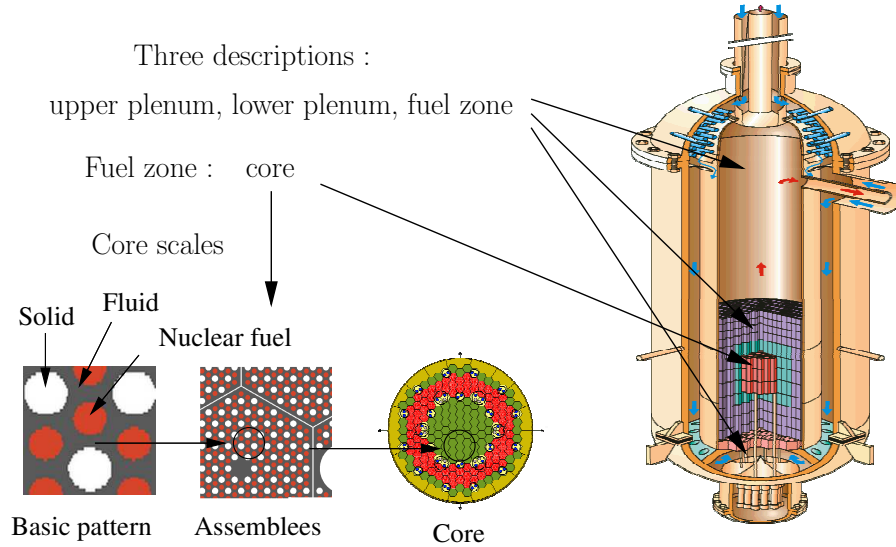


Figure 1.1: Description of a nuclear reactor vessel.

1.2 Modeling of transfers at a free-porous interface

The configuration where a porous medium succeeds to a free region is encountered in many industrial applications. Especially in the reactor vessel, that can be divided in three successive main zones as presented in Fig 1.1: a free medium (the lower plenum), a porous medium (the fuel zone) and another free medium (the upper plenum). The description of such geometries at the macroscopic scale using the porous formalism is relevant. At this scale of description, the domain is characterized by a macroscopic model in the homogeneous porous medium and standard models in the free regions connected by boundary conditions at the free-porous interfaces. The main modeling issue relies on the definition of appropriate boundary conditions at the free-porous interfaces. This issue has been the topic of many studies for momentum and heat transfers.

Momentum transfers

The transfers at a free-porous interface is studied first on the experiment of Beavers and Joseph (1967). In this experiment, Beavers and Joseph (1967) study a laminar flow over a porous medium. To model this problem, they consider the system as a porous medium and a free region separated by a surface of discontinuity. The models used in each region, Darcy in the porous region and Stokes in the free region, are coupled at the free-porous interface through a semi-empirical slip-condition:

$$\frac{\partial u}{\partial y} = \frac{\alpha}{\sqrt{K}}(u_B - U_D) \quad (1.1)$$

where u_B is the fluid velocity at the interface, U_D is the velocity in the porous medium far from the interface, \mathcal{K} is the permeability of the porous medium, α is a slip parameter and y is the direction normal to the interface. This heuristic approach gives information on the impact of the porous medium on the flow in the free channel through the slip parameter α . However, this parameter is not related to the macroscopic properties of the medium and the determination of its value requires many experiments. With this modeling, another question arises: the dependency of the slip coefficient with the interface location (Larson and Higdon, 1986, 1987; Saffman, 1971; Sahraoui and Kaviany, 1992).

The relation between the interfacial physical phenomena and the slip parameter α is made explicit deriving the boundary conditions with up-scaling methods based on the momentum balance. Using such an approach to couple the Darcy-Brinkman model in the porous region and the Stokes model in the free region, Ochoa-Tapia and Whitaker (1995a,b) show that the shear stress discontinuity at the interface arise from an excess quantity. In order to close this excess quantity, they postulate a jump condition involving a jump parameter β for a given interface:

$$\frac{\partial \langle u \rangle}{\partial y} \Big|_{y_m^+} - \frac{1}{\phi^p} \frac{\partial \langle u \rangle}{\partial y} \Big|_{y_m^-} = -\frac{\beta}{\sqrt{K}} \langle u \rangle \Big|_{y_m} \quad (1.2)$$

where ϕ^p is the porosity in the homogeneous porous medium, and $\langle u \rangle$ is the volume averaged velocity. Nevertheless, as for Beavers and Joseph (1967), the parameter β is not related to the macroscopic properties of the medium and depends on the interface location. Following the same idea Goyeau et al. (2003) succeed to relate the parameter β with continuous spatial variations of the porous structure within the transition zone. However β is also related to the variations of the velocity, which is an unknown of the problem.

To study this issue, Chandesris and Jamet (2006, 2007, 2009c,b,a) introduce an intermediate continuous scale of description, called *mesoscopic scale* (Fig 1.2). At this scale of description, the interface is continuous and the issue is to model the physical transfers specific of the interfacial region through a continuous modeling. Once the transfer characterisation is achieved, the continuous modeling obtained is replaced by an equivalent discontinuous model with jump conditions at the macroscopic scale. This approach, applied in the context of momentum transfer, allows to derive a closed jump condition. The jump condition involves closed excess values easily computable knowing the porosity and permeability profiles in the transition zone.

$$\frac{\partial \langle u \rangle}{\partial y} \Big|_{y_m^+} - \frac{1}{\phi^p} \frac{\partial \langle u \rangle}{\partial y} \Big|_{y_m^-} = \left(\left(\frac{\phi}{K} \right)^{ex} - (\phi)^{ex} \gamma \right) \langle u \rangle^{(0)} \quad (1.3)$$

where γ is a constant determined from the Darcy number and the porosity in the homogeneous porous medium. These excess quantities are linear functions of the interface location, and thus, the dependency between the jump parameter and the interface location is clarified.

Heat transfer

For heat transfer, successive works have brought valuable information to understand the issue of boundary conditions at a free-porous interface. First tests were performed using the application of boundary conditions at the nominal interface (defined by the position of the last solid grain (Beavers and Joseph, 1967)). Regarding conductive heat transfer, conditions of continuity for both the temperature and the heat flux can give good results (Prat, 1990). However, for more complex phenomena including convective transfer, these boundary conditions are inappropriate and may be corrected with a temperature jump involving a slip coefficient (Sahraoui and Kaviany, 1994) similar to the velocity jump introduced by Beavers and Joseph (1967). Thus, these studies show that it is possible to capture the interfacial heat transfer with semi-empirical boundary conditions, but the relation between the interfacial physical phenomena and the slip coefficient is not made explicit.

To study this issue, Ochoa-Tapia and Whitaker (1997) perform the up-scaling method developed for momentum transfer on the energy equations and derive a jump condition for the heat flux involving excess

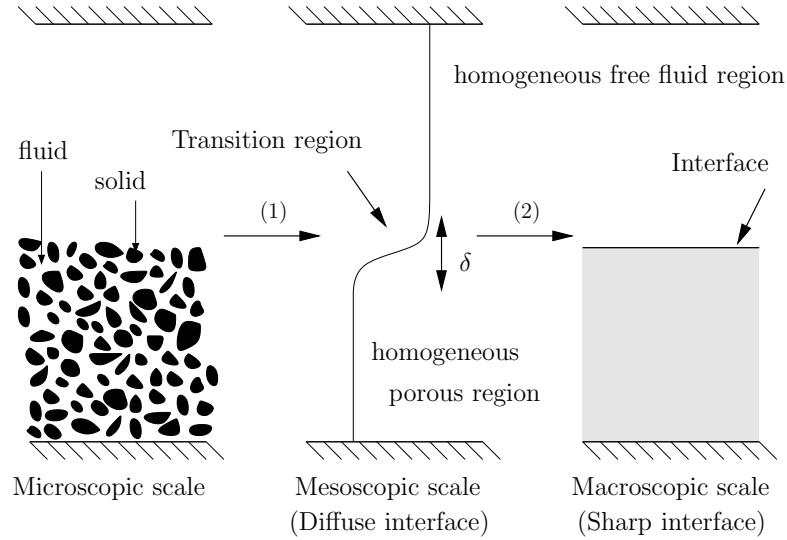


Figure 1.2: The three different scales of description of a free-porous interface.

values:

$$-\mathbf{n}_{pl} \left[\mathbf{K}^p \cdot \nabla \langle T \rangle^p - k^l \nabla \langle T \rangle^l \right] = \left((\langle \rho \rangle c_p) \frac{\partial \langle T \rangle}{\partial t} \right)^{ex} + (\nabla \cdot [(\langle \rho \rangle c_p) \langle \mathbf{u} \rangle \langle T \rangle - \mathbf{K} \cdot \nabla \langle T \rangle])^{ex} \quad (1.4)$$

where \mathbf{n}_{pl} is the unit vector normal to the interface from the porous region to the free region, $\langle T \rangle$ the volume-averaged temperature, \mathbf{K} the effective conductivity vector and the indices p and l stand for the porous and free regions respectively. These excess values are not closed due to the presence of averaged quantities unknown in the interfacial transition zone. Furthermore, the closure of the excess values by postulating a jump condition is inadequate because the jump parameter depends on the interface location. The use of an intermediate continuous scale of description, as proposed by Chandesris and Jamet (2006, 2007, 2009c) for momentum transfer allows to separate these two difficulties and will be used in the present work.

The main objective of this work is to study the heat transfers at the interface between a porous medium and a free region using the multi-scale approach presented by Chandesris and Jamet (2006, 2007, 2009c) for momentum transfer (see Fig 1.2).

At the microscopic scale, each solid grain is described and the interface is located considering the geometry of the solid matrix. For this scale of description, transfers are characterized by the Navier-Stokes equations for the momentum and energy conservation equation for the heat transfer. The first up-scaling step changes the scale of description from microscopic to mesoscopic using the volume averaging operator.

At the mesoscopic scale, the solid and fluid phases are substituted by an equivalent medium in the porous region and the interface is diffuse. Thus, the domain is composed of three regions: a homogeneous porous region where the effective properties are constant, a transition zone where the effective properties vary continuously and a free region with constant properties. The issue is to characterize the transfers by equations valid in the whole domain including the transition zone with continuous effective coefficients. To proceed a modeling step must be achieved for which questions arise:

- the form of the closed mesoscopic equations: How to model the non-closed terms characteristic of the porous description-type? Are the usual models available in the literature valid in the transition zone?

- the determination of the effective coefficients: How to determine the effective coefficients in the transition zone?

For the laminar momentum transfer, these questions are easily answered. Indeed, only one non-closed term exists that is modeled through a permeability coefficient known in the transition zone. For the heat transfer, there are four non-closed terms (tortuosity for the fluid phase, tortuosity for the solid phase, heat transfer coupling and dispersion) that require complex modelings involving numerous effective transfer coefficients.

The second up-scaling step changes the scale of description from mesoscopic to macroscopic using conservation principles.

At the macroscopic scale, the interface is modeled by a surface of discontinuity that separates the domain in two homogeneous regions, a porous and a free one. The issue is to replace the continuous modeling of the interface by equivalent closed jump conditions. Considering this issue, questions arise:

- the form of the boundary conditions that must apply at the interface: Are the physical quantities continuous or discontinuous at the free-porous interface?
- the value of the jump parameters related to these jump conditions: Are these jump parameters intrinsic quantities? How to determine them?
- the location of the surface of discontinuity.

The conservation constraints allow to derive the jump conditions from the difference between the macroscopic and mesoscopic descriptions (see 1.3). It results a surface excess quantity defined for a mesoscopic quantity ψ such that:

$$(\psi)^{(ex)} = \int_H (\psi - \psi_m) dH \quad (1.5)$$

where ψ_m is the macroscopic description of ψ . Among the existing conservation methods, the matched asymptotic expansions establishes the relationship between the jump condition and the interface location through the surface excess quantity of effective properties.

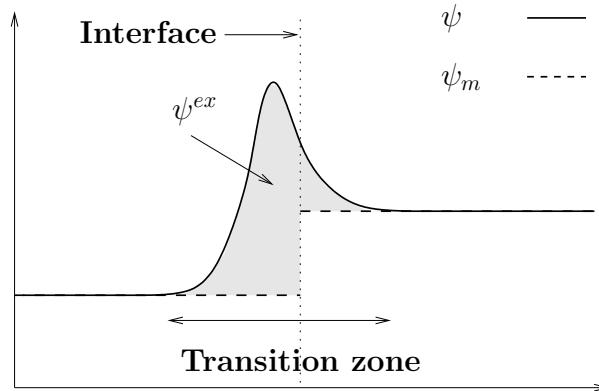


Figure 1.3: Surface excess definition

In this manuscript, we will use this multi scale approach for heat transfer problems (i) at local thermal equilibrium, (ii) at local thermal non-equilibrium and (ii) for a turbulent flow in partially porous domain.

1.3 Contents

This manuscript is organized as follows.

In Chapter 2, we review different macroscopic models existing in the literature to describe heat transfer

in a homogeneous porous medium at local thermal equilibrium and at local thermal non-equilibrium. Three methods to derive such models are presented:

- the heuristic method based on empirical modeling and the determination of the effective transfer coefficients using experiments;
- the volume averaging method based on homogenization methods and for which the effective transfer coefficients are determined using the length scale separation;
- the mixed method combining the volume averaging formalism with the empirical modelings and determining the effective transfer coefficients with numerical experiments.

In the context of the transfer modeling in a free-porous transition zone, these methods cannot be used directly. Thus, we develop another approach that is validated in a homogeneous porous medium through comparison with results given by the heuristic, volume averaging and mixed methods.

In Chapters 3 and 4, we study heat transfer in a system composed of a fluid-porous interface at local thermal equilibrium (LTE) and at local thermal non-equilibrium (LTNE). We apply the multi-scale approach based on three levels of description of the interface and two up-scaling steps presented by [Chandesris and Jamet \(2006, 2007, 2009c\)](#) for momentum transfer. The first up-scaling step gives a continuous modeling of the transfers in the whole domain including the interfacial transition zone using the models presented in Chapter 2. The second up-scaling step leads to the determination of the jump conditions that must be applied at the discontinuous interface between the homogeneous porous medium and the free medium at the macroscopic scale. Then, the closed macroscopic model obtained with this multi-scale approach is discussed to determine a preferred interface location.

Chapter 3 considers transfers at local thermal equilibrium and gives a clear understanding of the multi-scale approach and the discussion about the interface location.

Chapter 4 deals with transfers at local thermal non-equilibrium. In this case, a new issue appears: the coupling of a two-temperature model in the homogeneous porous region with a one-temperature model in the free region. To overcome this difficulty, related to the different number of equations in each domain, we introduce of a new writing. Thus, the whole multi-scale approach can be performed and the interface location discussed.

In Chapters 5 and 6, we study turbulent heat transfer in a fluid-porous domain. The issue is to bring a better understanding of the physics at the free-porous interface and to characterize the turbulent transfers through accurate models.

Chapter 5 presents a direct numerical simulation (DNS) of turbulent heat transfer realized on the configuration chosen in ([Breugem and Boersma, 2005](#); [Breugem et al., 2005](#)) to study turbulent flow at a fluid-porous interface. The DNS solves directly the Navier-Stokes equations and the energy conservation equation without requiring any closure model. Thus it is considered as a *numerical experiment* and gives access to local quantities of the heat transfer. The results (temperature fields, rms temperature fluctuations, heat flux, cross-correlation) of the DNS offer a first theoretical basis on the turbulent statistic of heat transfer at a free-porous interface. Furthermore, it gives access to valuable information about the turbulence modeling in a partially porous domain (turbulent viscosity, turbulent kinetic energy, dissipation rate, turbulent diffusivity)

Chapter 6 introduces the macroscopic RANS modeling in the homogeneous porous medium and the common RANS modeling in the free region. The issue is to determine the jump conditions that must be applied at the free-porous interface to couple the two turbulent models. The multi-scale approach, used in Chapters 3 and 4, is applied to the local k - ϵ with turbulent Prandtl model. Each up-scaling step is accompanied by a turbulence modeling for the momentum and heat transfers. At last, a closed macroscopic model is obtained for a unique interface location and its validity is verified by comparing the results with the DNS ones.

Chapter 2

Heat transfer modeling in homogeneous porous media

2.1 Porous medium modeling

2.1.1 Context

A porous medium is a heterogeneous system made of a solid matrix with its voids filled with fluids. Such a structure has the characteristic to possess various length scales of observation. In this study, we distinguish the two main length scales:

- the microscopic scale or pore scale where each solid grain is described individually, the associated lengthscale is the pore diameter l_c ;
- the macroscopic scale corresponding to the lengthscale l_M of the observed phenomena.

At the macroscopic scale, the porous medium is represented by an equivalent homogeneous medium. The homogeneous medium is characterized by effective properties standing for the overall effects of the physical phenomena occurring at the pore scale. Different methods exist to obtain the description of the porous medium at the macroscopic scale. However, we present here only the methods used in the remainder of the manuscript to study heat transfer at a free-porous interface.

As with any technological problem, the treatment of fluid flow and heat transfer starts from direct empirical relations where the macroscopic laws are postulated and the medium properties are determined experimentally. Such a method is called **heuristic** and has the advantage of being generally intuitive.

In 1967, Whitaker introduces a method based on homogenization principles to change the scale of description of a porous medium from microscopic to macroscopic (Whitaker, 1967, 1969). This method is named the **volume averaging method** and can be decomposed into three steps. First the governing equations at the local scale of a given quantity, ψ_α , are integrated on a volume of averaging to derive the governing equations at the macroscopic scale. The averaged quantity is noted $\langle \psi_\alpha \rangle$. This spatial smoothing process makes appear non-closed terms in the averaged equations that involve a spatial deviation term, noted $\tilde{\psi}_\alpha$. This term is characteristic of the microscopic scale, and thus, the averaged equations are not closed. The second step closes the open terms with a closure relation for the spatial deviation term $\tilde{\psi}_\alpha$. The closure relation expresses the spatial deviation $\tilde{\psi}_\alpha$ as a function of macroscopic averaged quantities and closure coefficients. These closure variables are characteristic of the microscale and can be related to the effective transfer coefficients. In the third step one determines the closure variables through the resolution of closure problems using the length scale separation between the spatial deviation term, the representative volume of averaging and the averaged term. Following the three steps of the volume

averaging method, the problem at the macroscopic scale is entirely closed and characterized. The advantage of this method is to derive the macroscopic model from the microscopic governing equations. It relies on the strong hypothesis of the length scale separation. However, in the context of the heat transfer study at a free-porous interface, this method cannot be directly used to characterize the transfers because the length scale separation is not verified at the interface.

In 1996, another approach is introduced in (Kuwahara et al., 1996; Kuwahara and Nakayama, 1999; Kuwahara et al., 2001) that we call the **mixed method**. This method uses the formalism and the first step of the volume averaging method to derive the non-closed macroscopic equations from the microscopic equations. However, the closed form of the governing macroscopic equations are postulated and not formally proved as in the volume averaging method. The expressions for the effective coefficients are determined analytically by identifying the terms in the postulated closed equations and the non-closed terms. Thanks to this identification, the effective coefficients are then computed with temperature and velocity fields solutions of numerical simulations. In this context, the numerical simulations correspond to experimentations with as many measuring points as mesh cells. The limits of this method are the postulation of the closed equations. Indeed, the postulated two-temperature model does not involve enough physical phenomena, that leads to incoherent results for the effective transfer coefficients, as we will see in Section 2.3.4. The advantage of this method is that it gives access to the determination of the effective transfer coefficients without consideration of length scale separation. Thus, this method of determination can be used in the transition zone where the length scale separation is not valid.

The present work proposes an alternative approach that improves the mixed method in the case of heat transfer at local thermal non-equilibrium (see Fig. 2.1). This alternative method uses the advantage of the mixed and volume averaging methods. First, the closed and the non-closed macroscopic models are derived from the microscopic governing equations with the first and second steps of the volume averaging method. Then, the determination of the effective coefficients is achieved by identification between the closed and the non-closed models following the mixed method. For homogeneous porous medium, this alternative method does not present any advantage because the volume averaging method gives more accurate results. The great interest is at the free-porous interface, where the volume averaging method cannot be used. On the contrary, the alternative method is easily applicable assuming the validity of the closed macroscopic model in this region. This alternative method is used in Chapter 4 to characterize heat transfer at a free-porous interface. The issue of this chapter is to verify this method for homogeneous porous media for which the corresponding results are numerous. We notice, that the approach cannot be discriminated at the free-porous interface

In the following, we present the macroscopic modelings obtained by the three different methods to characterize the heat transfer in a homogeneous porous medium at local thermal equilibrium (LTE) and at non-local thermal equilibrium (LTNE) (see Fig. 2.1). In the last section, the alternative method is presented and validated in a homogeneous porous medium comparing with the results given by the volume averaging method (Quintard et al., 1997). Furthermore, this chapter presents the closed macroscopic equations that will be used in Chapters 3 and 4 to study heat transfer at the free-porous interface.

2.1.2 The volume averaging formalism

In this section, we present the first step of the volume averaging method changing the scale of description from microscopic to macroscopic. From the governing equations at the local scale, the averaged equations are rigorously derived. These continuous equations characterize all the physical phenomena existing in the porous system, but are not closed.

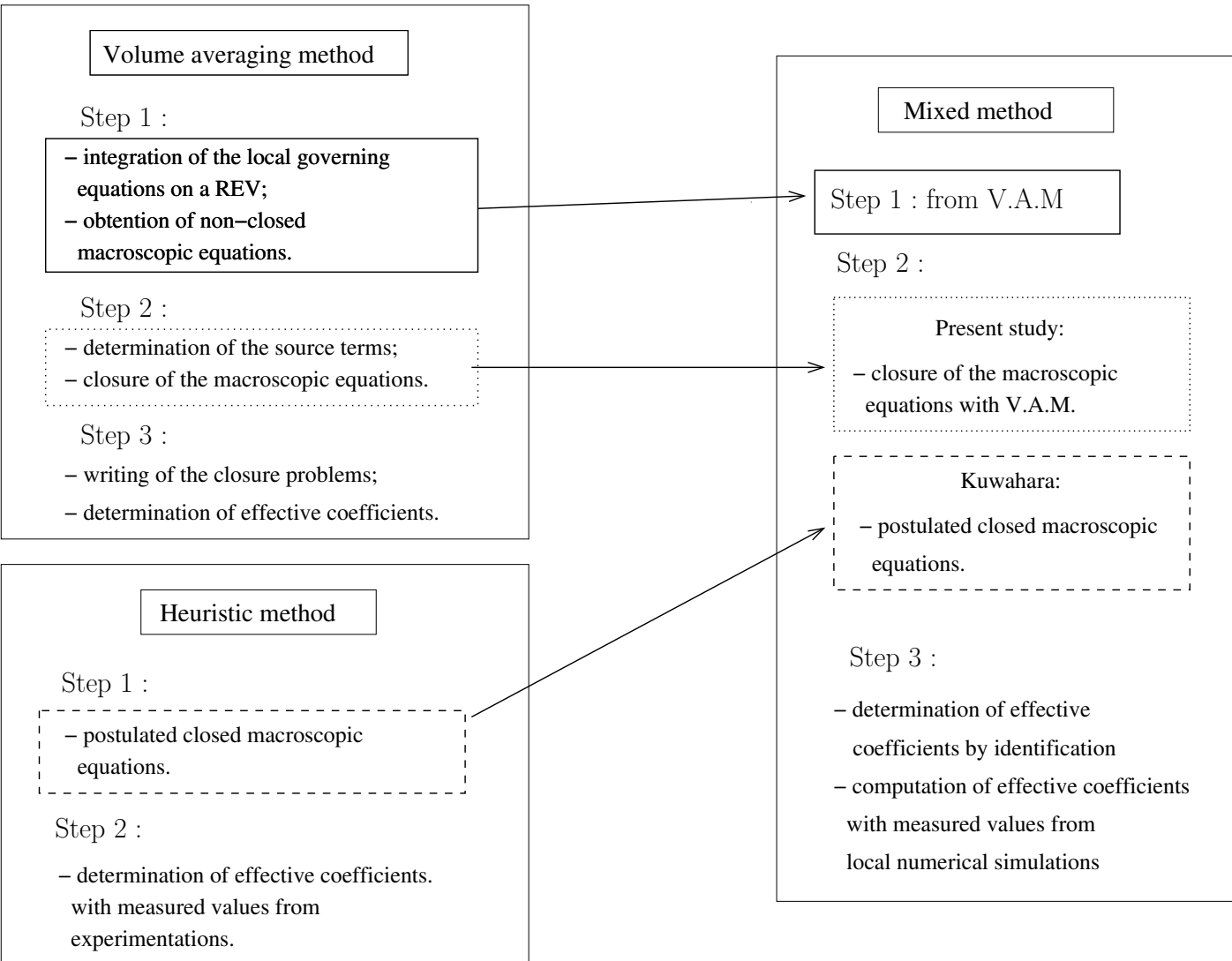


Figure 2.1: Synthesis of the different approaches.

Definition and properties

The spatial smoothing process is realized by combining a phase indicator function and a weighting function. The definition of the superficial volume average of any quantity ψ_α of the α phase α is:

$$\langle \psi_\alpha \rangle (\mathbf{x}) = \frac{\int_V m_p(\mathbf{r} - \mathbf{x}) \chi_\alpha(\mathbf{r}) \psi_\alpha(\mathbf{r}) dV}{\int_V m_p(\mathbf{r}) dV} \quad (2.11)$$

where χ_α is the indicator function of the phase α , m_p is a weighting function, \mathbf{x} is the centroid of the averaging volume related to the relative position vector by (see Fig. 2.2):

$$\mathbf{y} = \mathbf{r} - \mathbf{x} \quad (2.2)$$

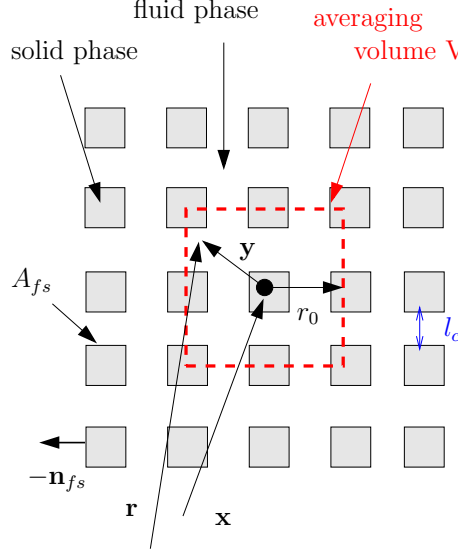


Figure 2.2: Illustration of the volume averaging technique for an ordered porous medium.

The intrinsic volume average is related to the superficial volume average $\langle \phi_\alpha \rangle^\alpha$ by the relation:

$$\langle \psi_\alpha \rangle^\alpha(\mathbf{x}) = \frac{\langle \psi_\alpha \rangle(\mathbf{x})}{\phi_\alpha(\mathbf{x})} \quad (2.3)$$

where ϕ_α is the volume fraction of the α phase within the averaging volume ($\phi_\alpha = V_\alpha(\mathbf{x})/V$). For conciseness, the following formalisms is introduced:

$$\langle \psi_\alpha \rangle(\mathbf{x}) = \frac{1}{V} \int_V \psi_\alpha(\mathbf{r}) dV \quad (2.4)$$

$$\langle \psi_\alpha \rangle^\alpha(\mathbf{x}) = \frac{1}{V_\alpha} \int_{V_\alpha} \psi_\alpha(\mathbf{r}) dV \quad (2.5)$$

and for the volume averaging on the $A_{\alpha\beta}$ interface (separating phases α and β) this formalism corresponds to:

$$\frac{1}{V} \int_{A_{\alpha\beta}} \psi_\alpha(\mathbf{r}) dA = \frac{\int_{A_{\alpha\beta}} m_p(\mathbf{r} - \mathbf{x}) \chi_\alpha(\mathbf{r}) \psi_\alpha(\mathbf{r}) dA}{\int_V m_p(\mathbf{r}) dV} \quad (2.6)$$

In addition, the field ψ_α can be splitted into an averaged value and a spatial deviation term as follows (Gray and Lee, 1977):

$$\psi_\alpha = \langle \psi_\alpha \rangle^\alpha + \tilde{\psi}_\alpha \quad (2.7)$$

The volume averaging operator verifies two properties:

- the linearity, due to the linearity of the summation on a closed volume;
- the idempotence $\langle \tilde{\psi}_\alpha \rangle^\alpha \approx 0$, when the length scales separation between the microscopic and the macroscopic scale is verified. This property is valid in a homogeneous porous medium, but not at the free-porous interface inside the transition zone.

In particular the length scale separation in a periodic porous medium imposes the following condition for the filter size r_0 :

$$l_c \approx r_0 \ll L_M$$

where l_c and L_M are respectively the length scales of the microscopic and the macroscopic variations.

Theorem and classical developments

The averaged equations involve gradients and to express the terms $\langle \nabla \psi_\alpha \rangle$ as functions of the macroscopic variable $\langle \psi_\alpha \rangle$, the differentiation and integration operators must be interchanged. This can be done with the spatial averaging theorem (Whitaker, 1999):

$$\langle \nabla \psi_\alpha \rangle (\mathbf{x}) = \nabla \langle \psi_\alpha \rangle (\mathbf{x}) + \frac{1}{V} \int_{A_{\alpha\beta}} \psi_\alpha(\mathbf{r}) \mathbf{n}_{\alpha\beta} dA \quad (2.8)$$

where $\mathbf{n}_{\alpha\beta}$ is the unit normal vector directed from the phase α to the phase β .

Introducing the spatial deviation term $\tilde{\psi}_\alpha$, the intrinsic average $\langle \psi_\alpha \rangle^\alpha$ (see equations (2.7) and (2.3)) and the following relation for the porosity gradient,

$$\nabla \phi_\alpha(\mathbf{x}) = -\frac{1}{V} \int_{A_{\alpha\beta}} \mathbf{n}_{\alpha\beta} dA \quad (2.9)$$

the theorem (2.8) is rewritten:

$$\langle \nabla \psi_\alpha \rangle (\mathbf{x}) = \phi_\alpha \nabla \langle \psi_\alpha \rangle^\alpha (\mathbf{x}) + \frac{1}{V} \int_{A_{\alpha\beta}} \left(\langle \psi_\alpha \rangle^\alpha (\mathbf{r}) - \langle \psi_\alpha \rangle^\alpha (\mathbf{x}) + \tilde{\psi}_\alpha(\mathbf{r}) \right) \mathbf{n}_{\alpha\beta} dA \quad (2.10)$$

Based on the theorem (2.10), two classical relations are derived.

$$\langle \nabla \cdot \nabla \psi_\alpha \rangle (\mathbf{x}) = \nabla \cdot \langle \nabla \psi_\alpha \rangle (\mathbf{x}) + \frac{1}{V} \int_{A_{\alpha\beta}} \left(\nabla \langle \psi_\alpha \rangle^\alpha (\mathbf{r}) + \nabla \tilde{\psi}_\alpha(\mathbf{r}) \right) \cdot \mathbf{n}_{\alpha\beta} dA \quad (2.11)$$

$$\langle \nabla \cdot \mathbf{v}_f \psi_\alpha \rangle (\mathbf{x}) = \nabla \cdot \langle \mathbf{v}_f \psi_\alpha \rangle (\mathbf{x}) + \underbrace{\frac{1}{V} \int_{A_{\alpha\beta}} \mathbf{n}_{\alpha\beta} \cdot \mathbf{v}_f(\mathbf{r}) \psi_\alpha(\mathbf{r}) dA}_{=0} \quad (2.12)$$

because the velocity is zero at the fluid-solid interfaces: $\mathbf{v}_f = 0$ on $A_{\alpha\beta}$.

Derivation of the volume averaged conductive-convective equations

We consider a laminar flow through a rigid homogeneous porous medium where the fluid and solid properties (density, viscosity, heat capacity) are assumed constant. For stationary cases, the governing equations at the microscopic scale are given, in the fluid phase by, the Navier-Stokes equations and the convective-conductive equation, and, in the solid phase, by the conductive equation:

$$\nabla \cdot \mathbf{v}_f = 0 \quad (2.13)$$

$$(\mathbf{v}_f \cdot \nabla) \mathbf{v}_f = -\frac{1}{\rho} \nabla p + \nu \nabla^2 \mathbf{v}_f \quad (2.14)$$

$$(\rho c_p)_f \nabla \cdot (\mathbf{v}_f T_f) = \nabla \cdot (k_f \nabla T_f), \text{ for the fluid phase} \quad (2.15)$$

$$0 = \nabla \cdot (k_s \nabla T_s), \text{ for the solid phase} \quad (2.16)$$

associated to the continuity conditions and the no-slip condition at the fluid-solid interfaces A_{fs} :

$$T_f = T_s \quad (2.17)$$

$$\mathbf{n}_{fs} \cdot (k_f \nabla T_f) = \mathbf{n}_{fs} \cdot (k_s \nabla T_s) \quad (2.18)$$

$$\mathbf{v}_f = 0 \quad (2.19)$$

where the subscripts f and s stand for the fluid and solid phases respectively.

The up-scaling process is obtained applying the volume average to the local temperature equations (2.15), (2.16).

The convective term is rewritten introducing a dispersive flux τ_{Tv} :

$$\langle (\rho c_p)_f \nabla \cdot (\mathbf{v}_f T_f) \rangle = (\rho c_p)_f \nabla \cdot \left(\langle \mathbf{v}_f \rangle \langle T_f \rangle^f \right) + (\rho c_p)_f \nabla \cdot \tau_{Tv} \quad (2.20)$$

$$\text{where} \quad \tau_{Tv} = \langle \mathbf{v}_f T_f \rangle - \langle \mathbf{v}_f \rangle \langle T_f \rangle^f \quad (2.21)$$

Using equation (2.11) to express the conductive term of equation (2.15), one obtains:

$$\langle \nabla \cdot (k_f \nabla T_f) \rangle = \nabla \cdot \langle k_f \nabla T_f \rangle + \frac{k_f}{V} \int_{A_{fs}} \mathbf{n}_{fs} \cdot \left(\nabla \langle T_f \rangle^f(\mathbf{r}) + \nabla \tilde{T}_f(\mathbf{r}) \right) dA \quad (2.22)$$

Then, applying the relation (2.10), this term can be rewritten as:

$$\begin{aligned} \langle \nabla \cdot (k_f \nabla T_f) \rangle &= \nabla \cdot \left(k_f \phi_f \nabla \langle T_f \rangle^f \right) + \nabla \cdot \left(\frac{k_f}{V} \int_{A_{fs}} \tilde{T}_f(\mathbf{r}) \mathbf{n}_{fs} dA \right) + \\ &\quad \nabla \cdot \left(\frac{k_f}{V} \int_{A_{fs}} \left(\langle T_f \rangle^f(\mathbf{r}) - \langle T_f \rangle^f(\mathbf{x}) \right) \mathbf{n}_{fs} dA \right) + \\ &\quad \frac{k_f}{V} \int_{A_{fs}} \mathbf{n}_{fs} \cdot \left(\nabla \langle T_f \rangle^f(\mathbf{r}) + \nabla \tilde{T}_f(\mathbf{r}) \right) dA \end{aligned} \quad (2.23)$$

The same process is applied to the conductive term of the solid phase, which gives:

$$\begin{aligned} \langle \nabla \cdot (k_s \nabla T_s) \rangle &= \nabla \cdot k_s \phi_s \nabla \langle T_s \rangle^s + \nabla \cdot \frac{k_s}{V} \int_{A_{sf}} \tilde{T}_s(\mathbf{r}) \mathbf{n}_{sf} dA + \\ &\quad \nabla \cdot \frac{k_s}{V} \int_{A_{sf}} \left(\langle T_s \rangle^s(\mathbf{r}) - \langle T_s \rangle^s(\mathbf{x}) \right) \mathbf{n}_{sf} dA + \\ &\quad \frac{k_s}{V} \int_{A_{sf}} \mathbf{n}_{sf} \cdot \left(\nabla \langle T_s \rangle^s(\mathbf{r}) + \nabla \tilde{T}_s(\mathbf{r}) \right) dA \end{aligned} \quad (2.24)$$

Finally, the governing equations for the heat transfer at the macroscopic scale can be written as:

For the fluid phase

$$\begin{aligned} (\rho c_p)_f \nabla \cdot \left(\langle \mathbf{v}_f \rangle \langle T_f \rangle^f \right) &= \underbrace{\nabla \cdot k_f \phi_f \nabla \langle T_f \rangle^f}_{\text{diffusion}} + \underbrace{\nabla \cdot \frac{k_f}{V} \int_{A_{fs}} \tilde{T}_f(\mathbf{r}) \mathbf{n}_{fs} dA}_{\text{tortuosity}} - \underbrace{(\rho c_p)_f \nabla \cdot \tau_{Tv}}_{\text{thermal dispersion}} \\ &\quad + \underbrace{\nabla \cdot \left[\frac{k_f}{V} \int_{A_{fs}} \left(\langle T_f \rangle^f(\mathbf{r}) - \langle T_f \rangle^f(\mathbf{x}) \right) \mathbf{n}_{fs} dA \right]}_{\approx 0 \text{ when } l_c \approx r_0 < l_M} + \\ &\quad \underbrace{\frac{k_f}{V} \int_{A_{fs}} \mathbf{n}_{fs} \cdot \left(\nabla \langle T_f \rangle^f(\mathbf{r}) + \nabla \tilde{T}_f(\mathbf{r}) \right) dA}_{\text{heat coupling}} \end{aligned} \quad (2.25)$$

For the solid phase

$$0 = \underbrace{\nabla \cdot k_s \phi_s \nabla \langle T_s \rangle^s}_{\text{diffusion}} + \underbrace{\nabla \cdot \frac{k_s}{V} \int_{A_{sf}} \tilde{T}_s(\mathbf{r}) \mathbf{n}_{sf} dA}_{\text{tortuosity}} + \underbrace{\nabla \cdot \left[\frac{k_s}{V} \int_{A_{sf}} (\langle T_s \rangle^s(\mathbf{r}) - \langle T_s \rangle^s(\mathbf{x})) \mathbf{n}_{sf} dA \right]}_{\approx 0 \text{ when } l_c \approx r_0 < l_M} + \underbrace{\frac{k_s}{V} \int_{A_{sf}} \mathbf{n}_{sf} \cdot (\nabla \langle T_s \rangle^s(\mathbf{r}) + \nabla \tilde{T}_s(\mathbf{r})) dA}_{\text{heat coupling}} \quad (2.26)$$

At the macroscopic scale, the governing equations are composed of:

- terms of diffusion for the fluid and solid phases;
- terms of tortuosity traducing the resistance to the fluid diffusion caused by the presence of the solid phase and inversely;
- a term of dispersion in the fluid phase corresponding to effects of the velocity spatial variations on the heat transfer;
- terms of coupling between the phases through fluid-solid heat transfer;
- a term that vanishes when the length scale separation is verified, written here to show all the hypotheses.

These macroscopic governing equations (2.25), (2.26) are not closed because the dispersive flux τ_{T_v} and the integral terms involve spatial deviation terms characteristic of the microscopic scale (see equations (2.21) and (2.25)-(2.26)). To close the macroscopic equations, these terms have to be modeled, *i.e* expressed as functions of macroscopic variables only.

As we have just recalled, the first step of the volume averaging method allows to derive the governing macroscopic equations from the microscopic scale equations. These equations have been obtained without any length scale consideration and present all the physical phenomena existing at the macroscopic scale. For this reason, there are used in the chapters 3 and 4 to characterize the heat transfer at the porous-free interface where the length scale separation is not valid. However the topic of this chapter is about homogeneous porous media, and the validity of the length scale separation allows some simplifications.

Length scale separation and associated simplifications

In a homogeneous porous medium where the length scale separation is valid, the gradient of volume averaged terms can be considered constant within the representative elementary volume, which leads to, using the relation (2.9):

$$\frac{1}{V} \int_{A_{sf}} \mathbf{n}_{sf} \cdot \nabla \langle T_s \rangle^s(\mathbf{r}) dA \approx -\nabla \langle T_s \rangle^s(\mathbf{x}) \cdot \nabla \phi_f = 0 \quad (2.27)$$

because the porosity is constant in a homogeneous porous medium.

Furthermore, the additional term $1/V \int_{A_{fs}} (\langle T_f \rangle^f(\mathbf{r}) - \langle T_f \rangle^f(\mathbf{x})) \mathbf{n}_{fs} dA$ of equation (2.25) can be neglected. Using a Taylor expansion in \mathbf{y} limited to first order, $\langle T_f \rangle^f(\mathbf{r})$ is rewritten as

$$\langle T_f \rangle^f(\mathbf{r}) = \langle T_f \rangle^f(\mathbf{x}) + \mathbf{y} \cdot \frac{\partial \langle T_f \rangle^f(\mathbf{x})}{\partial \mathbf{x}} + O(\mathbf{y}^2) \quad (2.28)$$

$$\text{where } \mathbf{y} = \mathbf{r} - \mathbf{x} \quad (2.29)$$

Thus, with the same argument as previously, one obtains:

$$\frac{1}{V} \int_{A_{fs}} \left(\langle T_f \rangle^f(\mathbf{r}) - \langle T_f \rangle^f(\mathbf{x}) \right) \mathbf{n}_{fs} dA \approx \frac{1}{V} \frac{\partial \langle T_f \rangle^f(\mathbf{x})}{\partial \mathbf{x}} \int_{A_{fs}} \mathbf{y} dA = 0 \quad (2.30)$$

by definition of the integration of \mathbf{y} on the representative elementary volume for a periodic porous medium.

The dispersive flux τ_{Tv} , defined by the relation (2.21) can be rewritten using spatial deviations for T_f and \mathbf{v}_f such that:

$$\tau_{Tv} = \left\langle (\langle \mathbf{v}_f \rangle^f + \tilde{\mathbf{v}}_f)(\langle T_f \rangle^f + \tilde{T}_f) \right\rangle - \left(\phi_f \langle \mathbf{v}_f \rangle^f \langle T_f \rangle^f \right) \quad (2.31)$$

Then, under the length scale separation constraint, the linearity and the idempotence of the volume averaging leads to (see (Carbonell and Whitaker, 1984)):

$$\tau_{Tv} = \left\langle \tilde{\mathbf{v}}_f \tilde{T}_f \right\rangle \quad (2.32)$$

Finally the governing equations for the heat transfer at the macroscopic scale take the following forms:
For the fluid phase

$$\begin{aligned} (\rho c_p)_f \nabla \cdot \left(\langle \mathbf{v}_f \rangle \langle T_f \rangle^f \right) = & \underbrace{\nabla \cdot k_f \phi_f \nabla \langle T_f \rangle^f}_{\text{diffusion}} + \underbrace{\nabla \cdot \frac{k_f}{V} \int_{A_{fs}} \tilde{T}_f \mathbf{n}_{fs} dA}_{\text{tortuosity}} - \underbrace{\nabla \cdot (\rho c_p)_f \left\langle \tilde{T}_f \tilde{\mathbf{v}}_f \right\rangle}_{\text{thermal dispersion}} + \\ & \underbrace{\frac{k_f}{V} \int_{A_{fs}} \mathbf{n}_{fs} \cdot \nabla \tilde{T}_f dA}_{\text{heat coupling}} \end{aligned} \quad (2.33)$$

For the solid phase

$$0 = \underbrace{\nabla \cdot k_s \phi_s \nabla \langle T_s \rangle^s}_{\text{diffusion}} + \underbrace{\nabla \cdot \frac{k_s}{V} \int_{A_{sf}} \tilde{T}_s \mathbf{n}_{sf} dA}_{\text{tortuosity}} + \underbrace{\frac{k_s}{V} \int_{A_{sf}} \mathbf{n}_{sf} \cdot \nabla \tilde{T}_s dA}_{\text{heat coupling}} \quad (2.34)$$

The averaged equations (2.33) and (2.34) are not closed, because the terms of tortuosity, dispersion and heat coupling involve spatial deviation terms characteristic of the local scale. In order to close the equations, these terms have to be modeled.

In this section, we presented the volume averaging formalism and performed the first step of the volume averaging method. From the governing equations at the microscopic scale, the averaged equations (2.33) and (2.34) are derived. These equations characterize all the physical phenomena existing for porous transfers, but they are not closed. The heuristic method, the mixed method and the volume averaging method suggest different modelings to close the averaged equations (2.33) and (2.34). In the following, we present the closed averaged equations existing for heat transfer at local thermal equilibrium and local thermal non-equilibrium.

2.2 One-temperature model

In this section, we study heat transfer at local thermal equilibrium where the temperature difference between the fluid and solid phases is assumed negligible. For such a heat transfer, the closed macroscopic model is presented as well as the determination of the associated effective coefficient using the volume averaging method. This case is very simple and the three approaches agree on the form of the closed macroscopic model and the values of the effective coefficient.

2.2.1 Closure of the macroscopic equation

At local thermal equilibrium the intrinsic average temperature of the fluid and solid phases are assumed to be equal:

$$\langle T_f \rangle^f \approx \langle T_s \rangle^s \quad (2.35)$$

with at the fluid-solid interface A_{fs} :

$$\tilde{T}_f \approx \tilde{T}_s \quad (2.36)$$

Let us recall that inside V_f and V_s , the distribution of deviations \tilde{T}_f and \tilde{T}_s differ.

A spatial averaged temperature $\langle T \rangle$ is introduced such that:

$$\langle T \rangle = \langle T_f \rangle + \langle T_s \rangle \quad (2.37)$$

It verifies

$$\langle T \rangle \approx \langle T_f \rangle^f \approx \langle T_s \rangle^s \quad (2.38)$$

In this context, the macroscopic equations (2.33) and (2.34) are added to give a one-temperature transport equation:

$$\begin{aligned} (\rho c_p)_f \nabla \cdot (\langle \mathbf{v}_f \rangle \langle T \rangle) = & \underbrace{\nabla \cdot (k_f \phi_f + k_s \phi_s) \nabla \langle T \rangle}_{\text{diffusion}} + \underbrace{\nabla \cdot \left[\frac{k_f - k_s}{V} \int_{A_{fs}} \tilde{T}_f(\mathbf{r}) \mathbf{n}_{fs} dA \right]}_{\text{tortuosity}} \\ & - \underbrace{\nabla \cdot (\rho c_p)_f \langle \tilde{T}_f \tilde{\mathbf{v}}_f \rangle}_{\text{thermal dispersion}} \end{aligned} \quad (2.39)$$

The macroscopic transport equation is not closed because the integral term and the thermal dispersion term involve quantities characteristic of the local scale: \tilde{T}_f and $\tilde{\mathbf{v}}_f$.

The heuristic and the mixed method postulate the form of the closed macroscopic equation from empirical considerations. It allows to close the tortuosity and dispersion terms with a temperature gradient $\nabla \langle T \rangle$ (Fried and Combarnous, 1971; Kaviani, 1995; Han et al., 1985; Kuwahara et al., 1996; Kuwahara and Nakayama, 1999). The volume averaging method, performing the second step, gives an identical form of the closed macroscopic equation (Carbonell and Whitaker, 1984). Following this approach we detail here the developments.

In order to close the macroscopic equation (2.39), the spatial deviation terms \tilde{T}_f must be expressed as functions of the source terms characteristic of the macroscopic scale. For this reason, one looks for the differential equation and boundary condition of \tilde{T}_f . They are obtained by subtracting the non-closed macroscopic equations (2.39) divided by the porosity ϕ_f with the local governing equation for the fluid phase (2.15). Thus:

$$\begin{aligned} (\rho c_p)_f \nabla \cdot (\langle \mathbf{v}_f \rangle^f \tilde{T}_f) + (\rho c_p)_f \tilde{\mathbf{v}}_f \cdot \nabla \tilde{T}_f + (\rho c_p)_f \tilde{\mathbf{v}}_f \cdot \underbrace{\nabla \langle T \rangle}_{\text{source term}} = & \nabla \cdot k_f \nabla \tilde{T}_f + \nabla \cdot k_s \frac{\phi_s}{\phi_f} \underbrace{\nabla \langle T \rangle}_{\text{source term}} \\ & - \nabla \cdot \frac{k_f - k_s}{\phi_f V} \int_{A_{fs}} \tilde{T}_f(\mathbf{r}) \mathbf{n}_{fs} dA + \nabla \cdot (\rho c_p)_f \langle \tilde{T}_f \tilde{\mathbf{v}}_f \rangle^f \end{aligned} \quad (2.40)$$

since $\nabla \cdot \tilde{\mathbf{v}}_f = 0$.

The equation (2.40) makes appear the source term $\nabla \langle T \rangle$. Thus, one can relate the spatial deviation \tilde{T}_f to the macroscopic quantity $\nabla \langle T \rangle$ such as

$$\tilde{T}_f = \mathbf{b}_f \cdot \nabla \langle T \rangle \quad (2.41)$$

where \mathbf{b}_f is a vector .

Introducing the writing for the fluid fluctuation in the non-closed macroscopic equation (2.39) and considering the length scale separation, one obtains the following closed one-temperature model:

$$(\rho c_p)_f \nabla \cdot (\langle \mathbf{v}_f \rangle^f \langle T \rangle) = \nabla \cdot (\overline{\overline{K}} \cdot \nabla \langle T \rangle) \quad (2.42)$$

where $\overline{\overline{K}}$ is the total effective thermal conductivity tensor defined by:

$$\overline{\overline{K}} = k_f \phi_f + k_s \phi_s + \underbrace{\frac{k_f - k_s}{V} \int_{A_{fs}} \mathbf{b}_f \mathbf{n}_{fs} dA}_{\text{tortuosity tensor}} - (\rho c_p)_f \underbrace{\langle \mathbf{b}_f \tilde{\mathbf{v}}_f \rangle}_{\text{dispersion tensor}} \quad (2.43)$$

For heat transfer at local thermal equilibrium, the closed macroscopic equation is a one-temperature model (2.42) involving a convective and effective conductive phenomena. The effective conductive phenomenon is characterized by an effective thermal conductivity tensor $\overline{\overline{K}}$ at the macroscopic scale. In the following, we present the determination of $\overline{\overline{K}}$ for the three approaches.

2.2.2 Determination of the effective thermal conductivity tensor

The literature associated to the characterization of the effective thermal conductivity tensor is significant and this paragraph does not draw up a detailed list. For more informations, we suggest Kaviany's book (Kaviany, 1995).

For the heuristic approach

The heuristic approach was the first to give information on the tortuosity tensor and on the dispersion tensor. Despite the lack of formalism, this approach gives the right physics and the correlations connecting the effective coefficients with the Peclet number are still relevant. The results for the tortuosity phenomenon are abounding and we recommend the reader to refer to Kaviany's literature review (Kaviany, 1995). For the dispersion phenomenon, we summarize here the mean observations. Thus, the dispersion in the flow direction is constant for Peclet numbers $Pe < 1$, then increases as Pe^2 for Peclet numbers $Pe > 1$. In the direction normal to the flow, the dispersion is independent of the Peclet number. These experimental results obtained by Fried and Combarous (1971) and Han et al. (1985) are usually used as reference by the mixed and volume averaging methods, that involve numerical tools.

For the mixed approach

Kuwahara et al. (1996) and Kuwahara and Nakayama (1999) present a method to determine the effective thermal conductivity. In their study (Kuwahara et al., 1996; Kuwahara and Nakayama, 1999), they distinguish different parts of the effective thermal conductivity such as:

$$\overline{\overline{K}} = k_e \overline{\overline{I}} + \overline{\overline{K}}_{tor} + \overline{\overline{K}}_{dis} \quad (2.44)$$

where k_e is the equivalent conductivity, $\overline{\overline{K}}_{tor}$ the tortuosity tensor and $\overline{\overline{K}}_{dis}$ the dispersion tensor. The relations for the different effective thermal conductivities are obtained by identification between the non-closed macroscopic equation (2.39) and the closed one (2.42). It leads to:

$$k_e = k_f \phi_f + k_s \phi_s \quad (2.45)$$

$$\overline{\overline{K}}_{tor} \cdot \nabla \langle T \rangle = \frac{k_f - k_s}{V} \int_{A_{fs}} \tilde{T}_f(\mathbf{r}) \mathbf{n}_{fs} dA \quad (2.46)$$

$$\overline{\overline{K}}_{dis} \cdot \nabla \langle T \rangle = (\rho c_p)_f \langle \tilde{T}_f \tilde{\mathbf{v}}_f \rangle \quad (2.47)$$

To determine the tensors $\overline{\overline{K}}_{tor}$ and $\overline{\overline{K}}_{dis}$, the fields $\tilde{\mathbf{v}}_f$, \tilde{T}_f and $\nabla \langle T \rangle$ are computed from microscopic temperature and velocity fields obtained through a numerical simulation. The numerical simulation is realized on a representative elementary volume with well-posed boundary conditions of periodicity (see Fig. 2.3) and an imposed macroscopic temperature gradient. On such a physical system, the variation in the flow direction allows the computation of the longitudinal and tangential components of the tortuosity and dispersion tensors. The obtained results are in good agreement with the experimental data (Fried and Combarnous, 1971; Han et al., 1985), which validates their method of identification.

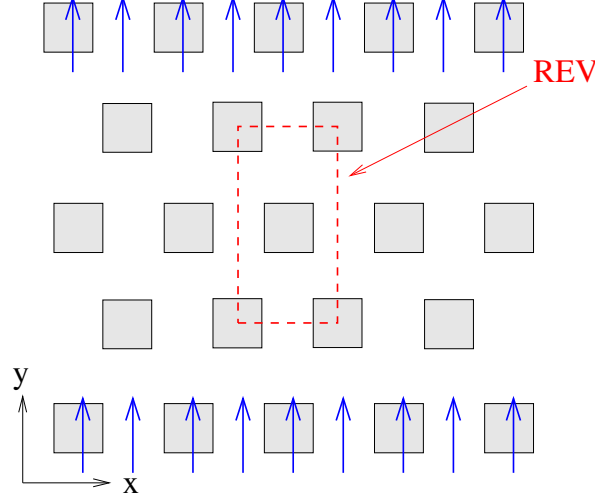


Figure 2.3: Physical system and its coordinate system.

For the volume averaging approach

In this paragraph, we briefly present the developments used to compute the effective coefficients. The issue is to present the main assumptions and, to simplify the resolution, we present the simplified case $k_s = 0$ (Kaviany, 1995).

From the relation (2.43), the determination of the effective thermal coefficient requires the knowledge of the vector field \mathbf{b}_f . It is obtained from the equation of the spatial deviation \tilde{T}_f (2.40) associated to orders of magnitude considerations. The length scale l_c and l_M represent the length scale of the non-averaged and averaged terms respectively. The no-slip condition at the fluid-solid interface gives:

$$\langle \mathbf{v}_f \rangle^f \approx \tilde{\mathbf{v}}_f, \text{ on } A_{fs} \quad (2.48)$$

The different orders of magnitude of the different terms of the relation (2.40) are presented in Tab. 2.1

Finally, the equation (2.40) reduces to:

$$(\rho c_p)_f \nabla \cdot (\langle \mathbf{v}_f \rangle^f \tilde{T}_f) + (\rho c_p)_f \tilde{\mathbf{v}}_f \cdot \nabla \tilde{T}_f + (\rho c_p)_f \tilde{\mathbf{v}}_f \cdot \nabla \langle T \rangle = \nabla \cdot (k_f \nabla \tilde{T}_f) \quad (2.49)$$

Substituting \tilde{T}_f by its closure relation (2.41), and using the order-of-magnitude consideration due to constant source term at the scale of the deviation, thus $\nabla \langle T \rangle \ll \nabla \mathbf{b}_f$ one obtains:

$$(\rho c_p)_f \nabla \cdot (\langle \mathbf{v}_f \rangle^f \mathbf{b}_f) + (\rho c_p)_f \tilde{\mathbf{v}}_f \cdot \nabla \mathbf{b}_f + (\rho c_p)_f \tilde{\mathbf{v}}_f = \nabla \cdot (k_f \nabla \mathbf{b}_f) \quad (2.50)$$

The boundary conditions on the fluid-solid interface give the following condition:

$$-\mathbf{n}_{fs} \cdot \nabla \mathbf{b}_f = \mathbf{n}_{fs} \quad (2.51)$$

terms of equation (2.40)	Order of magnitude	neglected/conserved
$(\rho c_p)_f \nabla \cdot (\langle \mathbf{v}_f \rangle^f \tilde{T}_f)$	$\langle \mathbf{v}_f \rangle^f \tilde{T}_f / l_c$	conserved
$(\rho c_p)_f \tilde{\mathbf{v}}_f \cdot \nabla \tilde{T}_f$	$\langle \mathbf{v}_f \rangle^f \tilde{T}_f / l_c$	conserved
$(\rho c_p)_f \tilde{\mathbf{v}}_f \cdot \nabla \langle T \rangle$	$\langle \mathbf{v}_f \rangle^f \langle T \rangle / l_M$	conserved
$\nabla \cdot k_f \nabla \tilde{T}_f$	$k_f \tilde{T}_f / l_c^2$	conserved
$\nabla \cdot k_s \phi_s / \phi_f \nabla \langle T \rangle$	$k_s \phi_s / \phi_f \langle T \rangle / l_M^2$	neglected
$\nabla \cdot (k_f - k_s) / (V \phi_f) \int_{A_{fs}} \tilde{T}_f(\mathbf{r}) \mathbf{n}_{fs} dA$	$k_f \tilde{T}_f / l_M^2$	neglected
$\nabla \cdot (\rho c_p)_f \langle \tilde{T}_f \tilde{\mathbf{v}}_f \rangle^f$	$\langle \mathbf{v}_f \rangle^f \tilde{T}_f / l_M$	neglected

 Table 2.1: Orders of magnitude for the terms composing the equation of the spatial deviation \tilde{T}_f

Furthermore, to complete the closure problem, one must consider boundary conditions of periodicity of spatial period r_0 for the unit cells:

$$[\mathbf{b}_f(\mathbf{x} + r_0)] = [\mathbf{b}_f(\mathbf{x})] \quad (2.52)$$

The computation of the closure function has been done by Koch and Brady (1985, 1987a,b); Koch et al. (1989), by Quintard and Whitaker (1993), and by Kaviany (1995).

We notice that this method of determination cannot be directly used at the free-porous interface. Indeed the separation between the length scales is not verified and the simplifications leading to the equation (2.50) cannot be done. Furthermore, the unit cell is not periodic and the relation (2.52) cannot be applied. Thus, at the free-porous interface, the closure problem becomes very complex and its resolution requires additional assumptions. For this reason, we do not use this method of determination to characterize the heat transfer at the free-porous interface.

In this section, we presented the closed one-temperature model and the associated effective transfer coefficient using the volume averaging method. This method is very rigorous and gives a good understanding of the origin of the different phenomena existing at the macroscopic scale. The heuristic method and the mixed method are also presented. The three methods are consistent. They use an identical closure model for the dispersion and tortuosity terms and obtain similar correlations in Peclet numbers for the effective conductive tensor.

2.3 Two-temperature models: literature review

In this section, we present, in the case of local thermal non-equilibrium, the closure of the two-temperature model and the determination of the associated effective coefficients using the three different approaches. Following the summarizing work done by Kaviany (1995) chapter 7, we present the results of Wakao and Kaguei (1982) for the heuristic method, the recent results found by Kuwahara et al. (2001) for the mixed method and we detail the closure of the two-temperature modeling obtained by Quintard et al. (1997) with the volume averaging method. The positive and negative points of each method are detailed. Thus, we are able to propose an alternative approach especially adapted to study the interfacial transition zone. This alternative approach is presented in Section 2.4 and will be used in Chapter 4.

2.3.1 The heuristic approach

The determination of a closed two-temperature model giving a good understanding of heat transfer processes in a porous media is complicated. Thus, there are many models proposed in the literature for the heuristic approach. From all the propositions, we consider here the more complete one, which, at the steady state, reads as follows (Wakao and Kaguei, 1982):

$$(\rho c_p)_f \nabla \cdot (\langle \mathbf{v}_f \rangle \langle T_f \rangle^f) = \nabla \cdot (\bar{\bar{\mathbf{K}}}_f + \bar{\bar{\mathbf{K}}}_{dis}) \cdot \nabla \langle T_f \rangle^f - a_V h (\langle T_f \rangle^f - \langle T_s \rangle^s) \quad (2.53)$$

$$0 = \nabla \cdot (\bar{\bar{\mathbf{K}}}_s \cdot \nabla \langle T_s \rangle^s) + a_V h (\langle T_f \rangle^f - \langle T_s \rangle^s) \quad (2.54)$$

This two-temperature model is heuristic since the closure relations are not derived from the local governing equations but are based on experimental observations. In this model, one considers effective thermal conductivities $\bar{\bar{\mathbf{K}}}_f$ and $\bar{\bar{\mathbf{K}}}_s$, a thermal coupling term between the phases modeled with an effective heat transfer coefficient $a_V h$ where a_V is an interfacial area per unit volume, and a dispersion phenomenon in the fluid phase characterized by the tensor $\bar{\bar{\mathbf{K}}}_{dis}$. If the modeling of the local conductivity at the macroscopic scale using the phases continua is intuitive, the modelings of the dispersion and the thermal coupling between the phases deserve to be commented. The dispersion is modeled as a conductive phenomenon with the fluid temperature gradient $\nabla \langle T_f \rangle^f$. The thermal coupling between the phases is modeled as a heat transfer phenomenon with a temperature difference $(\langle T_f \rangle^f - \langle T_s \rangle^s)$. With these modelings, both phenomena (dispersion and thermal coupling) are modeled through two independant macroscopic source terms: the temperature gradient and the temperature difference.

The modeling via independent source terms allows the computation of the effective coefficients separately. The effective coefficients $\bar{\bar{\mathbf{K}}}_f$, $\bar{\bar{\mathbf{K}}}_s$ and $\bar{\bar{\mathbf{K}}}_{dis}$ are measured experimentally at local thermal equilibrium. Indeed, if the dispersion is independent of the fluid-solid heat transfer, the results obtained at LTE are still valid at LTNE.

The effective transfer coefficient $a_V h$ is then computed using correlations based on boundary layer theory according to Wakao and Kaguei (1982):

$$a_V h (\langle T_s \rangle^s - \langle T_f \rangle^f) = -\frac{k_s}{V} \int_{A_{fs}} \nabla T_s \cdot \mathbf{n}_{fs} dA \quad (2.55)$$

The effective transfer coefficient $a_V h$ depends on the Peclet number and, for packed beds, Wakao and Kaguei (1982) obtain the following correlation:

$$\frac{a_V h d_p^2}{k_f} = 2 + 1.1 Re^{0.6} Pe^{1/3} \quad (2.56)$$

In the following, the mixed method uses this correlation and improves its precision by using more *experimental* data. Conversely, the volume averaging method disproves this correlation with arguments that are presented in the following.

2.3.2 The mixed approach

Kuwahara et al. (2001) study heat transfer at local thermal non-equilibrium. They use the formalism and perform the first step of the volume averaging method to determine the non-closed macroscopic equations. But instead of pursuing with the second step and use closure relations for the spatial temperature deviations, they postulate the closed macroscopic equations from the heuristic literature. Thus, Kuwahara et al. (2001) model the phenomena of dispersion and thermal coupling between the phases by two independent macroscopic source terms. As for the heuristic method, this assumption has an impact on the determination of the effective transfer coefficients.

In order to determine the analytical relation of the effective transfer coefficients, [Kuwahara et al. \(2001\)](#) start from the following non-closed macroscopic equations:

$$(\rho c_p)_f \nabla \cdot (\phi_f \langle \mathbf{v}_f \rangle^f \langle T_f \rangle^f) = \nabla \cdot k_f \phi_f \nabla \langle T_f \rangle^f + \nabla \cdot \frac{k_f}{V} \int_{A_{fs}} \mathbf{n}_{fs} \tilde{T}_f dA - \nabla \cdot (\rho c_p)_f \langle \tilde{T}_f \tilde{\mathbf{v}}_f \rangle + \frac{k_f}{V} \int_{A_{fs}} \mathbf{n}_{fs} \cdot \nabla \tilde{T}_f dA \quad (2.57)$$

$$0 = \nabla \cdot k_s \phi_s \nabla \langle T_s \rangle^s - \nabla \cdot \frac{k_s}{V} \int_{A_{fs}} \mathbf{n}_{fs} \tilde{T}_f dA - \frac{k_f}{V} \int_{A_{fs}} \mathbf{n}_{fs} \cdot \nabla \tilde{T}_f dA \quad (2.58)$$

These equations are equivalent to the equations (2.33) and (2.34) using the temperature and heat flux continuity relations at the fluid-solid interface. Then, the non-closed macroscopic equations (2.57)-(2.58) are compared with the closed model (2.53)-(2.54). The effective transfer coefficient $a_V h$ is identified to the term existing in equations (2.57) and (2.58) with opposite sign. The determination of the effective thermal conductivities and the dispersive tensors relies on the assumption that the non-closed terms inside the divergence of (2.57) and (2.58) vary with $\nabla \langle T_f \rangle^f$ for the fluid phase and with $\nabla \langle T_s \rangle^s$ for the solid phase. All these considerations lead to the following analytical relations:

$$\bar{\bar{\mathbf{K}}}_f \cdot \nabla \langle T_f \rangle^f = k_f \phi_f \nabla \langle T_f \rangle^f + \frac{k_f}{V} \int_{A_{fs}} \mathbf{n}_{fs} \tilde{T}_f dA \quad (2.59)$$

$$\bar{\bar{\mathbf{K}}}_{dis} \cdot \nabla \langle T_f \rangle^f = -(\rho c_p)_f \langle \tilde{T}_f \tilde{\mathbf{v}}_f \rangle \quad (2.60)$$

$$\bar{\bar{\mathbf{K}}}_s \cdot \nabla \langle T_s \rangle^s = k_s \phi_s \nabla \langle T_s \rangle^s - \frac{k_s}{V} \int_{A_{fs}} \mathbf{n}_{fs} \tilde{T}_f dA \quad (2.61)$$

$$a_V h (\langle T_f \rangle^f - \langle T_s \rangle^s) = -\frac{k_f}{V} \int_{A_{fs}} \mathbf{n}_{fs} \cdot \nabla \tilde{T}_f dA \quad (2.62)$$

In a second step, each term of the analytical relations (2.59) to (2.62) is computed from the microscopic temperature and velocity fields obtained by a numerical simulation.

From the choice of the dispersion modeling, [Kuwahara et al. \(2001\)](#) assume that the determination of $\bar{\bar{\mathbf{K}}}_f$ and $\bar{\bar{\mathbf{K}}}_{dis}$ done at local thermal equilibrium ([Kuwahara et al., 1996](#); [Kuwahara and Nakayama, 1999](#)) is still valid at local thermal non-equilibrium.

The effective transfer coefficient $a_V h$ is obtained from a numerical simulation realized on an elementary volume with isothermal cubes (see Fig. 2.4). The obtained values are in good agreement with the ones obtained from the experimental data of [Wakao and Kaguei \(1982\)](#).

2.3.3 The volume averaging approach

An alternative to these approaches is to derive the form of the closed model from the non-closed one. To obtain this closed form, the second step of the volume averaging method must be performed. The non-closed equations (2.33) and (2.34) involve averaged terms ($\langle T_f \rangle^f$ and $\langle T_s \rangle^s$) characteristic of the macroscopic scale and spatial deviations (\tilde{T}_f and \tilde{T}_s) characteristic of the microscopic scale. In order to close the equations (2.33) and (2.34), the spatial deviation terms must be expressed as functions of averaged quantities. These averaged quantities are given by the equations of \tilde{T}_f and \tilde{T}_s . They are at the origin of the spatial deviations and are called *source terms*. Thus, closure relations can be postulated that as relating the spatial deviations to the source terms via closure variables independent of macroscopic phenomena. Then, the closure variables are brought together to make appear effective coefficients. At last, one obtains closed macroscopic equations.

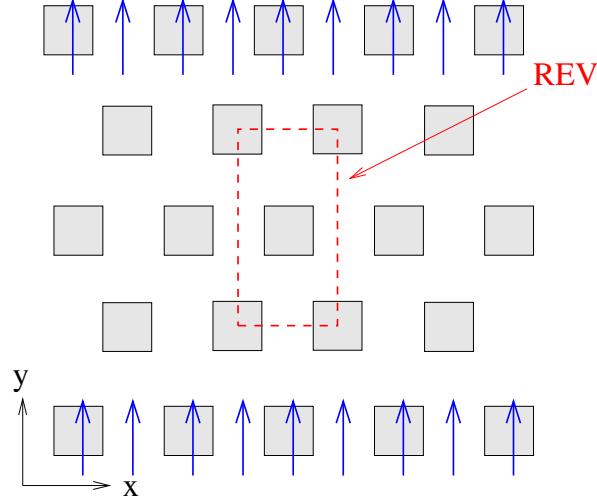


Figure 2.4: Physical system and its coordinate system.

The equation for the fluid temperature deviation is established subtracting the equation of $\langle T_f \rangle^f$ (see (2.33)) divided by the porosity ϕ_f :

$$\begin{aligned}
 (\rho c_p)_f \nabla \cdot (\langle \mathbf{v}_f \rangle^f \langle T_f \rangle^f) = & \underbrace{\nabla \cdot k_f \nabla \langle T_f \rangle^f}_{\text{diffusion}} + \underbrace{\nabla \cdot \frac{k_f}{\phi_f V} \int_{A_{fs}} \tilde{T}_f \mathbf{n}_{fs} dA}_{\text{tortuosity}} - \underbrace{\nabla \cdot (\rho c_p)_f \langle \tilde{T}_f \tilde{\mathbf{v}}_f \rangle^f}_{\text{thermal dispersion}} \\
 & + \underbrace{\frac{k_f}{V \phi_f} \int_{A_{fs}} \mathbf{n}_{fs} \cdot \nabla \tilde{T}_f dA}_{\text{fluid/solid heat transfer}} \quad (2.63)
 \end{aligned}$$

and the equation of T_f :

$$(\rho c_p)_f \nabla \cdot (\mathbf{v}_f T_f) = \nabla \cdot (k_f \nabla T_f) \quad (2.64)$$

One obtains:

$$\begin{aligned}
 (\rho c_p)_f \nabla \cdot (\langle \mathbf{v}_f \rangle^f \tilde{T}_f) = & \nabla \cdot k_f \nabla \tilde{T}_f - (\rho c_p)_f \tilde{\mathbf{v}}_f \underbrace{\nabla \langle T_f \rangle^f}_{\text{source}} - (\rho c_p)_f \nabla \cdot (\tilde{\mathbf{v}}_f \tilde{T}_f) \\
 & - \nabla \cdot \frac{k_f}{\phi_f V} \int_{A_{fs}} \tilde{T}_f \mathbf{n}_{fs} dA + (\rho c_p)_f \nabla \cdot \langle \tilde{T}_f \tilde{\mathbf{v}}_f \rangle^f + \frac{k_f}{\phi_f V} \int_{A_{fs}} \mathbf{n}_{fs} \cdot \nabla \tilde{T}_f dA \quad (2.65)
 \end{aligned}$$

Proceeding identically for the solid phase and for the conditions at the fluid-solid interfaces A_{fs} , one obtains:

$$0 = \nabla \cdot k_s \nabla \tilde{T}_s - \nabla \cdot \frac{k_s}{\phi_s V} \int_{A_{sf}} \tilde{T}_s \mathbf{n}_{sf} dA + \frac{k_s}{\phi_s V} \int_{A_{sf}} \mathbf{n}_{sf} \cdot \nabla \tilde{T}_s dA \quad (2.66)$$

$$\tilde{T}_f - \tilde{T}_s = \underbrace{\langle T_s \rangle^s - \langle T_f \rangle^f}_{\text{source}}, \text{ on } A_{fs} \quad (2.67)$$

$$k_f \mathbf{n}_{fs} \cdot \nabla \tilde{T}_f - k_s \mathbf{n}_{fs} \cdot \nabla \tilde{T}_s = k_s \mathbf{n}_{fs} \cdot \underbrace{\nabla \langle T_s \rangle^s}_{\text{source}} - k_f \mathbf{n}_{fs} \cdot \underbrace{\nabla \langle T_f \rangle^f}_{\text{source}}, \text{ on } A_{fs} \quad (2.68)$$

In the deviation equations (2.65) to (2.68), there are three macroscopic sources terms: $\nabla \langle T_f \rangle^f$, $\nabla \langle T_s \rangle^s$ and $(\langle T_s \rangle^s - \langle T_f \rangle^f)$. The scale of variation of these macroscopic terms is very large compared to

the size of the REV. Thus, these source terms can be supposed to remain constant at the scale of the deviations, which suggests the following closure relations for \tilde{T}_f and \tilde{T}_s :

$$\tilde{T}_f = \mathbf{b}_{ff} \cdot \nabla \langle T_f \rangle^f + \mathbf{b}_{fs} \cdot \nabla \langle T_s \rangle^s - s_f \left(\langle T_f \rangle^f - \langle T_s \rangle^s \right) \quad (2.69)$$

$$\tilde{T}_s = \mathbf{b}_{ss} \cdot \nabla \langle T_s \rangle^s + \mathbf{b}_{sf} \cdot \nabla \langle T_f \rangle^f + s_s \left(\langle T_s \rangle^s - \langle T_f \rangle^f \right) \quad (2.70)$$

where for the fluid phase, \mathbf{b}_{ff} , \mathbf{b}_{fs} and s_f are the vectors and scalar field mapping $\nabla \langle T_f \rangle^f$, $\nabla \langle T_s \rangle^s$ and $\left(\langle T_f \rangle^f - \langle T_s \rangle^s \right)$ onto \tilde{T}_f , and respectively for the solid phase.

The closure relations for the pore scale deviation of \tilde{T}_f is introduced in the terms of tortuosity and wall heat transfer of the macroscopic equations (2.33), which, combined with the scale separation considerations, gives:

$$\begin{aligned} \frac{k_f}{V} \int_{A_{fs}} \mathbf{n}_{fs} \tilde{T}_f dA &= \frac{k_f}{V} \int_{A_{fs}} \mathbf{b}_{ff} \mathbf{n}_{fs} dA \cdot \nabla \langle T_f \rangle^f + \frac{k_f}{V} \int_{A_{fs}} \mathbf{b}_{fs} \mathbf{n}_{fs} dA \cdot \nabla \langle T_s \rangle^s \\ &\quad - \left(\langle T_f \rangle^f - \langle T_s \rangle^s \right) \frac{k_f}{V} \int_{A_{fs}} s_f \mathbf{n}_{fs} dA \end{aligned} \quad (2.71)$$

$$\frac{k_f}{V} \int_{A_{fs}} \mathbf{n}_{fs} \cdot \nabla \tilde{T}_f dA = \mathbf{u}_{ff} \cdot \nabla \langle T_f \rangle^f + \mathbf{u}_{fs} \cdot \nabla \langle T_s \rangle^s - a_v h_f \left(\langle T_f \rangle^f - \langle T_s \rangle^s \right) \quad (2.72)$$

where

$$a_v h_f = \frac{k_f}{V} \int_{A_{fs}} \mathbf{n}_{fs} \cdot \nabla s_f dA \quad (2.73)$$

$$\mathbf{u}_{ij} = \frac{k_f}{V} \int_{A_{fs}} \mathbf{n}_{ij} \cdot \nabla \mathbf{b}_{ij} dA \quad (2.74)$$

are respectively effective heat transfer and transport coefficients.

Similarly, the dispersion term is closed as follows:

$$\left\langle \tilde{T}_f \tilde{\mathbf{v}}_f \right\rangle = \langle \mathbf{b}_{ff} \tilde{\mathbf{v}}_f \rangle \cdot \nabla \langle T_f \rangle^f + \langle \mathbf{b}_{fs} \tilde{\mathbf{v}}_f \rangle \cdot \nabla \langle T_s \rangle^s - \langle s_f \tilde{\mathbf{v}}_f \rangle \left(\langle T_f \rangle^f - \langle T_s \rangle^s \right) \quad (2.75)$$

To lighten the writing for future discussions, we introduce the following notations for the dispersion term and the tortuosity term:

$$\left\langle \tilde{T}_f \tilde{\mathbf{v}}_f \right\rangle = -\overline{\overline{D}}_p^f \cdot \nabla \langle T_f \rangle^f - \overline{\overline{D}}_p^s \cdot \nabla \langle T_s \rangle^s - \mathbf{D}_a \left(\langle T_f \rangle^f - \langle T_s \rangle^s \right) \quad (2.76)$$

$$\frac{k_f}{V} \int_{A_{fs}} \mathbf{n}_{fs} \tilde{T}_f dA = \overline{\overline{K}}_{tor}^{ff} \cdot \nabla \langle T_f \rangle^f + \overline{\overline{K}}_{tor}^{fs} \cdot \nabla \langle T_s \rangle^s + \mathbf{K}_{tor}^a \left(\langle T_f \rangle^f - \langle T_s \rangle^s \right) \quad (2.77)$$

where

$$\begin{aligned} \overline{\overline{D}}_p^f &= -\langle \mathbf{b}_{ff} \tilde{\mathbf{v}}_f \rangle, & \overline{\overline{D}}_p^s &= -\langle \mathbf{b}_{fs} \tilde{\mathbf{v}}_f \rangle, & \mathbf{D}_a &= \langle s_f \tilde{\mathbf{v}}_f \rangle \\ \overline{\overline{K}}_{tor}^{ff} &= \frac{k_f}{V} \int_{A_{fs}} \mathbf{b}_{ff} \mathbf{n}_{fs} dA, & \overline{\overline{K}}_{tor}^{fs} &= \frac{k_f}{V} \int_{A_{fs}} \mathbf{b}_{fs} \mathbf{n}_{fs} dA, & \mathbf{K}_{tor}^a &= -\frac{k_f}{V} \int_{A_{fs}} s_f \end{aligned}$$

From equations (2.76) and (2.77), one introduces an additional transport coefficient \mathbf{d}_f :

$$\mathbf{d}_f = (\rho c_p)_f \mathbf{D}_a + \mathbf{K}_{tor}^a \quad (2.78)$$

Then, the other terms can be brought together to make appear the mean effective conductivity tensor and the coupled tensor

$$\bar{\bar{\mathbf{K}}}_{ff} = \phi_f k_f \bar{\mathbf{I}} + \bar{\bar{\mathbf{K}}}_{tor}^{ff} + (\rho c_p)_f \bar{\bar{\mathbf{D}}}_p^f \quad (2.79)$$

$$\bar{\bar{\mathbf{K}}}_{fs} = \bar{\bar{\mathbf{K}}}_{tor}^{fs} + (\rho c_p)_f \bar{\bar{\mathbf{D}}}_p^s \quad (2.80)$$

The effective thermal conductivity tensors are composed of a tortuosity part and a dispersive part. Proceeding identically with the solid phase, the non-closed equations (2.33) and (2.34) can be rewritten under the following closed forms:

$$(\rho c_p)_f \phi_f \langle \mathbf{v}_f \rangle^f \cdot \nabla \langle T_f \rangle^f - \mathbf{u}_{ff} \cdot \nabla \langle T_f \rangle^f - \mathbf{u}_{fs} \cdot \nabla \langle T_s \rangle^s = \nabla \cdot \left(\bar{\bar{\mathbf{K}}}_{ff} \nabla \langle T_f \rangle^f + \bar{\bar{\mathbf{K}}}_{fs} \nabla \langle T_s \rangle^s + \mathbf{d}_f (\langle T_f \rangle^f - \langle T_s \rangle^s) \right) - a_V h_f \left(\langle T_f \rangle^f - \langle T_s \rangle^s \right) \quad (2.81)$$

$$-\mathbf{u}_{sf} \cdot \nabla \langle T_f \rangle^f - \mathbf{u}_{ss} \cdot \nabla \langle T_s \rangle^s = \nabla \cdot \left(\bar{\bar{\mathbf{K}}}_{sf} \nabla \langle T_f \rangle^f + \bar{\bar{\mathbf{K}}}_{ss} \nabla \langle T_s \rangle^s + \mathbf{d}_s (\langle T_s \rangle^s - \langle T_f \rangle^f) \right) + a_V h_s \left(\langle T_s \rangle^s - \langle T_f \rangle^f \right) \quad (2.82)$$

where

$$\begin{aligned} \mathbf{u}_{ss} &= \frac{k_s}{V} \int_{A_{sf}} \mathbf{n}_{sf} \cdot \nabla \mathbf{b}_{ss} dA, & \mathbf{u}_{sf} &= \frac{k_s}{V} \int_{A_{sf}} \mathbf{n}_{sf} \cdot \nabla \mathbf{b}_{sf} dA \\ \bar{\bar{\mathbf{K}}}_{sf} &= -\frac{k_s}{V} \int_{A_{sf}} \mathbf{n}_{sf} \mathbf{b}_{ss} dA, & \bar{\bar{\mathbf{K}}}_{ss} &= \phi_s k_s \bar{\mathbf{I}} + \frac{k_s}{V} \int_{A_{sf}} \mathbf{n}_{sf} \mathbf{b}_{sf} dA \\ \mathbf{d}_s &= \frac{k_s}{V} \int_{A_{sf}} \mathbf{n}_{sf} s_s dA, & a_V h_s &= \frac{k_s}{V} \int_{A_{sf}} \mathbf{n}_{sf} \cdot \nabla s_s dA \end{aligned}$$

The temperature continuity and the heat flux continuity at the fluid-solid interface allow to make the following simplifications:

$$\mathbf{u}_{fs} = -\mathbf{u}_{ss}, \quad \mathbf{u}_{ff} = -\mathbf{u}_{sf}, \quad a_V h_f = -a_V h_s = a_V h$$

Thus, the closed macroscopic equations are rewritten as follows:

For the fluid phase

$$(\rho c_p)_f \phi_f \langle \mathbf{v}_f \rangle^f \cdot \nabla \langle T_f \rangle^f - \mathbf{u}_{ff} \cdot \nabla \langle T_f \rangle^f - \mathbf{u}_{fs} \cdot \nabla \langle T_s \rangle^s = \nabla \cdot \left(\bar{\bar{\mathbf{K}}}_{ff} \nabla \langle T_f \rangle^f + \bar{\bar{\mathbf{K}}}_{fs} \nabla \langle T_s \rangle^s + \mathbf{d}_f (\langle T_f \rangle^f - \langle T_s \rangle^s) \right) - a_V h \left(\langle T_f \rangle^f - \langle T_s \rangle^s \right) \quad (2.83)$$

For the solid phase

$$\mathbf{u}_{ff} \cdot \nabla \langle T_f \rangle^f + \mathbf{u}_{fs} \cdot \nabla \langle T_s \rangle^s = \nabla \cdot \left(\bar{\bar{\mathbf{K}}}_{sf} \nabla \langle T_f \rangle^f + \bar{\bar{\mathbf{K}}}_{ss} \nabla \langle T_s \rangle^s + \mathbf{d}_s (\langle T_s \rangle^s - \langle T_f \rangle^f) \right) - a_V h \left(\langle T_s \rangle^s - \langle T_f \rangle^f \right) \quad (2.84)$$

The equations (2.83)-(2.84) are closed and involve nine effective transfer coefficients (\mathbf{u}_{ff} , \mathbf{u}_{fs} , $a_V h$, $\bar{\bar{\mathbf{K}}}_{ff}$, $\bar{\bar{\mathbf{K}}}_{fs}$, $\bar{\bar{\mathbf{K}}}_{sf}$, $\bar{\bar{\mathbf{K}}}_{ss}$, \mathbf{d}_s , \mathbf{d}_f). These effective coefficients correspond to nine separated macroscopic phenomena, whose origin have been made explicit in the previous developments. This closed macroscopic model is more complete than the one presented previously (see equations (2.53)-(2.54). However it is not used and no study gives the values of the effective coefficients related to this model. The study using the closest form of model is the one proposed by Quintard et al. (1997). By gathering some terms, they obtained a slightly different model. They compute the effective coefficients for various Peclet numbers,

conductivity ratios and geometries. We will use these values of effective coefficients to verify the results obtained with our alternative approach (see Section 2.4.2)

Quintard et al. (1997) make the choice to associate the different transport terms of the two-temperature model (2.83)-(2.84). Indeed, the transport coefficients \mathbf{d}_i are constant in a homogeneous medium allowing the following writing:

$$\nabla \cdot (\mathbf{d}_i (\langle T_f \rangle^f - \langle T_s \rangle^s)) = \mathbf{d}_i \cdot \nabla \langle T_f \rangle^f - \mathbf{d}_i \cdot \nabla \langle T_s \rangle^s \quad (2.85)$$

and the association of the transport terms according to their respective gradients gives:

$$\begin{aligned} \mathbf{c}_{ff} &= \mathbf{u}_{ff} + \mathbf{d}_f, & \mathbf{c}_{fs} &= \mathbf{u}_{fs} - \mathbf{d}_f \\ \mathbf{c}_{sf} &= \mathbf{u}_{ff} - \mathbf{d}_s, & \mathbf{c}_{ss} &= \mathbf{u}_{fs} + \mathbf{d}_s \end{aligned} \quad (2.86)$$

Thus, the two-temperature model becomes:

$$(\rho c_p)_f \langle \mathbf{v}_f \rangle \cdot \nabla \langle T_f \rangle^f - \mathbf{c}_{ff} \cdot \nabla \langle T_f \rangle^f - \mathbf{c}_{fs} \cdot \nabla \langle T_s \rangle^s = \nabla \cdot (\bar{\bar{\mathbf{K}}}_{ff} \nabla \langle T_f \rangle^f + \bar{\bar{\mathbf{K}}}_{fs} \nabla \langle T_s \rangle^s) - a_V h (\langle T_f \rangle^f - \langle T_s \rangle^s) \quad (2.87)$$

$$-\mathbf{c}_{sf} \cdot \nabla \langle T_f \rangle^f - \mathbf{c}_{ss} \cdot \nabla \langle T_s \rangle^s = \nabla \cdot (\bar{\bar{\mathbf{K}}}_{sf} \nabla \langle T_f \rangle^f + \bar{\bar{\mathbf{K}}}_{ss} \nabla \langle T_s \rangle^s) + a_V h (\langle T_f \rangle^f - \langle T_s \rangle^s) \quad (2.88)$$

The two-temperature model (2.87)-(2.88) possesses 9 effective coefficients that must be determined. The determination of the effective coefficients is achieved during the third step of the volume averaging method. This method of determination is complex and involves numerous closure problems. This is not the subject of this chapter and for more information we recommend the paper of Quintard et al. (1997). Furthermore, we recall that this method of determination cannot be directly used at the free-porous interface as explained in Section 2.2.

We presented the volume averaging method applied to heat transfer at local thermal non-equilibrium. The resulting closed macroscopic model (equations (2.87)-(2.88)) is different from the one of the heuristic and mixed methods (equations (2.53)-(2.54)). In the following we discuss this difference.

2.3.4 Discussion

This discussion is about the difference between the macroscopic closed two-temperature models proposed by the heuristic and volume averaging approaches. This difference has two origins. The first difference comes from the lack of formalism to derive the macroscopic equations in the heuristic method. The second difference arises from the way to determine the effective coefficients. Indeed, in the heuristic approach, the determination of the effective coefficients with experimentation is difficult. Thus, the issue is to look for the simplest closed macroscopic model possessing the main physical phenomena. Conversely, the volume averaging method is not concerned by this problematic. The effective transfer coefficients are determined from the resolution of independent microscopic closure problems inside the REV, one for each closure variable. This independence cannot be obtained in experiments. The difference between the two approaches affects the modeling of the dispersion and heat coupling phenomena as presented in Fig 2.5. The heuristic approach models the dispersive flux as proportional to a fluid temperature gradient and the heat coupling as proportional to a difference between the phase temperatures. Quintard et al. (1997) show that the modeling of the dispersion and heat coupling phenomena is not that simple. They must be both modeled as functions of the source terms $\nabla \langle T_s \rangle^s$, $\nabla \langle T_f \rangle^f$ and $(\langle T_f \rangle^f - \langle T_s \rangle^s)$. Such a modeling has important consequences on the effective coefficients obtained

and the associated correlations. In particular, the resulting effective transfer coefficient h does not depend or very weakly on the Peclet number instead to verify the dependency in $Re^n Pr^m$ expressed by [Wakao and Kaguei \(1982\)](#) or [Kuwahara et al. \(2001\)](#). Why such a difference of appreciation for the thermal coupling between the two modeling approaches has not been corrected?

The following explanation comes from the results that we have obtained performing many simulations to determine the effective coefficients. For porous media composed of aligned cubes where the heat transfer is created by volume sources in the solid matrix with k_s/k_f in $[10^{-4}, +\infty]$, we have observed in our *numerical simulations* that the averaged terms $\nabla \langle T_s \rangle^s$, $\nabla \langle T_f \rangle^f$ and $(\langle T_f \rangle^f - \langle T_s \rangle^s)$ are proportional in the whole domain. In such situations, the effective coefficients computed with the heuristic closed two-temperature model have the following characteristics: they are independent of the various solicitations at their origin and seem to characterize the macroscopic properties of the studied porous medium. This is why the users of the heuristic or mixed approaches that perform studies verifying such thermal configurations, do not notice the modeling error. Especially, it is the case for ([Kuwahara et al., 1996](#); [Kuwahara and Nakayama, 1999](#); [Kuwahara et al., 2001](#)). Comparing their modeling choice of the thermal coupling with that of [Quintard et al. \(1997\)](#), we conclude that instead of considering the transfer coefficients $a_V h$, they compute the contributions of the three terms: \mathbf{u}_{ff} , \mathbf{u}_{fs} and $a_V h$. That explains the difference between the two studies for the values of the effective transfer coefficient. For the dispersion, the difference of modeling is similar. [Kuwahara et al. \(1996\)](#) and [Kuwahara and Nakayama \(1999\)](#) compute the contributions of the three terms $(\overline{\overline{D}}_p^f, \overline{\overline{D}}_p^s$ and $\mathbf{D}_a)$ instead of $\overline{\overline{D}}_p^f$. However, the modeling error has a limited effect because $\overline{\overline{D}}_p^f \gg \overline{\overline{D}}_p^s + \mathbf{D}_a$. Thus, the two authors find similar correlation for the Peclet dependency of $\overline{\overline{D}}_p^f$.

In the context of the study of heat transfer at a free-porous interface none of these methods can be used directly. Indeed, the mixed method postulates a closed macroscopic model that does not characterized properly the macroscopic properties of the porous medium. Furthermore, the second and third steps of the volume averaging method require a length scale separation that is not valid in the transition zone. At the free-porous interface, the non validity of the length scale separation hypothesis encourages us to determine the effective coefficients by identification following the mixed method. However, this determination by identification is accurate only if the closed macroscopic model is as complete as possible. Based on these considerations, we develop another method. The non-closed macroscopic model is derived from the governing microscopic equations performing the first step of the volume averaging method. This leads to the equations (2.25) and (2.26) that are valid everywhere in the domain and in particular within the interfacial transition zone since no length-scale constraint has been used. The closed-macroscopic model is determined in the homogeneous porous medium with the closure relations using the second step of the volume averaging method. The obtained equations are then assumed to be valid in the continuous transition zone. Then the effective coefficients are determined by identification between the closed and non-closed macroscopic models in the whole domain including the free-porous transition zone.

For this alternative approach, we cannot use directly the closed macroscopic models given by the second step of the volume averaging method. Indeed the equations (2.87) and (2.88) cannot be used to determine the effective coefficients with the identification approach because dispersive and heat coupling terms are mixed. Furthermore, the equations (2.83) and (2.84) involve too many effective coefficients that must be determined. Thus, we propose a new form of closed macroscopic model inspired from the work of [Pinson et al. \(2007\)](#) and [Drouin et al. \(2010\)](#). This new model keeps the dispersion separated from the heat coupling and considers passive and active phenomena. This modeling is very accurate to characterize heat transfer for which the averaged terms $\nabla \langle T_s \rangle^s$, $\nabla \langle T_f \rangle^f$ and $(\langle T_f \rangle^f - \langle T_s \rangle^s)$ are not proportional as we will see in the following.

The next section presents the work of [Pinson et al. \(2007\)](#) and [Drouin et al. \(2010\)](#) and shows the validity of our alternative method in the homogeneous porous medium comparing with the results given by [Quintard et al. \(1997\)](#).

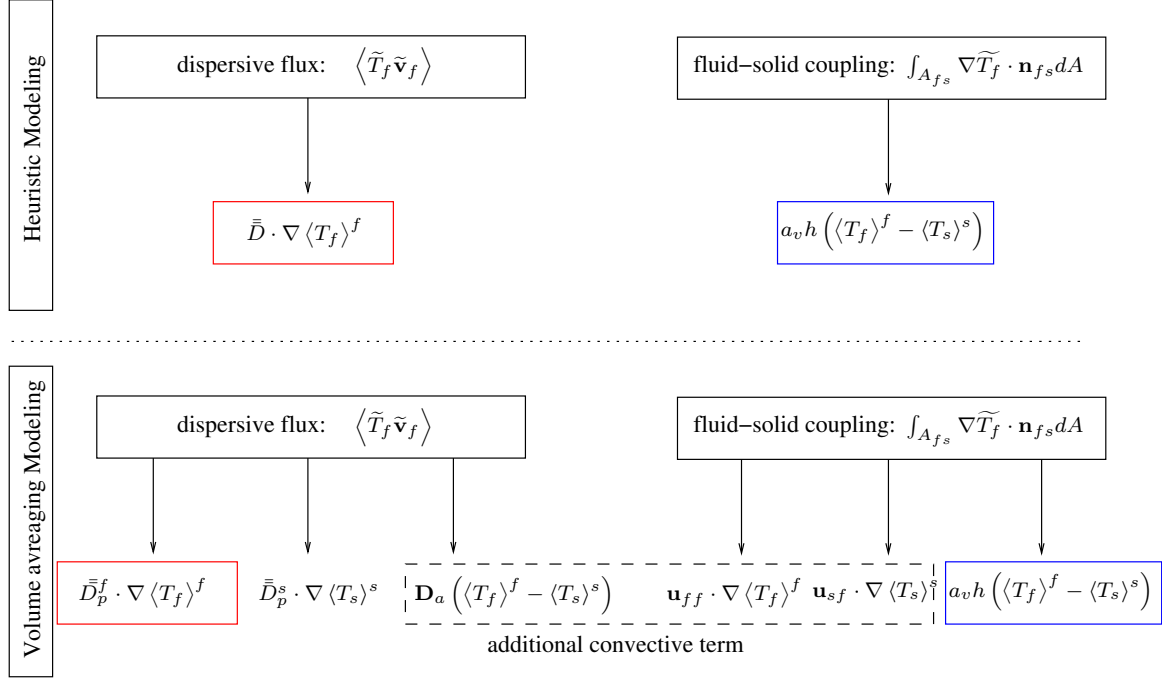


Figure 2.5: Synthesis of the differences between the modelings

2.4 Two-temperature modeling: another interpretation

As presented previously, the dispersion and the heat coupling can be modeled through macroscopic terms, that deserves particular attention. This modeling issue is studied by [Pinson et al. \(2007\)](#) and [Drouin et al. \(2010\)](#) for the fluid equation only, and they illustrate it on practical examples where a non-constant heat flux is imposed at channel walls. For such cases, the dispersive phenomena at the macroscopic scale is composed of a *passive part* proportional to a temperature gradient and an *active part* proportional to the flux imposed at the solid boundaries. Extending this result to the heat coupling between the fluid and solid phases, we compare the active and passive parts to determine domains where one phenomenon dominates the other. From this discussion, we propose three different models.

2.4.1 Active dispersion

[Pinson et al. \(2007\)](#) and [Drouin et al. \(2010\)](#) show in their respective works, the modifications caused by non-constant local heat fluxes. To simplify their study, the solid temperature equation is not solved and they impose directly the wall heat flux. For 1D laminar flows in pipes, the tortuosity phenomenon vanishes and the averaged equation of the fluid phase (2.33) reduces to:

$$(\rho c_p)_f \nabla \cdot (\langle \mathbf{v}_f \rangle \langle T_f \rangle^f) = \nabla \cdot k_f \phi_f \nabla \langle T_f \rangle^f - \nabla \cdot (\rho c_p)_f \langle \tilde{T}_f \tilde{\mathbf{v}}_f \rangle + \frac{1}{V} \int_{A_{fs}} \Phi dA \quad (2.89)$$

where Φ is an incoming flux at the fluid-solid walls such that:

$$\Phi = k_f \nabla T_f \cdot \mathbf{n}_{fs} \quad (2.90)$$

At the macroscopic scale, only the diffusion and dispersion phenomena are present in the governing equations. The macroscopic equation is not closed due to the spatial deviation \tilde{T}_f in the dispersive term. Looking for the closure relation, they determine the source terms at the origin of the deviation. These source terms are the temperature gradient and the imposed flux at the walls, which leads to the following closure relation:

$$\tilde{T}_f = \mathbf{b}_{ff} \cdot \nabla \langle T_f \rangle^f + s_f \frac{1}{V} \int_{A_{fs}} \Phi dA \quad (2.91)$$

Introducing this relation in the dispersive term, one obtains:

$$\langle \tilde{T}_f \tilde{\mathbf{v}}_f \rangle = \langle \mathbf{b}_{ff} \tilde{\mathbf{v}}_f \rangle \cdot \nabla \langle T_f \rangle^f + \langle s_f \tilde{\mathbf{v}}_f \rangle \frac{1}{V} \int_{A_{fs}} \Phi dA \quad (2.92)$$

They define dispersion coefficients as follows:

$$\overline{\overline{D}}_p^f = -\langle \mathbf{b}_{ff} \tilde{\mathbf{v}}_f \rangle, \quad \mathbf{D}_a = -\langle s_f \tilde{\mathbf{v}}_f \rangle \quad (2.93)$$

where $\overline{\overline{D}}_p^f$ is a *passive* dispersion tensor corresponding to an additional diffusion due to the velocity deviations, and \mathbf{D}_a is an *active* dispersion vector seen as the macroscopic representation of the effect of the wall heat transfer.

Thus, the closed macroscopic model can be written as follows:

$$(\rho c_p)_f \nabla \cdot (\langle \mathbf{v}_f \rangle \langle T_f \rangle^f) = \nabla \cdot k_f \phi_f \nabla \langle T_f \rangle^f + \nabla \cdot \left(\overline{\overline{D}}_p^f \cdot \nabla \langle T_f \rangle^f \right) + \nabla \cdot \left(\mathbf{D}_a \frac{1}{V} \int_{A_{fs}} \Phi dA \right) + \frac{1}{V} \int_{A_{fs}} \Phi dA \quad (2.94)$$

where the effective coefficients of passive and active dispersion are determined from the closure problems.

To validate the model, [Drouin et al. \(2010\)](#) study the impact of the imposed wall heat flux on the dispersion. For a constant heat flux, the active dispersion vanishes and the passive dispersion is needed to model heat transfer for transient problems. For a non-constant imposed heat flux with a triangular form, the macroscopic modeling requires the passive and active dispersions to recover the total heat transfer. Furthermore, comparing the passive and the active dispersions, [Drouin et al. \(2010\)](#) show that the active dispersion dominates the passive dispersion. For laminar cases, the active/passive ratios are 7/2 in channels and 2 in circular pipes. However the dispersion ratio is not enough to suppress the passive dispersion for the active dispersion. Thus, the appropriate macroscopic model to reflect the heat transfer is the equation (2.94).

In this study, [Drouin et al. \(2010\)](#) are able to illustrate the influence of the wall heat transfer on the macroscopic phenomenon of dispersion. In the following, we use this result to study the more complex case of two-temperature modeling. As for the dispersive phenomenon studied by [citeDrouin2010](#), we write the heat coupling with a passive part and an active part. Then, the relative importance of the two parts are discussed.

2.4.2 The two-temperature model

In this Section, we study heat transfer configurations where the temperature gradients are not proportional to the temperature difference. The closed two-temperature model is derived from the local governing equations with the volume averaging method. Then, to determine the effective transfer coefficients, the identification method used by [Kuwahara et al. \(1996\)](#); [Kuwahara and Nakayama \(1999\)](#); [Kuwahara et al. \(2001\)](#) is applied. Thus, we characterize the heat transfer at the macroscopic scale and we are able to discuss the different modeling options.

2.4.2.1 Setting up of a modeling

To study the heat coupling between the phases at the macroscopic scale, we apply a volume heat source in the solid matrix that gives temperature gradients that are not proportional to the temperature difference. Furthermore, this heating configuration is the one used in Chapter 4 for the computation of the effective coefficients. The first two steps of the volume averaging method gives identical closed and non-closed macroscopic equations as that presented previously ((2.83), (2.84), (2.33) and (2.34)) with an additional averaged solid source term. More specifically the closed macroscopic equations take the following forms:

For the fluid phase

$$(\rho c_p)_f \phi_f \langle \mathbf{v}_f \rangle^f \cdot \nabla \langle T_f \rangle^f - \mathbf{u}_{ff} \cdot \nabla \langle T_f \rangle^f - \mathbf{u}_{fs} \cdot \nabla \langle T_s \rangle^s = \nabla \cdot \left(\bar{\bar{\mathbf{K}}}_{ff} \nabla \langle T_f \rangle^f + \bar{\bar{\mathbf{K}}}_{fs} \nabla \langle T_s \rangle^s + \mathbf{d}_f (\langle T_f \rangle^f - \langle T_s \rangle^s) \right) - a_V h \left(\langle T_f \rangle^f - \langle T_s \rangle^s \right) \quad (2.95)$$

For the solid phase

$$\mathbf{u}_{ff} \cdot \nabla \langle T_f \rangle^f + \mathbf{u}_{fs} \cdot \nabla \langle T_s \rangle^s = \nabla \cdot \left(\bar{\bar{\mathbf{K}}}_{sf} \nabla \langle T_f \rangle^f + \bar{\bar{\mathbf{K}}}_{ss} \nabla \langle T_s \rangle^s + \mathbf{d}_s (\langle T_s \rangle^s - \langle T_f \rangle^f) \right) - a_V h \left(\langle T_s \rangle^s - \langle T_f \rangle^f \right) + \langle S_s \rangle \quad (2.96)$$

The two-temperature model is composed of 9 effective coefficients that must be determined. To simplify their determination, we want to decrease the number of effective coefficients involved in the two-temperature model. For that purpose, one looks for an acceptable simplification of the modeling. Considering the dispersion and heat coupling modelings (2.76), (2.72), we determine the passive and active parts for each phenomena:

$$\langle \tilde{T}_f \tilde{\mathbf{v}}_f \rangle = \underbrace{\langle \mathbf{b}_{ff} \tilde{\mathbf{v}}_f \rangle \cdot \nabla \langle T_f \rangle^f}_{\text{fluid passive dispersion}} + \underbrace{\langle \mathbf{b}_{fs} \tilde{\mathbf{v}}_f \rangle \cdot \nabla \langle T_s \rangle^s}_{\text{solid passive dispersion}} - \underbrace{\langle s_f \tilde{\mathbf{v}}_f \rangle \left(\langle T_f \rangle^f - \langle T_s \rangle^s \right)}_{\text{active dispersion}} \quad (2.97)$$

$$\frac{k_f}{V} \int_{A_{fs}} \mathbf{n}_{fs} \cdot \nabla \tilde{T}_f dA = \underbrace{\mathbf{u}_{ff} \cdot \nabla \langle T_f \rangle^f}_{\text{fluid active coupling}} + \underbrace{\mathbf{u}_{fs} \cdot \nabla \langle T_s \rangle^s}_{\text{solid active coupling}} - \underbrace{a_v h_f \left(\langle T_f \rangle^f - \langle T_s \rangle^s \right)}_{\text{passive coupling}} \quad (2.98)$$

We choose to use the adjective passive and active for the heat coupling to make a bond with the dispersive phenomena.

To simplify the modeling, we assume that the fluid and solid passive terms of the dispersive phenomenon are correlated and can be modeled together. We do the same for the fluid and solid active terms of the heat coupling phenomenon. Furthermore, our preliminary numerical studies show the equality between the fluid and solid gradients:

$$\nabla \langle T_f \rangle^f \approx \nabla \langle T_s \rangle^s \quad (2.99)$$

The dispersion and heat coupling can thus be rewritten as follows:

$$\langle \tilde{T}_f \tilde{\mathbf{v}}_f \rangle = \bar{\bar{\mathbf{D}}}_p \cdot \nabla \langle T_f \rangle^f + \mathbf{D}_a \left(\langle T_f \rangle^f - \langle T_s \rangle^s \right) \quad (2.100)$$

$$\frac{k_f}{V} \int_{A_{fs}} \mathbf{n}_{fs} \cdot \nabla \tilde{T}_f dA = \mathbf{u} \cdot \nabla \langle T_f \rangle^f - a_v h_f \left(\langle T_f \rangle^f - \langle T_s \rangle^s \right) \quad (2.101)$$

where

$$\bar{\bar{\mathbf{D}}}_p = \bar{\bar{\mathbf{D}}}_p^f + \bar{\bar{\mathbf{D}}}_p^s, \quad \mathbf{u} = \mathbf{u}_{ff} + \mathbf{u}_{fs} \quad (2.102)$$

Using the equality between the temperature gradients, the effective conductivity tensor are brought together such that:

$$\bar{\bar{\mathbf{K}}}_f = \bar{\bar{\mathbf{K}}}_{ff} + \bar{\bar{\mathbf{K}}}_{fs}, \quad \bar{\bar{\mathbf{K}}}_s = \bar{\bar{\mathbf{K}}}_{ss} + \bar{\bar{\mathbf{K}}}_{sf}, \quad (2.103)$$

where

$$\bar{\bar{\mathbf{K}}}_f = \phi_f k_f \bar{\mathbf{I}} + \frac{k_f}{V} \int_{A_{fs}} \mathbf{b}_f \mathbf{n}_{fs} dA + (\rho c_p)_f \bar{\bar{D}}_p \quad (2.104)$$

$$\bar{\bar{\mathbf{K}}}_s = \phi_s k_s \bar{\mathbf{I}} - \frac{k_s}{V} \int_{A_{fs}} \mathbf{b}_f \mathbf{n}_{fs} dA \quad (2.105)$$

Thus, a simplified two-temperature model can be written as follows:

$$(\rho c_p)_f \langle \mathbf{v}_f \rangle \cdot \nabla \langle T_f \rangle^f - \mathbf{u} \cdot \nabla \langle T_f \rangle^f = \nabla \cdot \left(\bar{\bar{\mathbf{K}}}_f \cdot \nabla \langle T_f \rangle^f + \mathbf{d}_f (\langle T_f \rangle^f - \langle T_s \rangle^s) \right) - a_V h \left(\langle T_f \rangle^f - \langle T_s \rangle^s \right) \quad (2.106)$$

$$\mathbf{u} \cdot \nabla \langle T_f \rangle^f = \nabla \cdot \left(\bar{\bar{\mathbf{K}}}_s \cdot \nabla \langle T_s \rangle^s + \mathbf{d}_s (\langle T_f \rangle^f - \langle T_s \rangle^s) \right) + a_V h \left(\langle T_f \rangle^f - \langle T_s \rangle^s \right) + \langle S_s \rangle \quad (2.107)$$

This two-temperature model is composed of 6 effective coefficients that must be determined. The effective coefficients are determined in the next paragraph using the identification method of (Kuwahara et al., 1996; Kuwahara and Nakayama, 1999; Kuwahara et al., 2001).

In this paragraph we introduced a new closed macroscopic model that verifies the constraints imposed by the identification method. Indeed, the identification method imposes to keep separated the modelings of the dispersive and heat coupling phenomena. These macroscopic phenomena are modeled considering a passive and an active part with two different microscopic origins (see Fig. 2.6). We will discuss these modelings in the following.

2.4.2.2 Determination of the effective coefficients

Geometry and boundary conditions

We consider laminar flows through an infinite porous medium made of in-line squares (see Fig. 2.7). The mean flow is directed towards the y -direction. The study is performed for various Peclet numbers ($0, 1 < Pe < 300$) and thermal conductivity ratios ($0, 001 < k_s/k_f < 10000$). The numerical computations are realized for a fixed porosity $\phi_p = 5/9$ and a fixed Prandtl number $Pr = 1$.

The boundary conditions at the outlet and at the inlet are conditions of pseudo-periodicity for the temperature and the pressure. The variable change used to compute the temperature field resulting of boundary conditions of pseudo-periodicity is presented in appendix A. At the steady-state, the boundary conditions of pseudo-periodicity impose $\nabla \langle T_f \rangle^f \cdot \mathbf{e}_y = cste$. In order to create temperature gradients not proportional to the temperature difference ($(\langle T_f \rangle^f - \langle T_s \rangle^s) \neq cste$), we combine the solid heat source with an incoming heat flux on the lateral boundaries.

The microscopic temperature field is obtained by solving numerically the equations (2.13) to (2.16) on a uniform Cartesian grid. The finite-volume method is used with a second-order central-differencing scheme for the spatial discretization.

Identification method

The expression for the effective coefficients are obtained by identification between the non-closed macroscopic equations (2.33), (2.34) and the closed ones (2.106), (2.107). One can write:

$$\bar{\bar{\mathbf{K}}}_f \cdot \nabla \langle T_f \rangle^f + \mathbf{d}_f \left(\langle T_f \rangle^f - \langle T_s \rangle^s \right) = k_f \nabla \langle T_f \rangle + \frac{k_f}{V} \int_{A_{fs}} \mathbf{n}_{fs} \tilde{T}_f dA - (\rho c_p)_f \left\langle \tilde{T}_f \tilde{\mathbf{v}}_f \right\rangle \quad (2.108)$$

$$\bar{\bar{\mathbf{K}}}_s \cdot \nabla \langle T_s \rangle^s + \mathbf{d}_s \left(\langle T_f \rangle^f - \langle T_s \rangle^s \right) = k_s \nabla \langle T_s \rangle - \frac{k_s}{V} \int_{A_{fs}} \mathbf{n}_{fs} \tilde{T}_f dA \quad (2.109)$$

$$a_V h \left(\langle T_f \rangle^f - \langle T_s \rangle^s \right) - \mathbf{u} \cdot \nabla \langle T_f \rangle^f = -\frac{k_f}{V} \int_{A_{fs}} \mathbf{n}_{fs} \cdot \nabla \tilde{T}_f dA \quad (2.110)$$

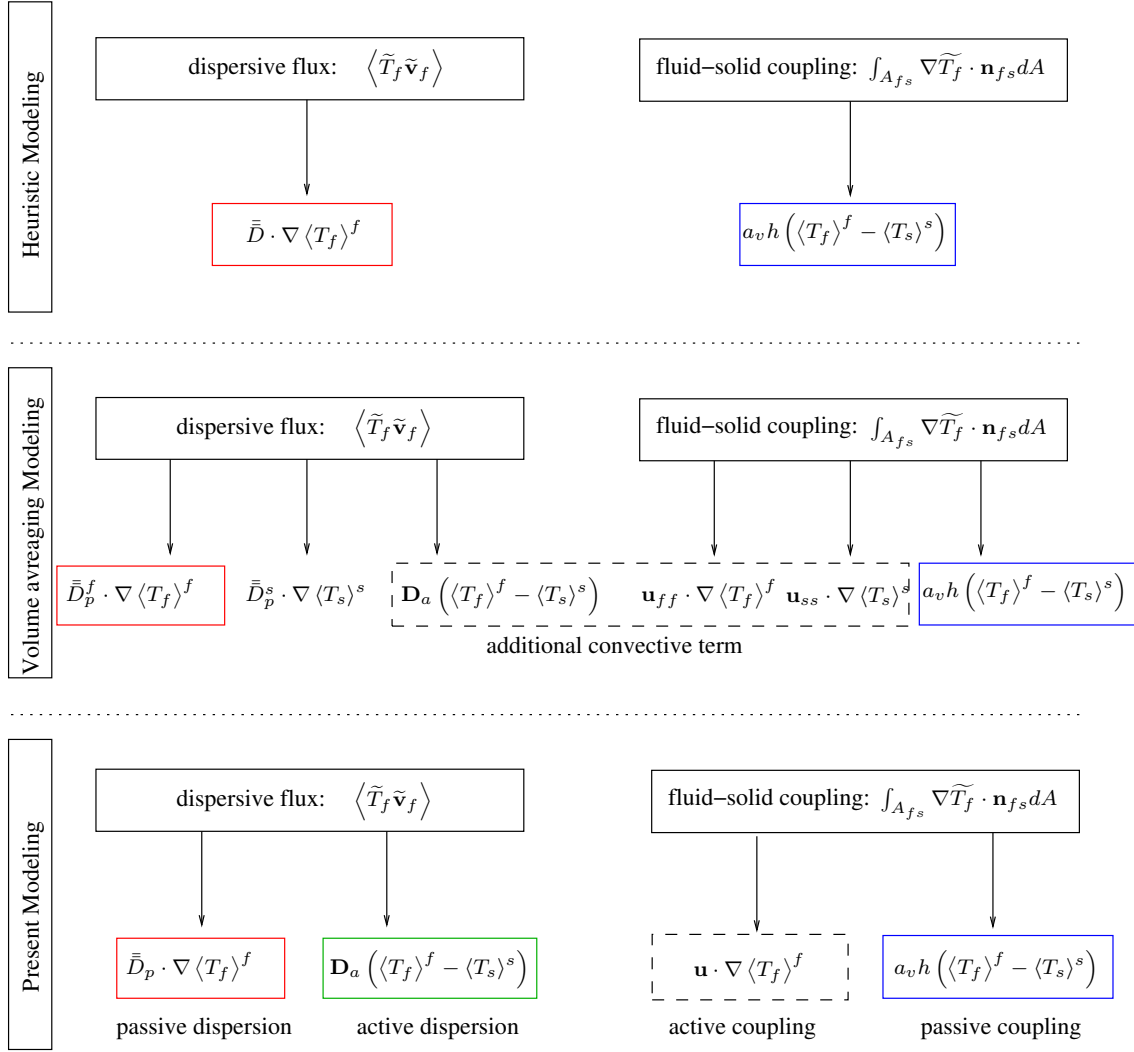


Figure 2.6: Synthesis of the different modelings.

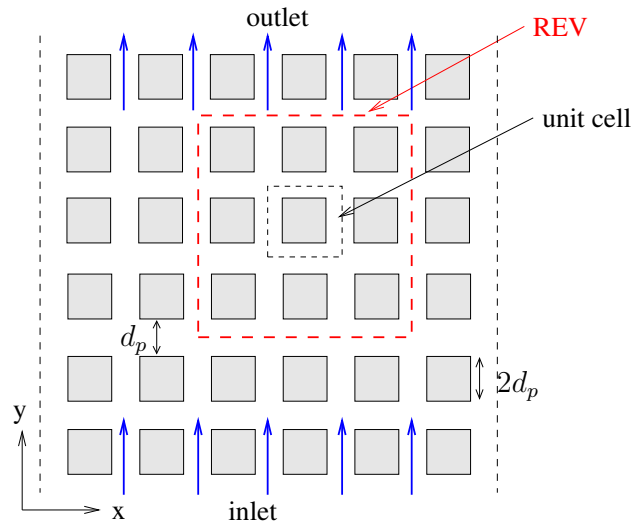


Figure 2.7: Geometry and its coordinate system.

Then, each term of the above relations is computed using the microscopic temperature and velocity fields of the numerical simulations.

The porous medium is isotropic and the averaged velocity field is uniform on the whole domain, thus, the effective transfer coefficients are constant and do not depend on the y - and x -directions. Consequently, the knowledge of the microscopic temperature and velocity fields in the REV is sufficient to compute the effective coefficients. Furthermore, one recalls that the boundary conditions are chosen to obtain temperature gradients valid for the determination of the effective coefficients. In order to verify the effective nature of the coefficients obtained with the identification method, we change the boundary conditions and we verify that the coefficients are independent of the temperature fields.

Introducing the following writings:

$$\bar{\mathbf{K}}_i = \begin{pmatrix} K_{xx}^i & K_{xy}^i \\ K_{yx}^i & K_{yy}^i \end{pmatrix}, \quad \mathbf{d}_i = \begin{pmatrix} d_x^i \\ d_y^i \end{pmatrix}, \quad \mathbf{u} = \begin{pmatrix} u_x \\ u_y \end{pmatrix} \quad (2.111)$$

the equations (2.108), (2.109) can be developed such that:

In the x -direction

$$K_{xx}^f \frac{\partial \langle T_f \rangle^f}{\partial x} + K_{xy}^f \frac{\partial \langle T_f \rangle^f}{\partial y} + d_x^f (\langle T_f \rangle^f - \langle T_s \rangle^s) = k_f \frac{\partial \langle T_f \rangle}{\partial x} + \frac{k_f}{V} \int_{A_{fs}} \mathbf{n}_{fs} \tilde{T}_f dA \cdot \mathbf{e}_x - (\rho c_p)_f \langle \tilde{T}_f \tilde{\mathbf{v}}_f \rangle \cdot \mathbf{e}_x \quad (2.112)$$

$$K_{xx}^s \frac{\partial \langle T_s \rangle^s}{\partial x} + K_{yx}^s \frac{\partial \langle T_s \rangle^s}{\partial y} + d_x^s (\langle T_f \rangle^f - \langle T_s \rangle^s) = k_s \frac{\partial \langle T_s \rangle}{\partial x} - \frac{k_s}{V} \int_{A_{fs}} \mathbf{n}_{fs} \tilde{T}_f dA \cdot \mathbf{e}_x \quad (2.113)$$

In the y -direction

$$K_{yy}^f \frac{\partial \langle T_f \rangle^f}{\partial y} + K_{yx}^f \frac{\partial \langle T_f \rangle^f}{\partial x} + d_y^f (\langle T_f \rangle^f - \langle T_s \rangle^s) = k_f \frac{\partial \langle T_f \rangle}{\partial y} + \frac{k_f}{V} \int_{A_{fs}} \mathbf{n}_{fs} \tilde{T}_f dA \cdot \mathbf{e}_y - (\rho c_p)_f \langle \tilde{T}_f \tilde{\mathbf{v}}_f \rangle \cdot \mathbf{e}_y \quad (2.114)$$

$$K_{yy}^s \frac{\partial \langle T_s \rangle^s}{\partial y} + K_{yx}^s \frac{\partial \langle T_s \rangle^s}{\partial x} + d_y^s (\langle T_f \rangle^f - \langle T_s \rangle^s) = k_s \frac{\partial \langle T_s \rangle}{\partial y} - \frac{k_s}{V} \int_{A_{fs}} \mathbf{n}_{fs} \tilde{T}_f dA \cdot \mathbf{e}_y \quad (2.115)$$

And the relation (2.110) can be rewritten as:

$$a_V h (\langle T_f \rangle^f - \langle T_s \rangle^s) - u_x \frac{\partial \langle T_f \rangle^f}{\partial x} - u_y \frac{\partial \langle T_f \rangle^f}{\partial y} = -\frac{k_f}{V} \int_{A_{fs}} \left(\frac{\partial \tilde{T}_f}{\partial x} + \frac{\partial \tilde{T}_f}{\partial y} \right) dA \quad (2.116)$$

The equations (2.112) to (2.116) are composed of 15 unknowns. To solve this system, three numerical simulations with different solid heat sources or incoming heat fluxes are realized to obtain 15 equations. Thus, for example, the system corresponding to the relation (2.112) takes the following form:

$$K_{xx}^f \frac{\partial \langle T_f^1 \rangle^f}{\partial x} + K_{xy}^f \frac{\partial \langle T_f^1 \rangle^f}{\partial y} + d_x^f (\langle T_f^1 \rangle^f - \langle T_s^1 \rangle^s) = f(T_f^1) \quad (2.117)$$

$$K_{xx}^f \frac{\partial \langle T_f^2 \rangle^f}{\partial x} + K_{xy}^f \frac{\partial \langle T_f^2 \rangle^f}{\partial y} + d_x^f (\langle T_f^2 \rangle^f - \langle T_s^2 \rangle^s) = f(T_f^2) \quad (2.118)$$

$$K_{xx}^f \frac{\partial \langle T_f^3 \rangle^f}{\partial x} + K_{xy}^f \frac{\partial \langle T_f^3 \rangle^f}{\partial y} + d_x^f (\langle T_f^3 \rangle^f - \langle T_s^3 \rangle^s) = f(T_f^3) \quad (2.119)$$

where

$$f(T_f^i) = k_f \frac{\partial \langle T_f^i \rangle}{\partial x} + \frac{k_f}{V} \int_{A_{fs}} \mathbf{n}_{fs} \tilde{T}_f^i dA \cdot \mathbf{e}_x - (\rho c_p)_f \langle \tilde{T}_f^i \tilde{\mathbf{v}}_f \rangle \cdot \mathbf{e}_x \quad (2.120)$$

The simulation results show that $K_{yx}^f \approx K_{xy}^f \approx K_{yx}^s \approx K_{xy}^s \approx 0$. Thus, the effective conductivity tensors are diagonal. This result can be explained by the isotropic porous matrix and the uni-directed mean flow. Furthermore, one obtains $u_x \approx d_x^f \approx d_x^s \approx 0$, resulting from the no-transportation and the no-active dispersion in the x -direction since the mean flow is 1D in the y -direction.

Figs. 2.8(a), 2.8(b), 2.9(a), 2.9(b), 2.10(a), 2.10(b), 2.11(a) and 2.11(b) present the effective transfer coefficients as functions of the Peclet number and for various conductivity ratios.

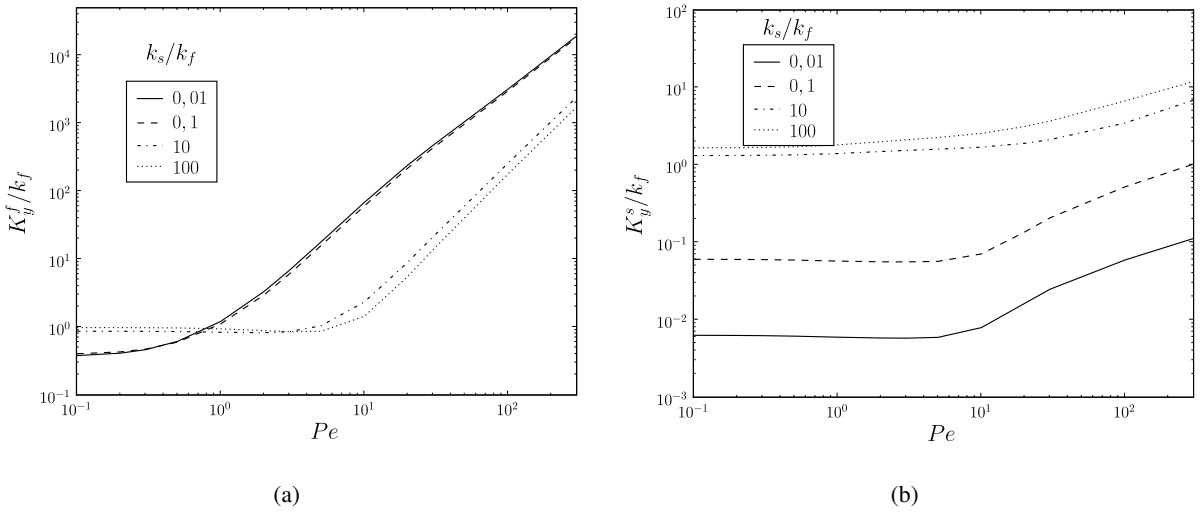


Figure 2.8: Effective thermal conductivity coefficient in the flow direction (a) for the fluid phase K_{yy}^f ; (b) for the solid phase K_{yy}^s .

The fluid and solid effective thermal conductivities in the flow direction are illustrated in Figs. 2.8(a) and 2.8(b). For the fluid phase, the usual behavior of the longitudinal thermal conductivity coefficient is recovered (Quintard et al., 1997). The values can be divided in three domains. For low Peclet numbers ($Pe < 0.2$ for $k_s/k_f < 1$ and $Pe < 3$ for $k_s/k_f > 1$), the values are constant and diffusion dominates, then follows a transition regime ($0.2 < Pe < 1$ for $k_s/k_f < 1$ and $3 < Pe < 10$ for $k_s/k_f > 1$) and an asymptotic increase in Pe^n characteristic of the passive dispersion phenomenon at large Peclet numbers (> 1 for $k_s/k_f < 1$ and $Pe > 10$ for $k_s/k_f > 1$). For the solid phase, the values of K_y^s correspond to the diffusion and the tortuosity phenomena, which are weakly dependent on the Peclet number.

The effective transport coefficients in the flow direction d_y^f and d_y^s are presented in Figs. 2.9(a) and 2.9(b). Let us remind that d_y^f is composed of the tortuosity and the active dispersion phenomena, whereas for the solid phase, d_y^s is composed of the tortuosity phenomenon exclusively. The tortuosity values are close for the solid and fluid phase and are estimated to 10^{-2} (see Figs. 2.9(b)). Considering the order of magnitude of d_y^f at 10^{-1} , one can assume that the active dispersion dominates the tortuosity in d_y^f .

The transverse effective thermal conductivities are showed in Figs. 2.10(a) and 2.10(b). The profiles of K_x^f depend on the conductivity ratio. For $k_s/k_f > 10$, the diffusion phenomenon dominates and the profiles weakly depend on the Peclet numbers. For $k_s/k_f < 10$, the profiles can be divided in three

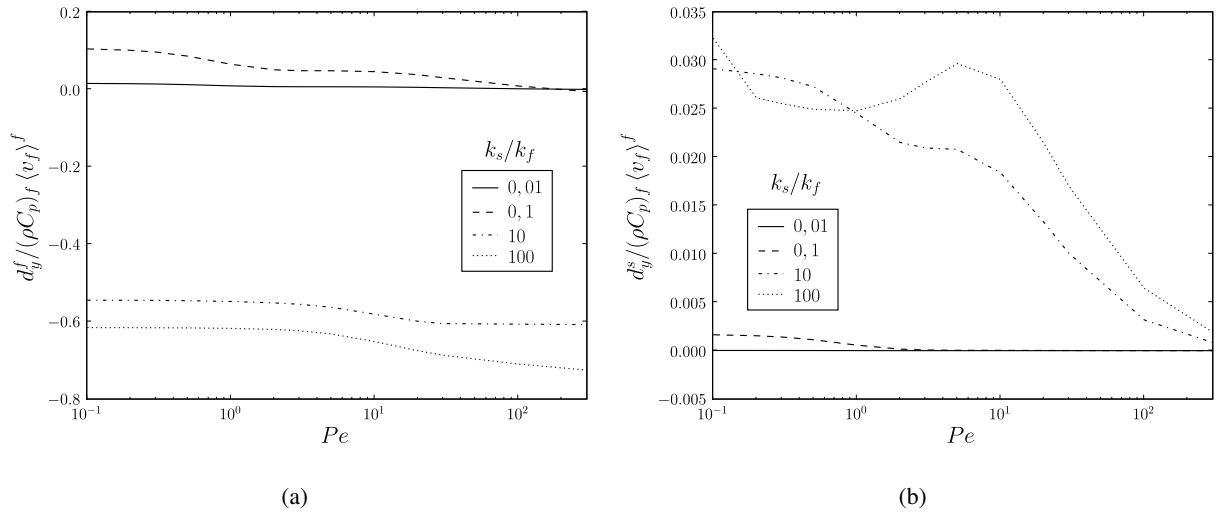


Figure 2.9: Effective transport coefficient in the flow direction (a) for the fluid phase d_y^f ; (b) for the solid phase d_y^s .

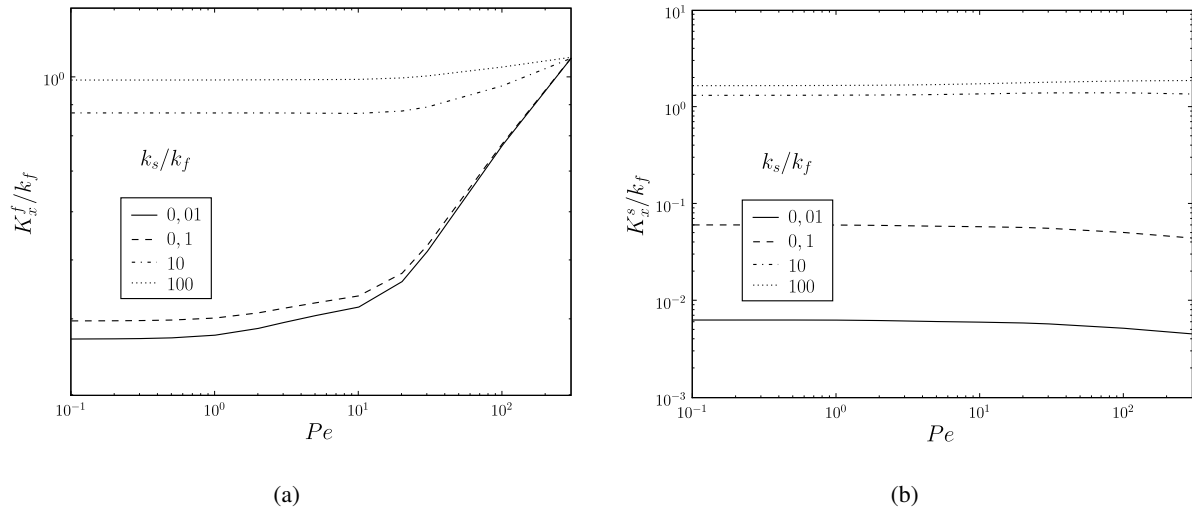


Figure 2.10: Transverse effective transport coefficient (a) for the fluid phase K_{xx}^f ; (b) for the solid phase K_{xx}^s .

domains: a domain for low Peclet numbers ($Pe < 1$) where the diffusion phenomenon dominates, a domain of transition ($1 < Pe < 40$) and at high Peclet numbers ($Pe > 40$) a domain where the values increase. In this last domain, the values of K_x^f are lower than K_y^f . Thus, one can conclude that the dispersion phenomenon is directed for a large part in the y -direction. For the solid phase, K_x^s does not depend of the Peclet numbers and the values of K_y^s for low Peclet numbers are recovered.

The effective transport coefficient u_y and the effective heat transfer coefficient $a_V h$ are presented in Figs. 2.11(a) and 2.11(b). The effective heat transfer coefficient does not depend on the Peclet numbers for conductivity ratios $k_f/k_s < 1$, and for $k_f/k_s > 1$ a slight influence appears at $Pe > 10$. However, this dependence is smaller than the behavior in $Re^{0.6} Pe^{1/3}$ found by the heuristic approach (see (Wakao and Kaguei, 1982)).

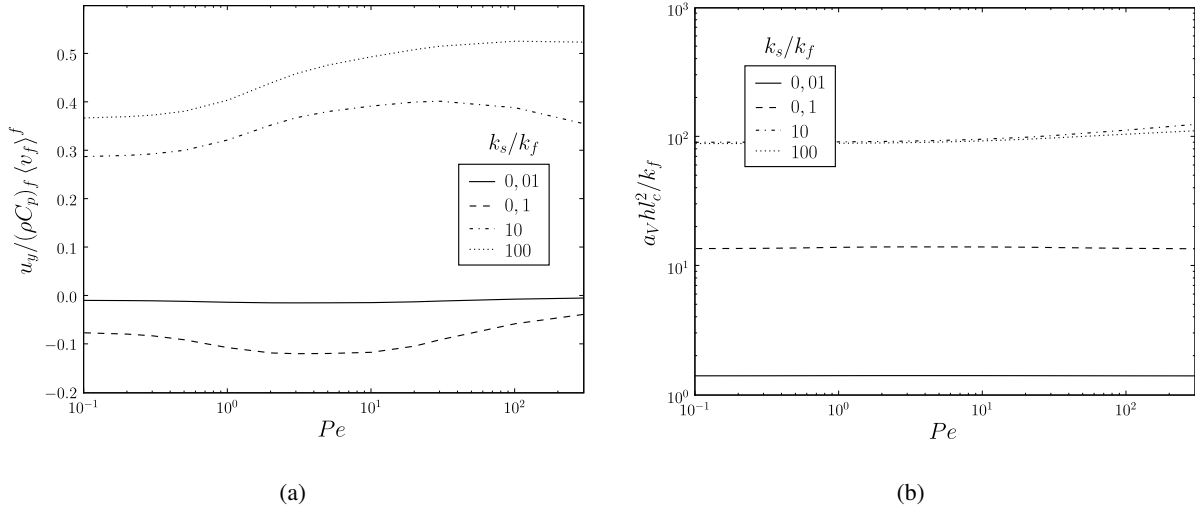


Figure 2.11: (a) Effective convective coefficient u_y . (b) Effective heat transfer coefficient $a_v h$.

In order to compare the results with those published in (Quintard et al., 1997), we recall the quantities illustrated. Quintard et al. (1997) present the tensors $\bar{\bar{K}}_{ii}^i$ and $\bar{\bar{K}}_{ij}^i$ that are related to our values according to $\bar{\bar{K}}^i = \bar{\bar{K}}_{ii}^i + \bar{\bar{K}}_{ij}^i$ for the fluid and solid phases respectively. Allowing for the different choices of the geometry, in-line cubes instead of in-line cylinders, the main behaviors of the effective coefficients are recovered.

Furthermore, even if the negative values of the effective coefficients u_y and d_y^f seem to be inaccurate, such results are valid. Similar results are observed by Quintard et al. (1997) for the effective transport coefficients \mathbf{c}_{ff} , \mathbf{c}_{fs} and \mathbf{c}_{sf} in the flow direction (see equations (2.87), (2.88)). From the relation $\mathbf{c}_{ff} + \mathbf{c}_{fs} = \mathbf{u}$, Fig. 2.11(a) can be compared with the added profiles of Figs. 9 and 10 page 87 in (Quintard et al., 1997).

In this Section we have presented an alternative approach to the volume averaging and mixed methods. This method allows to characterize a homogeneous porous medium (determination of a macroscopic model and of effective coefficients) and can be extended to the study of heat transfer at a free-porous interface. The advantages are that the effective coefficients are determined without length scale considerations and the macroscopic model is derived from the microscopic equations in a homogeneous porous medium. The obtained effective coefficients are in accordance with the results presented by Quintard et al. (1997), which validates the method. In the following, these results are used to discuss further different modeling options for the dispersion and heat coupling phenomena.

2.4.2.3 Determination of the main heat transfer phenomena

This paragraph is about the modeling of the dispersion and the heat coupling phenomena. As the dispersion phenomenon is negligible in the x -direction, the discussion focuses on the heat transfer modeling in the y -direction only.

The dispersion and the heat coupling are composed of a passive part and of an active part. The objective of this paragraph is to determine which part dominates the other. In order to discuss the modeling, the passive and active part are computed and compared using the following definition of percentage:

$$\% = \frac{|\text{part}|}{|\text{passive part}| + |\text{active part}|} * 100 \quad (2.121)$$

2.4 Two-temperature modeling: another interpretation

For the dispersive flux, the passive part $\overline{\overline{D_p}} \cdot \nabla \langle T_f \rangle^f$ and the active part $\mathbf{D}_a(\langle T_f \rangle^f - \langle T_s \rangle^s)$ in the y -direction are determined using the identification method for various Peclet numbers and conductivity ratios. The results are presented in Figs. 2.12(a), 2.12(b), 2.13(a) and 2.13(b).

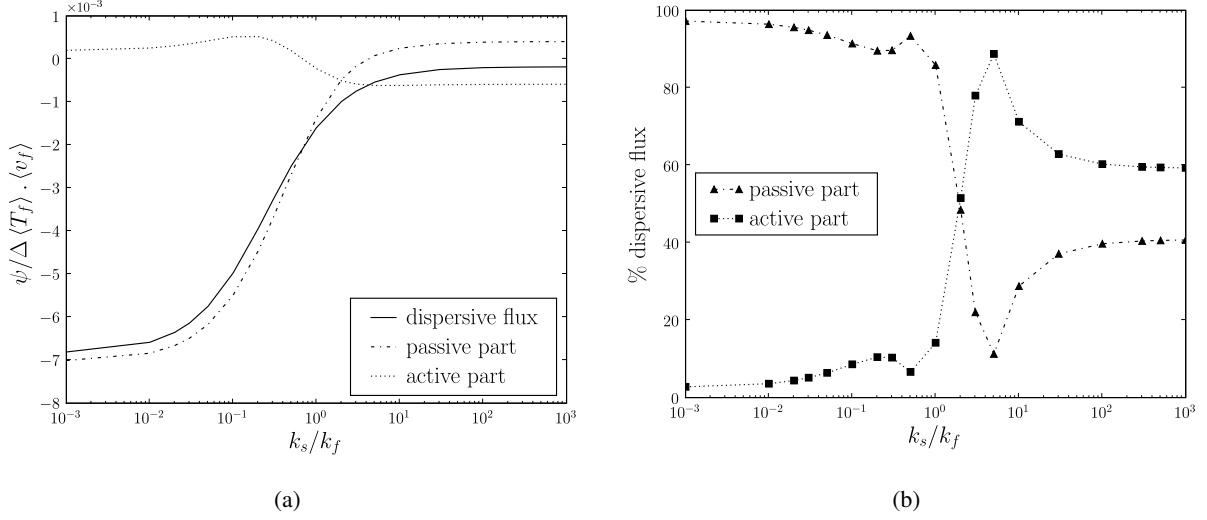


Figure 2.12: (a) Comparison between active and passive dispersive flux for $Pe = 0, 1$; (b) Comparison in percent for $Pe = 0, 1$.

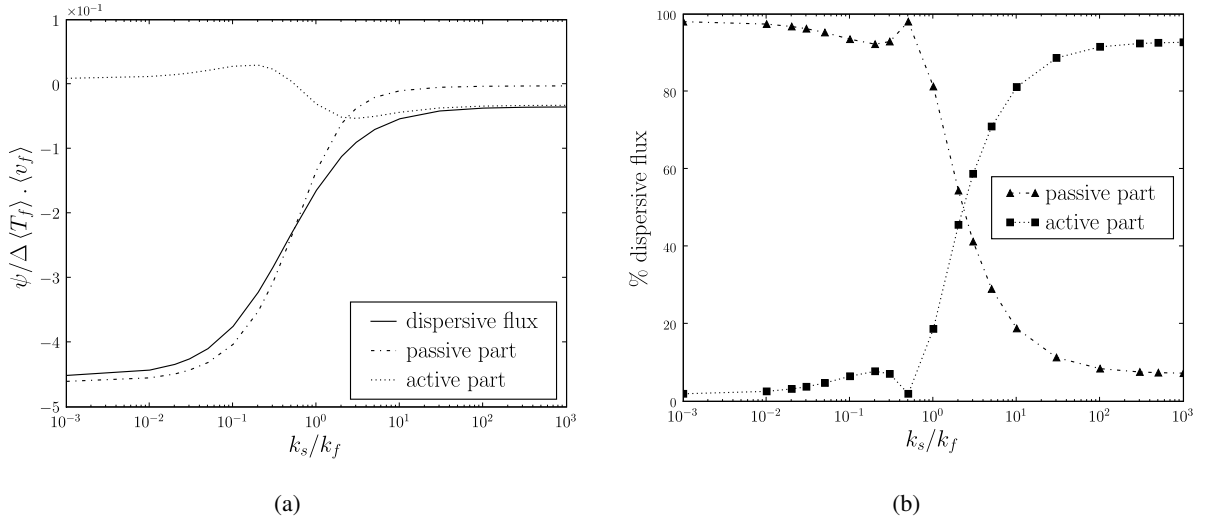


Figure 2.13: (a) Comparison between active and passive dispersive flux for $Pe = 10$; (b) Comparison in percent for $Pe = 10$.

The composition of the dispersive flux varies with the thermal conductivity ratio k_s/k_f and can be divided in two parts for Peclet numbers $Pe < 5$:

- for $k_s/k_f < 2$, the passive part dominates the active part. The dispersive flux is created by the spatial deviation of the velocity field.
- for $k_s/k_f > 2$, the passive part and the active part are of the same order.

For Peclet numbers $Pe > 5$, an additional zone appears:

- for $k_s/k_f > 10$, the active part $\mathbf{D}_a(\langle T_f \rangle^f - \langle T_s \rangle^s)$ dominates the passive part $\overline{\overline{\mathbf{D}_p}} \cdot \nabla \langle T_f \rangle^f$.

For the heat coupling between the phases, the passive part $a_V h(\langle T_f \rangle^f - \langle T_s \rangle^s)$ and the active part $\mathbf{u} \cdot \nabla \langle T_f \rangle^f$ are computed for various Peclet numbers and conductivity ratios. The results are presented in Figs. 2.14(a), 2.14(b), 2.15(a) and 2.15(b).

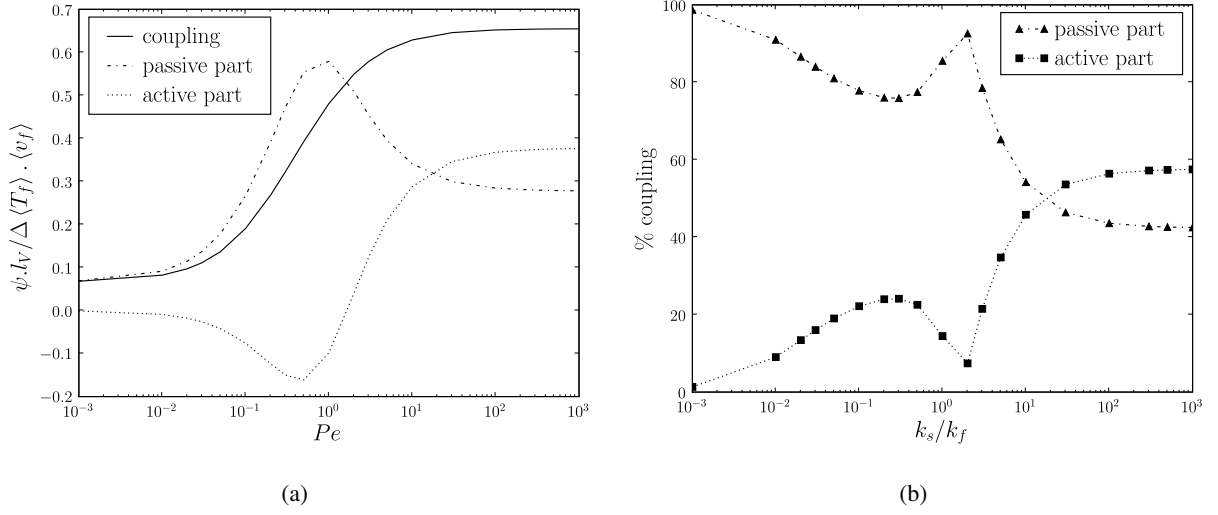


Figure 2.14: (a) Comparison between active and passive heat coupling for $Pe = 0, 1$; (b) Comparison in percent for $Pe = 0, 1$.

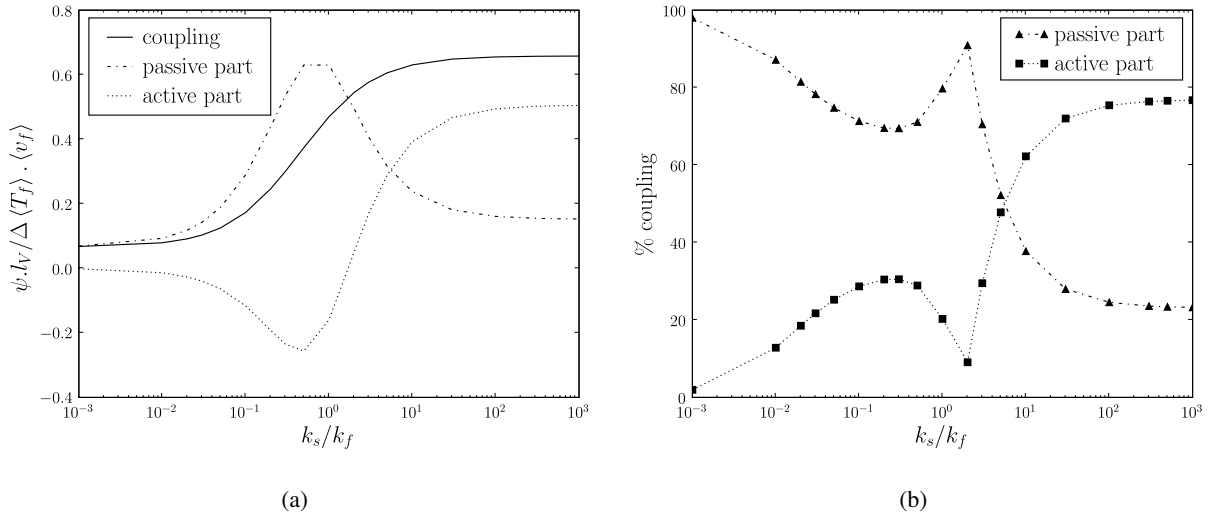


Figure 2.15: (a) Comparison between active and passive heat coupling for $Pe = 10$; (b) Comparison in percent for $Pe = 10$.

The composition of the coupling between the phases varies with the thermal conductivity ratio k_s/k_f and can be divided in two parts for $Pe < 5$:

- for $k_s/k_f < 2$, the passive part dominates the active part;
- for $k_s/k_f > 2$, the passive part and the active part are of the same order.

For $Pe > 5$, an additional zone appears:

- for $k_s/k_f > 10$, the active part $\mathbf{u} \cdot \nabla \langle T_f \rangle^f$ dominates the passive part $a_V h (\langle T_f \rangle^f - \langle T_s \rangle^s)$.

Furthermore, we assume some simplifications for the tortuosity term, whose definition (2.77) is rewritten using the temperature gradient equality $\nabla \langle T_f \rangle^f = \nabla \langle T_s \rangle^s$:

$$\frac{k_f}{V} \int_{A_{fs}} \mathbf{n}_{fs} \widetilde{T}_f dA = \overline{\overline{K}}_{tor}^f \cdot \nabla \langle T_f \rangle^f + \mathbf{K}_{tor}^a \left(\langle T_f \rangle^f - \langle T_s \rangle^s \right) \quad (2.122)$$

where

$$\overline{\overline{K}}_{tor}^f = \overline{\overline{K}}_{tor}^{ff} + \overline{\overline{K}}_{tor}^{fs} \quad (2.123)$$

The quantity \mathbf{K}_{tor}^a is involved in the effective transport coefficient \mathbf{d}_f through the relation (2.78). In the y -direction, the dispersive term dominates the tortuosity term (see note in Section 2.4.2.2). Thus the effective transport coefficients can be simplified:

$$d_y^f = D_y^a \quad (2.124)$$

To consider the passive dispersion in the effective conductivity tensor, we use the following decompositions:

$$\overline{\overline{K}}_f = \phi_f k_f \overline{\overline{I}} + \overline{\overline{K}}_{tor}^f + \overline{\overline{D}}_p^f \quad (2.125)$$

Extending this writing to the solid phase, one has:

$$\overline{\overline{K}}_s = k_s \overline{\overline{I}} + \overline{\overline{K}}_{tor}^s \quad (2.126)$$

From all these results, one can construct two-temperature models based on the modeling of the dispersive flux and the coupling between the phase phenomena:

- **For $Pe < 5$ and $k_s/k_f < 2$**

$$(\rho c_p)_f \frac{\partial}{\partial y} \left(\phi_f \langle \mathbf{v}_f \rangle^f \langle T_f \rangle^f \right) = \frac{\partial}{\partial y} \left((\phi_f k_f + K_{yy}^{tor,f} + D_{yy}^p) \frac{\partial \langle T_f \rangle^f}{\partial y} \right) - a_V h_f \left(\langle T_f \rangle^f - \langle T_s \rangle^s \right) \quad (2.127)$$

$$0 = \frac{\partial}{\partial y} \left((\phi_s k_s + K_{yy}^{tor,s}) \frac{\partial \langle T_s \rangle^s}{\partial y} + d_y^s \left(\langle T_f \rangle^f - \langle T_s \rangle^s \right) \right) + a_V h_f \left(\langle T_f \rangle^f - \langle T_s \rangle^s \right) \quad (2.128)$$

This two-temperature model is quite similar to the one used by the heuristic approach. This modeling reflects, that the dispersion is mainly due to the velocity fluctuations and the heat coupling by the thermal disequilibrium between the fluid and the solid temperatures. However this kind of conductivity ratio is rarely observed in real cases.

- **For $Pe < 5$ and $k_s/k_f > 2$** , the model cannot be simplified and all the phenomena have to be taken into account.

$$(\rho c_p)_f \frac{\partial}{\partial y} \left(\langle \mathbf{v}_f \rangle \langle T_f \rangle^f \right) - u_y^f \frac{\partial \langle T_f \rangle^f}{\partial y} = \frac{\partial}{\partial y} \left((k_f + K_{yy}^{tor,f} + D_{yy}^p) \frac{\partial \langle T_f \rangle^f}{\partial y} \right) + \frac{\partial}{\partial y} \left(D_y^a \left(\langle T_f \rangle^f - \langle T_s \rangle^s \right) \right) - a_V h_f \left(\langle T_f \rangle^f - \langle T_s \rangle^s \right) \quad (2.129)$$

$$u_y^f \frac{\partial \langle T_f \rangle^f}{\partial y} = \frac{\partial}{\partial y} \left((k_s + K_{yy}^{tor,s}) \frac{\partial \langle T_s \rangle^s}{\partial y} + d_y^s \left(\langle T_f \rangle^f - \langle T_s \rangle^s \right) \right) + a_V h_f \left(\langle T_f \rangle^f - \langle T_s \rangle^s \right) \quad (2.130)$$

Apart from the difference in the writing, such a modeling corresponds to one obtained with the volume averaging method (Quintard et al., 1997). In this case, this two-temperature model seems to be the most

appropriate to describe the heat transfer.

• **For higher Peclet number** ($Pe > 5$) **and conductivity ratios** $k_s/k_f > 10$, there exists another form of two-temperature model. Indeed, in such a configuration, the dispersion and the coupling between the phase phenomena are directed by their active part and the associate modeling is the following:

$$(\rho c_p)_f \frac{\partial}{\partial y} \left(\phi_f \langle \mathbf{v}_f \rangle^f \langle T_f \rangle^f \right) - u_y \frac{\partial \langle T_f \rangle^f}{\partial y} = \frac{\partial}{\partial y} \left((k_f + K_{yy}^{tor,f}) \frac{\partial \langle T_f \rangle^f}{\partial y} \right) + \frac{\partial}{\partial y} \left(D_y^a \left(\langle T_f \rangle^f - \langle T_s \rangle^s \right) \right) \quad (2.131)$$

$$u_y \frac{\partial \langle T_f \rangle^f}{\partial y} = \frac{\partial}{\partial y} \left((k_s + K_{yy}^{tor,s}) \frac{\partial \langle T_s \rangle^s}{\partial y} + d_y^s \left(\langle T_f \rangle^f - \langle T_s \rangle^s \right) \right) \quad (2.132)$$

To conclude, the form of the two-temperature model depends strongly on the conductivity ratio and in the case of high ratio it depends also of the velocity fields. For small conductivity ratios ($k_s/k_f < 2$), the simplified modeling of [Wakao and Kaguei \(1982\)](#) is valid. For higher conductivity ratios, this modeling is not appropriate and all the phenomena must be considered. Indeed, the two-temperature model cannot be simplified and the determination of the 6 effective coefficients is required to correctly reflect the transfers. For high Peclet numbers and for conductivity ratio $k_s/k_f > 10$, the complete two-temperature modeling can be simplified again as equations (2.131) and (2.132).

In this Section, we have compared the passive and active parts of the dispersion and heat coupling phenomena. It results in some simplifications for the closed macroscopic model. Thus, we have proposed three different closed macroscopic models depending on the conductivity ratio and Peclet numbers.

2.5 Conclusion

In this chapter, we reviewed different macroscopic models existing in the literature to describe the heat transfer at local thermal equilibrium and local thermal non-equilibrium in a homogeneous porous medium. We present three methods to derive such models:

- the heuristic method based on empirical modeling and the determination of the effective transfer coefficients with experimentation;
- the volume averaging method that characterizes the porous medium following three steps. First a smoothing process changes the scale of description from microscopic to macroscopic. This process makes appear non-closed terms involving spatial deviations characteristic of the microscopic scale. The second step closes the macroscopic model by connecting the non-closed terms with the macroscopic phenomena at the origin of the deviations. The third step consists in determining the effective transfer coefficients with closure problems based on length scales considerations. The advantage of this method is to derive a closed model from the microscopic governing equations that gives all the phenomena existing at the macroscopic scale. However this method relies on the strong hypotheses of length scale separation that is not valid in a transition zone;
- the mixed method that uses the volume averaging method and the heuristic method. The non-closed macroscopic model is derived from the governing microscopic equations performing the first step of the volume averaging method, while the closed macroscopic model is postulated following the literature of the heuristic method. The determination of the effective coefficient is obtained by identification between the non-closed and closed macroscopic models. The advantage of this method relies on the absence of length scale considerations to determine the relations of the effective coefficients. However, these relations strongly depend on the form of the closed macroscopic model.

In the context of the transfer modeling in a transition zone, these methods cannot be used directly. Indeed the steps 2 and 3 of the volume averaging method cannot be performed in the transition zone where the length scale separation is not valid. Furthermore, the closed macroscopic model used by the mixed method is not appropriate to study heat transfer at the local thermal non-equilibrium. Thus, we developed another approach to characterize the heat transfer. First the non-closed macroscopic model is derived from the microscopic equations performing the first step of the volume averaging method. Second, the macroscopic model is closed using the second step of the volume averaging method. Then the effective coefficients are determined by identification between the closed and non-closed macroscopic model as for the mixed method. We remind, that this identification method requires to keep separated the macroscopic dispersion and heat coupling phenomena. This is the reason why we propose a different closed macroscopic model from the one presented by [Quintard et al. \(1997\)](#). Finally, this method is validated by comparing with the results given by the volume averaging method ([Quintard et al., 1997](#)).

The models presented in this chapter (see Tab. (2.2) hereafter) are used in Chapters 3 and 4 to study heat transfer at a free-porous interface.

In Chapter 3, we study heat transfer at local thermal equilibrium for a flow normal to the free-porous interface. The first step of the volume averaging method is performed given the one-temperature equation (2.133a) valid in the whole domain including the transition zone. The second step of the volume averaging model leads to the closed macroscopic model (2.133b) in the homogeneous porous region and we assume that it is valid in the transition zone. Then, the effective coefficients are determined in the whole domain following the mixed method.

In Chapter 4, we study heat transfer at the local thermal non-equilibrium for a flow normal to the free-porous interface. Performing an identical process, we obtain two-temperature macroscopic models (see equations (2.133c) to (2.133f)). By construction, the non-closed model (2.133c) and (2.133d) is valid in the whole domain including the transition zone, while the closed model (2.133e) and (2.133f) is derived in the homogeneous porous medium and then extended to the transition zone. At last, the effective coefficients are computed in the whole domain including the transition zone.

At local thermal equilibrium

Non-closed one-temperature model:

$$\begin{aligned}
 (\rho c_p)_f \nabla \cdot (\phi_f \langle \mathbf{v}_f \rangle^f \langle T \rangle) &= \nabla \cdot ((k_f \phi_f + k_s \phi_s) \nabla \langle T \rangle) + \nabla \cdot \left(\frac{k_f - k_s}{V} \int_{A_{fs}} \tilde{T}_f(\mathbf{r}) \mathbf{n}_{fs} dA \right) + \\
 &\nabla \cdot \left(\frac{k_f - k_s}{V} \int_{A_{fs}} (\langle T \rangle(\mathbf{r}) - \langle T \rangle(\mathbf{x})) \mathbf{n}_{fs} dA \right) - \nabla \cdot ((\rho c_p)_f \langle \tilde{T}_f \tilde{\mathbf{v}}_f \rangle) \quad (2.133a)
 \end{aligned}$$

Closed one-temperature model:

$$(\rho c_p)_f \nabla \cdot (\phi_f \langle \mathbf{v}_f \rangle^f \langle T \rangle) = \nabla \cdot (\bar{\bar{K}} \cdot \nabla \langle T \rangle) \quad (2.133b)$$

At the local thermal non-equilibrium

Non-closed two-temperature model:

$$\begin{aligned}
 (\rho c_p)_f \nabla \cdot (\phi_f \langle \mathbf{v}_f \rangle^f \langle T_f \rangle^f) &= \nabla \cdot \left(k_f \phi_f \nabla \langle T_f \rangle^f + \frac{k_f}{V} \int_{A_{fs}} \mathbf{n}_{fs} \tilde{T}_f dA - (\rho c_p)_f \tau_{Tv} \right) + \\
 &\nabla \cdot \left(\frac{k_f}{V} \int_{A_{fs}} (\langle T_f \rangle^f(\mathbf{r}) - \langle T_f \rangle^f(\mathbf{x})) \mathbf{n}_{sf} dA \right) + \\
 &\frac{k_f}{V} \int_{A_{fs}} \mathbf{n}_{fs} \cdot (\nabla \langle T_f \rangle^f(\mathbf{r}) + \nabla \tilde{T}_f(\mathbf{r})) dA \quad (2.133c)
 \end{aligned}$$

$$\begin{aligned}
 0 &= \nabla \cdot \left(k_s \phi_s \nabla \langle T_s \rangle^s - \frac{k_s}{V} \int_{A_{fs}} \mathbf{n}_{fs} \tilde{T}_f dA - \frac{k_s}{V} \int_{A_{fs}} (\langle T_f \rangle^f(\mathbf{r}) - \langle T_f \rangle^f(\mathbf{x})) \mathbf{n}_{sf} dA \right) - \\
 &\frac{k_f}{V} \int_{A_{fs}} \mathbf{n}_{fs} \cdot (\nabla \langle T_f \rangle^f(\mathbf{r}) + \nabla \tilde{T}_f(\mathbf{r})) dA \quad (2.133d)
 \end{aligned}$$

Closed two-temperature model:

$$\begin{aligned}
 (\rho c_p)_f \phi_f \langle \mathbf{v}_f \rangle^f \cdot \nabla \langle T_f \rangle^f - \mathbf{u}_f \cdot \nabla \langle T_f \rangle^f &= \nabla \cdot (\bar{\bar{K}}_f \nabla \langle T_f \rangle^f + \mathbf{d}_f (\langle T_f \rangle^f - \langle T_s \rangle^s)) - \\
 &a_V h (\langle T_f \rangle^f - \langle T_s \rangle^s) \quad (2.133e)
 \end{aligned}$$

$$\mathbf{u}_f \cdot \nabla \langle T_f \rangle^f = \nabla \cdot (\bar{\bar{K}}_s \nabla \langle T_s \rangle^s + \mathbf{d}_s (\langle T_s \rangle^s - \langle T_f \rangle^f)) - a_V h (\langle T_s \rangle^s - \langle T_f \rangle^f) \quad (2.133f)$$

Table 2.2: Synthesis of porous medium models.

Chapter 3

Free-porous interface modeling for laminar heat transfer at local thermal equilibrium

3.1 Introduction

In the introduction, we have presented different issues related to the computation of heat transfer in a nuclear reactor. An important issue is the coupling between the models used in the free regions and in the fuel region. However many questions about the boundary conditions that must be applied at a free-porous interface remain, even for laminar heat transfer. Where is the interface located? What jump conditions to apply? The answer to these questions is essential to correctly model the heat transfer in practical applications.

Due to the complexity of the method, we first study the simple problem of heat transfer at local thermal equilibrium in a free-porous domain.

An interesting idea is to derive the boundary conditions at the free-porous interface using up-scaling methods based on the energy conservation. Using such an approach, [Ochoa-Tapia and Whitaker \(1997\)](#) show that the boundary conditions involve surface excess quantities that can be modeled with jump parameters. However, this method does not make explicit the observed dependence between the value of the jump parameters and the interface location ([Larson and Higdon, 1986, 1987](#)).

In order to study this issue, we propose to use the multi-scale method presented by [Chandesris and Jamet \(2006, 2007, 2009c,b,a\)](#) for momentum transfer at a fluid-porous interface. This approach is based on two up-scaling steps and three levels of descriptions of the interface. The first up-scaling step consists in characterizing the transfer at a continuous scale, called mesoscopic, where the interface is diffuse. The second up-scaling step introduces the method of matched asymptotic expansions and allows to make explicit the dependency between the jump parameters and the interface location.

Nevertheless, applying this method to heat transfer, a question arises at the first up-scaling step: how to characterize the heat transfer in the transition zone?

In a recent study, [Aguilar-Madera and Ochoa-Tapia \(2011\)](#) adapt the volume averaging method in the transition zone. The adaptation relies on two modifications of the method. First, to verify the validity of the length scale separation, they consider a large volume of average larger than the elementary cell ($2r_0 = 15l_c$). Second, to complete the closure problem, they fix conditions other than the periodicity at the boundaries of the volume of average. Using these modifications, they are able to derive a closed temperature model and determine effective coefficients in the transition zone. We choose not to pursue this work and found a substitutive method to characterize the heat transfer in the transition zone. This approach, presented in Chapter 1, is inspired from ([Kuwahara et al., 1996](#); [Kuwahara and Nakayama,](#)

1999; Kuwahara et al., 2001). It postulates a closed continuous model in the transition zone and determines the effective coefficients by identification using numerical experiments.

The obtained results regarding the jump conditions that must be applied at a free-porous interface in the case of the local thermal equilibrium are presented as an article published in the *International Journal of Heat and Mass Transfer*.

3.2 Article 1: Boundary conditions at a fluid-porous interface for a convective heat transfer problem: Analysis of the jump relations

A. d'Hueppe ^a, M. Chandesris ^a, D. Jamet ^a, B. Goyeau ^b

International Journal of Heat and Mass Transfer 54 (2011) 3683-3693

^a CEA, DEN, DER/SSTH/LDAL, 17 rue des martyrs, F-38054 Grenoble, France

^b EM2C, UPR-CNRS 288, Ecole Centrale Paris, Grande Voie des Vignes, Châtenay-Malabry, France

Abstract. This paper presents a two-step up-scaling approach to determine the jump relations that must be imposed at the interface between a homogeneous porous domain and a free domain. We study convective heat transfer at such an interface under the assumption of local thermal equilibrium. The two-step approach has the capability of providing closed jump relations depending on intrinsic characteristic of the interface. In addition, from the resulting jump relations, it is possible to determine a particular interface location where the condition of continuity are sufficient. Thus, the use of jump or continuity conditions depend only on the interface location inside the fluid-porous transition region.

Keywords. Porous media, Convection, Interface, Boundary conditions, Excess quantity

3.3 Introduction

Heat and mass transfers at the fluid-porous interface play an important role in many industrial or environmental applications. At the microscopic scale, where each pore of the porous media is described, the direct numerical simulation gives the exact description of the transfers. However, this approach is not relevant to study application cases for two reasons:

- (i) the required meshing and associated costs would be prohibitive;
- (ii) it is not always possible to describe exactly the geometry at the microscopic scale.

For these reasons it is necessary to lower down the precision of the porous region by using a macroscopic description scale. At this level, the domain is characterized by homogeneous models for the porous and free media connected by boundary conditions at the fluid-porous interface. Far away from the interface, the physic is well understood and the established models give good results. In the interface region, other transfer phenomena occur due to the disappearing of the solid phase. These complex transfer phenomena are difficult to model through appropriate boundary conditions. However, this information can be the key of the model success. This is the reason why the recent challenging problems related to the determination of the boundary conditions at a fluid/porous interface are the topic of many studies ([Shavit, 2009](#); [Nield, 2009](#); [Hirata et al., 2009](#); [de Lemos, 2009](#); [Pokrajac and Manes, 2009](#); [Ghisalberti and Nepf, 2009](#)).

This paper focuses on the convective heat transfer problems at a fluid/porous interface and on the associated boundary conditions. Different types of boundary conditions can be found in the literature, as summarized by [Alazmi and Vafai \(2001\)](#). They are obtained using different approaches. A first one is to postulate the boundary conditions for the heat flux and the temperature at the nominal interface ([Beavers and Joseph, 1967](#)) defined by the position of the last solid grain. [Prat \(1989, 1990, 1992\)](#) shows that conditions of continuity for both the temperature and the heat flux give reasonable results for conductive

heat transfer. For convective transfers, assuming heat flux continuity, [Sahraoui and Kaviany \(1994\)](#) introduce a temperature jump with a slip coefficient, similar to the velocity jump introduced by [Beavers and Joseph \(1967\)](#). However, the a priori determination of this slip coefficient remains difficult and very sensitive to the interface location. Another approach is to derive the boundary conditions using up-scaling methods based on the energy conservation. Using such an approach, [Ochoa-Tapia and Whitaker \(1997\)](#) show that the boundary conditions involve surface excess quantities which can be modeled with jump parameters. [Valdés-Parada et al. \(2006, 2007a,b, 2009a,b\)](#) compute these jump parameters by solving closure problem in the case of mass transport. However, this method does not allow us to understand the observed dependence between the value of the jump parameters and the interface location ([Larson and Higdon, 1986, 1987](#)). To study this issue for momentum problems, [Chandesris and Jamet \(2006, 2007, 2009c,b,a\)](#) introduce an intermediate continuous scale of description, called the *mesoscopic scale* (see Fig. 3.1). First, the physical transfers specific of the interfacial region are modeled at this continuous scale. Then, the continuous model of the transfers is replaced by an equivalent discontinuous model with jump conditions at the macroscopic scale. With this approach, the mesoscopic and the macroscopic scales are dissociated and the dependence between the value of the jump parameters and the interface location can be explained.

The objective of the present study is to determine the jump conditions for 2D convective heat transfer problems with a laminar flow perpendicular to the fluid-porous interface using the two steps up-scaling approach of [Chandesris and Jamet \(2006\)](#). Section 3.4 describes the first up-scaling step. The heat transfers are modeled by a closed mesoscopic one-temperature equation and the associated effective thermal coefficients are computed for several Péclet numbers. Then, in Section 3.5, the second up-scaling step allows to derive the jump relations and to determine the surface excess quantities required to close the macroscopic model. Finally, given the obtained results and in order to simplify the method, we look for a particular interface location such that the jump relations vanish and the conditions of continuity are sufficient.

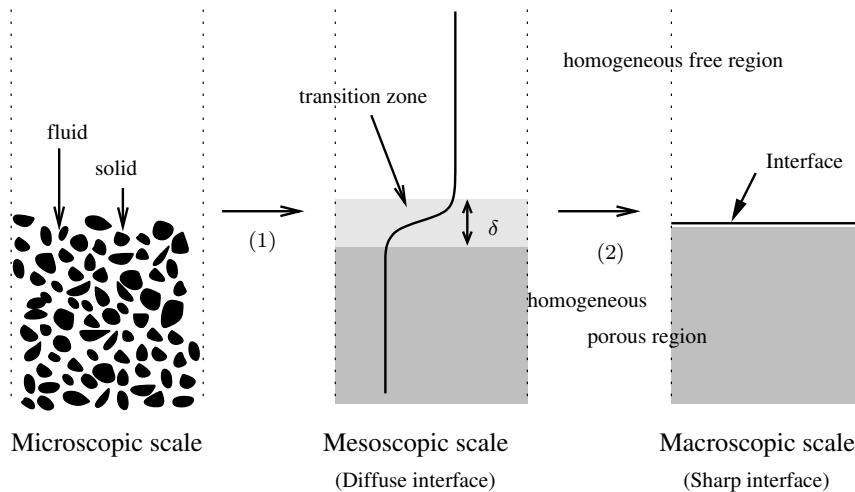


Figure 3.1: Interface between the porous media and the fluid media for various scales of description (figure adapted from [Chandesris and Jamet \(2007\)](#)).

3.4 First up-scaling step

3.4.1 Microscopic model

We consider a laminar flow in a domain partially filled with a model porous medium. As illustrated in Fig. 3.2(a), the mean flow is in the y-direction and is thus perpendicular to the fluid-porous interface. The porous region is composed of arranged lines of squares with a porosity $\phi = 5/9$. The study is performed for moderate Peclet numbers between 0.1 and 10, where the dispersive phenomenon is smaller than the diffusive one. The thermal conductivity ratio is fixed to $k_f/k_s = 1/50$ and the Prandtl number to $Pr = 1$. Regarding the boundary conditions at the edges of the domain, at the lateral boundaries, symmetry conditions are used for the velocity to obtain a 1D mean flow. For the temperature, an incoming heat flux is imposed to obtain a 2D temperature field with gradients appropriate for the computation of the different components of the effective thermal conductivity tensor (see Eqs (3.20) and (3.21)). At the inlet, the boundary conditions are established profiles of temperature and velocity to report the result that would be obtained with an infinite porous medium. These profiles are computed with a recirculation box whose characteristics are identical to those of the main geometry. To handle the periodicity of the recirculation box, the classical change of variables for the pressure and the temperature is used (Kawamura et al., 1999; Stalio and Nobile, 2003).

The problem is considered stationary and the physical properties of the fluid and solid are assumed to be constant. The fluid motion is governed by the Navier-Stokes equations and the heat transfer by the convective equations

In the fluid phase

$$\nabla \cdot \mathbf{v}_f = 0 \quad (3.1)$$

$$(\mathbf{v}_f \cdot \nabla) \mathbf{v}_f = -\frac{1}{\rho} \nabla p + \nu \nabla^2 \mathbf{v}_f \quad (3.2)$$

$$(\rho c_p)_f \nabla \cdot (\mathbf{v}_f T_f) = \nabla \cdot (k_f \nabla T_f) \quad (3.3)$$

In the solid phase

$$0 = \nabla \cdot (k_s \nabla T_s) \quad (3.4)$$

At the fluid-solid interface A_{fs} , the boundary conditions are given by:

$$T_f = T_s \quad (3.5)$$

$$\mathbf{n}_{fs} \cdot (k_f \nabla T_f) = \mathbf{n}_{fs} \cdot (k_s \nabla T_s) \quad (3.6)$$

$$\mathbf{v}_f = 0 \quad (3.7)$$

where \mathbf{n}_{fs} is the unit normal vector directed from the fluid phase to the solid phase.

The microscopic temperature field is obtained by solving numerically Eqs. (3.1)-(3.7) on a uniform Cartesian grid with a finite-volume method based on a second-order central-differencing scheme. Thus, Fig. 3.2(b) represents the iso-contours of the microscopic fluid temperature computed for the geometry presented in Fig. 3.2(a) at a Peclet number $Pe = 5$ and with an incoming flux on the lateral boundaries $q_w = 5$ (non-dimensional value).

3.4.2 Mesoscopic model

3.4.2.1 Averaging filter

The fluid and the solid phases in the porous region are substituted by an equivalent continuous medium with the volume averaging method (Whitaker, 1999). Two types of averages are introduced

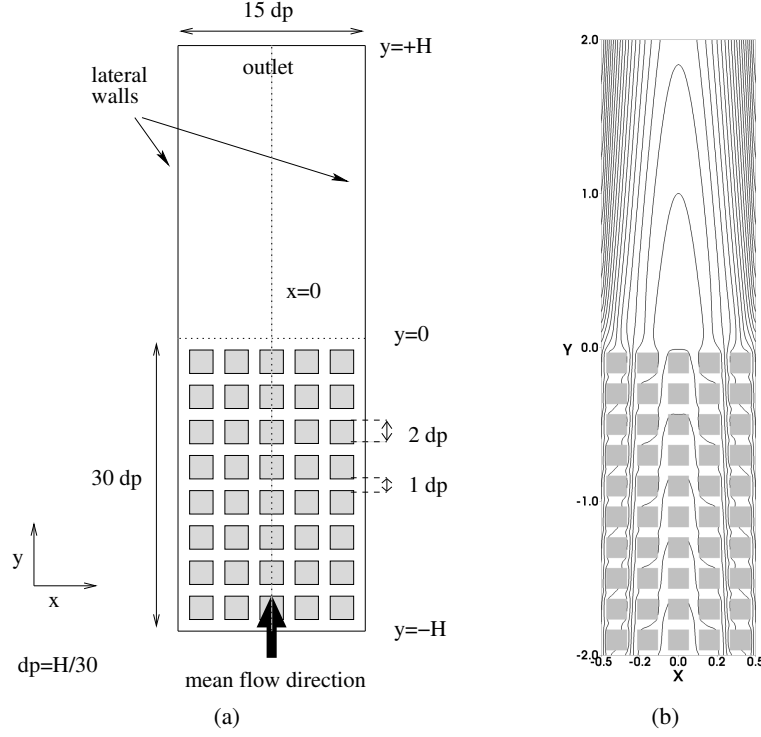


Figure 3.2: (a) Geometrical configuration. (b) Iso-contours of the microscopic fluid temperature.

(Whitaker, 1969; Gray, 1975): the superficial average of any quantity ψ_α of the α phase is given by

$$\langle \psi_\alpha \rangle(\mathbf{x}) = \frac{\int_V m_p(\mathbf{r} - \mathbf{x}) \chi_\alpha(\mathbf{r}) \psi_\alpha(\mathbf{r}) dV}{\int_V m_p(\mathbf{r}) dV} \quad (3.8)$$

where \mathbf{x} is the centroid of the averaging volume, χ_α is the indicator function of the α phase and m_p is a weighting function. The intrinsic average is related to the superficial volume average by the relation

$$\langle \psi_\alpha \rangle^\alpha = \frac{\langle \psi_\alpha \rangle}{\phi_\alpha} \quad (3.9)$$

where ϕ_α is the volume fraction of the α phase within the averaging volume ($\phi_\alpha = V_\alpha/V$). When choosing the weighting function $m_p(\mathbf{x})$ involved in Eq. (3.8), some points have to be considered. First the averaging volume should match the topology of the porous medium. Secondly, the volume averaged fields should contain negligible variations on scales smaller than the filter size while being sufficiently small to preserve as much information as possible (Quintard and Whitaker, 1994; Breugem et al., 2005). Given the topology of the porous medium, a top-hat filter based on a unit cell with one obstacle could be used. However, the computation with different filters: top-hat, triangular shaped (top-hat convoluted twice), quadratic shaped (top-hat convoluted three times) show that only the quadratic filter succeeds to create averaged fields gradients free of fluctuations. These gradients are needed for the determination of the effective coefficients (see 3.4.3). Thus, for the rest of this study, we use the quadratic weighting function obtained from the top-hat filter convoluted three times. The size of the quadratic filter, $2r_o$, is three times bigger than the top-hat filter and contains three elementary obstacles (see Figs. 3.3(a)-3.3(b)). The size of the transition zone is $2r_o$ and it is the smallest size which, with our method, gives access to the effective thermal conductive coefficients.

Finally, for conciseness, the following formalism is introduced:

$$\langle \psi_\alpha \rangle = \frac{1}{V} \int_V \psi_\alpha dV \quad (3.10)$$

and for the volume averaged on the fluid-solid surfaces this formalism corresponds to

$$\frac{1}{V} \int_{A_{fs}} \psi_\alpha dA = \frac{\int_{A_{fs}} m_p(\mathbf{r} - \mathbf{x}) \chi_\alpha(\mathbf{r}) \psi_\alpha(\mathbf{r}) dA}{\int_V m_p(\mathbf{r}) dV} \quad (3.11)$$

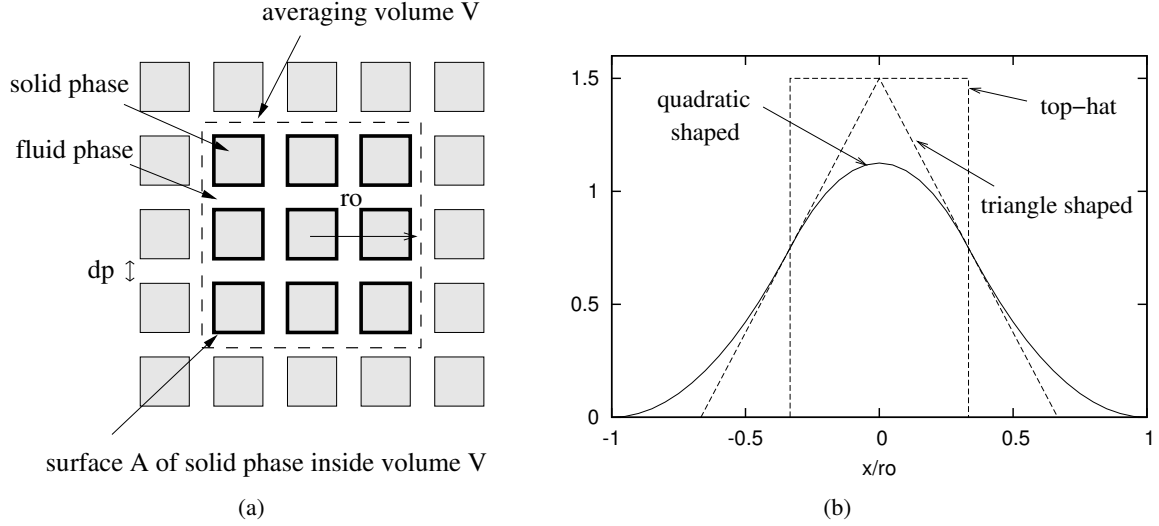


Figure 3.3: (a) Illustration of the averaging volume. (b) Quadratic weighting function $m_p(\mathbf{x})$.

3.4.2.2 Mesoscopic one-temperature equation

Let us apply the superficial average operator to the governing microscopic equations (3.3), (3.4). Classical developments (Quintard and Whitaker, 1993; Kaviany, 1995), using the spacial averaging theorems to interchange differentiation and integration, give an averaged heat transfer equation valid in the homogeneous regions and in the interfacial transition zone:

For the fluid

$$(\rho c_p)_f \nabla \cdot (\langle \mathbf{v}_f \rangle \langle T_f \rangle^f) = \nabla \cdot \left[k_f \nabla \langle T_f \rangle + \frac{k_f}{V} \int_{A_{fs}} \mathbf{n}_{fs} T_f dA - (\rho c_p)_f \tau_{vT} \right] + \frac{k_f}{V} \int_{A_{fs}} \mathbf{n}_{fs} \cdot \nabla T_f dA \quad (3.12)$$

where $\tau_{vT} = \langle T_f \mathbf{v}_f \rangle - \phi_f \langle T_f \rangle^f \langle \mathbf{v}_f \rangle^f$ is a dispersive flux.

For the solid

$$0 = \nabla \cdot \left[k_s \nabla \langle T_s \rangle - \frac{k_s}{V} \int_{A_{fs}} \mathbf{n}_{fs} T_f dA \right] - \frac{k_f}{V} \int_{A_{fs}} \mathbf{n}_{fs} \cdot \nabla T_f dA \quad (3.13)$$

Assuming the local thermal equilibrium in the homogeneous porous region and in the interfacial transition zone, we have the approximation $\langle T \rangle \approx \langle T_f \rangle^f \approx \langle T_s \rangle^s$, where $\langle T \rangle$ is the spatial volume averaged temperature defined by $\langle T \rangle = \phi \langle T_f \rangle^f + (1 - \phi) \langle T_s \rangle^s$. The one equation model is obtained by adding Eqs. (3.12), (3.13) to give (Kaviany, 1995)

$$(\rho c_p)_f \nabla \cdot (\langle \mathbf{v}_f \rangle \langle T \rangle) = \nabla \cdot \left[k_f \nabla \langle T_f \rangle + k_s \nabla \langle T_s \rangle + \frac{k_f - k_s}{V} \int_{A_{fs}} \mathbf{n}_{fs} T_f dA - (\rho c_p)_f \tau'_{vT} \right] \quad (3.14)$$

where the dispersive vector is built based on the total spatial volume averaged temperature $\langle T \rangle$ instead of the intrinsic volume averaged temperature $\langle T_f \rangle^f$:

$$\tau'_{vT} = \langle T_f \mathbf{v}_f \rangle - \phi_f \langle T \rangle \langle \mathbf{v}_f \rangle^f \quad (3.15)$$

At this stage, Eq. (3.14) is not closed due to the microscopic variables existing in the area integral term and in the dispersive vector. Thus to close Eq. (3.14), the right hand side of the equality is substituted by a model traducing the same transfer phenomena.

In the homogeneous porous region, the length scale constraint ($r_o \ll H$) is satisfied and therefore according to Quintard and Whitaker (1993) and Kaviany (1995) we have

$$(\rho c_p)_f \nabla \cdot (\langle \mathbf{v}_f \rangle \langle T \rangle) = \nabla \cdot (\bar{\bar{\mathbf{K}}}^p \cdot \nabla \langle T \rangle) \quad (3.16)$$

where $\bar{\bar{\mathbf{K}}}^p$ is the effective thermal conductivity tensor of the porous medium.

In the homogeneous fluid region, $\langle T \rangle = \langle T_f \rangle$ and the dispersive vector τ'_{vT} is negligible¹, therefore Eq. (3.14) reduces to

$$(\rho c_p)_f \nabla \cdot (\langle \mathbf{v}_f \rangle \langle T \rangle) = \nabla \cdot (k_f \bar{\mathbf{I}} \cdot \nabla \langle T \rangle) \quad (3.17)$$

In the interfacial transition region, we postulate that the transfer phenomenon is well represented by an effective thermal conductivity tensor $\bar{\bar{\mathbf{K}}}(\mathbf{x})$, where \mathbf{x} is the position vector. This effective thermal conductivity tensor varies continuously in the transition zone from $\bar{\bar{\mathbf{K}}}^p$ in the homogeneous porous region to $k_f \bar{\mathbf{I}}$ in the free region. Thus, the closed one-temperature equation valid in the whole domain takes the form

$$(\rho c_p)_f \nabla \cdot (\langle \mathbf{v}_f \rangle \langle T \rangle) = \nabla \cdot (\bar{\bar{\mathbf{K}}}(\mathbf{x}) \cdot \nabla \langle T \rangle) \quad (3.18)$$

To close the model at the mesoscopic scale, the effective thermal conductivity tensor $\bar{\bar{\mathbf{K}}}(\mathbf{x})$ must be determined.

3.4.3 Determination of the effective thermal conductivity tensor

As shown in Fig. 3.2(b), the domain is submitted to a temperature stress in the x- and y- directions. As the effective thermal tensor is a property of the medium and of the flow, it should not be dependent on the temperature stress. Consequently the effective thermal tensor should not be dependent on the x- direction in accordance with both the geometry of the domain and the imposed flow. The effective thermal conductivity tensor $\bar{\bar{\mathbf{K}}}(y)$ is obtained by comparing the unclosed equation (3.14) with the closed one (3.18). Therefore

$$\bar{\bar{\mathbf{K}}}(y) \cdot \nabla \langle T \rangle = k_f \nabla \langle T_f \rangle + k_s \nabla \langle T_s \rangle + \frac{k_f - k_s}{V} \int_{A_{fs}} \mathbf{n}_{fs} T_f dA_{fs} - (\rho c_p)_f \tau'_{vT} \quad (3.19)$$

where the two first terms of the right hand side of Eq. (3.19) represent the conductive contribution while the third one represents the tortuosity, the last one being the dispersion contribution. The components of $\bar{\bar{\mathbf{K}}}(y)$ are evaluated by computing the right hand side of the relation (3.19) in the x- and y- directions. Due to the shape of the temperature field, there exists a position, $x = 0$, where the gradient of the temperature in the x- direction is nul. At this particular position, the components of the tensor are easily computable and reveals the nullity of the extra-diagonal terms. Thus, the diagonal components K_{xx} and K_{yy} are given by

$$K_{xx}(y) = \left[k_f \frac{\partial \langle T_f \rangle}{\partial x} + k_s \frac{\partial \langle T_s \rangle}{\partial x} + \frac{k_f - k_s}{V} \int_{A_{fs}} \mathbf{n}_{fs} T_f dA_{fs} \cdot \mathbf{x} - (\rho c_p)_f \tau'_{vT} \cdot \mathbf{x} \right] / \frac{\partial \langle T \rangle}{\partial x} \quad (3.20)$$

$$K_{yy}(y) = \left[k_f \frac{\partial \langle T_f \rangle}{\partial y} + k_s \frac{\partial \langle T_s \rangle}{\partial y} + \frac{k_f - k_s}{V} \int_{A_{fs}} \mathbf{n}_{fs} T_f dA_{fs} \cdot \mathbf{y} - (\rho c_p)_f \tau'_{vT} \cdot \mathbf{y} \right] / \frac{\partial \langle T \rangle}{\partial y} \quad (3.21)$$

¹ in the homogeneous free region, the fluctuations are negligible and $\psi_f \sim \langle \psi_f \rangle^f$

3.4 First up-scaling step

Furthermore, the assumption that the effective thermal conductivity tensor is not dependent on the x -direction has been confirmed by computing the profiles of K_{xx} and K_{yy} for different x locations.

Figs. 3.4 and 3.5 present the influence of the Péclet number on the effective conductive components K_{xx} and K_{yy} . As expected, the values of the effective thermal conductivities K_{xx} and K_{yy} are constant in the homogeneous regions and vary continuously in the transition zone. In the homogeneous porous region, the dependency of K_{yy} with the Péclet number is more important than for K_{xx} . This result is expected since the mean flow is normal to the interface. As the Péclet number increases, the convective part of the transfer increases in the y -direction and affects directly K_{yy} , which represents the heat transfer in this direction. In the interfacial zone, the variation zone of K_{yy} spreads over with the Péclet number and a bump comes out at $Pe = 10$. At the same Péclet number, a small bump is also observed on the K_{xx} profile at the end of the interfacial zone. These behaviors are due to recirculations at the exit of the porous media that become more and more important with the increase of the Reynolds number.

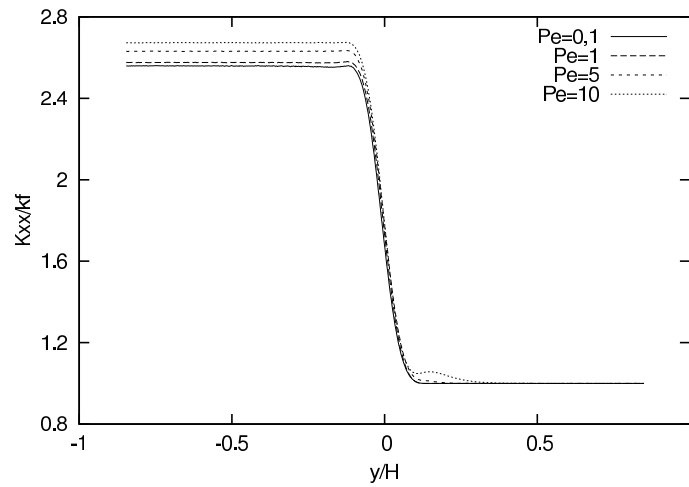


Figure 3.4: Profiles of K_{xx} for various Péclet numbers.

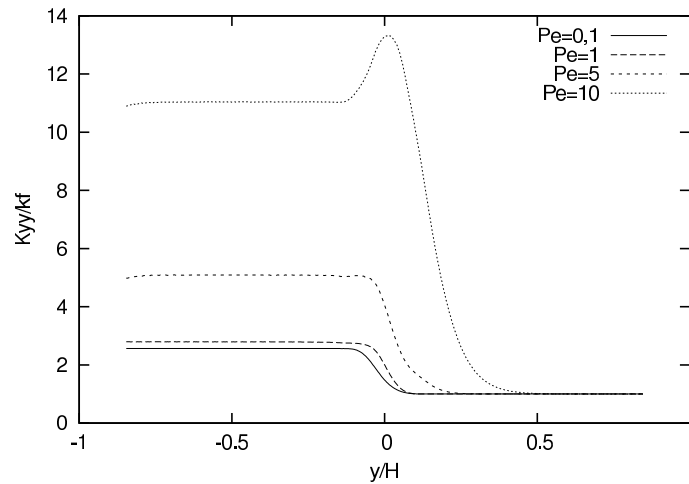


Figure 3.5: Profiles of K_{yy} for various Péclet numbers.

The homogeneous porous values of K_{yy} and K_{xx} obtained for various Péclet numbers are reported in Fig. 3.6. On the same figure, the associated dispersive values $K_{ii}^{\text{dis}} = -(\rho c_p)_f \tau'_{vT} \cdot \mathbf{i} / \frac{\partial \langle T \rangle}{\partial i}$ in the x - and y -direction are added. As expected, K_{yy}^{dis} varies with Pe^2 (see Fig. 3.6 where the Pe^2 tendency is drawn)

and $K_{xx}^{\text{dis}} \approx 0$ for low Péclet numbers ($Pe < 10$) in accordance with the results reported in (Kaviany, 1995).

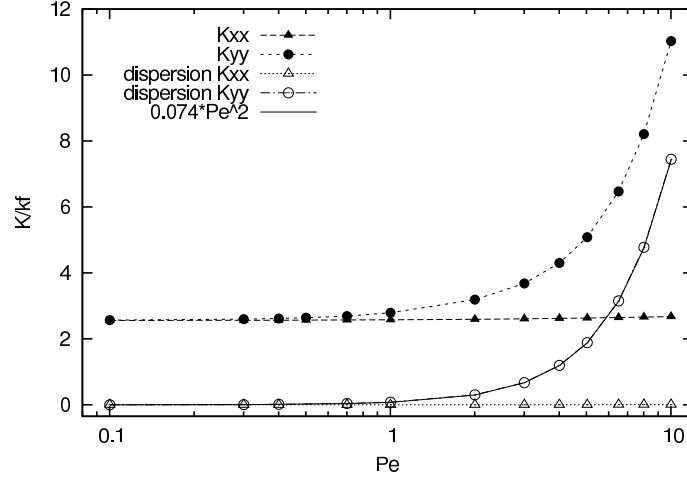


Figure 3.6: Values of the effective thermal conductivities and their dispersive part in the porous medium.

3.5 Second up-scaling step

At the macroscopic scale, the problem is composed of homogeneous porous and free regions separated by a discontinuous interface. In the homogeneous regions, the media properties are constant and the energy transfer is modeled by partial differential equations equivalent to the mesoscopic ones far away from the interface. However the exact interface location and the jump relations that must be imposed are unknown. The purpose of this section is to derive the macroscopic jump relations from the mesoscopic scale using conservation principles and to investigate the choice of the interface location, written y_m .

3.5.1 Generic analysis

To ensure the conservation of the transfers between the macroscopic and mesoscopic modelings, we use the generic analysis method (Edwards et al., 1991) based on two principles:

- (i) the comparison of the conservation equations in the whole domain between the macroscopic and mesoscopic scales;
- (ii) the equivalence between the macroscopic and the mesoscopic terms in the homogeneous regions.

Therefore, the remainder terms represent the transfers not considered by the macroscopic modeling in comparison with the mesoscopic one. Indeed the continuous description of the interface at the mesoscopic scale is replaced by a surface of discontinuity with constant values on each side at the macroscopic scale. Thus, the macroscopic model forgets the variations of the effective properties existing in the interfacial transition zone, and the generic analysis method reports this difference.

At the macroscopic scale, the transfer phenomena are modeled using constant properties:

$$\text{In the homogeneous porous region: } (\rho c_p)_f \nabla \cdot (\mathbf{v}_m T_m^p) = \nabla \cdot (\bar{\bar{\mathbf{K}}}^p \cdot \nabla T_m^p) \quad (3.22)$$

$$\text{In the homogeneous fluid region: } (\rho c_p)_f \nabla \cdot (\mathbf{v}_m T_m^l) = \nabla \cdot (k_f \bar{\bar{\mathbf{I}}}_d \cdot \nabla T_m^l) \quad (3.23)$$

3.5 Second up-scaling step

where T_m^p and T_m^l are the temperatures in the porous and the fluid regions, respectively at the macroscopic scale corresponding to the mesoscopic spatial volume averaged temperature $\langle T \rangle$; and \mathbf{v}_m is the velocity at the macroscopic scale corresponding to the mesoscopic superficial averaged velocity $\langle \mathbf{v}_f \rangle$. The principle (i) of the generic analysis method is applied to Eqs. (3.18), (3.22), (3.23) and leads to

$$\int_{H^-}^{y_m} (\rho c_p)_f \nabla \cdot (\langle \mathbf{v}_f \rangle \langle T \rangle - \mathbf{v}_m T_m^p) dy + \int_{y_m}^{H^+} (\rho c_p)_f \nabla \cdot (\langle \mathbf{v}_f \rangle \langle T \rangle - \mathbf{v}_m T_m^l) dy = \int_{H^-}^{y_m} \nabla \cdot (\bar{\mathbf{K}}(y) \cdot \nabla \langle T \rangle - \bar{\mathbf{K}}^p \cdot \nabla T_m^p) dy + \int_{y_m}^{H^+} \nabla \cdot (\bar{\mathbf{K}}(y) \cdot \nabla \langle T \rangle - k_f \bar{\mathbf{I}}_d \cdot \nabla T_m^l) dy \quad (3.24)$$

Using the equivalence between the macroscopic and the mesoscopic terms in the homogeneous regions (see (ii)), Eq. (3.24) reduces to:

$$q_{Ym}^l(x, y_m) - q_{Ym}^p(x, y_m) = \int_{H^-}^{y_m} \left[\frac{\partial}{\partial x} \left(K_{xx}(y) \frac{\partial \langle T \rangle}{\partial x} - K_{xx}^p \frac{\partial T_m^p}{\partial x} \right) \right] dy + \int_{y_m}^{H^+} \left[\frac{\partial}{\partial x} \left(K_{xx}(y) \frac{\partial \langle T \rangle}{\partial x} - k_f \frac{\partial T_m^l}{\partial x} \right) \right] dy \quad (3.25)$$

where $q_{Ym} = (\rho c_p)_f v_m T_m - K_{yy} \partial T_m / \partial y$ stands for the macroscopic total heat flux in the y - direction. The right hand side of the equation (3.25) corresponds to the quantity not considered by the macroscopic modeling in comparison with the mesoscopic one. This quantity is called *surface-excess quantity* and noted as (Jamet and Chandesris, 2009):

$$(\psi)^{ex}(y_m) = \int_{H^-}^{y_m} (\langle \psi \rangle - \psi_m^p) dy + \int_{y_m}^{H^+} (\langle \psi \rangle - \psi_m^l) dy \quad (3.26)$$

According to this notation the jump relation on the heat flux (3.25) is rewritten

$$q_{Ym}^l(x, y_m) - q_{Ym}^p(x, y_m) = \left[\frac{\partial}{\partial x} \left(K_{xx} \frac{\partial \langle T \rangle}{\partial x} \right) \right]^{ex} \quad (3.27)$$

The jump relation for the total heat flux corresponds to the energy conservation between the lower part and the upper part of the transition region. In our case, an incoming heat flux on the lateral boundaries creates a temperature gradient in the x - direction. Consequently, the conservation of the energy between the macroscopic and mesoscopic descriptions results with an excess surface convective transport in the x - direction.

The temperature jump is obtained from the difference between the mesoscopic conductive heat flux in the y - direction $\langle q_{cY} \rangle = -K_{yy} \partial \langle T \rangle / \partial y$ and the following macroscopic equations

$$\text{In the homogeneous fluid region: } q_{cYm}^l = -k_f \frac{\partial T_m^l}{\partial y} \quad (3.28)$$

$$\text{In the homogeneous porous region: } q_{cYm}^p = -K_{yy}^p \frac{\partial T_m^p}{\partial y} \quad (3.29)$$

Performing the same developments as previously, the temperature jump relation takes the following form:

$$T_m^l(x, y_m) - T_m^p(x, y_m) = - \left(\langle q_{cY} \rangle \frac{1}{K_{yy}} \right)^{ex} \quad (3.30)$$

The jump relation for the temperature involves the excess quantity of the product of the conductive flux time to the thermal resistance. This jump relation is identical to the one presented by Jamet and Chandesris (2009) for a purely conductive heat transfer problem.

Jump relations for the temperature and the heat flux have been derived. However, they depend on the mesoscopic unknowns $\langle T \rangle$ and $\langle q_{eY} \rangle$ and are thus not closed. To obtain closed jump relations, another method called the matched asymptotic expansions is used. This method allows us to determine the macroscopic temperature as Taylor series expansions solution of the mesoscopic equation.

3.5.2 Method of matched asymptotic expansions

The method of the matched asymptotic expansion is a mathematical tool used to solve partial differential equations with variable coefficients (Zwillinger, 1989; Zeytounian, 1986; Chandesris and Jamet, 2006). It is commonly used to study diffuse interface problem (Emmerich, 2003) and therefore well adapted for the resolution of Eq. (3.18) of the mesoscopic scale. Indeed, the coefficient $\bar{K}(y)$ in (3.18) strongly varies in function of y/ε , ε being the ratio between the width of the interfacial transition zone and the characteristic length of the whole domain (see Figs. 3.4-3.5). Macroscopic approximated solutions of the mesoscopic equation will be obtained at different orders. The detailed developments are presented in Appendix 3.8. Only the main results are presented in the following.

3.5.2.1 Resolution at order 0

The approximated solution at order 0 of the mesoscopic model is given by:

$$T_m = T_m^{(0)} \quad (3.31)$$

where $T_m^{(0)}$ satisfies the system of equations (3.22) and (3.23) and the following jump relations (see Appendix 3.8 Eqs. (3.58) and (3.65)):

$$q_{Ym}^{l(0)}(x, y_m^+) - q_{Ym}^{p(0)}(x, y_m^-) = 0 \quad (3.32)$$

$$T_m^{l(0)}(x, y_m^+) - T_m^{p(0)}(x, y_m^-) = 0 \quad (3.33)$$

Thus, at order 0, continuity of the temperature and of the total heat flux in the y-direction is obtained. The surface-excess quantities do not appear in these boundary conditions compared to the results obtained in 3.5.1.

The solutions T_m for different interface locations are presented with the averaged microscopic solution in Fig. 3.7. The values of the macroscopic temperatures in the homogeneous free region vary with the interface location. The error is due to the no-conservation of the energy between the mesoscopic modeling and the macroscopic one when conditions of continuity are used. As the error depends on the interface location, there exists one particular position ($y_m \approx 0$) where the conservation of the energy is verified. In that case, the macroscopic temperature T_m matches the averaged microscopic temperature of reference.

3.5.2.2 Resolution at order 1

The approximated solution at order 1 corresponds to the increase of the resolution order of the mesoscopic equation (3.18). This solution takes the form in ε

$$T_m = T_m^{(0)} + \varepsilon T_m^{(1)} \quad (3.34)$$

where $T_m^{(0)}$ is the solution at order 0 while $T_m^{(1)}$ is the correction term at first order and ε the non-dimensional parameter related to the transition zone. At this order, T_m satisfies the system of equations

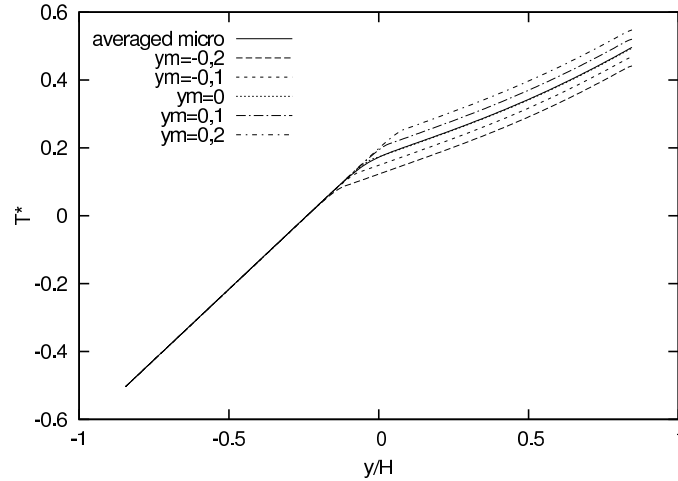


Figure 3.7: Macroscopic temperature at zeroth order for $x = 0$
 $\left(T^* = \frac{T - (\langle T \rangle(0; H^-) + \langle T \rangle(0; H^+))/2}{\langle T \rangle(0; H^+) - \langle T \rangle(0; H^-)} \right).$

(3.22) and (3.23) and the following jump relations (see Appendix 3.8 Eqs. (3.68) and (3.66)):

$$q_{Ym}^l(x, y_m^+) - q_{Ym}^p(x, y_m^-) = \frac{\partial^2 T_m^{(0)}}{\partial x^2}(x, y_m) (K_{xx})^{ex} \quad (3.35)$$

$$T_m^l(x, y_m^+) - T_m^p(x, y_m^-) = -q_{Y,c m}^{(0)}(x, y_m) \left(\frac{1}{K_{yy}} \right)^{ex} \quad (3.36)$$

The jump relations at order 1 are characterized by the same transfer phenomena that exist in the jump relations obtained using the generic analysis (3.27)-(3.30). However, the form of the jump relations at order 1 is different. It is indeed composed of a macroscopic unknown term and an excess quantity of a component of the effective thermal conductivity tensor that is known. Thus, the macroscopic problem is closed.

Since the effective conductivities in the homogeneous regions are constant and different, the excess quantity (3.26) can be rewritten such as (Jamet and Chandris, 2009)

$$(\psi)^{ex}(y_m) = (\psi^l - \psi^p)(y_m - y_\psi) \quad (3.37)$$

where y_ψ is the *center of gravity* of the effective coefficient ψ . Actually, y_ψ corresponds to the particular location of the interface where $(\psi)^{ex}(y_m) = 0$. It is characteristic of the ψ profile in the interfacial transition region, and consequently of the interfacial transfer. Here, the involved centers of gravity are $y_{\frac{1}{K_{yy}}}$ and $y_{K_{xx}}$ associated to the excess values $\left(\frac{1}{K_{yy}} \right)^{ex}$ and $(K_{xx})^{ex}$. Thus, $y_{\frac{1}{K_{yy}}}$ and $y_{K_{xx}}$ are computed for several Péclet numbers and compared with the nominal interface location y_{nom} according to $(y_\psi - y_{nom})/d_p$ (see Fig. 3.8). We recall that the nominal interface corresponds to the position of the last solid grain (Beavers and Joseph, 1967). The center of gravity $y_{K_{xx}}$ is located near the nominal interface and hardly varies with the Péclet number in accordance with the mean flow in the y -direction. On the contrary, the center of gravity $y_{\frac{1}{K_{yy}}}$ depends on the Péclet number and strongly differs from the nominal interface when the fluid velocity increases. This reflects the expansion of the dispersive transfer in the direction normal to the interface.

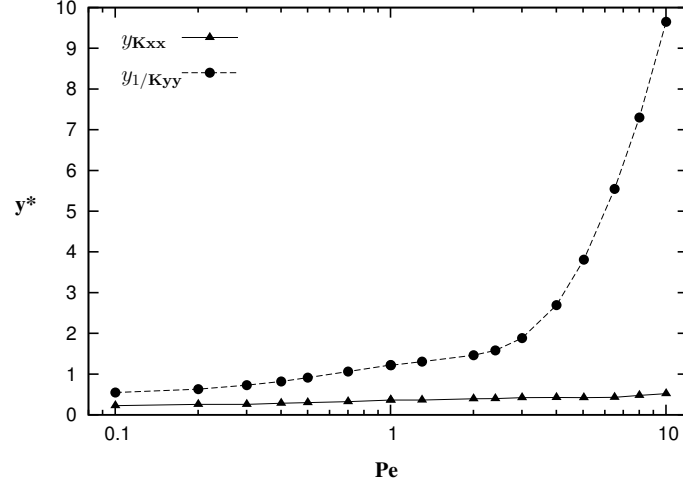


Figure 3.8: Center of gravity for various Péclet values ($y^* = (y_\psi - y_{\text{nom}})/d_p$).

Using the formulation of the above excess quantities, the jump relations at order 1 can be rewritten as follows:

$$q_{Y_m}^l(x, y_m^+) - q_{Y_m}^p(x, y_m^-) = \frac{\partial^2 T_m^{(0)}}{\partial x^2}(x, y_m) (K_{xx}^l - K_{xx}^p) (y_m - y_{K_{xx}}) \quad (3.38)$$

$$T_m^l(x, y_m^+) - T_m^p(x, y_m^-) = -q_{Y,c m}^{(0)}(x, y_m) \left(\frac{1}{K_{yy}^l} - \frac{1}{K_{yy}^p} \right) (y_m - y_{\frac{1}{K_{yy}}}) \quad (3.39)$$

Thus, the jump relations at order 1 depend on intrinsic interfacial properties ($y_{\frac{1}{K_{yy}}}, y_{K_{xx}}$), on the location of the interface y_m and on the properties of the homogeneous media ($K_{yy}^l, K_{yy}^p, K_{xx}^l, K_{xx}^p$). Therefore, the jump relations at order 1 are easy to compute and the solutions of the macroscopic model at order 1 obtained for several interface locations are presented in Fig. 3.10. The macroscopic solutions exactly match the temperature of reference in both homogeneous regions. In particular, the values in the homogeneous fluid region do not vary with the interface location unlike the order 0. The first order correction ensures the conservation of the energy between the macroscopic and mesoscopic models for each interface location (see Fig. 3.9).

In fact, the macroscopic temperature at first order is obtained in two steps. First, it is necessary to solve the macroscopic model at zeroth order to obtain the coefficients $\partial^2 T_m^{(0)}/\partial x^2$ and $q_{Y,c m}^{(0)}$, and then the macroscopic model at order 1 can be solved. This two-step resolution gives correct temperature in the homogeneous regions whatever the interface location. However, it requires two numerical resolutions and the numerical implementation of the jump conditions. For these reasons, we will try to determinate if the conditions of continuity can be used at a particular interface location.

3.6 Determination of the apparent interface

3.6.1 Procedure

At this stage, the jump conditions are determined and the dependence of the jump parameters with the interface location is understood. However, to avoid the numerical implementation of the jump conditions and the two-step numerical resolution, we investigate the alternative approach of [Duman and Shavit \(2009\)](#) and look for the apparent interface which is defined as the interface location where the boundary conditions of continuity are sufficient.

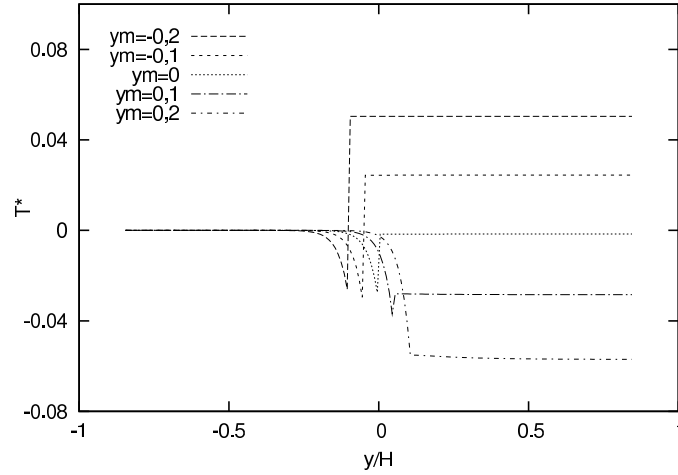


Figure 3.9: Correction term at first order $T_m^{(1)}$ for $x = 0$ $\left(T^* = \frac{T_m^{(1)}}{\langle T \rangle (0; H^+) - \langle T \rangle (0; H^-)} \right)$.

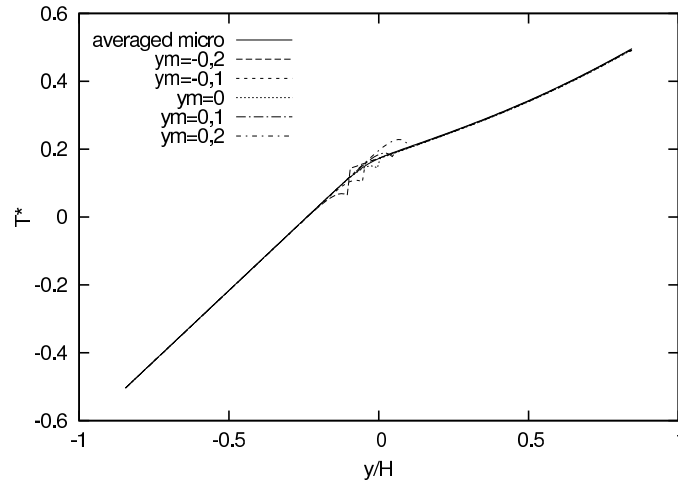


Figure 3.10: Macroscopic temperature at first order for $x = 0$ $\left(T^* = \frac{T - (\langle T \rangle (0; H^-) + \langle T \rangle (0; H^+))/2}{\langle T \rangle (0; H^+) - \langle T \rangle (0; H^-)} \right)$.

A first idea to locate the apparent interface is to find the position y_m where the jump at order 1 vanishes thanks to $(1/K_{yy})^{ex} = (K_{xx})^{ex} = 0$. In such a case, the apparent interface would be defined by $y_m = y_{K_{xx}} = y_{1/K_{yy}}$. However, this is available only if the centers of gravity $y_{K_{xx}}$ and $y_{1/K_{yy}}$ coincide. For low Péclet numbers, the previous results show that the locations of the centers of gravity are almost equal (see Fig. 3.8). Thus, the two jump relations at order 1 vanish at the same location and the apparent interface location is easily found. For high Péclet numbers, the locations of the centers of gravity are different (see Fig. 3.8) and no obvious apparent interface location can be proposed.

Since $T_m^{(1)}$ depends on the interface location (see Fig. 3.9), another idea is to look for the interface location such that the correction term $T_m^{(1)}(x, y)$ has no-contribution in the homogeneous regions. Thus, $T_m^{(1)}(x, y)$ must verify the condition $\lim_{y \rightarrow \pm\infty} T_m^{(1)} = 0$. The correction term $T_m^{(1)}(x, y)$ verifies Eqs. (3.22),

(3.23) and the convergent solution in each homogeneous regions is:

$$\text{In the free region: } T_m^{(1)l}(x, y) = A(x) \exp \left(-\frac{(\rho c_p)_f v_m y}{K_{yy}^l} \left(\frac{\sqrt{1 + X^l/P e^2} - 1}{2} \right) \right) \quad (3.40)$$

$$\text{In the porous region: } T_m^{(1)p}(x, y) = B(x) \exp \left(\frac{(\rho c_p)_f v_m y}{K_{yy}^p} \left(\frac{1 + \sqrt{1 + X^p/P e^2}}{2} \right) \right) \quad (3.41)$$

where $A(x)$ and $B(x)$ are unknown functions of x , and $X^i = 4(K_{yy}^i K_{xx}^i / k_f^2) (2k\pi)^2 (d_p / (x_g - x_d))^2$ with x_g and x_d the lateral boundaries. For high Péclet numbers, $1 + X^i/P e^2 \approx 1$ and the solutions in the homogeneous regions (3.40) and (3.41) simplify as follows:

$$T_m^{(1)l}(x, y) = A(x) \quad (3.42)$$

$$T_m^{(1)p}(x, y) = B(x) \exp \left(\frac{(\rho c_p)_f v_m y}{K_{yy}^p} \right) \quad (3.43)$$

The jump relations at the interface (3.35) and (3.36) allow to determine $A(x)$ and $B(x)$ and leads to

$$T_m^{(1)l}(x, y) = \frac{\partial^2 T_m^{(0)}}{\partial x^2}(x, y_m) (K_{xx})^{ex} \quad (3.44)$$

$$T_m^{(1)p}(x, y) = \left(\frac{\partial^2 T_m^{(0)}}{\partial x^2}(x, y_m) (K_{xx})^{ex} + (\rho c_p)_f v_m q_{Y,c m}^{(0)}(x, y_m) \left(\frac{1}{K_{yy}} \right)^{ex} \right) \exp \left(\frac{(\rho c_p)_f v_m (y - y_m)}{K_{yy}^p} \right) \quad (3.45)$$

which correspond to the profile of Fig. 3.9. At this point, the correction term $T_m^{(1)}$ is general and satisfies Eqs. (3.44) and (3.45) in both the homogeneous regions. To determine the particular correction term $T_m^{(1)}$, the condition $\lim_{y \rightarrow \pm\infty} T_m^{(1)} = 0$ is imposed to Eqs. (3.44) and (3.45). In the homogeneous porous region, $T_m^{(1)p}$ verifies this condition for any interface locations because of the exponential decay. In the homogeneous free region, $T_m^{(1)l}$ verifies the condition only if $(K_{xx})^{ex} = 0$. Therefore, there is only one interface location $y_m = y_{K_{xx}}$, for which the contribution of the correction term $T_m^{(1)}$ is zero in the homogeneous regions.

Under these circumstances, we claim that the apparent interface exists for 2D convective problems and is located at $y_m = y_{K_{xx}}$ for low and high Péclet numbers. Let us note that the apparent interface corresponds to the location where the flux continuity is verified. The flux conservation leads the transfers at the interface and must be carefully considerate. In the following, we will illustrate this result on complex interfacial geometries.

3.6.2 Illustration

Commonly, the macroscopic problem is solved with boundary conditions of continuity applied at the nominal interface (the plane tangential to the last cube). This modeling can give sometimes good results, but for complex cases the use of the apparent interface is more appropriate. In the previous section, developments have been made to characterize the location of the apparent interface and we will illustrate here the suitability of the result. To do this, rough interfaces are used with different locations of the nominal interface (see Fig. 3.11). The microscopic simulations are made for a moderate Péclet number such as $Pe = 5$. The components of the effective thermal tensor and their associated center of gravity are reported on Fig. 3.12. It is found that the center of gravity $y_{K_{xx}}$ does not depend on the interface

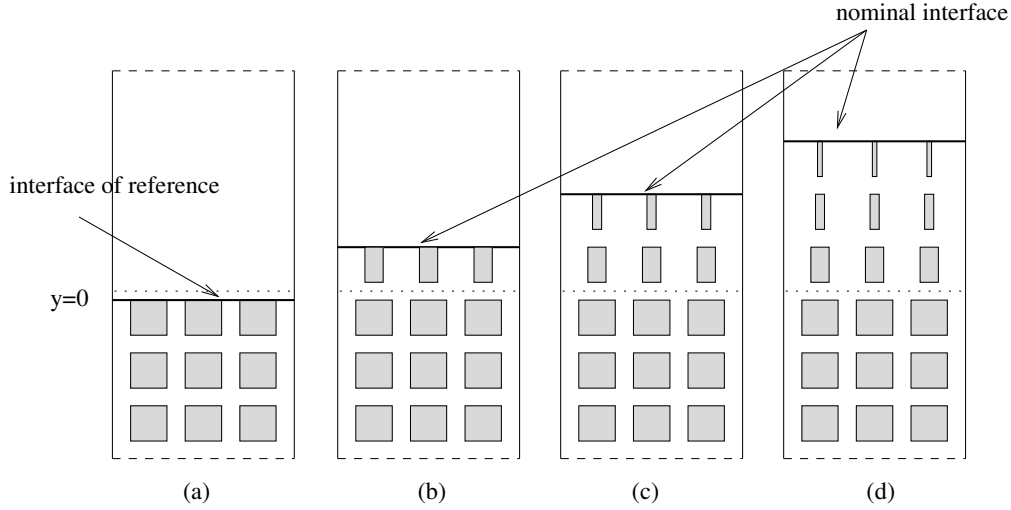


Figure 3.11: Geometry of the interface.

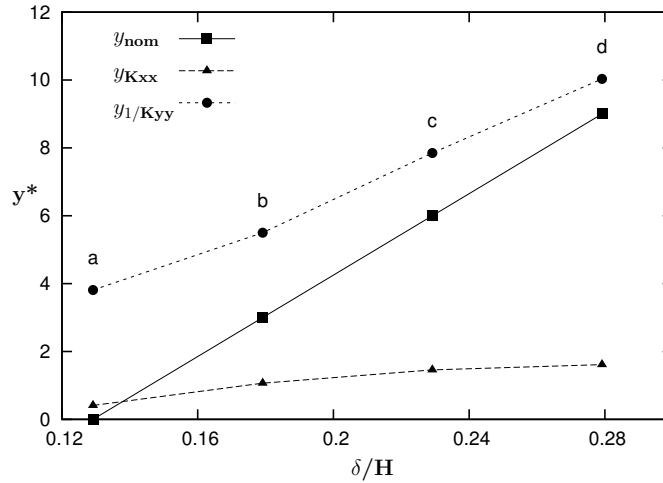


Figure 3.12: Center of gravity for various interfacial geometries $\left(y^* = \frac{y - y_{ref}}{d_p}\right)$ with y_{ref} being the nominal interface for the geometry without rugosity.

geometry and is clearly separated from the nominal interface. Thus the flux continuity is not always verified at the nominal interface and the use of rough interface illustrates it.

Using the geometry (d), the macroscopic models with boundary conditions of continuity at the apparent interface and at the nominal one are solved respectively. The resulting macroscopic temperatures are compared to the averaged microscopic temperature of reference. In Fig. 3.13 the temperature profile at $x = 0$ are represented. They show that the correct temperature profiles in the homogeneous region are recovered when the interface is located at $y_m = y_{K_{xx}}$. If the interface is located at the nominal interface, the corresponding macroscopic profile in the homogeneous free region exhibits a large difference with the correct profile. The qualitative results in two-dimension are illustrated in Fig. 3.14. These results are obtained for the geometry (d) with the Péclet number $Pe = 5$ and an incoming flux $q_w = 5$ (non-dimensional value) at the lateral boundaries. Fig. 3.14 shows that the mesoscopic temperature field obtained from the averaged microscopic results is identical to the solution of the macroscopic model computed for boundary conditions of continuity at $y_m = y_{K_{xx}}$.

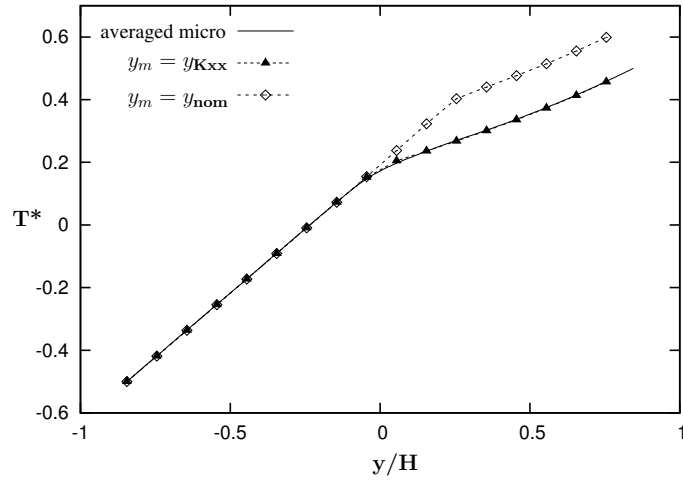


Figure 3.13: Macroscopic temperature at zeroth order for $x = 0$

$$\left(T^* = \frac{T - (\langle T \rangle (0; H^-) + \langle T \rangle (0; H^+))/2}{\langle T \rangle (0; H^+) - \langle T \rangle (0; H^-)} \right).$$

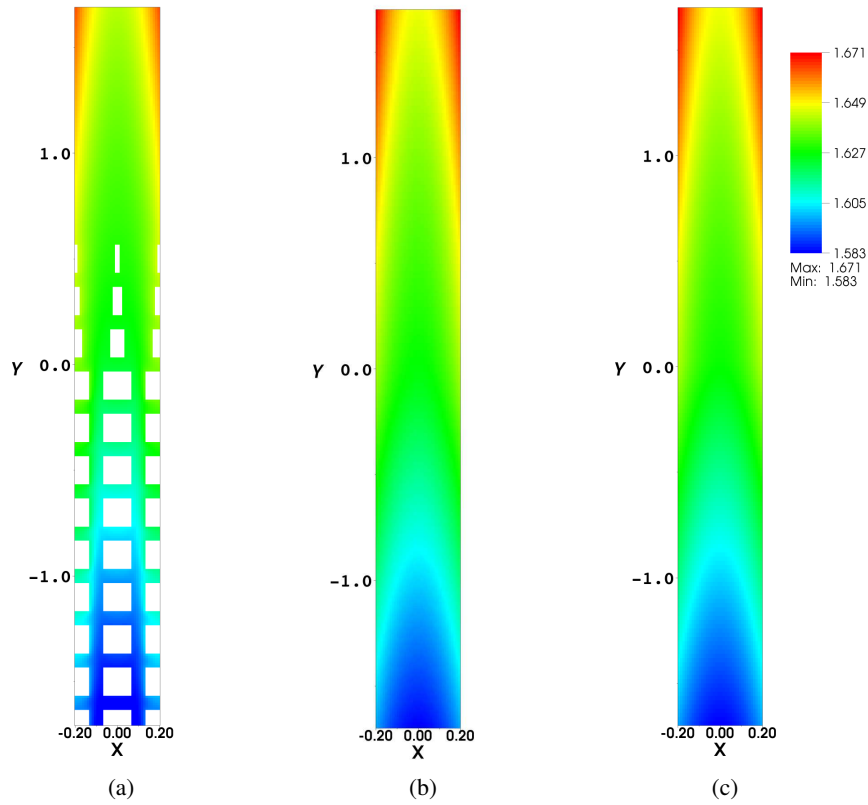


Figure 3.14: 2D temperature field: (a) microscopic scale, (b) averaged microscopic solution, (c) macroscopic solution.

For complex interfacial geometries, the question of the interface location is crucial. Indeed, the boundary conditions of continuity cannot be applied anywhere to get accurate macroscopic solution and only the apparent interface is pertinent. Thus, the determination of the apparent interface developed here answers

this question and the results illustrate in Figs. 3.13-3.14 show the relevance and the generality of the location.

3.7 Conclusion

The main objective of this paper is to determine the boundary conditions that must be applied at a fluid/porous interface in the case of convective heat transfer. A multi-scale approach based on three descriptions of the interface and two distinct up-scaling steps has been presented.

The first up-scaling step corresponds to the switch over between the microscopic and the mesoscopic scales. It is performed using the volume averaging method. A mesoscopic model is derived and the physical transfers specific of the interfacial transition region are modeled through effective transfer coefficients determined in the whole domain. At this scale, the interface is diffuse and there is no need to specify an exact interface location.

The second up-scaling step consists in determining the boundary conditions at the fluid/porous interface to close the macroscopic problem. The generic analysis is one method to provide boundary conditions containing surface excess quantities. However, the obtained relations involve unknown mesoscopic terms. For this reason, the method of the matched asymptotic expansion has been used. It provides approximated solutions of the mesoscopic equation at different orders, which satisfy jump relations at the interface. At order 0, the continuity of the heat flux and of the temperature are satisfied. At first order, the jump relations involve excess quantities of the effective thermal conductivities determined at the mesoscopic scale. Therefore, the jump relations at zeroth and first order are closed and depend only on intrinsic characteristic of the interface. Thus, the macroscopic problem can be solved. After solving the macroscopic model at different orders, we conclude that only the resolution at first order gives the correct temperature profile in the homogeneous regions whatever the location of the interface. For this, it is necessary to proceed in two steps. The macroscopic model at order 0 has to be solved first to get the macroscopic terms involved in order 1 jump relations, then the macroscopic model at first order can be solved.

Furthermore, the existence and the location of an apparent interface has been obtained. It allows the correct determination of the macroscopic temperature using only the continuity condition. For the studied 2D convective problem, it corresponds to the center of gravity of K_{xx} . This apparent interface presents the advantage to considerably simplify the numerical implementations required to solve the macroscopic problem.

Future work will examine the case of the two-temperature model.

3.8 Appendix

3.8.1 Appendix1: The matched asymptotic expansion method

In the case of heat transfer between a porous layer and a plain fluid, let us write the mesoscopic one-temperature equation (see Eq. 3.18)

$$(\rho c_p)_f \nabla \cdot (\langle \mathbf{v}_f \rangle \langle T \rangle) = \nabla \cdot [\bar{\bar{\mathbf{K}}}(y) \cdot \nabla \langle T \rangle] \quad (3.46)$$

which is equivalent to

$$\nabla \cdot \langle \mathbf{q} \rangle = 0 \quad (3.47)$$

where $\langle \mathbf{q} \rangle$ is the mesoscopic total heat flux. The method of the matched asymptotic expansion consists in breaking up the domain in three parts: an inside region where the tensor $\bar{\bar{\mathbf{K}}}(y)$ strongly varies and two outside regions where it is constant. Furthermore, the tensor depends on ε in the interfacial transition zone where $\varepsilon = \delta/L$, δ being the size of the inside region and L the length of the domain. In the outside

regions, the macroscopic temperatures solution of Eq. (3.46) take the shape of asymptotic expansions in ε

$$T_m^l(x, y) = T_m^{l(0)}(x, y) + \varepsilon T_m^{l(1)}(x, y) + \mathcal{O}(\varepsilon^2), \quad \text{in the fluid region} \quad (3.48)$$

$$T_m^p(x, y) = T_m^{p(0)}(x, y) + \varepsilon T_m^{p(1)}(x, y) + \mathcal{O}(\varepsilon^2), \quad \text{in the porous region} \quad (3.49)$$

In the inside region, the tensor strongly varies. Thus, a new variable $\hat{y} = (y - y_m)/\varepsilon$ is introduced to make the coefficients $\hat{K}_{xx}(\hat{y})$ and $\hat{K}_{yy}(\hat{y})$ go slower and to be able to perform the expansion. With this change of variable, the expression of the temperature in the inside region is:

$$\hat{T}(x, \hat{y}) = \hat{T}^{(0)}(x, \hat{y}) + \varepsilon \hat{T}^{(1)}(x, \hat{y}) + \mathcal{O}(\varepsilon^2) \quad (3.50)$$

and $\hat{K}_{xx}(\hat{y})$ and $\hat{K}_{yy}(\hat{y})$ do not depend on ε .

In the outside regions, the interface is located at the boundary y_m^+ for the free medium and y_m^- for the porous medium. From the inside region standpoint, the free and porous homogeneous regions are placed at $\hat{y} = \pm\infty$. To obtain a solution in the whole domain, a tie must be made between the inside and the outside regions. This tie is given by the matching conditions (Zwillinger, 1989). At zeroth and first orders, they can be written for any physical term ψ

$$\lim_{\hat{y} \rightarrow \pm\infty} \hat{\psi}^{(0)}(x, \hat{y}) = \lim_{y \rightarrow \pm y_m} \psi_m^{(0)}(x, y) \quad (3.51)$$

$$\lim_{\hat{y} \rightarrow \pm\infty} \left[\hat{\psi}^{(1)}(x, \hat{y}) - \hat{y} \lim_{y \rightarrow \pm y_m} \frac{\partial \psi_m^{(0)}(x, y)}{\partial y} \right] = \lim_{y \rightarrow \pm y_m} \psi_m^{(1)}(x, y) \quad (3.52)$$

3.8.1.1 Jump relations for the total heat flux

The asymptotic expansions in ε are introduced in Eq. (3.47) in the inside region and in the outside regions. Consequently, the system of equations at zeroth and first order in ε is obtained:

Outside problem, fluid region (for the porous region, the equations are similar):

$$\frac{\partial q_{Xm}^{l(0)}}{\partial x} + \frac{\partial q_{Ym}^{l(0)}}{\partial y} = 0; \quad \frac{\partial q_{Xm}^{l(1)}}{\partial x} + \frac{\partial q_{Ym}^{l(1)}}{\partial y} = 0 \quad (3.53)$$

Inside problem:

$$\frac{\partial \hat{q}_Y^{(0)}}{\partial \hat{y}} = 0 \quad (3.54)$$

$$\frac{\partial \hat{q}_X^{(0)}}{\partial x} + \frac{\partial \hat{q}_Y^{(1)}}{\partial \hat{y}} = 0 \quad (3.55)$$

To provide the jump relation for the total heat flux at order 0, Eq. (3.54) is integrated

$$\hat{q}_Y^{(0)}(x, \hat{y}) = k_1(x) \quad (3.56)$$

where $k_1(x)$ does not depend on \hat{y} and must be determined. The matching condition (3.51) applied at the boundaries between the inside/outside regions gives the values of the total heat flux on each side of the interface:

$$\lim_{\hat{y} \rightarrow \pm\infty} \hat{q}_Y^{(0)}(x, \hat{y}) = k_1(x) = q_{Ym}^{l,p(0)}(x, y_m^\pm) \quad (3.57)$$

Then, the difference between the fluid and porous values leads to:

$$q_{Ym}^{l(0)}(x, y_m^+) - q_{Ym}^{p(0)}(x, y_m^-) = 0 \quad (3.58)$$

Thus, the total heat flux in the y - direction is continuous at zeroth order at the interface.

To provide the jump relation for the total heat flux at order 1, Eq. (3.55) is rewritten with the appropriate macroscopic term on each side of the equality and is then integrated over the fluid region:

$$\int_0^{+\infty} \frac{\partial}{\partial \hat{y}} \left[\hat{q}_Y^{(1)} - \hat{y} \lim_{y \rightarrow +y_m} \frac{\partial q_{Ym}^{l(0)}}{\partial y}(x, y) \right] d\hat{y} = - \int_0^{+\infty} \left[\frac{\partial \hat{q}_X^{(0)}}{\partial x} + \lim_{y \rightarrow +y_m} \frac{\partial q_{Ym}^{l(0)}}{\partial y}(x, y) \right] d\hat{y} \quad (3.59)$$

Using the boundary y_m^+ of Eq. (3.53), the matching condition (3.52) for the total heat flux and the relation $\hat{y} = (y - y_m)/\varepsilon$, Eq. (3.59) takes the following form:

$$q_{Ym}^{l(1)}(x, y_m^+) - \hat{q}_Y^{(1)}(x, 0) = -\frac{1}{\varepsilon} \int_{y_m^+}^{+\infty} \left[\frac{\partial \hat{q}_X^{(0)}}{\partial x} - \frac{\partial q_{Xm}^{l(0)}}{\partial x}(x, y_m^+) \right] dy \quad (3.60)$$

A similar development is realized for the porous region and the sum of the two results gives:

$$\begin{aligned} q_{Ym}^{l(1)}(x, y_m^+) - q_{Ym}^{p(1)}(x, y_m^-) &= -\frac{1}{\varepsilon} \int_{y_m^+}^{+\infty} \left[\frac{\partial \hat{q}_X^{(0)}}{\partial x} - \frac{\partial q_{Xm}^{l(0)}}{\partial x}(x, y_m^+) \right] dy \\ &\quad - \frac{1}{\varepsilon} \int_{-\infty}^{y_m^-} \left[\frac{\partial \hat{q}_X^{(0)}}{\partial x} - \frac{\partial q_{Xm}^{p(0)}}{\partial x}(x, y_m^-) \right] dy \end{aligned}$$

With the definition of the excess value, the expression of the jump relation of the total heat flux at order 1 in the y - direction becomes:

$$q_{Ym}^{l(1)}(x, y_m^+) - q_{Ym}^{p(1)}(x, y_m^-) = -\frac{1}{\varepsilon} \left(\frac{\partial \hat{q}_X^{(0)}}{\partial x} \right)^{ex} \quad (3.61)$$

3.8.1.2 Jump relations for the temperature

The jump relations for the temperature are computed from the definition of the conductive heat flux. Using the asymptotic expansion (3.48), (3.49) and (3.50) in the conductive flux equation, the differential equations at zeroth and first order for the outside regions and for the inside region are obtained. Only the equations for the conductive heat flux in the inside region and in the y - direction are written here:

$$0 = -\hat{K}_{yy} \frac{\partial \hat{T}^{(0)}}{\partial \hat{y}} \quad (3.62)$$

$$\hat{q}_{Y,c}^{l(0)} = -\hat{K}_{yy} \frac{\partial \hat{T}^{(1)}}{\partial \hat{y}} \quad (3.63)$$

To get the jump relation for the temperature at zeroth order, Eq. (3.62) is integrated, which gives, since \hat{K}_{yy} is not nul:

$$\hat{T}^{(0)}(x, \hat{y}) = k_2(x) \quad (3.64)$$

where $k_2(x)$ does not depend on \hat{y} and must be determined. Then, the matching condition (3.51) gives the continuity of the temperature at order 0:

$$T_m^{l(0)}(x, y_m^+) - T_m^{p(0)}(x, y_m^-) = 0 \quad (3.65)$$

To determine the jump relation for the temperature at first order, the previous developments are realized from Eq. (3.63) and leads to:

$$T_m^{l(1)}(x, y_m^+) - T_m^{p(1)}(x, y_m^-) = -q_{Y,c m}^{l(0)}(x, y_m) \frac{1}{\varepsilon} \left(\frac{1}{K_{yy}} \right)^{ex} \quad (3.66)$$

Furthermore, the temperature at zeroth order in the inside region $\hat{T}^{(0)}$ is constant and worths $T_m^{(0)}(x, y_m)$. Thus, the heat flux in the x - direction takes the following form:

$$\hat{q}_X^{(0)} = -K_{xx} \frac{dk_2}{dx}(x) = -K_{xx} \frac{\partial T_m^{(0)}}{\partial x}(x, y_m) \quad (3.67)$$

Thanks to this writting, the jump relation of the total heat flux (3.61) at order 1 becomes:

$$q_{Y_m}^{l(1)}(x, y_m^+) - q_{Y_m}^{p(1)}(x, y_m^-) = \frac{1}{\varepsilon} \frac{\partial^2 T_m^{(0)}}{\partial x^2}(x, y_m) (K_{xx})^{ex} \quad (3.68)$$

3.9 Conclusion

The issue of this chapter is to derive the jump conditions that must be applied at a free-porous interface for heat transfer at local thermal equilibrium. Using a multi-scale approach, we perform two up-scaling steps and obtain three descriptions of the interface (see Tab. 3.1 hereafter).

In the first up-scaling step, we change the scale of description from microscopic to mesoscopic using the method presented in Chapter 1. At this scale of description, the interface is diffuse and the domain is separated in three parts: an homogeneous porous region where the effective properties are constant, a transition zone where the effective properties vary continuously and a free region with constant properties. The issue is to characterize the heat transfer with a continuous one-temperature equation (3.69c) valid in the whole domain and to determine the effective coefficient $\overline{\overline{K}}$.

Performing the first and second steps of the volume averaging method, we obtain a non-closed model and a closed model. By construction, the non-closed model is valid in the whole domain including the transition zone, while we derive the closed model in the homogeneous porous region, then we extend it to the rest of the domain. The relations given the effective coefficients are determined by identification between the closed and the non-closed models and computed with microscopic temperature and velocity fields of a numerical simulation. However, the relation involves the division by a temperature gradient and its computation requires specific microscopic temperature fields with non-zero gradients. This constraint is very limiting at a free-porous interface. Indeed, at the exit of the porous matrix, it exists in the microscopic velocity field, recirculating structures that change the local temperature gradient. In order to verify the constraint, we use complex boundary conditions to impose the non-zero temperature gradient in the transition zone. Thus, we determine the effective coefficient $\overline{\overline{K}}$ for different Peclet numbers.

In the second up-scaling step, we change the scale of description from mesoscopic to macroscopic. At this scale of description, the interface is modeled as a surface of discontinuity that separates the domain in two homogeneous regions, a porous one and a free one. The issue is to replace the continuous modeling of the interface by equivalent closed jump conditions. The most appropriate method is the method of matched asymptotic expansion that gives an approximate solution of the continuous problem.

We obtain solutions at order 0 that result from a macroscopic model made of the equations (3.69d) and (3.69e) in the homogeneous porous and free region, coupled at the free-porous interface by boundary conditions of continuity for the temperature and the heat flux. However, these solutions depend of the interface location.

Then, increasing the order of resolution, we derive boundary conditions at order 1 with jump conditions for the temperature (3.69f) and the heat flux (3.69g). These jump conditions involve excess values of effective transfer coefficients, macroscopic quantities of the solution at order 0, and the interface location. Thus, the jump conditions are closed and the dependence with the interface location is made explicit. As a consequence, we obtain solutions at order 1 free of the interface location.

Furthermore, we propose a best interface location for which the boundary conditions of continuity give an accurate modeling of the heat transfer. This interface is called apparent interface and located at the center of gravity of $\left(K_{xx}^f\right)^{\text{ex}}$. For continuity boundary conditions at any other location, the total heat flux is not conserved and it results in an error estimated by the relation (3.69h).

In Chapter 4, we increase the complexity of the heat transfer problem by adding a volume source in the solid matrix to create a local thermal non-equilibrium.

At the microscopic scale

$$(\rho c_p)_f \nabla \cdot (\mathbf{v}_f T_f) = -\nabla \cdot (k_f \nabla T_f) \text{ , for the fluid phase} \quad (3.69a)$$

$$0 = -\nabla \cdot (k_s \nabla T_s) \text{ , for the solid phase} \quad (3.69b)$$

At the mesoscopic scale

$$(\rho c_p)_f \langle \mathbf{v}_f \rangle \cdot \nabla \langle T \rangle = \nabla \cdot \left(\overline{\mathbf{K}}(\mathbf{x}) \nabla \langle T \rangle \right) \quad (3.69c)$$

At the macroscopic scale

In the porous region ($H^- < y < y_m$)

$$(\rho c_p)_f \mathbf{V} \cdot \nabla T_m^p = \nabla \cdot \left(\overline{\mathbf{K}}^p \cdot \nabla T_m^p \right) \quad (3.69d)$$

In the free region ($y_m < y < H^+$)

$$(\rho c_p)_f \mathbf{V} \cdot \nabla T_m^l = \nabla \cdot \left(\overline{\mathbf{K}}^l \cdot \nabla T_m^l \right) \quad (3.69e)$$

At the porous-free interface y_m

$$[T_m^f] = - \left(\frac{1}{K_{yy}} \right)^{\text{ex}} q_{cym}^{(0)} \quad (3.69f)$$

$$[q_{ym}^f] = (K_{xx}(y))^{\text{ex}} \frac{\partial^2 T_m^{f(0)}}{\partial x^2} \quad (3.69g)$$

The correction term in the free region is:

$$T_m^{(1)} = \left(K_{xx}^f \right)^{\text{ex}} \frac{\partial^2 T_m^{f(0)}}{\partial x^2} \quad (3.69h)$$

Table 3.1: Synthesis of the models used for the three scales descriptions.

Chapter 4

Free-porous interface modeling for laminar heat transfer at local thermal non-equilibrium

4.1 Introduction

In Chapter 2, we applied the multi-scale approach, proposed by [Chandesris and Jamet \(2006, 2007, 2009c,b,a\)](#) for momentum problems, to heat transfer at local thermal equilibrium. Thus, we have determined the jump conditions for 2D convective heat transfer with a laminar flow perpendicular to the fluid-porous interface. These jump conditions are easily computable knowing the profile of the effective conductivity tensor in the interfacial transition zone and the interface location. This profile can be obtained through a numerical simulation. However, beyond the closure of the macroscopic model with jump conditions, we obtained two essential pieces of information about the heat transfer at a free-porous interface:

- to correctly capture the heat transfer phenomena at a free-porous interface the essential is to conserve the total heat flux;
- we can evaluate the error done using boundary conditions of continuity for a chosen interface location.

Getting similar information in the case of heat transfer at local thermal non-equilibrium is the main objective of this chapter.

In this chapter, we increase the complexity by adding a volume source in the solid matrix to create a local thermal non-equilibrium between the solid and fluid phases. Performing the multi-scale approach on such a heat transfer problem, a new difficulty arises: the coupling at the free-porous interface of the two-temperature model in the porous region with the one-temperature model in the free region. To restore an identical number of equations on each side of the interface, we introduce a new writing. Thus, we can discuss the heat transfer modeling at the free-porous interface and bring the essential information that we are looking for.

The results regarding the jump conditions that must be applied at a free-porous interface in the case of local thermal non-equilibrium are presented in an article submitted to the *International Journal of Heat and Mass Transfer*.

Finally in Section 4.8, the results obtained allow to discuss the existence of an apparent interface where continuity boundary conditions can be applied. The discussion on the apparent interface is illustrated with several examples relevant for nuclear applications.

This chapter is a step in the understanding of the transfer phenomena existing in a reactor core. Even if

we use for the study a very low Reynolds number $Re = 5$, the form of the jump conditions and the key results are independent of the velocity. They are valid for laminar flows with high Peclet number and for turbulent flows as we will see in Chapter 6. Thus, the knowledge of the physical phenomena created by the local thermal non-equilibrium can be used for turbulent flows as we will see in Chapters 4 and 5.

4.2 Article 2: Coupling a two-temperature model and a one-temperature model at a fluid-porous interface

A. d'Hueppe ^a, M. Chandesris ^a, D. Jamet ^a, B. Goyeau ^b

submitted at *International Journal of Heat and Mass Transfer*

^a CEA, DEN, DER/SSTH/LDAL, 17 rue des martyrs, F-38054 Grenoble, France

^b EM2C, UPR-CNRS 288, Ecole Centrale Paris, Grande Voie des Vignes, Châtenay-Malabry, France

Abstract. We study a convective heat transfer problem in a fluid-porous domain in the case of the local thermal non-equilibrium assumption (LTNE). The issue of this study is to determine appropriate boundary conditions to model heat transfer, while using models with a different number of equations: a two-temperature model in the homogeneous porous region versus a one-temperature model in the free region. To proceed, a two-step up-scaling approach is used, which has the particularity to provide closed jump relations depending on intrinsic characteristic of the interface. Thus, the use of jump or continuity conditions depend only on the interface location inside the fluid-porous transition region. The pertinence of the approach is illustrated on a 2D convective heat transfer problem considering a solid heat source in the porous medium.

4.3 Introduction

The configuration of a free flow above a porous medium with a heat source in the solid matrix is present in many environmental or industrial applications. Such a configuration is commonly modeled by an homogeneous porous medium and a free medium separated by a surface of discontinuity. In the heated homogeneous porous medium, the local thermal non-equilibrium (LTNE) must be considered and the transfer can be modeled using the porous formalism through accurate two-temperature models (Kaviany, 1995; Quintard et al., 1997; Whitaker, 1999). In the free medium, a classical one-temperature model can be used. To complete the modeling, boundary conditions must be applied at the fluid-porous interface to couple the models used in both homogeneous regions and take into account the transfers in the transition region. However, given the different number of equations used in each region, questions regarding the general form of the boundary conditions arise. Up to now, these questions are still opened and the determination of the boundary conditions at the fluid-porous interface remains a scientific challenge.

For heat transfer at the local thermal equilibrium (LTE), successive works using one-temperature models in each region have brought valuable informations to better understand the complex question of the boundary conditions at the fluid-porous interface. First tests were performed using the application of boundary conditions at the nominal interface (defined by the position of the last solid grain (Beavers and Joseph, 1967)). Regarding the conductive heat transfer, conditions of continuity for both the temperature and the heat flux can give good results (Prat, 1990). However, for more complex phenomena including convective transfer, these boundary conditions are inappropriate and can be corrected with a temperature jump involving a slip coefficient (Sahraoui and Kaviany, 1994) similar to the velocity jump introduced by Beavers and Joseph (1967). Thus, these studies show that it is possible to capture the interfacial transfer with semi-empirical boundary conditions, but the relation between the interfacial physical phenomena and the slip coefficient is not explicated. This relation can be obtained deriving the boundary conditions

with up-scaling methods based on the energy conservation. Using such an approach, [Ochoa-Tapia and Whitaker \(1997\)](#) show that boundary conditions involve surface excess quantities which can be modeled with jump parameters. However, these jump parameters can not be determined because of two problems identified by some authors for momentum transfer ([Larson and Higdon, 1986](#); [Saleh et al., 1993](#)): the characterization of the transfer in the interfacial region is complex due to the spatial change of the local porous structure, and the jump parameters show a strong dependence with the interface location. The first problem is studied in [Aguilar-Madera and Ochoa-Tapia \(2011\)](#) via the resolution of closure problems in the transition zone at the local thermal equilibrium and non-equilibrium. Another approach consists in separating the two difficulties by introducing an intermediate continuous scale of description, called the *mesoscopic scale* (see Fig. 4.1). This method has been introduced by [Chandesris and Jamet \(2006, 2007, 2009c\)](#) for momentum problem and used by [d'Hueppe et al. \(2010\)](#) for convective transfer in the case of the local thermal equilibrium (LTE). First, the physical transfer specific of the interfacial region is modeled at this continuous scale. Then, the transfer is traduced at the macroscopic scale through equivalent jump conditions and the dependence with the interface location is clarified.

The paper presents appropriate boundary conditions at the fluid-porous interface in the case of convective heat transfer problem with local thermal non-equilibrium (LTNE) in the porous region. A 2D convective heat transfer problem with a laminar flow perpendicular to the fluid-porous interface is studied. The method used is based on the two steps up-scaling approach of [Chandesris and Jamet \(2006\)](#) and Section 4.4 describes the first up-scaling step. At the mesoscopic scale, the heat transfer is modeled by closed two-temperature equations valid in the whole domain and the associated effective thermal coefficients are computed from numerical simulations. In Section 4.5, the second up-scaling step gives the jump relations needed to couple the two-temperature model of the porous region with the one-temperature model of the free region. Then, the surface excess quantities involved in the jump relations are determined. Finally, the relevance of the macroscopic model is illustrated on a 2D practical case.

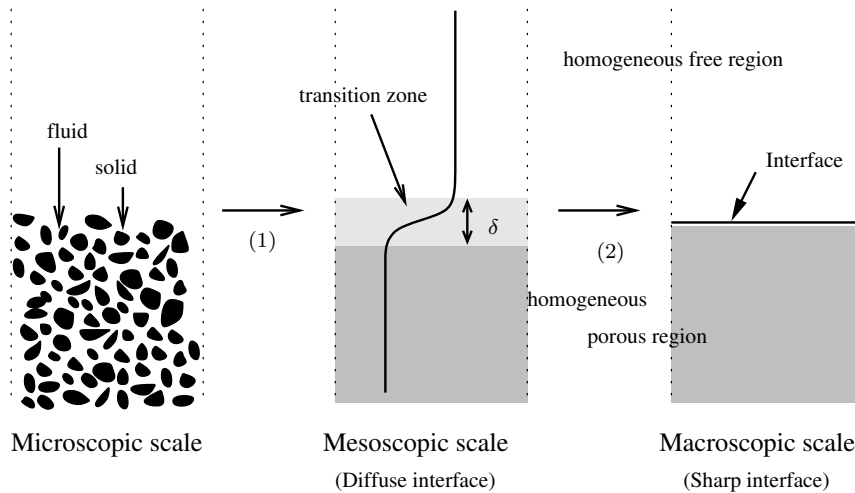


Figure 4.1: Interface between the porous medium and the fluid medium for various scales of description (figure adapted from [Chandesris and Jamet \(2007\)](#)).

4.4 The first up-scaling step

4.4.1 Microscopic equations

We consider a stationary laminar flow through a rigid porous medium followed by a free medium. The mean flow is directed towards the normal at the fluid-porous interface in the y -direction as illustrated

in Fig. 4.2(a).

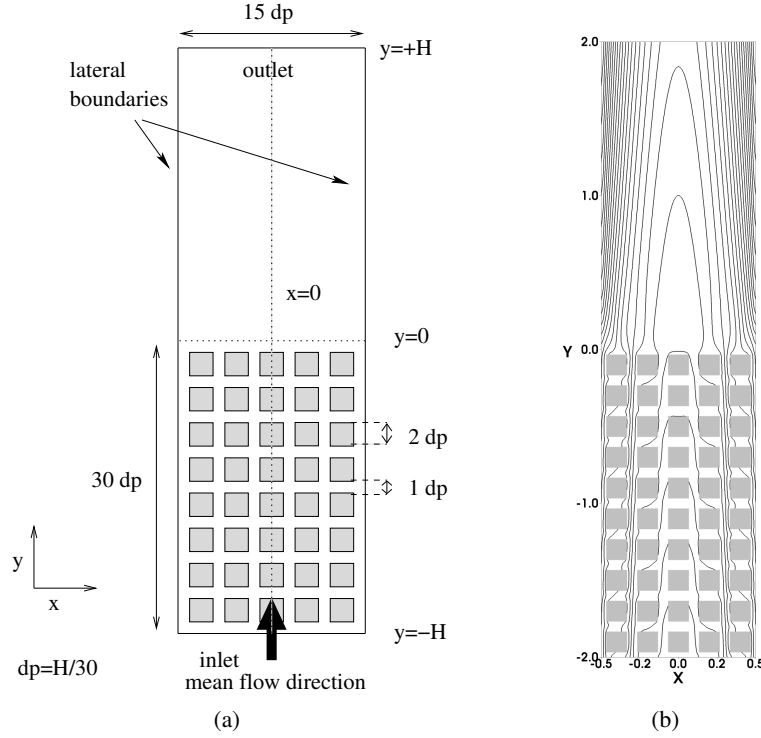


Figure 4.2: (a) Geometrical configuration. (b) Iso-contours of the microscopic fluid temperature.

The study of the two-temperature model at the mesoscopic scale requires a physical situation where the local thermal equilibrium assumption fails. This situation occurs when the convective term is important or also for large volumique heat sources S_s in the solid. In this work, we consider this second case. Fluid and solid properties (density, viscosity, heat capacity) are assumed constant, thus the velocity field can be determined independently. The numerical computations are realized for a porosity $\phi_p = 5/9$, a thermal conductivity ratio $k_s/k_f = 3$, a Prandtl number $Pr = 1$ and a Péclet number $Pe = 5$. The boundary conditions are established profiles of temperature and velocity representative of an infinite porous medium at the inlet, and a constant pressure for the velocity at the outlet. At the lateral boundaries, the boundary conditions will be discussed in the following (see section 4.4.3).

For stationnary cases, the governing equations at the microscopic scale are given by:

$$\nabla \cdot \mathbf{v}_f = 0 \quad (4.1)$$

$$(\mathbf{v}_f \cdot \nabla) \mathbf{v}_f = -\frac{1}{\rho} \nabla p + \nu \nabla^2 \mathbf{v}_f \quad (4.2)$$

$$(\rho c_p)_f \nabla \cdot (\mathbf{v}_f T_f) = -\nabla \cdot (k_f \nabla T_f), \text{ for the fluid phase} \quad (4.3)$$

$$0 = -\nabla \cdot (k_s \nabla T_s) + S_s, \text{ for the solid phase} \quad (4.4)$$

The associated boundary conditions at the fluid-solid interface A_{fs} are:

$$T_f = T_s \quad (4.5)$$

$$\mathbf{n}_{fs} \cdot (k_f \nabla T_f) = \mathbf{n}_{fs} \cdot (k_s \nabla T_s) \quad (4.6)$$

$$\mathbf{v}_f = 0 \quad (4.7)$$

where \mathbf{n}_{fs} is the unit normal vector directed from the fluid phase to the solid phase.

4.4.2 Mesoscopic model

Following [Whitaker \(1967\)](#) in the porous region, the up-scaling process is carried out using the volume averaging method. However, the averaging is not performed only in the porous region but in the whole domain. For any quantity ψ_α of the α phase, the superficial volume average is given by

$$\langle \psi_\alpha \rangle (\mathbf{x}) = \frac{\int_V m_p(\mathbf{r} - \mathbf{x}) \chi_\alpha(\mathbf{r}) \psi_\alpha(\mathbf{r}) dV}{\int_V m_p(\mathbf{r}) dV} \quad (4.8)$$

where \mathbf{x} is the centroid of the averaging volume and χ_α is the indicator function of the α phase. For the weighting function m_p , given the methodology chosen to compute the effective coefficients, we use the quadratic function obtained from the box function convoluted three times in ([d'Hueppe et al., 2010](#)) and with a filter size of $2r_0 = 9d_p$ (Fig. 4.2(a)). The intrinsic volume average is related to the superficial volume average by the relation

$$\langle \psi_\alpha \rangle^\alpha = \frac{\langle \psi_\alpha \rangle}{\phi_\alpha} \quad (4.9)$$

where ϕ_α is the volume fraction of the α phase within the averaging volume. The pore-scale deviation $\tilde{\psi}_\alpha$ in the α phase is defined using Gray's decomposition ([Gray, 1975](#))

$$\tilde{\psi}_\alpha = \langle \psi_\alpha \rangle^\alpha - \psi_\alpha \quad (4.10)$$

For conciseness, the following formalism is introduced:

$$\langle \psi_\alpha \rangle = \frac{1}{V} \int_V \psi_\alpha dV \quad (4.11)$$

and for the volume averaged on the fluid-solid surfaces this formalism corresponds to

$$\frac{1}{V} \int_{A_{fs}} \psi_\alpha dA = \frac{\int_{A_{fs}} m_p(\mathbf{r} - \mathbf{x}) \chi_\alpha(\mathbf{r}) \psi_\alpha(\mathbf{r}) dA}{\int_V m_p(\mathbf{r}) dV} \quad (4.12)$$

The application of the volume average to Eqs. (4.3), (4.4) combined with the spatial averaging theorems to interchange differentiation and integration ([Whitaker, 1967](#)) gives mesoscopic equations valid in the whole domain

For the fluid

$$\begin{aligned} (\rho c_p)_f \nabla \cdot (\langle \mathbf{v}_f \rangle \langle T_f \rangle^f) &= \nabla \cdot k_f \nabla \langle T_f \rangle + \nabla \cdot \underbrace{\frac{k_f}{V} \int_{A_{fs}} \mathbf{n}_{fs} \langle T_f \rangle^f dA}_{\text{tortuosity}} + k_f \nabla \cdot \underbrace{\frac{1}{V} \int_{A_{fs}} \mathbf{n}_{fs} \tilde{T}_f dA}_{\text{tortuosity}} \\ &\quad - \underbrace{\nabla \cdot (\rho c_p)_f \tau_{vT}}_{\text{thermal dispersion}} + \underbrace{\frac{k_f}{V} \int_{A_{fs}} \mathbf{n}_{fs} \cdot \nabla T_f dA}_{\text{fluid/solid heat transfer}} \end{aligned} \quad (4.13)$$

where $\tau_{vT} = \langle T_f \mathbf{v}_f \rangle - \phi_f \langle T_f \rangle^f \langle \mathbf{v}_f \rangle^f$ is a dispersive flux.

For the solid

$$\begin{aligned} 0 &= \nabla \cdot k_s \nabla \langle T_s \rangle - \nabla \cdot \underbrace{\frac{k_s}{V} \int_{A_{fs}} \mathbf{n}_{fs} \langle T_f \rangle^f dA}_{\text{tortuosity}} - k_s \nabla \cdot \underbrace{\frac{1}{V} \int_{A_{fs}} \mathbf{n}_{fs} \tilde{T}_f dA}_{\text{tortuosity}} \\ &\quad - \underbrace{\frac{k_f}{V} \int_{A_{fs}} \mathbf{n}_{fs} \cdot \nabla T_f dA}_{\text{fluid/solid heat transfer}} + \langle S_s \rangle \end{aligned} \quad (4.14)$$

This non-closed mesoscopic representation needs to be closed by modeling the tortuosity, dispersion and wall heat transfer contributions which involve local deviation terms.

In the homogeneous porous region, where the local constraint is satisfied (i.e., r_0 the size of the volume averaging is small compared to the scale of variation of the averaged quantities H), the spatial deviation temperature can be closed in terms of macroscopic sources (Kaviany, 1995; Quintard and Whitaker, 1993; Carbonell and Whitaker, 1984)

$$\tilde{T}_f = \mathbf{b}_{ff} \cdot \nabla \langle T_f \rangle^f + \mathbf{b}_{fs} \cdot \nabla \langle T_s \rangle^s - s_f \left(\langle T_f \rangle^f - \langle T_s \rangle^s \right) \quad (4.15)$$

where \mathbf{b}_{ff} , \mathbf{b}_{fs} and s_f are the vector and scalar fields mapping $\nabla \langle T_f \rangle^f$, $\nabla \langle T_s \rangle^s$ and $\left(\langle T_f \rangle^f - \langle T_s \rangle^s \right)$ onto \tilde{T}_f . Introducing the closure (4.15) in Eqs. (4.13), (4.14) leads to the closed mesoscopic equations (see Appendix A for more details)

For the fluid

$$(\rho c_p)_f \langle \mathbf{v}_f \rangle \cdot \nabla \langle T_f \rangle^f - \mathbf{u}_{ff}^p \cdot \nabla \langle T_f \rangle^f - \mathbf{u}_{fs}^p \cdot \nabla \langle T_s \rangle^s = \nabla \cdot \left(\bar{\bar{\mathbf{K}}}_{ff}^p \nabla \langle T_f \rangle^f + \bar{\bar{\mathbf{K}}}_{fs}^p \nabla \langle T_s \rangle^s + \mathbf{d}_f^p (\langle T_f \rangle^f - \langle T_s \rangle^s) \right) - a_V h^p \left(\langle T_f \rangle^f - \langle T_s \rangle^s \right) \quad (4.16)$$

For the solid

$$\mathbf{u}_{ff}^p \cdot \nabla \langle T_f \rangle^f + \mathbf{u}_{fs}^p \cdot \nabla \langle T_s \rangle^s = \nabla \cdot \left(\bar{\bar{\mathbf{K}}}_{sf}^p \nabla \langle T_f \rangle^f + \bar{\bar{\mathbf{K}}}_{ss}^p \nabla \langle T_s \rangle^s + \mathbf{d}_s^p (\langle T_f \rangle^f - \langle T_s \rangle^s) \right) + a_V h^p \left(\langle T_f \rangle^f - \langle T_s \rangle^s \right) + \langle S_s \rangle \quad (4.17)$$

where $\bar{\bar{\mathbf{K}}}_{ii}^p$ is the main effective conductive tensor, $\bar{\bar{\mathbf{K}}}_{ij}^p$ the coupled one, h^p the film heat transfer coefficient, a_V the interfacial area per unit volume, \mathbf{u}_{ii}^p , \mathbf{u}_{ij}^p and \mathbf{d}_i^p are the transport coefficients in the homogeneous porous medium.

This two-temperature model is very general but involves 9 different effective coefficients, which have to be determined. This high degree of complexity can explain why this model is rarely used under this form. In the present study, the local thermal non-equilibrium $\langle T_f \rangle^f \neq \langle T_s \rangle^s$ is verified. Furthermore in our preliminary numerical studies we have observed that $\nabla \langle T_f \rangle^f = \nabla \langle T_s \rangle^s$. Thus, we use this result as an assumption to simplify the model and reduce the number of effective coefficients. We define

$$\bar{\bar{\mathbf{K}}}_f^p = \bar{\bar{\mathbf{K}}}_{ff}^p + \bar{\bar{\mathbf{K}}}_{fs}^p, \bar{\bar{\mathbf{K}}}_s^p = \bar{\bar{\mathbf{K}}}_{ss}^p + \bar{\bar{\mathbf{K}}}_{sf}^p, \mathbf{u}^p = \mathbf{u}_{ff}^p + \mathbf{u}_{fs}^p \quad (4.18)$$

In the transition region, the local constraint, $r_0 \ll H$, used to derive the model in the homogeneous porous region is no longer valid. The characterization of the transfer is complex due to the spatial change of the local porous structure. However, we assume that the simplified two-temperature model with variable effective coefficients is able to capture the transfer in the transition zone. In the free region, since there is no solid and that $T_f = \langle T_f \rangle^f$ with $v_f = \langle v_f \rangle^f$, the model reduces to the governing equation (4.3). Thus, one can write the following closed two-temperature model valid in the whole domain:

For the fluid

$$(\rho c_p)_f \langle \mathbf{v}_f \rangle \cdot \nabla \langle T_f \rangle^f - \mathbf{u}(\mathbf{x}) \cdot \nabla \langle T_f \rangle^f = \nabla \cdot \left(\bar{\bar{\mathbf{K}}}_f(\mathbf{x}) \nabla \langle T_f \rangle^f + \mathbf{d}_f(\mathbf{x}) (\langle T_f \rangle^f - \langle T_s \rangle^s) \right) - a_V h(\mathbf{x}) \left(\langle T_f \rangle^f - \langle T_s \rangle^s \right) \quad (4.19)$$

For the solid

$$\mathbf{u}(\mathbf{x}) \cdot \nabla \langle T_f \rangle^f = \nabla \cdot \left(\bar{\bar{\mathbf{K}}}_s(\mathbf{x}) \nabla \langle T_s \rangle^s + \mathbf{d}_s(\mathbf{x}) (\langle T_f \rangle^f - \langle T_s \rangle^s) \right) + a_V h(\mathbf{x}) \left(\langle T_f \rangle^f - \langle T_s \rangle^s \right) + \langle S_s \rangle \quad (4.20)$$

where \mathbf{x} is the position vector, $\overline{\overline{\mathbf{K}}}_i$ the effective thermal conductivity tensor for the fluid and the solid respectively, h is the film heat transfer coefficient, \mathbf{u} is the transport coefficient related to the fluid/solid heat transfer modeling and \mathbf{d}_i is the transport coefficient related to the dispersion modeling. The effective coefficients are constant in the homogeneous regions and vary in the transition zone. Let us notice that due to the variation of \mathbf{d}_i in the interfacial transition zone, this term can not be taken out of the divergence operator. Thus, we make the modeling choice to keep separated the terms \mathbf{u} and \mathbf{d}_i for the rest of the study. To close the problem at the mesoscopic scale all the presented effective coefficients have to be determined.

4.4.3 Determination of the effective transfer coefficients

The effective coefficients are obtained from a microscopical simulation using an identification method introduced by Kuwahara et al. (1996) and used by d'Hueppe et al. (2010). First, the comparison of the non-closed model with the closed one gives by identification analytical relations for the effective coefficients. Then, each term of the analytical relations is computed with the microscopic temperature and velocity fields of the simulation.

The non-closed model (4.13)-(4.14) is compared with the closed one (4.19)-(4.20) that leads to the following analytical relations for the effective coefficients

$$\overline{\overline{\mathbf{K}}}_f \cdot \nabla \langle T_f \rangle^f + \mathbf{d}_f \left(\langle T_f \rangle^f - \langle T_s \rangle^s \right) = k_f \nabla \langle T_f \rangle + \frac{k_f}{V} \int_{A_{fs}} \mathbf{n}_{fs} T_f dA - (\rho c_p)_f \tau_{vT} \quad (4.21)$$

$$\overline{\overline{\mathbf{K}}}_s \cdot \nabla \langle T_s \rangle^s + \mathbf{d}_s \left(\langle T_f \rangle^f - \langle T_s \rangle^s \right) = k_s \nabla \langle T_s \rangle - \frac{k_s}{V} \int_{A_{fs}} \mathbf{n}_{fs} T_f dA \quad (4.22)$$

$$a_V h \left(\langle T_f \rangle^f - \langle T_s \rangle^s \right) - \mathbf{u} \cdot \nabla \langle T_f \rangle^f = -\frac{k_f}{V} \int_{A_{fs}} \mathbf{n}_{fs} \cdot \nabla T_f dA \quad (4.23)$$

Thus, the analytical relations for the effective coefficients are easily obtained, but a limit of the identification method appears at the evaluation step. Indeed, to have effective coefficients defined in the whole domain, the system (4.21)-(4.23) cannot be solved for any temperature fields. The averaged y-gradients and the temperature difference must be non zero. In addition, a temperature field with a symmetry axis in $x = 0$ where the averaged x-gradients are null simplifies the computation of the effective coefficients as one can see thereafter. The conditions at the lateral boundaries are chosen for this purpose and correspond to a condition of symmetry for the velocity and an incoming flux for the temperature. Furthermore, due to the invariance of the geometry and of the velocity field in the x -direction, the effective coefficients only depend on the y -direction and the conductivity tensors are diagonal. One can write

$$K_{ii}^f(y) \frac{\partial \langle T_f \rangle^f}{\partial i} + d_i^f(y) \left(\langle T_f \rangle^f - \langle T_s \rangle^s \right) = k_f \frac{\partial \langle T_f \rangle}{\partial i} + \frac{k_f}{V} \int_{A_{fs}} \mathbf{n}_{fs} T_f dA \cdot \mathbf{i} - (\rho c_p)_f \tau_{vT} \cdot \mathbf{i} \quad (4.24)$$

$$K_{ii}^s(y) \frac{\partial \langle T_s \rangle^s}{\partial i} + d_i^s(y) \left(\langle T_f \rangle^f - \langle T_s \rangle^s \right) = k_s \frac{\partial \langle T_s \rangle}{\partial i} + \frac{k_s}{V} \int_{A_{fs}} \mathbf{n}_{fs} T_f dA \cdot \mathbf{i} \quad (4.25)$$

$$a_V h(y) \left(\langle T_f \rangle^f - \langle T_s \rangle^s \right) - u_y^f(y) \frac{\partial \langle T_f \rangle^f}{\partial y} - u_x^f(y) \frac{\partial \langle T_f \rangle^f}{\partial x} = -\frac{k_f}{V} \int_{A_{fs}} \mathbf{n}_{fs} \cdot \nabla T_f dA \quad (4.26)$$

with the index i for x and y respectively.

The relation (4.24) for the index $i = x$ at the position x such as $\frac{\partial \langle T_f \rangle^f}{\partial x}(x, y) = 0$ (symmetry at $x = 0$) gives $d_x^f = 0$ and an easy computation of $K_{xx}^f(y)$ for any else x location. The determination of $K_{yy}^f(y)$ and d_y^f requires two numerical simulations with two different values of the solid source S_s to obtain a

system composed of two-unknowns and two-equations. The solid effective coefficients are computed with the same method that gives in particular $d_x^s = 0$. Identically, one determines $a_V h(y)$ and $u_y^f(y)$ with Eq. (4.26) computed at $x = 0$. Then using this values at another x-location, one gets $u_x^f(y) = 0$. Let us notice, that these developments rely on the assumption that the effective coefficients do not depend on the local fields or on the x-location (given the geometry). This assumption has been verified by computing the effective coefficients at different x-location.

First, to verify the value of the effective coefficients in the homogeneous porous region, a comparison is realized with the results from Quintard et al. (1997) obtained with a similar heat transfer modeling. To proceed, the effective coefficients are determined with the identification method for various Peclet numbers and four thermal conductivity ratios k_s/k_f (see Figs. 4.3(a), 4.3(b) and 4.4). Let us remains that Quintard et al. (1997) give the tensors $\bar{\bar{K}}_{ii}^{i,p}$ and $\bar{\bar{K}}_{ij}^{i,p}$ that are related to our values according to $\bar{\bar{K}}^{i,p} = \bar{\bar{K}}_{ii}^{i,p} + \bar{\bar{K}}_{ij}^{i,p}$ for the fluid and the solid phases respectively. Thus, Fig. 4.3(a) must be compared with the sum of Figs. 5(a) and 7(b) in Quintard et al. (1997) for the fluid phase, and Fig. 4.3(b) must be compared with the sum of Figs. 8(a) and 7(a) in Quintard et al. (1997) for the solid phase. Allowing for the different choice of the geometry, in-line cubes instead of in-line cylinders, the main behaviors of the effective coefficients are recovered.

Figs. 4.5(a)-4.6(b) present the profiles of the different effective coefficients. As expected, the values of the effective coefficients are constant in the homogeneous regions and continuously vary in the interfacial transition zone. Especially, the transition zone of reference is the porosity one, that varies between $-0,13 < y/H < 0,13$ and represents the averaged geometry only. In the interfacial transition zone, the bumps observed on the different profiles result from recirculations in the velocity field at the outlet of the porous media. In the free region, as expected, the effective coefficient values of the solid phase, $K_{ii}^{s,l}$, are zero, along with the coefficients associated to the fluid/solid transfer (h^l and $u_y^{f,l}$). For the fluid coefficient, the characteristics of the fluid phase are recovered, thus $K_{xx}^{f,l} = K_{yy}^{f,l} = k_f = 1$.

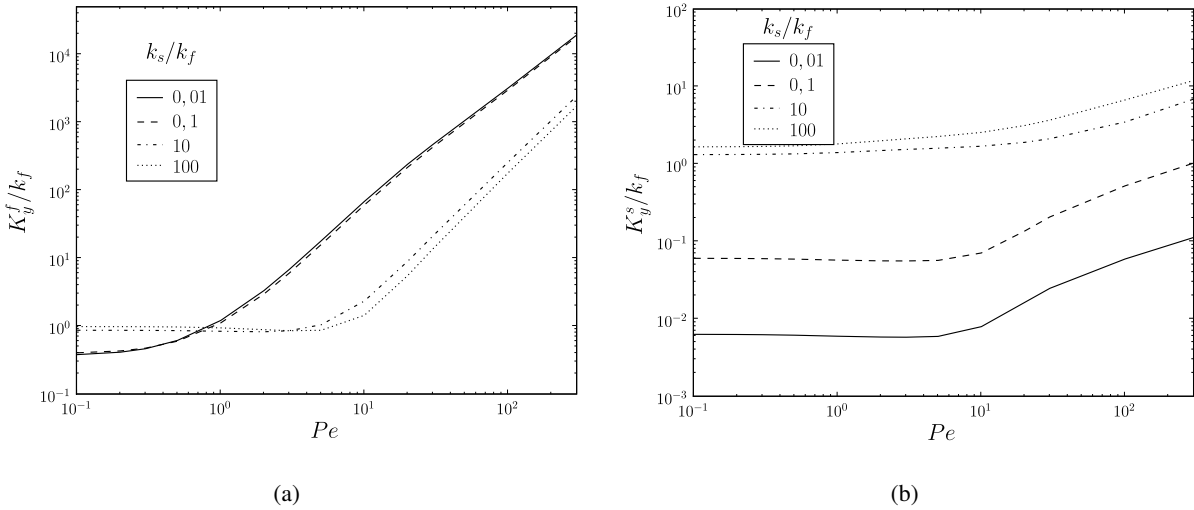


Figure 4.3: Effective thermal conductivity coefficient in the flow direction (a) for the fluid phase K_{yy}^f ; (b) for the solid phase K_{yy}^s .

At this point, the microscopic problem has been replaced by a mesoscopic model where each phase is described by a continuous equation in the whole domain. Thus, at the mesoscopic scale, the heat transfer is characterized by a two-temperature closed model valid in the entire domain. As the effective

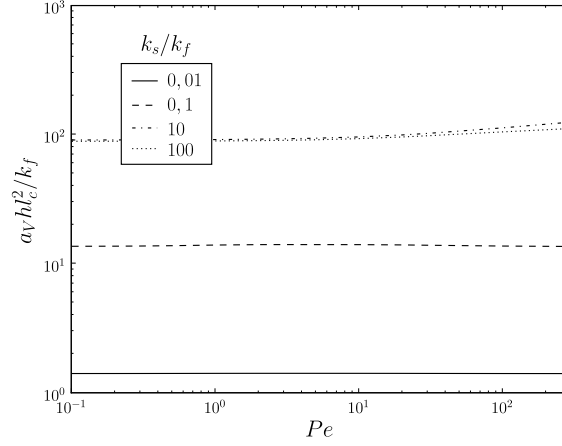


Figure 4.4: Profiles of h for various k_s/k_f .

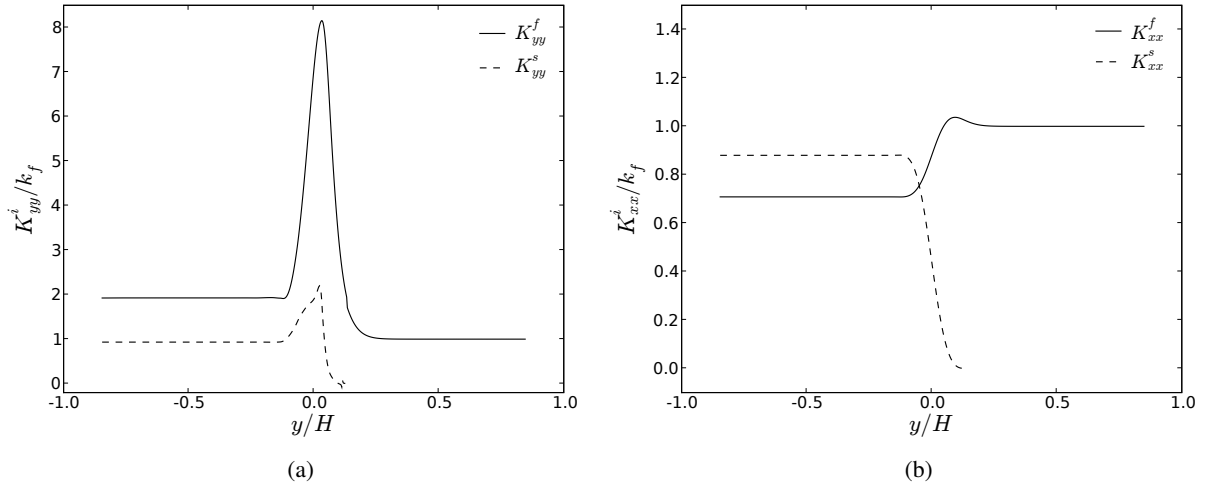


Figure 4.5: Profiles of the effective conductivities (a) K_{yy}^f and K_{yy}^s for $Pe = 5$; (b) K_{xx}^f and K_{xx}^s for $Pe = 5$.

coefficients have been determined, the problem at the mesoscopic scale is solved and we are able to perform the second up-scaling step.

4.5 The second up-scaling step

In the previous section, the heat transfer has been modeled at the mesoscopic scale through equations with continuous variable coefficients. However, for practical applications, the use of highly variable coefficients in the transition zone is not adequate because it requires a fine meshing to simulate the transfer. Thus, the modeling process must be pursued to substitute the transition zone by a surface of discontinuity with associated jump boundary conditions. To proceed, a new scale of description, called macroscopic scale, is introduced, and the second up-scaling step is performed to derive a discontinuous model from the mesoscopic continuous one (4.19)-(4.20). At the macroscopic scale, the heat transfer is described using the following equations characterised by constant properties in each region:

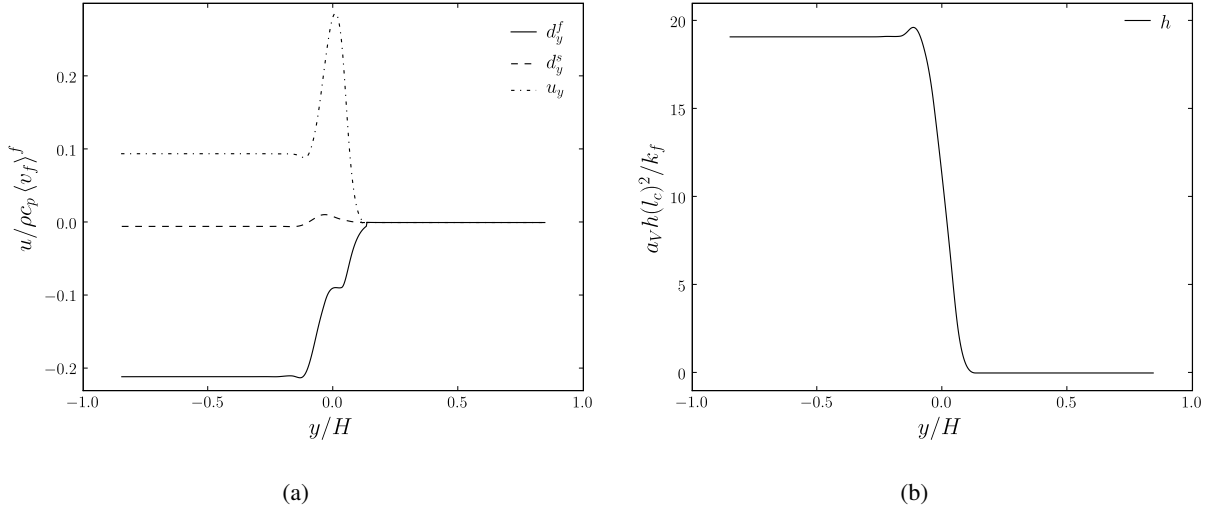


Figure 4.6: Profiles of (a) the heat transfer coefficient h for $Pe = 5$, where $l_c (= 3d_p)$ is the length of one unit cell; (b) the transport coefficients u_y , d_y^f and d_y^s for $Pe = 5$.

In the porous region ($H^- < y < y_m$); a two-temperature model

$$(\rho c_p)_f \mathbf{v}_m \cdot \nabla T_m^{f,p} - \mathbf{u}^p \cdot \nabla T_m^{f,p} = \nabla \cdot \left(\bar{\mathbf{K}}_f^p \cdot \nabla T_m^{f,p} + \mathbf{d}_f^p (T_m^{f,p} - T_m^{s,p}) \right) - a_V h^p (T_m^{f,p} - T_m^{s,p}) \quad (4.27)$$

$$\mathbf{u}^p \cdot \nabla T_m^{f,p} = \nabla \cdot \left(\bar{\mathbf{K}}_s^p \cdot \nabla T_m^{s,p} \right) + a_V h^p (T_m^{f,p} - T_m^{s,p}) + \phi_s^p S_s \quad (4.28)$$

In the free region ($y_m < y < H^+$); a one-temperature model

$$(\rho c_p)_f \mathbf{v}_m \cdot \nabla T_m^{f,l} = \nabla \cdot \left(k_f \bar{\mathbf{I}} \cdot \nabla T_m^{f,l} \right) \quad (4.29)$$

where y_m is the interface location. Let us notice that due to the diffuse nature of the interface at the mesoscopic scale, the interface location at the macroscopic scale is an unknown parameter.

At the macroscopic scale, the solid equation is not defined in the free region. In this up-scaling modeling approach, we choose to introduce an equivalent writing of the system (4.27)- (4.29), with a two-temperature model in both homogeneous regions:

$$(\rho c_p)_f \mathbf{v}_m \cdot \nabla T_m^{f,i} - \mathbf{u}^i \cdot \nabla T_m^{f,i} = \nabla \cdot \left(\bar{\mathbf{K}}_f^i \cdot \nabla T_m^{f,i} + \mathbf{d}_f^i (T_m^{f,i} - T_m^{s,i}) \right) - a_V h^i (T_m^{f,i} - T_m^{s,i}) \quad (4.30)$$

$$\mathbf{u}^i \cdot \nabla T_m^{f,i} = \nabla \cdot \left(\bar{\mathbf{K}}_s^i \cdot \nabla T_m^{s,i} \right) + a_V h^i (T_m^{f,i} - T_m^{s,i}) + \phi_s^i S_s \quad (4.31)$$

with the indice i being p or l in the porous and the free media respectively. In the free media, the coefficients \mathbf{u}^l , $\bar{\mathbf{K}}_s^l$, h^l , \mathbf{d}_f^l , ϕ_s^l are zero and $\bar{\mathbf{K}}_f^l = k_f \bar{\mathbf{I}}$. Under these circumstances, the solid temperature is undefined in the free region. To define it, one assumes that the solid temperature is continuous at the interface and there is no solid heat flux in the y -direction in the free region. Thus, the number of equations in the porous and in the free media is the same and the developments are identical for the solid and the fluid phases.

At this step the macroscopic model is not closed since it must be completed by boundary conditions

at the interface. Two different methods based on conservation principles are used: the first one is the generic analysis and the second one is the method of the matched asymptotic expansions. Both methods are presented in the following subsections.

4.5.1 The generic analysis

The method of the generic analysis (Edwards et al., 1991) ensures the conservation of the energy between the macroscopic and the mesoscopic scales by comparing the governing equations integrated over the transition region. The remainders terms represent the variations existing in the transition zone at the mesoscopic scale and not considered by the macroscopic model in the two homogeneous regions. To proceed, the macroscopic equations (4.30) and the mesoscopic equation (4.19) are integrated on $[H^-; y_m]$ and substracted

$$\begin{aligned} & \left[(\rho c_p)_f \langle v_f \rangle \langle T_f \rangle^f - v_{my} T_m^{f,p} \right]_{H^-}^{y_m} - \int_{H^-}^{y_m} \left(u_y(y) \frac{\partial \langle T_f \rangle^f}{\partial y} - u_y^p \frac{\partial T_m^{f,p}}{\partial y} \right) dy = \\ & \left[K_{yy}^f(y) \frac{\partial \langle T_f \rangle^f}{\partial y} - K_{yy}^{f,p} \frac{\partial T_m^{f,p}}{\partial y} \right]_{H^-}^{y_m} + \left[d_y(y) (\langle T_s \rangle^s - \langle T_f \rangle^f) - d_y^p (T_m^{f,p} - T_m^{s,p}) \right]_{H^-}^{y_m} \\ & + \int_{H^-}^{y_m} \frac{\partial}{\partial x} \left(K_{xx}^f(y) \frac{\partial \langle T_f \rangle^f}{\partial x} - K_{xx}^{f,p} \frac{\partial T_m^{f,p}}{\partial x} \right) dy \\ & - \int_{H^-}^{y_m} a_V \left(h(y) (\langle T_f \rangle^f - \langle T_s \rangle^s) - h^p (T_m^{f,p} - T_m^{s,p}) \right) dy \quad (4.32) \end{aligned}$$

One reminds that $u_x = d_x^f = 0$. To compare the energy transfer over the whole transition region, Eqs. (4.31) and (4.19) are compared on $[y_m; H^+]$ and added to Eq. (4.32). Then using the equivalence between the macroscopic and the mesoscopic terms in the homogeneous regions¹, one can write

$$\begin{aligned} & q_{y,m}^{f,l}(x, y_m) - q_{y,m}^{f,p}(x, y_m) = \\ & \int_{H^-}^{y_m} \frac{\partial}{\partial x} \left(K_{xx}^f(y) \frac{\partial \langle T_f \rangle^f}{\partial x} - K_{xx}^{f,p} \frac{\partial T_m^{f,p}}{\partial x} \right) dy + \int_{y_m}^{H^+} \frac{\partial}{\partial x} \left(K_{xx}^f(y) \frac{\partial \langle T_f \rangle^f}{\partial x} - K_{xx}^{f,l} \frac{\partial T_m^{f,l}}{\partial x} \right) dy \\ & - a_V \int_{H^-}^{y_m} \left[h(y) (\langle T_f \rangle^f - \langle T_s \rangle^s) - h^p (T_m^{f,p} - T_m^{s,p}) \right] dy \\ & - a_V \int_{y_m}^{H^+} \left[h(y) (\langle T_f \rangle^f - \langle T_s \rangle^s) - h^l (T_m^{f,l} - T_m^{s,l}) \right] dy \\ & + \int_{H^-}^{y_m} \left(u_y(y) \frac{\partial \langle T_f \rangle^f}{\partial y} - u_y^p \frac{\partial T_m^{f,p}}{\partial y} \right) dy + \int_{y_m}^{H^+} \left(u_Y(y) \frac{\partial \langle T_f \rangle^f}{\partial y} - u_y^l \frac{\partial T_m^{f,l}}{\partial y} \right) dy \quad (4.33) \end{aligned}$$

where for the rest of the study, the total fluid heat flux in the y -direction is

$$q_{y,m}^{f,i} = (\rho c_p)_f v_{my} T_m^{f,i} - K_{yy}^{f,i} \frac{\partial T_m^{f,i}}{\partial y} - d_y (T_m^{f,i} - T_m^{s,i}).$$

The right hand side of the equality (4.33) corresponds to the difference of the interface modelisation between the macroscopic and mesoscopic models. They can be gathered into terms called *surface-excess quantities* and noted for any field ψ as

$$(\psi)^{ex} = \int_{H^-}^{y_m} (\psi - \psi_m^p) dy + \int_{y_m}^{H^+} (\psi - \psi_m^l) dy \quad (4.34)$$

¹ $\langle v_f \rangle = V_{my} = cst$ in the whole domain due to the mass conservation.

4.5 The second up-scaling step

where ψ_m^l and ψ_m^p are the macroscopic representations of the field ψ in the free and porous homogeneous regions respectively. According to this notation, Eq. (4.33) becomes:

$$q_{y,m}^{f,l}(x, y_m) - q_{y,m}^{f,p}(x, y_m) = \left(\frac{\partial}{\partial x} \left(K_{xx}^f(y) \frac{\partial \langle T_f \rangle^f}{\partial x} \right) \right)^{ex} - \left(a_V h(y) \left(\langle T_f \rangle^f - \langle T_s \rangle^s \right) \right)^{ex} + \left(u_y(y) \frac{\partial \langle T_f \rangle^f}{\partial y} \right)^{ex} \quad (4.35)$$

The jump condition for the solid flux is obtained with an identical development and takes the form

$$q_{y,m}^{s,l}(x, y_m) - q_{y,m}^{s,p}(x, y_m) = \left(\frac{\partial}{\partial x} \left(K_{xx}^s(y) \frac{\partial \langle T_s \rangle^s}{\partial x} \right) \right)^{ex} + \left(a_V h(y) \left(\langle T_f \rangle^f - \langle T_s \rangle^s \right) \right)^{ex} - \left(u_y(y) \frac{\partial \langle T_f \rangle^f}{\partial y} \right)^{ex} + (\langle S_s \rangle)^{ex} \quad (4.36)$$

where for the rest of the study, the total solid heat flux is $q_{y,m}^{s,i} = -K_{yy}^s \frac{\partial T_m^{s,i}}{\partial y}$. The jump relations for the fluid and solid total heat flux correspond to the energy conservation between the lower part and the upper part of the transition region. The effect of the temperature gradient in the x -direction is captured as in (d'Hueppe et al., 2010) and two terms characteristic of the two-temperature transfer appear. $\left(h(y) \left(\langle T_f \rangle^f - \langle T_s \rangle^s \right) \right)^{ex}$ and $\left(u_y(y) \frac{\partial \langle T_f \rangle^f}{\partial y} \right)^{ex}$ come from Eq. (4.26) and model the transfer between the fluid and the solid phases. In the heat flux jumps, they traduce the excess amount of heat received by the fluid when the solid phase disappears in the interfacial transition zone.

The jump condition for the fluid temperature is determined comparing the mesoscopic conductive heat flux in the y -direction $\langle q_{y,cf} \rangle^f = -K_{yy}^f(y) \frac{\partial \langle T_f \rangle^f}{\partial y}$ and the following macroscopic equations:

$$q_{cm,y}^{f,l} = -K_{yy}^{f,l} \frac{\partial T_m^{f,l}}{\partial y}, \text{ in the free region} \quad (4.37)$$

$$q_{cm,y}^{f,p} = -K_{yy}^{f,p} \frac{\partial T_m^{f,p}}{\partial y}, \text{ in the porous region} \quad (4.38)$$

Performing the same developments as previously, the temperature jump for the fluid takes the form:

$$T_m^{f,l}(x, y_m) - T_m^{f,p}(x, y_m) = - \left(\langle q_{cy} \rangle^f \frac{1}{K_{yy}^f} \right)^{ex} \quad (4.39)$$

The jump relation for the temperature involves the excess quantity of the conductive flux time the thermal resistance. This jump relation is identical to the one presented in (d'Hueppe et al., 2010) for a one-temperature problem. Regarding a possible jump for the solid temperature, the question is not relevant, since it is continuous due to the chosen definition.

The two-equation/one-equation formalism is recovered using the chosen assumption of no solid heat

flux in the free region for Eq. (4.36). Thus, one obtains

$$T_m^{f,l}(x, y_m) - T_m^{f,p}(x, y_m) = - \left(\langle q_{cy} \rangle^f \frac{1}{K_{yy}^f} \right)^{ex} \quad (4.40)$$

$$q_{y,m}^{f,l}(x, y_m) - q_{y,m}^{f,p}(x, y_m) = \left(\frac{\partial}{\partial x} \left(K_{xx}^f(y) \frac{\partial \langle T_f \rangle^f}{\partial x} \right) \right)^{ex} - \left(a_V h(y) \left(\langle T_f \rangle^f - \langle T_s \rangle^s \right) \right)^{ex} + \left(u_y(y) \frac{\partial \langle T_f \rangle^f}{\partial y} \right)^{ex} \quad (4.41)$$

$$q_{y,m}^{s,p}(x, y_m) = - \left(\frac{\partial}{\partial x} \left(K_{xx}^s(y) \frac{\partial \langle T_s \rangle^s}{\partial x} \right) \right)^{ex} - \left(a_V h(y) \left(\langle T_f \rangle^f - \langle T_s \rangle^s \right) \right)^{ex} + \left(u_y(y) \frac{\partial \langle T_f \rangle^f}{\partial y} \right)^{ex} - \langle S_s \rangle^{ex} \quad (4.42)$$

The generic analysis gives the form of the jump relations to close the macroscopic system. Thus, for the two-equation/one-equation formalism, the closure requires jump conditions for the temperature and total heat flux for the fluid phase, and one boundary condition for the solid total heat flux. However these boundary conditions can not be computed because of the presence of mesoscopic unknowns in the excess values. To obtain closed boundary conditions the alternative method of the matched asymptotic expansion is used.

4.5.2 The method of the matched asymptotic expansion

The method of the matched asymptotic expansion, also called boundary layer method, can be applied to solve differential equations with a small parameter ε and gives a solution in terms of this small parameter (Zwillinger, 1989). This method used in the context of diffuse interface modeling, establishes the relationship between the diffuse interface and sharp interface modeling equations (Emmerich, 2003). In the present case, the small parameter is the ratio between the width of the interfacial transition zone and the characteristic length of the whole domain, that is $\varepsilon = \delta/L$. The sharp interface model is obtained when ε tends to zero. Thus, using the method of the matched asymptotic expansion, one obtains approximated solutions at different order of the mesoscopic equations. Therefore, it is possible to derive analytically, and at a given order, the boundary conditions of the macroscopic model such that the macroscopic problem is equivalent to the mesoscopic one. The detailed developments are presented in appendix B and only the main results are presented in the following, using the two-equation/one-equation formalism.

4.5.2.1 Resolution at order 0

The approximated solutions at order 0 of the mesoscopic model for the fluid and solid phases, $T_m^i = T_m^{i(0)}$, verify the macroscopic equations in the homogeneous regions (Eqs. (4.30), (4.31)) and the conditions of continuity for the flux and the temperature at the interface (see Appendix B)

$$T_m^{f,l}(x, y_m) = T_m^{f,p}(x, y_m) \quad (4.43)$$

$$q_{ym}^{f,l}(x, y_m) = q_{ym}^{f,p}(x, y_m) \quad (4.44)$$

$$q_{ym}^{s,p}(x, y_m) = 0 \quad (4.45)$$

The fluid and solid macroscopic temperatures obtained with this model are presented with the averaged microscopic solution in Fig. 4.7 for three different locations of the interface representative of the transition zone defined between $(-0, 13 < y/H < 0, 13)$. The presented macroscopic temperatures depend

on the interface location in the homogeneous free region. This behavior has been observed by [d'Hueppe et al. \(2010\)](#) and can be explained by the no-conservation of the energy balance between the mesoscopic and macroscopic models at 0 order. Thus, it is necessary to increase the resolution order to make appear jump conditions.

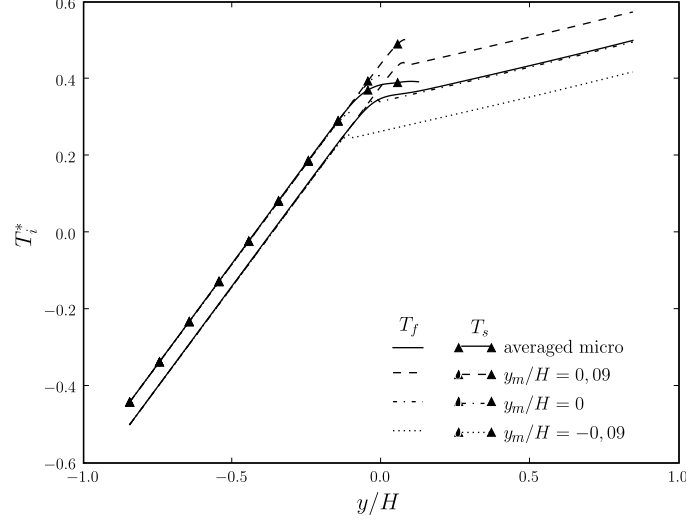


Figure 4.7: Macroscopic temperature at zeroth order for $x = 0$ ($T_i^* = [T_i - (\langle T_f \rangle^f(0; H^-) + \langle T_f \rangle^f(0; H^+))/2] / [\langle T_f \rangle^f(0; H^+) - \langle T_f \rangle^f(0; H^-)]$).

4.5.2.2 Resolution at order 1

At order 1, the approximated solutions of the mesoscopic problem, $T_m^i = T_m^{i(0)} + \varepsilon T_m^{i(1)}$ for the fluid and solid phases, verify the macroscopic equations in the homogeneous regions Eqs. (4.30)-(4.31) and the following jump conditions (see Appendix B Eqs. (4.98)-(4.100))

$$T_m^{f,l}(x, y_m) - T_m^{f,p}(x, y_m) = - \left(\frac{1}{K_{yy}^f(y)} \right)^{ex} q_{cym}^{f(0)}(x, y_m) \quad (4.46)$$

$$q_{ym}^{f,l}(x, y_m) - q_{ym}^{f,p}(x, y_m) = \left(K_{xx}^f(y) \right)^{ex} \frac{\partial^2 T_m^{f(0)}}{\partial x^2}(x, y_m) - a_V (h(y))^{ex} (T_m^{f(0)} - T_m^{s(0)})(x, y_m) - \left(\frac{u_y(y)}{K_{yy}^f(y)} \right)^{ex} q_{cym}^{f(0)}(x, y_m) \quad (4.47)$$

$$q_{ym}^{s,p}(x, y_m) = - (K_{xx}^s(y))^{ex} \frac{\partial^2 T_m^{s(0)}}{\partial x^2}(x, y_m) - a_V (h(y))^{ex} (T_m^{f(0)} - T_m^{s(0)})(x, y_m) - \left(\frac{u_y(y)}{K_{yy}^f(y)} \right)^{ex} q_{cym}^{f(0)}(x, y_m) - (\phi_s(y))^{ex} S_s \quad (4.48)$$

The excess quantities of the effective transfer coefficients and the associated centers of gravity are introduced in the jump conditions via the relation ([Jamet and Chandesris, 2009](#))

$$(\psi)^{ex}(y_m) = (\psi^l - \psi^p)(y_m - y_\psi) \quad (4.49)$$

$y_{\frac{1}{K_{yy}^f}}/H$	$y_{K_{xx}^f}/H$	$y_{K_{xx}^s}/H$	$y_{\frac{u_y}{K_{yy}^f}}/H$	y_h/H	y_{ϕ_s}/H
0.3	-0.02	-0.001	0.03	0.005	-0.001

Table 4.1: Values of the centers of gravity for $k_f/k_s = 3$, $Pe = 5$, $\phi_p = 5/9$

where y_ψ is the *center of gravity* of the effective coefficient ψ and corresponds to the particular location $(\psi)^{ex}(y_m) = 0$. Thus, Eqs. (4.101)-(4.103) can be rewritten as follow

$$T_m^{f,l}(x, y_m) - T_m^{f,p}(x, y_m) = -q_{cym}^{f(0)} \left(\frac{1}{K_{yy}^{f,l}} - \frac{1}{K_{yy}^{f,p}} \right) (y_m - y_{\frac{1}{K_{yy}^f}}) \quad (4.50)$$

$$q_{ym}^{f,l}(x, y_m) - q_{ym}^{f,p}(x, y_m) = \frac{\partial^2 T_m^{f(0)}}{\partial x^2} (K_{xx}^{f,l} - K_{xx}^{f,p}) (y_m - y_{K_{xx}^f}) - q_{cym}^{f(0)} \left(\frac{u_y^l}{K_{yy}^{f,l}} - \frac{u_y^p}{K_{yy}^{f,p}} \right) (y_m - y_{\frac{u_y}{K_{yy}^f}}) - (T_m^{f(0)} - T_m^{s(0)})_{aV} (h^l - h^p) (y_m - y_h) \quad (4.51)$$

$$q_{ym}^{s,p}(x, y_m) = -\frac{\partial^2 T_m^{s(0)}}{\partial x^2} (K_{xx}^{s,l} - K_{xx}^{s,p}) (y_m - y_{K_{xx}^s}) - q_{cym}^{f(0)} \left(\frac{u_y^l}{K_{yy}^{f,l}} - \frac{u_y^p}{K_{yy}^{f,p}} \right) (y_m - y_{\frac{u_y}{K_{yy}^f}}) - (T_m^{f(0)} - T_m^{s(0)})_{aV} (h^l - h^p) (y_m - y_h) - S_s (\phi_s^l - \phi_s^p) (y_m - y_{\psi_p}) \quad (4.52)$$

The jump relations at order 1 are similar to those obtained with the generic analysis (see Eqs. (4.35), (4.36) and (4.40)) and traduce the same transfer phenomena. However, the matched asymptotic expansion method allows to take out the terms $q_{cym}^{f(0)}$, $T_m^{i(0)}$ and $\frac{\partial^2 T_m^{i(0)}}{\partial x^2}$ of the exces values and to close the jump relations. Indeed they depend on intrinsic interfacial properties ($y_{\frac{1}{K_{yy}^f}}$, $y_{K_{xx}^f}$, $y_{K_{xx}^s}$, $y_{\frac{u_y}{K_{yy}^f}}$, y_h , y_{ϕ_s} see Tab. 4.1),

on the properties of the homogeneous media ($K_{yy}^{f,p}$, $K_{xx}^{f,p}$, $K_{xx}^{f,l}$, $K_{xx}^{s,p}$, h^p , u^p , ϕ_s^p) and on the interface location y_m . Therefore the jump relations at order 1 are easy to compute.

The solutions of the macroscopic model at order 1 for several interface locations are compared with the averaged microscopic solution in Fig. 4.8. Regarding the fluid macroscopic temperatures, its values in the homogeneous region are free of the interface location and match the averaged microscopic solution. Thanks to the first order correction, the energy between the macroscopic and mesoscopic model is conserved for any interface location. In addition, this result shows that the heat transfer between the solid phase and the fluid phase at the interface has been successfully modeled.

4.5.3 Illustration

Supported by the success of the previous results, we want to prospect the potency of the present up-scaling method on a heat transfer configuration closer to pratical cases existing in the industrial applications. The solid source is modified: a column of cubes is heating 20% higher than the others. The numerical simulation of reference is computed with a solid source such as (see Fig. 4.2(b))

$$S_s(x) = \begin{cases} 10, & \text{for } -0,5 < x < -0,2 \text{ and } -0,1 < x < 0,5 \\ 12, & \text{for } -0,2 < x < -0,1 \end{cases}$$

and the initial lateral boundary conditions for the temperature are replaced by condition of symmetry. The characteristic of the porous media are also conserved ($\phi_p = 5/9$, $k_s/k_f = 3$, $Pr = 1$, $Pe = 5$). The resulting fluid temperature field is represented in Fig. 4.10(a).

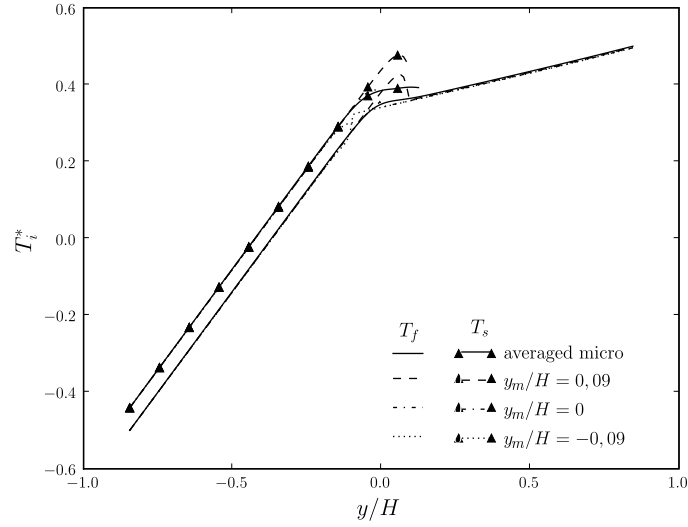


Figure 4.8: Macroscopic temperature at first order for $x = 0$
 $\left(T_i^* = [T_i - (\langle T_f \rangle^f(0; H^-) + \langle T_f \rangle^f(0; H^+))/2] / [\langle T \rangle^f(0; H^+) - \langle T_f \rangle^f(0; H^-)]\right)$.

It should be pointed out, that the transfer modeling realized through the multi-scale approach presented in the paper is still valid. As the characteristics of the porous medium in the homogeneous and transition regions have not changed, the effective transfer coefficients determined in the first up-scaling step (Section 4.4) can be used. Furthermore, the two-temperature equations and the boundary conditions at order 1 (see Eqs. (4.51)- (4.52)) do not depend on the value of the solid heat source and are thus still adapted. The resolution of this macroscopic model at order 1 for several interface location gives the fluid and solid temperature profiles presented in Fig. 4.9. In the porous region, the macroscopic temperatures match the averaged microscopic temperature of reference for the fluid and solid phases, that validates the values of the effective coefficients determined in Section 4.4. In the free region, the macroscopic fluid temperatures also match the averaged microscopic temperature of reference for different values of the interface location. This result shows the suitability of the boundary conditions that have been applied at the fluid/porous interface. Furthermore, it illustrates the asset of the modeling depending on intrinsic properties of the interface. Indeed, even if the heat transfer is different, a new modeling at the mesoscopic scale is not required. The qualitative macroscopic results in 2D are illustrated in Fig. 4.10(c).

4.6 Conclusion

This paper presents the question of the boundary conditions that must be applied at an interface between a heating porous medium and a free medium. The main difficulty of this study is to couple the two-temperature model in the homogeneous porous region with the one-temperature model in the free region. To proceed, a multi-scale approach based on three descriptions of the interface and two distinct up-scaling steps is used.

In the first up-scaling step, the heat transfer is modeled in the whole domain including the interface through a continuous description called mesoscopic. At this scale of description, the interface is diffuse and the information about the interface location is lost. A two-temperature model is derived applying the volume averaged method in the homogeneous porous region, and is extended to the interfacial zone. Then, to fully characterize the transfer, the effective properties are determined in the whole domain from microscopic simulations.

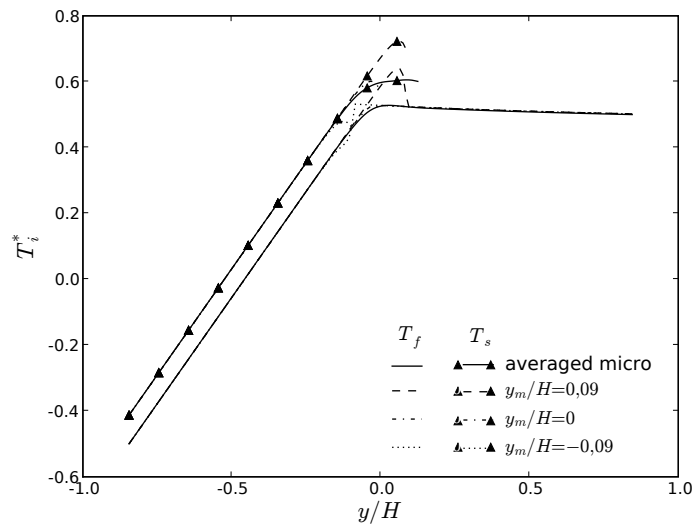


Figure 4.9: Macroscopic temperature at first order for $x = 0$
 $\left(T_i^* = [T_i - (\langle T_f \rangle^f(0; H^-) + \langle T_f \rangle^f(0; H^+))/2] / [\langle T_f \rangle^f(0; H^+) - \langle T_f \rangle^f(0; H^-)]\right)$.

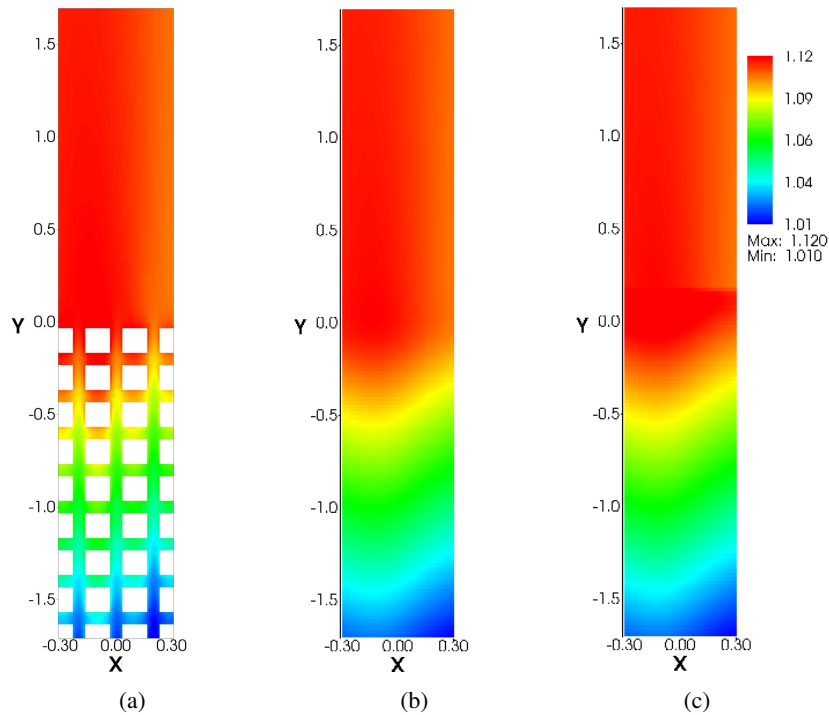


Figure 4.10: 2D fluid temperature field: (a) microscopic scale, (b) averaged microscopic solution, (c) macroscopic solution.

In the second up-scaling step, the continuous modeling of the transfer is replaced by a discontinuous one. At this new scale of description called macroscopic, the model is composed of a two-temperature model in the porous region and a one-temperature model in the free region separated by a surface of discontinuity where boundary condition must be applied. However the determination of appropriate

boundary conditions at the fluid/porous interface is complicated by the different number of equations used in each region. To proceed, one introduces a new equivalent writing of the modeling with an identical number of equations in both regions (see Fig.4.11). Thanks to this new formalism, two methods providing boundary conditions can be used. The first one is the generic analysis and gives three jump relations as boundary conditions at the fluid/interface: a temperature jump and a heat flux jump for the fluid phase and a heat flux condition for the solid phase. Although this method is able to characterize the transfer at the interface through surface excess quantities, the obtained relations involve unknown mesoscopic terms. The second method is the matched asymptotic expansion, that gives approximated solutions at different orders of the mesoscopic problem. Thus, boundary conditions at different orders can be derived such that the macroscopic description is equivalent to the mesoscopic one. At the order 1, the boundary conditions involve intrinsic properties of the interface, the properties of the homogeneous media and the interface location y_m . The associated model is closed and gives the correct macroscopic temperatures for the fluid and solid phases in the homogeneous regions. To end the study, the validity of the macroscopic model is illustrated on a different and more practical case of an overheating column of cubes.

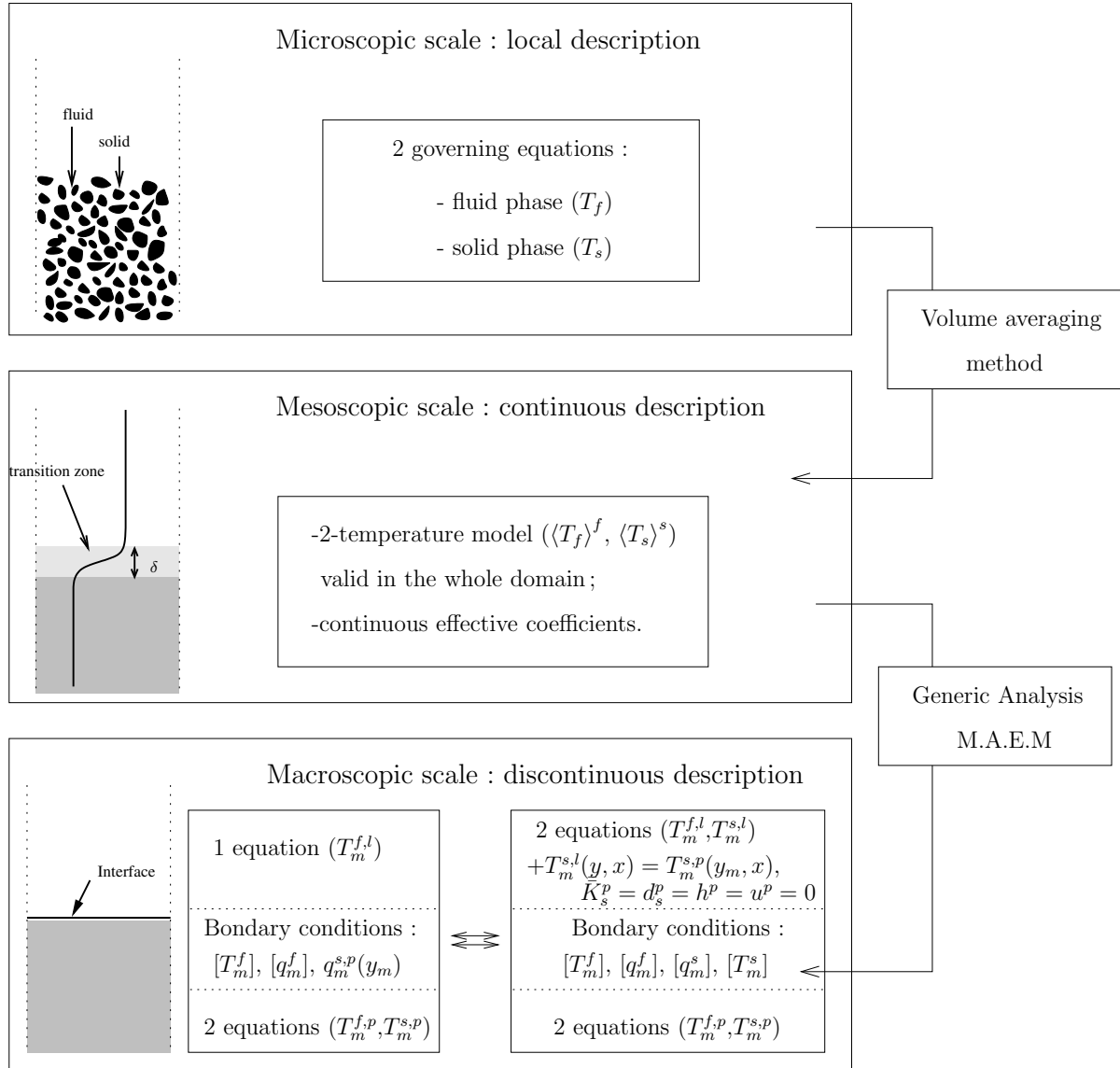


Figure 4.11: Two-upscaling method summarization with local thermal non-equilibrium (LTNE).

4.7 Appendix

4.7.1 Appendix A: Closed mesoscopic model

In this annexe, we recall how the two-temperature model is derived in the homogeneous porous medium. The developments are rather classical and can be found elsewhere ([Quintard and Whitaker, 1993](#); [Kaviany, 1995](#); [Carbonell and Whitaker, 1984](#)). They are recalled for completeness.

In the homogeneous porous medium, the averaged microscopic equations are
For the fluid

$$(\rho c_p)_f \nabla \cdot (\langle \mathbf{v}_f \rangle \langle T_f \rangle^f) = \nabla \cdot k_f \nabla \langle T_f \rangle + \nabla \cdot \frac{k_f}{V} \int_{A_{fs}} \mathbf{n}_{fs} \langle T_f \rangle^f dA + \nabla \cdot \frac{k_f}{V} \int_{A_{fs}} \mathbf{n}_{fs} \tilde{T}_f dA - \nabla \cdot (\rho c_p)_f \tau_{vT} + \frac{k_f}{V} \int_{A_{fs}} \mathbf{n}_{fs} \cdot \nabla T_f dA \quad (4.53)$$

where $\tau_{vT} = \langle T_f \mathbf{v}_f \rangle - \phi_f \langle T_f \rangle^f \langle \mathbf{v}_f \rangle^f$ is a dispersive flux.

For the solid

$$0 = \nabla \cdot k_s \nabla \langle T_s \rangle - \nabla \cdot \frac{k_s}{V} \int_{A_{fs}} \mathbf{n}_{fs} \langle T_f \rangle^f dA - \nabla \cdot \frac{k_s}{V} \int_{A_{fs}} \mathbf{n}_{fs} \tilde{T}_f dA - \frac{k_f}{V} \int_{A_{fs}} \mathbf{n}_{fs} \cdot \nabla T_f dA + \langle S_s \rangle \quad (4.54)$$

In the homogeneous porous region, via local theory provided by length-scale constraints ([Quintard and Whitaker, 1994](#)), the volume averaged temperature can be taken out of the area integral, that associated to the constant porosity leads to:

$$\frac{k_f}{V} \int_{A_{fs}} \mathbf{n}_{fs} \langle T_f \rangle^f dA \approx - \langle T_f \rangle^f \nabla \phi_f = 0 \quad (4.55)$$

Furthermore, using the Gray's decomposition for the temperature and the velocity in the dispersive flux τ_{vT} and the length-scale constraint consideration, this term becomes ([Kaviany, 1995](#)):

$$\tau_{vT} = \langle \tilde{T}_f \tilde{\mathbf{v}}_f \rangle \quad (4.56)$$

Thus, the averaged microscopic equations can be rewritten as follows:

For the fluid

$$(\rho c_p)_f \nabla \cdot (\langle \mathbf{v}_f \rangle \langle T_f \rangle^f) = \nabla \cdot \left(\phi_f k_f \nabla \langle T_f \rangle^f + \frac{k_f}{V} \int_{A_{fs}} \tilde{T}_f \mathbf{n}_{fs} dA - (\rho c_p)_f \langle \tilde{T}_f \tilde{\mathbf{v}}_f \rangle \right) + \frac{k_f}{V} \int_{A_{fs}} \nabla \tilde{T}_f \cdot \mathbf{n}_{fs} dA \quad (4.57)$$

For the solid

$$0 = \nabla \cdot \phi_s k_s \nabla \langle T_s \rangle^s - \nabla \cdot \frac{k_s}{V} \int_{A_{fs}} \tilde{T}_f \mathbf{n}_{fs} dA - \frac{k_f}{V} \int_{A_{fs}} \nabla \tilde{T}_f \cdot \mathbf{n}_{fs} dA + \langle S_s \rangle \quad (4.58)$$

To close the terms of tortuosity, dispersion and heat transfer, the representation of the spatial deviation temperature presented by ([Kaviany, 1995](#); [Quintard and Whitaker, 1993](#); [Carbonell and Whitaker, 1984](#)) is used

$$\tilde{T}_f = \mathbf{b}_{ff} \cdot \nabla \langle T_f \rangle^f + \mathbf{b}_{fs} \cdot \nabla \langle T_s \rangle^s - s_f (\langle T_f \rangle^f - \langle T_s \rangle^s) \quad (4.59)$$

where \mathbf{b}_{ff} , \mathbf{b}_{fs} and s_f are the vector and scalar fields mapping $\nabla \langle T_f \rangle^f$, $\nabla \langle T_s \rangle^s$ and $(\langle T_f \rangle^f - \langle T_s \rangle^s)$ onto \tilde{T}_f . Thus, under the hypothesis of scale separation, the surface integrals become

$$\begin{aligned} \frac{k_f}{V} \int_{A_{fs}} \mathbf{n}_{fs} \tilde{T}_f dA &= \nabla \langle T_f \rangle^f \cdot \frac{k_f}{V} \int_{A_{fs}} \mathbf{n}_{fs} \mathbf{b}_{ff} dA + \nabla \langle T_s \rangle^s \cdot \frac{k_f}{V} \int_{A_{fs}} \mathbf{n}_{fs} \mathbf{b}_{fs} dA \\ &- \left(\langle T_f \rangle^f - \langle T_s \rangle^s \right) \frac{k_f}{V} \int_{A_{fs}} \mathbf{n}_{fs} s_f dA \end{aligned} \quad (4.60)$$

$$\frac{k_f}{V} \int_{A_{fs}} \mathbf{n}_{fs} \cdot \nabla \tilde{T}_f dA = \mathbf{u}_{ff} \cdot \nabla \langle T_f \rangle^f + \mathbf{u}_{fs} \cdot \nabla \langle T_s \rangle^s - a_v h \left(\langle T_f \rangle^f - \langle T_s \rangle^s \right) \quad (4.61)$$

where $a_v h = \frac{k_f}{V} \int_{A_{fs}} \mathbf{n}_{fs} \cdot \nabla s_f dA$ and $\mathbf{u}_{ij} = \frac{k_f}{V} \int_{A_{fs}} \mathbf{n}_{ij} \cdot \nabla \mathbf{b}_{ij} dA$ are respectively heat transfer and transport coefficients.

Similarly, the term of dispersion takes the following shape

$$\langle \tilde{T}_f \tilde{\mathbf{v}}_f \rangle = \langle \mathbf{b}_{ff} \tilde{\mathbf{v}}_f \rangle \cdot \nabla \langle T_f \rangle^f + \langle \mathbf{b}_{fs} \tilde{\mathbf{v}}_f \rangle \cdot \nabla \langle T_s \rangle^s - \langle s_f \tilde{\mathbf{v}}_f \rangle \left(\langle T_f \rangle^f - \langle T_s \rangle^s \right) \quad (4.62)$$

From Eq. (4.60) and Eq. (4.62), one can introduce an additional transport coefficient

$$\mathbf{d}_f = (\rho c_p)_f \langle s_f \tilde{\mathbf{v}}_f \rangle - \frac{k_f}{V} \int_{A_{fs}} \mathbf{n}_{fs} s_f dA \quad (4.63)$$

The terms can be bring together to make appear the mean effective conductivity tensor and the coupled one

$$\bar{\bar{\mathbf{K}}}_{ff} = \phi_f k_f \bar{\mathbf{I}} + \frac{k_f}{V} \int_{A_{fs}} \mathbf{n}_{fs} \mathbf{b}_{ff} dA - (\rho c_p)_f \langle \mathbf{b}_{ff} \tilde{\mathbf{v}}_f \rangle \quad (4.64)$$

$$\bar{\bar{\mathbf{K}}}_{fs} = \frac{k_f}{V} \int_{A_{fs}} \mathbf{n}_{fs} \mathbf{b}_{fs} dA - (\rho c_p)_f \langle \mathbf{b}_{fs} \tilde{\mathbf{v}}_f \rangle \quad (4.65)$$

Therefore Eqs. (4.57) and (4.58) become

For the fluid

$$\begin{aligned} (\rho c_p)_f \langle \mathbf{v}_f \rangle \cdot \nabla \langle T_f \rangle^f - \mathbf{u}_{ff} \cdot \nabla \langle T_f \rangle^f - \mathbf{u}_{fs} \cdot \nabla \langle T_s \rangle^s &= \nabla \cdot \left(\bar{\bar{\mathbf{K}}}_{ff} \nabla \langle T_f \rangle^f + \bar{\bar{\mathbf{K}}}_{fs} \nabla \langle T_s \rangle^s + \right. \\ &\quad \left. \mathbf{d}_f (\langle T_f \rangle^f - \langle T_s \rangle^s) \right) - a_v h(y) \left(\langle T_f \rangle^f - \langle T_s \rangle^s \right) \end{aligned} \quad (4.66)$$

For the solid

$$\begin{aligned} \mathbf{u}_{ff} \cdot \nabla \langle T_f \rangle^f + \mathbf{u}_{fs} \cdot \nabla \langle T_s \rangle^s &= \nabla \cdot \left(\bar{\bar{\mathbf{K}}}_{sf} \nabla \langle T_f \rangle^f + \bar{\bar{\mathbf{K}}}_{ss} \nabla \langle T_s \rangle^s + \mathbf{d}_s (\langle T_f \rangle^f - \langle T_s \rangle^s) \right) \\ &\quad + a_v h(y) \left(\langle T_f \rangle^f - \langle T_s \rangle^s \right) + \langle S_s \rangle \end{aligned} \quad (4.67)$$

with $\mathbf{d}_s = \frac{k_s}{V} \int_{A_{fs}} \mathbf{n}_{fs} s_f dA$, $\bar{\bar{\mathbf{K}}}_{sf} = -\frac{k_s}{V} \int_{A_{fs}} \mathbf{n}_{fs} \mathbf{b}_{ff} dA$ and $\bar{\bar{\mathbf{K}}}_{ss} = \phi_s k_s \bar{\mathbf{I}} - \frac{k_s}{V} \int_{A_{fs}} \mathbf{n}_{fs} \mathbf{b}_{fs} dA$

4.7.2 Appendix B: The method of the matched asymptotic expansion

For a heating porous medium followed by a free medium in the case of the local thermal non equilibrium (LTNE), the heat transfer in the whole domain is well modeled by the two-temperature equations

(see Eqs. (4.19) and (4.20))

$$(\rho c_p)_f \langle \mathbf{v}_f \rangle \cdot \nabla \langle T_f \rangle^f - \mathbf{u}(\mathbf{x}) \cdot \nabla \langle T_f \rangle^f = \nabla \cdot \left(\overline{\overline{\mathbf{K}_f}}(\mathbf{x}) \nabla \langle T_f \rangle^f + \mathbf{d}_f(\mathbf{x}) (\langle T_f \rangle^f - \langle T_s \rangle^s) \right) - a_V h(\mathbf{x}) \left(\langle T_f \rangle^f - \langle T_s \rangle^s \right) \quad (4.68)$$

$$\mathbf{u}(\mathbf{x}) \cdot \nabla \langle T_f \rangle^f = \nabla \cdot \left(\overline{\overline{\mathbf{K}_s}}(\mathbf{x}) \nabla \langle T_s \rangle^s + \mathbf{d}_s(\mathbf{x}) (\langle T_f \rangle^f - \langle T_s \rangle^s) \right) + a_V h(\mathbf{x}) \left(\langle T_f \rangle^f - \langle T_s \rangle^s \right) + \langle S_s \rangle \quad (4.69)$$

The method of the matched asymptotic expansion consists in breaking up the domain in three parts: an inside region where the effective coefficients strongly vary and two outside regions where they are constant. Furthermore, the effective coefficients depend on ε in the interfacial transition zone where $\varepsilon = \delta/L$, δ being the size of the inside region and L the length of the domain. In the outside regions, the macroscopic temperatures solution of Eqs. (4.68) and (4.69) take the shape of asymptotic expansions in ε

$$T_m^{i,l}(x, y) = T_m^{i,l(0)}(x, y) + \varepsilon T_m^{i,l(1)}(x, y) + \mathcal{O}(\varepsilon^2), \quad \text{in the fluid region} \quad (4.70)$$

$$T_m^{i,p}(x, y) = T_m^{i,p(0)}(x, y) + \varepsilon T_m^{i,p(1)}(x, y) + \mathcal{O}(\varepsilon^2), \quad \text{in the porous region} \quad (4.71)$$

the index i being f or s for the fluid and the solid phases respectively.

In the inside region, the effective coefficients strongly vary. Thus, a new variable $\bar{y} = (y - y_m)/\varepsilon$ is introduced to make the coefficients go slower and to be able to perform the expansion. With this change of variable, the expression of the temperature in the inside region becomes:

$$\hat{T}^i(x, \hat{y}) = \hat{T}^{i,(0)}(x, \hat{y}) + \varepsilon \hat{T}^{i,(1)}(x, \hat{y}) + \mathcal{O}(\varepsilon^2) \quad (4.72)$$

and $\hat{K}_{xx}^i(\hat{y})$, $\hat{K}_{yy}^i(\hat{y})$, $\hat{u}_y(\hat{y})$, $\hat{d}_y^i(\hat{y})$ and $\hat{h}(\hat{y})$ do not depend on ε .

In the outside regions, the interface is located at the boundary y_m^+ for the free medium and y_m^- for the porous medium. From the inside region standpoint, the free and porous homogeneous regions are placed at $\hat{y} = \pm\infty$. To obtain a solution in the whole domain, a tie must be made between the inside and the outside regions. This tie is given by the matching conditions (Zwillinger, 1989). At zeroth and first orders, they can be written for any physical term ψ

$$\lim_{\hat{y} \rightarrow \pm\infty} \hat{\psi}^{(0)}(x, \hat{y}) = \lim_{y \rightarrow \pm y_m} \psi_m^{(0)}(x, y) \quad (4.73)$$

$$\lim_{\hat{y} \rightarrow \pm\infty} \left[\hat{\psi}^{(1)}(x, \hat{y}) - \hat{y} \lim_{y \rightarrow \pm y_m} \frac{\partial \psi_m^{(0)}(x, y)}{\partial y} \right] = \lim_{y \rightarrow \pm y_m} \psi_m^{(1)}(x, y) \quad (4.74)$$

At the mesoscopic scale, the averaged equations are valid in the whole domain and similar for the fluid and the solid phases. At the macroscopic scale, we use the two-equation/two-equation formalism (see section 3.). Thus, the developments are identical for the fluid and solid phases. In the following, only the analytical developments for the fluid phase will be explicated.

Jump relation for the temperature

The temperature jump is determined from the resolution of the conductive flux equation in the y -direction

$$\langle q_{cf} \rangle^f = -K_{yy}^f \frac{\partial \langle T_f \rangle^f}{\partial y} \quad (4.75)$$

Introducing the asymptotic expansion in Eq. (4.75), a system of equation at 0 and 1 order in ε is written : Outside problems,

$$q_{cym}^{f,i(0)} = -K_{yy}^{f,i} \frac{\partial T_m^{f,i(0)}}{\partial y} \quad (4.76)$$

$$q_{cym}^{f,i(1)} = -K_{yy}^{f,i} \frac{\partial T_m^{f,i(1)}}{\partial y} \quad (4.77)$$

with $i = p$ in the porous region and $i = l$ in the free region.

Inside problem,

$$0 = -K_{yy}^f \frac{\partial \hat{T}^{f(0)}}{\partial \hat{y}} \quad (4.78)$$

$$\hat{q}_{cy}^{f(0)} = -\hat{K}_{yy}^f \frac{\partial \hat{T}^{f(1)}}{\partial \hat{y}} \quad (4.79)$$

At order 0, Eq. (4.78) is integrated using the fact that \hat{K}_{yy}^f is not null. The matching condition (4.73) at inside/outside boundaries leads to the continuity of the temperature at the interface

$$T_m^{f,l(0)}(x, y_m) = T_m^{f,p(0)}(x, y_m) \quad (4.80)$$

At order 1, the temperature jump is obtained by integrating Eq. (4.79) on $[0; +\infty]$ with the appropriate macroscopic term on each side of the equality

$$\int_0^{+\infty} \frac{\partial}{\partial \hat{y}} \left[\hat{T}^{f(1)} - \hat{y} \lim_{y \rightarrow +\infty} \frac{\partial T_m^{f,l(0)}}{\partial y}(x, y) \right] d\hat{y} = - \int_0^{+\infty} \left[\hat{q}_{cy}^{f(0)} \frac{1}{\hat{K}_{yy}^f} + \lim_{y \rightarrow +\infty} \frac{\partial T_m^{f,l(0)}}{\partial y}(x, y) \right] d\hat{y} \quad (4.81)$$

Using the boundary y_m of Eq. (4.78), the matching condition (4.74) for the temperature and the change of variable $\hat{y} = (y - y_m)/\varepsilon$, Eq. (4.81) can be rewritten as

$$T_m^{f,l(1)}(x, y_m) - \hat{T}^{f(1)}(x, y_m) = -\frac{1}{\varepsilon} q_{cym}^{f,l(0)} \int_{y_m}^{+\infty} \left[\frac{1}{K_{yy}^f(y)} - \frac{1}{K_{yy}^{f,l}} \right] dy \quad (4.82)$$

A similar relation can be obtained on $[-\infty; 0]$. Added to Eq. (4.82) it gives the jump relation for the temperature at order 1 which implies an excess value

$$T_m^{f,l(1)}(x, y_m) - T_m^{f,p(1)}(x, y_m) = -\frac{1}{\varepsilon} \left(\frac{1}{K_{yy}^f} \right)^{ex} q_{cym}^{f(0)}(x, y_m) \quad (4.83)$$

Regarding a possible jump for the solid temperature, the question is not relevant due to the chosen assumption that the solid temperature is arbitrarily defined in the free region using continuity.

Jump relations for the total heat flux

The jump for the fluid total heat flux is determined from the resolution of the energy equation

$$\nabla \cdot \langle q_f \rangle^f = -a_V h (\langle T_f \rangle^f - \langle T_s \rangle^s) + \mathbf{u} \cdot \nabla \langle T_f \rangle^f \quad (4.84)$$

where $\langle q_f \rangle^f = (\rho c_p)_f \langle v_y \rangle \langle T_f \rangle^f - K_{yy}^f \partial \langle T_f \rangle^f / \partial y + d_y^f (\langle T_f \rangle^f - \langle T_s \rangle^s)$.

Introducing the asymptotic expansion and the change of variable in the inside region, the system of equations at 0 and 1 order in ε can be written as:

Outside problem,

$$\frac{\partial q_{xm}^{f,i(0)}}{\partial x} + \frac{\partial q_{ym}^{f,i(0)}}{\partial \hat{y}} = -a_V h^i (T_m^{f,i(0)} - T_m^{s,i(0)}) + u_y^i \frac{\partial T_m^{f,i(0)}}{\partial \hat{y}} \quad (4.85)$$

$$\frac{\partial q_{xm}^{f,i(1)}}{\partial x} + \frac{\partial q_{ym}^{f,i(1)}}{\partial \hat{y}} = -a_V h^i (T_m^{f,i(1)} - T_m^{s,i(1)}) + u_y^i \frac{\partial T_m^{f,i(1)}}{\partial \hat{y}} \quad (4.86)$$

with $i = p$ in the porous region and $i = l$ in the free region.

Inside problem,

$$\frac{\partial \hat{q}_y^{f(0)}}{\partial y} = \hat{u}_y \frac{\partial \hat{T}^{f(0)}}{\partial y} \quad (4.87)$$

$$\frac{\partial \hat{q}_x^{f(0)}}{\partial x} + \frac{\partial \hat{q}_y^{f(1)}}{\partial y} = -a_V \hat{h} (\hat{T}^{f(0)} - \hat{T}^{s(0)}) + \hat{u}_y \frac{\partial \hat{T}^{f(1)}}{\partial y} \quad (4.88)$$

At order 0, Eqs. (4.87) and (4.78) and the matching condition (4.73) give the continuity of the total heat flux at the interface

$$q_{ym}^{f,l(0)}(x, y_m) = q_{ym}^{f,p(0)}(x, y_m) \quad (4.89)$$

At order 1, the development is identical as the one for the temperature jump. Thus, by integrating Eq. (4.88) on $[0; +\infty]$ one obtains

$$\begin{aligned} q_{ym}^{f,l(1)}(x, y_m) - \hat{q}_y^{f(1)}(x, 0) &= \frac{1}{\varepsilon} \frac{\partial^2 T_m^{f(0)}}{\partial x^2}(x, y_m) \int_{y_m}^{+\infty} (K_{xx}^f(y) - K_{xx}^{f,l}) dy \\ &- \frac{1}{\varepsilon} (T_m^{f,l(0)} - T_m^{s,l(0)})(x, y_m) \int_{y_m}^{+\infty} a_V (h(y) - h^l) dy + \frac{1}{\varepsilon} \int_{y_m}^{+\infty} \left(u_y(y) \frac{\partial \hat{T}^{f(1)}}{\partial \hat{y}} - u_y^l \frac{\partial T_m^{f,l(0)}}{\partial y} \right) dy \end{aligned} \quad (4.90)$$

Then, using Eqs. (4.79) and (4.76) and $\hat{q}_{cy}^{f(0)}(\hat{y}) = q_{cym}^{f,l(0)}(y_m)$ in Eq. (4.90), one can write

$$\begin{aligned} q_{ym}^{f,l(1)}(x, y_m) - \hat{q}_y^{f(1)}(x, 0) &= \frac{1}{\varepsilon} \frac{\partial^2 T_m^{f(0)}}{\partial x^2}(x, y_m) \int_{y_m}^{+\infty} (K_{xx}^f(y) - K_{xx}^{f,l}) dy \\ &- \frac{1}{\varepsilon} (T_m^{f,l(0)} - T_m^{s,l(0)})(x, y_m) \int_{y_m}^{+\infty} a_V (h(y) - h^l) dy - \frac{1}{\varepsilon} q_{cym}^{f,l(0)} \int_{y_m}^{+\infty} \left(\frac{u_y(y)}{K_{yy}^f(y)} - \frac{u_y^l}{K_{yy}^{f,l}} \right) dy \end{aligned} \quad (4.91)$$

Finally, the jump condition for the total fluid heat flux at 1 order is

$$\begin{aligned} q_{ym}^{f,l(1)}(x, y_m) - q_{ym}^{f,p(1)}(x, y_m) &= \frac{1}{\varepsilon} (K_{xx}^f(y))^{ex} \frac{\partial^2 T_m^{f(0)}}{\partial x^2}(x, y_m) \\ &- \frac{1}{\varepsilon} a_V (h(y))^{ex} (T_m^{f(0)} - T_m^{s(0)})(x, y_m) - \frac{1}{\varepsilon} \left(\frac{u_y}{K_{yy}^f} \right)^{ex} q_{cym}^{f(0)}(x, y_m) \end{aligned} \quad (4.92)$$

For the solid phase, similar developments lead to

$$q_{ym}^{s,l(0)}(x, y_m) = q_{ym}^{s,p(0)}(x, y_m) \quad (4.93)$$

$$\begin{aligned} q_{ym}^{s,l(1)}(x, y_m) - q_{ym}^{s,p(1)}(x, y_m) &= (K_{xx}^s(y))^{ex} \frac{1}{\varepsilon} \frac{\partial^2 T_m^{s(0)}}{\partial x^2}(x, y_m) + a_V (h(y))^{ex} \frac{1}{\varepsilon} (T_m^{f(0)} - T_m^{s(0)})(x, y_m) \\ &+ \left(\frac{u_y}{K_{yy}^f} \right)^{ex} q_{cym}^{f(0)}(x, y_m) + (\langle S_s \rangle)^{ex} \end{aligned} \quad (4.94)$$

Summary

The two-equation/1-equation formalism is recovered using the chosen assumption of no solid heat flux in the y -direction for the free region. Thus, the jump relations becomes

At zeroth order

$$T_m^{f,l(0)}(x, y_m) - T_m^{f,p(0)}(x, y_m) = 0 \quad (4.95)$$

$$q_{ym}^{f,l(0)}(x, y_m) - q_{ym}^{f,p(0)}(x, y_m) = 0 \quad (4.96)$$

$$q_{ym}^{s,p(0)}(x, y_m) = 0 \quad (4.97)$$

At first order

$$T_m^{f,l}(x, y_m) - T_m^{f,p}(x, y_m) = - \left(\frac{1}{K_{yy}^f(y)} \right)^{ex} q_{cym}^{f(0)}(x, y_m) \quad (4.98)$$

$$\begin{aligned} q_{ym}^{f,l}(x, y_m) - q_{ym}^{f,p}(x, y_m) = & \left(K_{xx}^f(y) \right)^{ex} \frac{\partial^2 T_m^{f(0)}}{\partial x^2}(x, y_m) - a_V (h(y))^{ex} (T_m^{f(0)} - T_m^{s(0)})(x, y_m) \\ & - \left(\frac{u_y(y)}{K_{yy}^f(y)} \right)^{ex} q_{cym}^{f(0)}(x, y_m) \end{aligned} \quad (4.99)$$

$$\begin{aligned} q_{ym}^{s,p}(x, y_m) = & - (K_{xx}^s(y))^{ex} \frac{\partial^2 T_m^{s(0)}}{\partial x^2}(x, y_m) - a_V (h(y))^{ex} (T_m^{f(0)} - T_m^{s(0)})(x, y_m) \\ & - \left(\frac{u_y(y)}{K_{yy}^f(y)} \right)^{ex} q_{cym}^{f(0)}(x, y_m) - (\phi_s(y))^{ex} S_s \end{aligned} \quad (4.100)$$

4.8 Apparent interface

In this section, we look for the essential information presented in the introduction of the chapter: the heat flux conservation at the free-porous interface and the error done with a modeling using boundary conditions of continuity for a chosen interface location. In order to proceed, we consider the macroscopic model at order 1 obtained with method of the matched asymptotic expansions and we follow developments similar to those performed in Section 3.6.

The macroscopic model is closed with jump conditions at order 1 at the free-porous interface. These jump conditions at order 1 are:

$$T_m^{f,l}(x, y_m) - T_m^{f,p}(x, y_m) = - \left(\frac{1}{K_{yy}^f(y)} \right)^{ex} q_{cym}^{f(0)}(x, y_m) \quad (4.101)$$

$$q_{ym}^{f,l}(x, y_m) - q_{ym}^{f,p}(x, y_m) = \left(K_{xx}^f(y) \right)^{ex} \frac{\partial^2 T_m^{f(0)}}{\partial x^2}(x, y_m) - a_V (h(y))^{ex} (T_m^{f(0)} - T_m^{s(0)})(x, y_m) \\ - \left(\frac{u_y(y)}{K_{yy}^f(y)} \right)^{ex} q_{cym}^{f(0)}(x, y_m) \quad (4.102)$$

$$q_{ym}^{s,p}(x, y_m) = - (K_{xx}^s(y))^{ex} \frac{\partial^2 T_m^{s(0)}}{\partial x^2}(x, y_m) - a_V (h(y))^{ex} (T_m^{f(0)} - T_m^{s(0)})(x, y_m) \\ - \left(\frac{u_y(y)}{K_{yy}^f(y)} \right)^{ex} q_{cym}^{f(0)}(x, y_m) - (\langle S_s \rangle)^{ex} \quad (4.103)$$

Due to zeroth order macroscopic terms involved in these jump conditions, the macroscopic temperature at first order is obtained in two steps. First, the macroscopic model at zeroth order is solved to determine the coefficients $q_{cym}^{f(0)}$, $\partial^2 T_m^{f(0)} / \partial x^2$, $\partial^2 T_m^{s(0)} / \partial x^2$ and $(T_m^{f(0)} - T_m^{s(0)})$. Then, the macroscopic model at order 1 can be solved. This two-step resolution gives the correct temperatures in the homogeneous regions whatever the interface location as shown in Section 4.5.2. However, it requires two numerical resolutions and the determination of the effective coefficients in the transition zone. For these reasons, we look for an alternative and simpler approach to this two-step resolution.

4.8.1 Determination of an apparent interface

A first idea to simplify the two-step resolution is to investigate the approach of [Duman and Shavit \(2009\)](#) presented in the previous chapter. It consists in looking for the apparent interface y_m defined as the interface location where the boundary conditions of continuity are sufficient.

$$T_m^{f,l}(x, y_m) - T_m^{f,p}(x, y_m) = 0 \quad (4.104)$$

$$q_{ym}^{f,l}(x, y_m) - q_{ym}^{f,p}(x, y_m) = 0 \quad (4.105)$$

$$q_{ym}^{s,p}(x, y_m) = 0 \quad (4.106)$$

The apparent interface corresponds to the interface location where the correction term $T_m^{f(1)}(x, y)$ has no contribution in the homogeneous regions, thus $\lim_{y \rightarrow \pm\infty} T_m^{f(1)}(x, y) = 0$.

We notice that a condition for the solid phase such that $\lim_{y \rightarrow \pm\infty} T_s^{f(1)}(x, y) = 0$ does not give information about the interface location. In the free region, the solid phase is not defined, while the condition in the porous region is always verified whatever the interface location, as we will see in the following.

The velocity field is $1D$ and the geometry of the porous matrix at the free-porous interface is periodic in

the x -direction. Since the apparent interface location y_m is characteristic of the porous matrix and the flow, it should not depend of x . This result has been verified in the case of local thermal equilibrium. Due to the similarity between the one-temperature and two-temperature models for the direction dependency, we assume that y_m is also independent of x for the two-temperature model. Thus, for the sake of simplification, we use $T_m^{f(1)}$ invariant in the x -direction to determine the apparent interface location y_m . In the free region ($[y_m; +\infty[$), $T_m^{f(1)}$ verifies the following equation:

$$(\rho c_p)_f v_{my} \frac{\partial T_m^{f(1)}}{\partial y} = K_{yy}^{f,l} \frac{\partial^2 T_m^{f(1)}}{\partial y^2} \quad (4.107)$$

considering only the solutions with a finite value at the limits $\pm\infty$, one can write:

$$T_m^{f(1),l}(y) = \frac{A}{(\rho c_p)_f v_{my}}, \text{ where } A \text{ is an unknown} \quad (4.108)$$

In the homogeneous porous region ($]-\infty; y_m[$), $T_m^{f(1)}$ and $T_m^{s(1)}$ verify the following coupled system:

$$\begin{cases} (\rho c_p)_f v_{my} \frac{\partial T_m^{f(1)}}{\partial y} - u_y^p \frac{\partial T_m^{f(1)}}{\partial y} = K_{yy}^{f,p} \frac{\partial^2 T_m^{f(1)}}{\partial y^2} + d_y^{f,p} \frac{\partial}{\partial y} (T_m^{f(1)} - T_m^{s(1)}) - h^p (T_m^{f(1)} - T_m^{s(1)}) \\ u_y^p \frac{\partial T_m^{f(1)}}{\partial y} = K_{yy}^{s,p} \frac{\partial^2 T_m^{s(1)}}{\partial y^2} + d_y^{s,p} \frac{\partial}{\partial y} (T_m^{f(1)} - T_m^{s(1)}) + h^p (T_m^{f(1)} - T_m^{s(1)}) \end{cases} \quad (4.109)$$

The solution of the system (4.109) has the following form:

$$\begin{cases} T_m^{f(1),p} = \sum_{i=1}^3 B_i \exp(R_i y) \\ T_m^{s(1),p} = \sum_{i=1}^3 B'_i \exp(R_i y) \end{cases} \quad (4.110)$$

where B_i and B'_i are unknowns and the R_i are solutions of the following cubic equation:

$$K_{yy}^{f,p} K_{yy}^{s,p} R^3 + \left[K_{yy}^{s,p} d_y^{f,p} - K_{yy}^{f,p} d_y^{s,p} - (\rho c_p)_f v_{my} - u_y \right] R^2 + \left[d_y^{s,p} [(\rho c_p)_f v_{my} - u_y] - d_y^{f,p} u_y - h(K_{yy}^{s,p} + K_{yy}^{f,p}) \right] R + (\rho c_p)_f v_{my} h = 0 \quad (4.111)$$

In our case, the roots of the cubic function are:

$$R_1 = R_2 = a, \quad R_3 = -b, \text{ where } [a, b] \in \mathbb{R}^+ \quad (4.112)$$

which leads to the following temperature fields solution of the system (4.109):

$$\begin{cases} T_m^{f(1),p} = B_1 e^{ay} + B_2 e^{-by} \\ T_m^{s(1),p} = B_3 e^{ay} + B_4 e^{-by} \end{cases} \quad (4.113)$$

where B_i are unknowns that must be determined.

Considering only the convergent temperature fields on ($]-\infty; y_m[$), we have:

$$B_4 = B_2 = 0 \quad (4.114)$$

Introducing the temperature fields in the system (4.109), one obtains the following condition:

$$B_3 = \frac{K_{yy}^{f,p} a + d_y^{f,p} + d_y^{s,p} - (\rho c_p)_f v_{my}}{-K_{yy}^{s,p} a + d_y^{f,p} + d_y^{s,p}} B_1 \quad (4.115)$$

Thus, the temperature fields solution of the system (4.109) have the following form:

$$\begin{cases} T_m^{f(1),p} = B_1 \exp(ay) \\ T_m^{s(1),p} = B_1 \frac{K_{yy}^{f,p} a + d_y^{f,p} + d_y^{s,p} - (\rho c_p) f v_{my}}{-K_{yy}^{s,p} a + d_y^{f,p} + d_y^{s,p}} \exp(ay) \end{cases} \quad (4.116)$$

Using the jump conditions at the interface (4.102) and (4.103), the three unknowns are related by the relations:

$$[q_m^f]^{(1)}(y_m) = A - B_1 \exp(ay_m) \Psi_1 \quad (4.117)$$

$$-q_{ym}^{s,p}(y_m) = -B_1 \exp(ay_m) \Psi_2 \quad (4.118)$$

with

$$\Psi_1 = -a K_{yy}^{f,p} - d_y^f + (\rho c_p) f v_{my} + d_y^f \frac{K_{yy}^{f,p} a + d_y^{f,p} + d_y^{s,p} - (\rho c_p) f v_{my}}{-K_{yy}^{s,p} a + d_y^{f,p} + d_y^{s,p}} \quad (4.119)$$

$$\Psi_2 = -d_y^s + (d_y^s - a K_{yy}^{s,p}) \frac{K_{yy}^{f,p} a + d_y^{f,p} + d_y^{s,p} - (\rho c_p) f v_{my}}{-K_{yy}^{s,p} a + d_y^{f,p} + d_y^{s,p}} = -\Psi_1 \quad (4.120)$$

The unknown B_1 is given by the relation (4.118) and A is obtained adding the relations (4.117) and (4.118), which leads to:

$$A = \left(K_{xx}^f(y) \right)^{ex} \frac{\partial^2 T_m^{f(0)}}{\partial x^2}(x, y_m) + (K_{xx}^s(y))^{ex} \frac{\partial^2 T_m^{s(0)}}{\partial x^2}(x, y_m) + (\langle S_s \rangle)^{ex} \quad (4.121)$$

$$B_1 = \Psi_2 \exp(-ay_m) \left[- (K_{xx}^s(y))^{ex} \frac{\partial^2 T_m^{s(0)}}{\partial x^2}(x, y_m) - a_V (h(y))^{ex} (T_m^{f(0)} - T_m^{s(0)})(x, y_m) - \left(\frac{u_y(y)}{K_{yy}^f(y)} \right)^{ex} q_{cym}^{f(0)}(x, y_m) - (\langle S_s \rangle)^{ex} \right] \quad (4.122)$$

Thus, introducing the relations (4.121) and (4.122) in the equations of the first order temperature $T_m^{f(1)}$ in the homogeneous porous (4.116) and free regions (4.108), one obtains:

In the free region ($[y_m; +\infty[$)

$$T_m^{f(1)} = \left(K_{xx}^f(y) \right)^{ex} \frac{\partial^2 T_m^{f(0)}}{\partial x^2}(x, y_m) + (K_{xx}^s(y))^{ex} \frac{\partial^2 T_m^{s(0)}}{\partial x^2}(x, y_m) + (\langle S_s \rangle)^{ex} \quad (4.123)$$

In the homogeneous porous region ($] -\infty; y_m)$)

$$T_m^{f(1)} = \Psi_2 \left[- (K_{xx}^s(y))^{ex} \frac{\partial^2 T_m^{s(0)}}{\partial x^2}(x, y_m) - a_V (h(y))^{ex} (T_m^{f(0)} - T_m^{s(0)})(x, y_m) - \left(\frac{u_y(y)}{K_{yy}^f(y)} \right)^{ex} q_{cym}^{f(0)}(x, y_m) - (\langle S_s \rangle)^{ex} \right] \exp(a(y - y_m)) \quad (4.124)$$

a depending of the boundary conditions.

Now, to determine the apparent interface y_m , one looks for the particular correction term $T_m^{f(1)}$ that verifies $\lim_{y \rightarrow \pm\infty} T_m^{f(1)} = 0$. In the homogeneous porous region, this condition is verified for any interface location because of the exponential decay. In the free region, this condition leads to:

$$\left(K_{xx}^f(y) \right)^{ex} \frac{\partial^2 T_m^{f(0)}}{\partial x^2}(x, y_m) + (K_{xx}^s(y))^{ex} \frac{\partial^2 T_m^{s(0)}}{\partial x^2}(x, y_m) + (\langle S_s \rangle)^{ex} = 0 \quad (4.125)$$

This relation must be compared to the one obtained for model at local thermal equilibrium:

$$(K_{xx}(y))^{ex} \frac{\partial^2 T_m^{(0)}}{\partial x^2}(x, y_m) = 0 \quad (4.126)$$

We conclude that the relation (4.125) is coherent. It involves transverse heat flux as for the one-temperature model and the additional volume heat source.

For heat transfer with transverse heat flux and a volume heat source of same order-of-magnitude, the analytical determination of the apparent interface cannot be done. Indeed, its location depends of zeroth order terms $\frac{\partial^2 T_m^{f(0)}}{\partial x^2}(x, y_m)$ and $\frac{\partial^2 T_m^{s(0)}}{\partial x^2}(x, y_m)$ (see (4.125)) and thus, requires iterative methods using the jump conditions. In this context, the apparent interface location is not a characteristic of the porous medium and the approach proposed by [Duman and Shavit \(2009\)](#) is not appropriate.

For heat transfer without S_s , the apparent interface location can be determined if the center of gravity of the surface excess quantities of $K_{xx}^f(y)$ and $K_{xx}^s(y)$ are close to each other. In this case, the apparent interface location y_m is given by:

$$y_m = y_{K_{xx}^f} = y_{K_{xx}^s} \quad (4.127)$$

For heat transfer with transverse heat flux null or negligible, the relation (4.125) reduces to:

$$(\langle S_s \rangle)^{ex} = 0 \quad (4.128)$$

and the apparent interface location is $y_m = y_{S_s}$. In the following, we illustrate this result on three examples of heat transfers with S_s only.

4.8.2 Heat transfer driven by a heat source in the solid

In this example, we study heat transfer with a volume heat source in the solid matrix and without transverse heat flux. In this case, the apparent interface is located at the center of gravity of the surface excess $(\langle S_s \rangle)^{ex}$, thus $y_m = y_{S_s}$. To illustrate this point, we consider a rough interface as presented in Fig. 4.12. For such a geometry, the center of gravity y_{S_s} is separated from the nominal interface y_{nom} , which is the tangent plane to the last grain (this notion has been presented in Section 3.6.2). In our case, we have $y_{nom}/H = 0.28$, while the center of gravity of the volume source is located at $y_{S_s}/H = 0.09$.

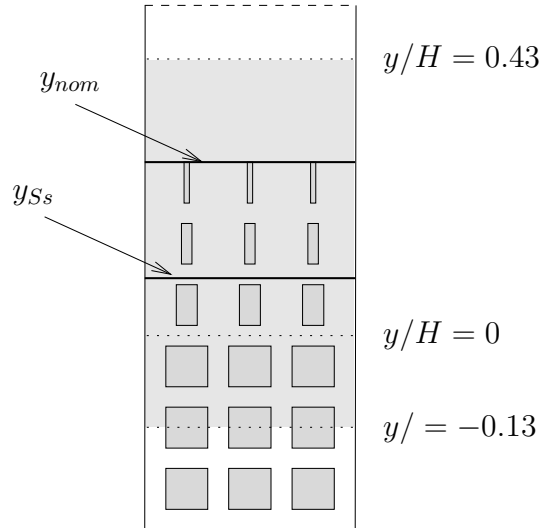


Figure 4.12: Geometry of the interface

The macroscopic temperatures are computed with boundary conditions of continuity for two interface locations: y_{nom} and y_{S_s} . The resulting profiles are compared with the averaged microscopic solutions in

Fig. 4.13. The correct temperature profile in the free region is recovered when the interface is located at $y_m = y_{S_s}$. If the interface is located at the nominal interface, the corresponding macroscopic profile exhibits a large difference with the profile of reference.

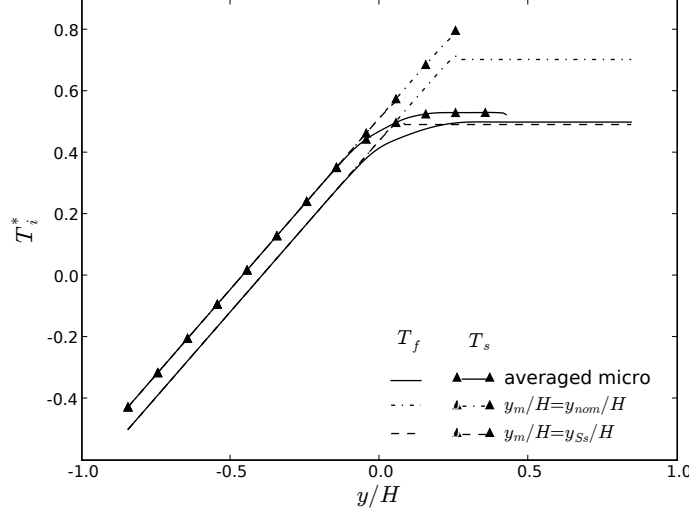


Figure 4.13: Macroscopic temperature at zeroth order for $x = 0$ ($T_i^* = [T_i - (\langle T_f \rangle^f(0; H^-) + \langle T_f \rangle^f(0; H^+))/2] / [\langle T_f \rangle^f(0; H^+) - \langle T_f \rangle^f(0; H^-)]$).

This heat transfer configuration shows the importance of the interface location when boundary conditions of continuity are used to couple the macroscopic models at the free-porous interface. These boundary conditions are valid only for a peculiar position of the interface and only if there is no lateral flux.

4.8.3 Variable heat source

Until now, the studied averaged temperature gradients were constant and the values of the effective conductivity tensor had no effect on the model. The issue of this example is to validate the effective conductivity tensors via non-constant averaged temperature gradients. Thus, we consider a volume source $S_s(y)$ varying in the solid matrix with a flat interface; the heat source variation considered corresponds to the heat distribution in a reactor core at steady state. The different scales of description are presented in Fig. 4.14. To characterize the heat transfer, we use the macroscopic model with boundary conditions of continuity at the interface $y_m = y_{S_s}$.

At the microscopic scale, the distribution of the heat source in the solid corresponds to

$$S_s(y) = \begin{cases} 6.9 & \text{for } -2 < y < -1.8 \text{ and } -0.2 < y < 0 \\ 9.6 & \text{for } -1.8 < y < -1.6 \text{ and } -0.4 < y < -0.2 \\ 12.3 & \text{for } -1.6 < y < -1.4 \text{ and } -0.6 < y < -0.4 \\ 14.8 & \text{for } -1.4 < y < -1.2 \text{ and } -0.8 < y < -0.6 \\ 16 & \text{for } -1.2 < y < -0.8 \\ 0 & \text{for } y > 0 \end{cases}$$

At the macroscopic scale, the heat source distribution corresponds to:

$$S_m(y) = \begin{cases} 2.6 \cos(2.4(y + 1)) + 4.5, & \text{in the homogeneous porous region} \\ 0, & \text{in the free region} \end{cases}$$

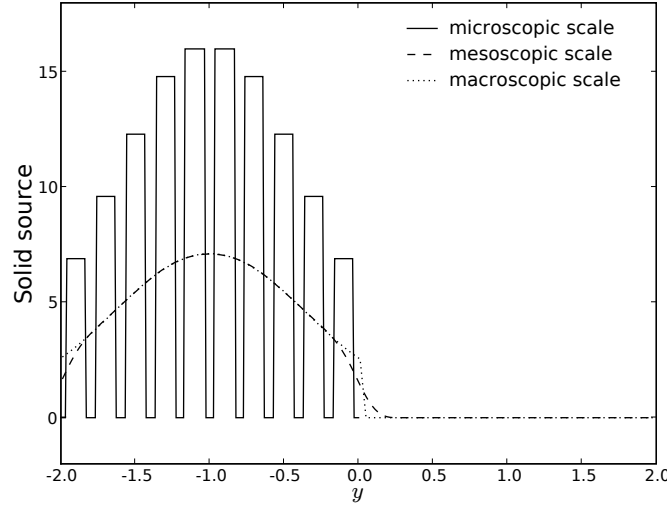


Figure 4.14: Solid heat source for the different scales of description

At the mesoscopic scale, $\langle S_s \rangle$ corresponds to the macroscopic source S_m in the homogeneous regions and differs in the transition zone where the values vary continuously. Since the volume source depends on y , the center of gravity y_{S_s} differs from the one computed in Section 4.5.2. In the present case, the center of gravity is given by the following relation:

$$\int_{H^-}^{y_{S_s}} (\langle S_s \rangle(y) - S_m(y)) dy = \int_{y_{S_s}}^{H^+} (\langle S_s \rangle(y) - S_m(y)) dy \quad (4.129)$$

leading to $y_{S_s}/H = -0.009$.

The macroscopic temperatures are computed with boundary conditions of continuity for three different interface locations: the boundaries of the transition zone $y_m/H = \pm 0.13$, and the center of gravity y_{S_s}/H . The resulting profiles are compared with the averaged microscopic solutions in Fig. 4.15. In the homogeneous porous region, due to the non constant temperature gradients, the good agreement between the macroscopic profiles and the temperatures of reference validates the computation of the effective coefficients in the y -direction. In the free region, the macroscopic profiles of the fluid phase depend on the interface location. For interfaces located at the boundaries of the transition zone, the profiles do not correspond to the temperature of reference. Conversely, if the interface is located at the center of gravity of the solid source, the macroscopic temperature fits the temperature of reference.

From the previous work, we can compute the error done, when the boundary conditions of continuity are applied at the wrong location. This information is directly given by the order 1 temperature $T_m^{f(1)}$ in the free region (see the relation (4.123)). When there is no transverse heat flux, the relation (4.123) reduces to

$$T_m^{f(1)}(y_m) = S_m^p(y_{S_s} - y_m) \quad (4.130)$$

where y_m is the interface location that can be chosen anywhere in the transition zone and $S_m^p = S_m^p(H + y_m)$ because S_m^p is not constant. In the case studied the maximum error is obtained for $y_m/H = -0.13$; which is one of the limit of the transition zone. Thus the error is:

$$error = 0.12 \quad (4.131)$$

Compared to the variation of the fluid temperature in the whole domain, this error is 12%.

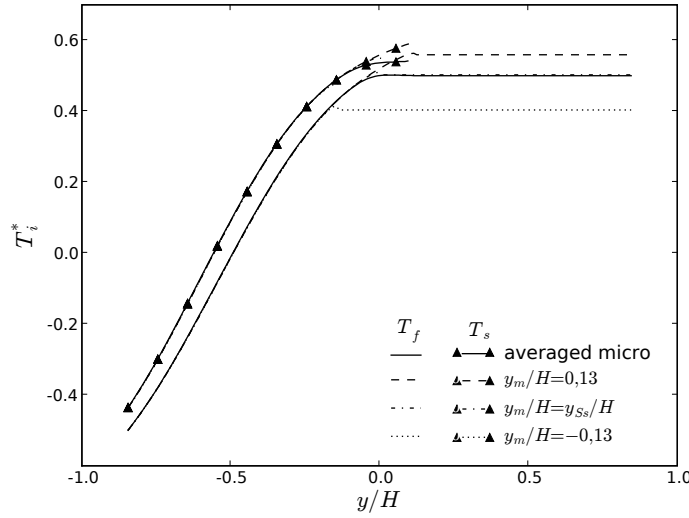


Figure 4.15: Macroscopic temperature at first order for $x = 0$
 $\left(T_i^* = [T_i - (\langle T_f \rangle^f(0; H^-) + \langle T_f \rangle^f(0; H^+))/2] / [\langle T_f \rangle^f(0; H^+) - \langle T_f \rangle^f(0; H^-)]\right)$.

4.8.4 Industrial nuclear codes

In the industrial nuclear codes, the conductive or dispersive phenomena are often neglected and only the fluid-solid heat transfer is computed. Such modelings would take the following form:

- In the homogeneous porous region

$$(\rho c_p)_f v_{my} \frac{\partial T_m^{f(1)}}{\partial y} - u_y^p \frac{\partial T_m^{f(1)}}{\partial y} = -h^p (T_m^{f(1)} - T_m^{s(1)}) \quad (4.132)$$

$$u_y^p \frac{\partial T_m^{f(1)}}{\partial y} = h^p (T_m^{f(1)} - T_m^{s(1)}) \quad (4.133)$$

- In the free region

$$(\rho c_p)_f v_{my} \frac{\partial T_m^{f(1)}}{\partial y} = 0 \quad (4.134)$$

- At the free-porous interface: boundary conditions of continuity at the nominal interface

$$y_{\text{nom}}/H = -0.016 \quad (4.135)$$

The solutions of this macroscopic model are compared to the averaged microscopic temperatures in Fig. 4.16. In the homogeneous porous regions, the macroscopic profiles do not correspond to the temperatures of reference. The difference between the fluid and the solid temperatures is recovered, but not the temperature gradients. In the free region, for the interface located at the nominal interface, the profiles do not correspond to the temperature of reference.

The error associated to this modeling is 4%, compared to variation of the fluid temperature in the whole domain. The approximation done for the heat transfer model in the homogeneous porous medium partly recapture the error created by the choice of a wrong interface location. At last, this error is small and one can conclude that the simplification made by the industrial models are relevant. However, what are

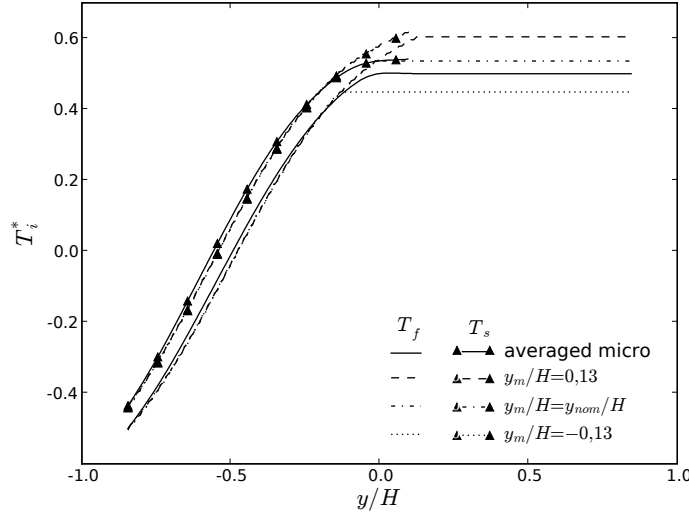


Figure 4.16: Macroscopic temperature at first order for $x = 0$
 $\left(T_i^* = [T_i - (\langle T_f \rangle^f(0; H^-) + \langle T_f \rangle^f(0; H^+))/2] / [\langle T_f \rangle^f(0; H^+) - \langle T_f \rangle^f(0; H^-)]\right)$.

the possibilities to reduce it? The determination of the center of gravity of the volume solid source is not a good choice, because for a flat interface, y_{S_s} is close to the nominal interface. Thus, the remaining solution is to consider the conductivity and the dispersive phenomena.

In this section, we have studied the heat transfer modeling at a free-porous interface.

For heat transfer dominated by a volume source in the porous matrix, the macroscopic modeling can be simplified. Instead of using jump conditions at the interface, the condition of continuity applied at the center of gravity of the solid source is enough to obtain accurate temperature values in homogeneous regions.

For the other cases of local thermal non-equilibrium, no simplification is available and only the macroscopic model at order 1 is able to characterize correctly the heat transfer at a free-porous interface.

4.9 Conclusion

This chapter presents a heat transfer problem at local thermal non-equilibrium in a free-porous domain. The issue is to determine appropriate boundary conditions in order to model the heat transfer at the free-porous interface. We use the multi-scale method, based on three levels of description of the interface and two distinct up-scaling steps, presented in Chapter 2 for heat transfer at local thermal equilibrium. The results are summarized in Tab. 4.2.

In the first up-scaling step, we change the scale of description from microscopic to mesoscopic with the volume averaging method. Applying the spatial smoothing with a representative elementary volume constant in the whole domain, we obtain a diffuse interface between the porous and free regions. To characterize the heat transfer, we determine a two-temperature model valid in the whole domain with effective coefficients constant in the homogeneous regions and varying continuously in the transition zone.

In the second up-scaling step, we change the scale of description from mesoscopic to macroscopic with methods using conservation principles. The issue is to gain computational time substituting the transi-

tion zone by a surface of discontinuity with jump boundary conditions. The most appropriate method to model diffuse interfaces is the method of the matched asymptotic expansion that gives approximate solutions at different orders of the mesoscopic problem. We obtain solutions at order 0 that verify boundary conditions of continuity at the interface. These solutions do not capture the overall transfer and depend on the interface location. Then, increasing the order of resolution, we determine solutions at order 1 verifying boundary conditions with excess quantities at the porous-free interface. These excess quantities involve intrinsic properties of the interface, properties of the homogeneous medium and the interface location y_m . Thus, we have characterized the interface and obtained a very good approximation of the mesoscopic temperature of reference whatever the interface location.

Furthermore, the macroscopic model at order 1 gives the two essential informations that we are looking for: the heat flux conservation at the free-porous interface and the error done with a modeling using boundary conditions of continuity for a chosen interface location. Thus, in order to verify the total heat flux conservation, we show that the transverse conduction and the volume solid source must be considered. These terms are also present in the evaluation of the error. In particular, for thermal configurations where the volume solid source dominates on the transverse conduction, the error is given by the excess value of the volume solid source, thus:

$$error(y_m) = (\langle S_s \rangle)^{ex} = S_m^p (y_{S_s} - y_m) \quad (4.136)$$

For high velocity, the model structure does not change and only the effective transfer coefficient are modified. The form of the boundary conditions and the relation giving the apparent interface are unchanged. Thus, similar conclusions will be applied.

In the following chapter, we present a direct numerical simulation (DNS) of turbulent heat transfer realized on the configuration chosen in (Breugem and Boersma, 2005; Breugem et al., 2005) to study turbulent flows at a fluid-porous interface. The DNS solves directly the Navier-Stokes equations and the conductive convective equations without the need of any closure model. Thus, these results are used in Chapter 5 as solutions of reference to validate the macroscopic turbulent models.

At the microscopic scale

$$(\rho c_p)_f \nabla \cdot (\mathbf{v}_f T_f) = -\nabla \cdot (k_f \nabla T_f) \text{ , for the fluid phase} \quad (4.137a)$$

$$0 = -\nabla \cdot (k_s \nabla T_s) + S_s \text{ , for the solid phase} \quad (4.137b)$$

At the mesoscopic scale

$$(\rho c_p)_f \langle \mathbf{v}_f \rangle \cdot \nabla \langle T_f \rangle^f - \mathbf{u}(\mathbf{x}) \cdot \nabla \langle T_f \rangle^f = \nabla \cdot \left(\bar{\bar{\mathbf{K}}}_f(\mathbf{x}) \nabla \langle T_f \rangle^f + \mathbf{d}_f(\mathbf{x}) (\langle T_f \rangle^f - \langle T_s \rangle^s) \right) - a_V h(\mathbf{x}) \left(\langle T_f \rangle^f - \langle T_s \rangle^s \right) \quad (4.137c)$$

$$\mathbf{u}(\mathbf{x}) \cdot \nabla \langle T_f \rangle^f = \nabla \cdot \left(\bar{\bar{\mathbf{K}}}_s(\mathbf{x}) \nabla \langle T_s \rangle^s + \mathbf{d}_s(\mathbf{x}) (\langle T_f \rangle^f - \langle T_s \rangle^s) \right) + a_V h(\mathbf{x}) \left(\langle T_f \rangle^f - \langle T_s \rangle^s \right) + \langle S_s \rangle \quad (4.137d)$$

At the macroscopic scale

In the porous region ($H^- < y < y_m$)

$$(\rho c_p)_f \mathbf{v}_m \cdot \nabla T_m^{f,p} - \mathbf{u}^p \cdot \nabla T_m^{f,p} = \nabla \cdot \left(\bar{\bar{\mathbf{K}}}_f^p \cdot \nabla T_m^{f,p} + \mathbf{d}_f^p (T_m^{f,p} - T_m^{s,p}) \right) - a_V h^p (T_m^{f,p} - T_m^{s,p}) \quad (4.137e)$$

$$\mathbf{u}^p \cdot \nabla T_m^{f,p} = \nabla \cdot \left(\bar{\bar{\mathbf{K}}}_s^p \cdot \nabla T_m^{s,p} \right) + a_V h^p (T_m^{f,p} - T_m^{s,p}) + \phi_s^p S_s \quad (4.137f)$$

In the free region ($y_m < y < H^+$)

$$(\rho c_p)_f \mathbf{v}_m \cdot \nabla T_m^{f,l} = \nabla \cdot \left(k_f \bar{\mathbf{I}} \cdot \nabla T_m^{f,l} \right) \quad (4.137g)$$

At the porous-free interface y_m

$$[T_m^f] = - \left(\frac{1}{K_{yy}^f} \right)^{ex} q_{cym}^{f(0)} \quad (4.137h)$$

$$[q_{ym}^f] = \left(K_{xx}^f(y) \right)^{ex} \frac{\partial^2 T_m^{f(0)}}{\partial x^2} - a_V (h)^{ex} (T_m^{f(0)} - T_m^{s(0)}) - \left(\frac{u_y}{K_{yy}^f} \right)^{ex} q_{cym}^{f(0)} \quad (4.137i)$$

$$q_{ym}^{s,p} = - (K_{xx}^s)^{ex} \frac{\partial^2 T_m^{s(0)}}{\partial x^2} - a_V (h)^{ex} (T_m^{f(0)} - T_m^{s(0)}) - \left(\frac{u_y}{K_{yy}^f} \right)^{ex} q_{cym}^{f(0)} - (\langle S_s \rangle)^{ex} \quad (4.137j)$$

The correction term in the free region is:

$$T_m^{f(1)} = \left(K_{xx}^f \right)^{ex} \frac{\partial^2 T_m^{f(0)}}{\partial x^2} + (K_{xx}^s)^{ex} \frac{\partial^2 T_m^{s(0)}}{\partial x^2} + (\langle S_s \rangle)^{ex} \quad (4.137k)$$

Table 4.2: Synthesis of models used for the different scales of description.

Chapter 5

Direct numerical simulation of a turbulent heat flow in a partially porous domain

In Chapters 2 and 3, we have studied jump conditions that must be applied at a free-porous interface for laminar heat transfers. However as presented in the introduction, heat transfer in a nuclear reactor is turbulent and its computation requires the use of turbulence modeling RANS-type combined to the porous description in the fuel zone. The modeling commonly used is the turbulent Prandtl model in free regions and the macroscopic turbulent Prandtl model in homogeneous porous regions. However, are these models valid at a free-porous interface? The issue of this chapter is to answer this question via a direct numerical simulation of a turbulent heat transfer problem in a three-dimensional domain partially filled with a porous medium.

5.1 Introduction

In practical applications, various turbulence models are used in software for computational fluid dynamics and heat transfer. However the turbulence is a complex phenomenon and the direct numerical simulation constitutes an important research tool to analyze and model the turbulent flows. The advances in large-scale computers during the last decade has allowed a better understanding of the turbulence for increasingly complex geometries. In this context, [Breugem and Boersma \(2005\)](#) study a turbulent flow over permeable walls. To validate a method of turbulence computation, they perform a DNS considered as a simulation of reference. This DNS gives the flow field in a channel over a porous medium constituted of a three-dimensional grid of cubes. For turbulent heat transfer, studies have been realized for flows in channel or in porous media as we will see in the following. However, to our knowledge, no result exists in a free-porous domain. Thus, using the geometry proposed by [Breugem and Boersma \(2005\)](#), we investigate the effect of such a configuration on the turbulent heat transfer through a new direct numerical simulation. With this DNS we obtain valuable information of the turbulence that develops in such a configuration. In order to understand the issues related to the study of turbulent heat transfer at a free-porous interface, we present the main mechanisms of the turbulence and the results existing for turbulent heat flows in channel and homogeneous porous media only.

The physics of the turbulence

Turbulence is a flow regime characterized by the appearance of unsteady vortices in a viscous fluid on many scales that interact with each other. It is a diffusive-dissipative mechanism continuously transferring the energy between the different scales from the larger eddies to the smaller ones. This energy cascade described by Kolmogorov is governed by three main phenomena:

- the production, that corresponds to the energy injected by the main flow;

- the inner redistribution of the turbulent agitation between the structures of decreasing sizes, which length scales are closed to each other;
- the dissipation at the scale of the smallest eddies.

The length scale of the smallest structures η can be determined using the Kolmogorov's first hypothesis that fixes the limiting condition of existence to the balance between the inertial and viscous forces. With dimensional considerations, it can be expressed as a function of the fluid viscosity ν_f and the dissipation rate ϵ computed from the largest eddies:

$$\eta = \left(\frac{\nu_f^3}{\epsilon} \right)^{1/4} = L Re_t^{-3/4} \quad (5.1)$$

where L and Re_t are the length scale and the Reynolds number of the largest turbulent structures.

Another property of the turbulence is its highly irregular nature. This is why turbulence problems are mostly treated statistically rather than deterministically.

Furthermore, turbulence is characterized by the generation of three-dimensional vortices. This mechanism corresponds to vortex stretching, which is essential to the process of the turbulence energy cascade.

Turbulent heat transfer in channel flows

Numerous direct numerical simulations have been provided for turbulent heat transfer in channel flows. The issue of these studies is to investigate the effects of the wall boundary conditions and the Prandtl and friction Reynolds numbers on the thermal boundary layer.

First DNS simulations are done by [Kim and Moin \(1989\)](#) for a Reynolds number $Re_\tau = 180$ and Prandtl numbers $Pr = 0.1, 0.71$ and 2.0 using isothermal boundary conditions at walls. They confirm the observed features of turbulent heat transfers such as the high correlation between the streamwise velocity and temperature fluctuations and the existence of thermal streaky structures. However, an isothermal boundary condition corresponds to the physical configuration where a fluid with a negligible density, heat capacity and thermal conductivity is heated by a thick wall with high density, high heat capacity and high thermal conductivity ($\alpha_f/\alpha_s \rightarrow 0$). Such a boundary condition is uncommon in practical heat transfer applications, thus for a more realistic heating condition, [Kasagi et al. \(1992\)](#) perform similar computation with isoflux walls. Despite the difference in the thermal boundary conditions they obtain thermal turbulence statistics close to those of [Kim and Moin \(1989\)](#). This result can be explained by the underestimation of the wall temperature fluctuations. To overcome this weakness, [Tiselj et al. \(2001a\)](#) couple the turbulent heat transfer and the unsteady conduction in solid wall. Thus, they obtain accurate predictions and show the influence of thermal boundary conditions on the thermal boundary layer.

At the same time, several researchers have directed their studies to higher Reynolds and Prandtl numbers. Thus, [Kawamura et al. \(1999\)](#) and [Abe et al. \(2004\)](#) perform DNS for Re_τ up to 1020 with $Pr = 0.025$ to 0.71 . [Na et al. \(1999\)](#) and [Tiselj et al. \(2001a\)](#) simulate turbulent channel flows for low $Re_\tau = 150$ and moderate Prandtl numbers $Pr = 0.71$ to 10 . These studies show the very weak influence of the friction Reynolds number on the turbulent heat transfer statistics, while the effect of Prandtl number is noteworthy. Furthermore, attention must be paid to the numerical accuracy and the spatial resolution must verified the Batchelor length scale η_0 as $\eta_0 = \eta Pr^{-1/2}$. Thus, increasing Pr requires finer spatial resolution and bigger amount of mesh cell number ([Tennekes and Lumley, 1972](#); [Kozuka et al., 2009](#)).

Turbulent flow in a porous medium

To our knowledge, no direct numerical simulation exists for porous media. However, an important modeling work has been done in the context of RANS simulations. As presented in the introduction, the turbulent transfers in porous media are studied using two distinct average operators: a time averaging operator to be independent from the turbulence irregularity and the volume averaging operator to replace the fluid and solid phase by an equivalent porous medium (see Chapter 1). In order to study the DNS and

to compare the results with those of the literature, we apply these filters. The two averages are applied one after another and the question of the application order arises. Pedras and de Lemos (2000) show that from a mathematical point of view, the order of averagings of the two operators (time averaging and volume averaging) leads to similar twice-averaged equations for the mean flow. A similar conclusion is obtained by Rocamora and de Lemos (2000) for the mean temperature. The problem of the order of application appears at the modeling step to close the twice-averaged equations and to obtain a closed macroscopic description. At this step, the order of application has an important impact on the modeling of the physical phenomena. Antohe and Lage (1997) and Getachew et al. (2000) apply the volume averaging operator first, perform a first modeling then apply the time averaging operator. Using the spatial averaging operator first implies that only the length scale larger than the representative elementary volume can be considered. However the turbulence structures larger than the REV are rapidly destroyed by the solid matrix, which constrains the eddy size to the pore size. Thus the validity of this approach is not accurate. On the contrary, Nakayama and Kuwahara (1999), de Lemos and Pedras (2001b), Nield (2001), Breugem and Boersma (2005), Chandesris et al. (2006), Pinson et al. (2006) choose to perform the volume averaging on the time averaged equations. In the remainder of the study, we follow Chandesris et al. (2006) and perform the time averaging process first.

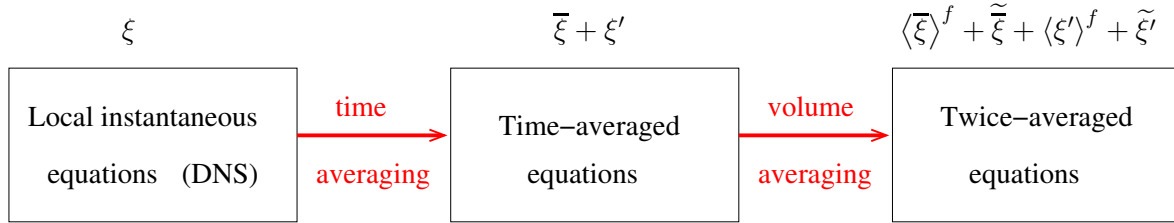


Figure 5.1: Description of the chosen averaging process.

This Chapter presents the direct numerical simulation of turbulent heat transfer in a domain with a free-porous interface. Section 5.2 describes the geometry, the boundary conditions and the numerical procedures. Section 5.3 expresses the fundamental equations and develops the two averaging processes (time and volume averaging) leading to the twice-averaged equations for the flow and the heat transfer. Section 5.4 presents the low-order turbulent statistics and the characteristic of the turbulent structures. We recall that each presented quantity is twice-averaged.

5.2 Problem description and numerical method

5.2.1 Geometry

We consider a turbulent flow in a domain partially filled with a model porous medium. As illustrated in Fig. 5.2, the mean flow is in the x -direction and is thus tangential to the fluid-porous interface. The domain dimension is $3H \times 2H \times 2H$ respectively in the direction parallel to the flow (x -direction), perpendicular to the flow (z -direction) and perpendicular to walls (y -direction). The porous medium is composed of arranged lines of $30 \times 20 \times 9 = 5400$ cubes with a porosity $\phi_p = 0.875$. The cube size is $d_p = H/20$ and the distance between cubes is $d_f = d_p$.

We consider two different regions: a free fluid or channel region between $y = 0$ and $y = H$ and a porous region between $y = -H$ and $y = 0$. The channel height H is defined following Breugem and Boersma (2005). It relies on the porosity profile and corresponds to the distance between the top wall and the plan $y = 0$ where the porosity starts to vary (see Fig. 5.3). We note δ the channel half width.

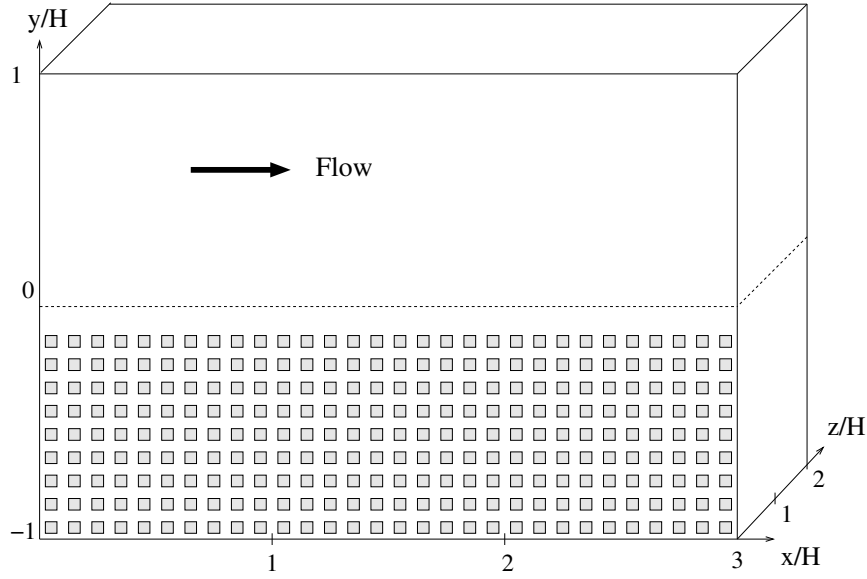


Figure 5.2: Three-dimensional geometry.

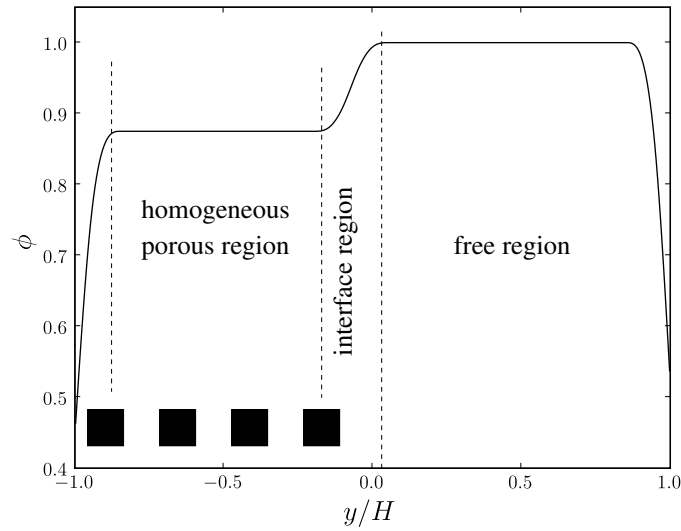


Figure 5.3: Porosity profile in the y -direction of the three-dimensional geometry (from Breugem (2005)).

5.2.2 Boundary conditions

The domain is limited by solid walls at $y = H$ and $y = -H$, and the inlet and outlet are located at $x = 0$ and $x = 3H$ respectively.

For the Navier-Stokes equations, boundary conditions of periodicity are imposed at the domain inlet and outlet. At the upper- and lower-walls boundary conditions of no-slip velocity are fixed.

For the heat transfer, the boundary conditions at the domain inlet and outlet depend of the heating configuration considered, the issue being to represent an infinite channel with an establish heat transfer. If there is no injected heat flux (flux null and constant temperature fixed at walls), one can use classical boundary conditions of periodicity on a finite channel. If heat flux is injected in the system with constant fluxes imposed at walls or at the cubes, the temperature cannot verify the boundary condition of periodicity

because its averaged value constantly increases in the flow direction. In order to represent an infinite channel with established heat transfer conditions using a finite channel, we introduce a new variable θ (Kawamura et al., 2000):

$$\theta = T - \frac{\Delta T}{L}x \quad (5.2)$$

where ΔT is the temperature increase on the domain of length L and is obtained performing an energy balance on the domain that gives (see Appendix A):

$$A = \frac{\Delta T}{L} = \frac{(q^b - q^h)L + \int_{A_{fs}} q dS}{(\rho c_p)_f L \int_{-H}^H \bar{u}(0; y) dy} \quad (5.3)$$

where q is the heat flux at the lower wall for q^b and at the upper wall for q^h . Such a change of variable makes appear an additional term in the energy equation such that (see Appendix A):

$$(\rho c_p)_f \nabla \cdot (\mathbf{v}\theta) + (\rho c_p)_f u A = \nabla \cdot (k_f \nabla \theta) \quad (5.4)$$

where u is the velocity in the flow direction. We notice that T and θ satisfy identical boundary conditions for the heat flux at the upper and lower walls. However, θ satisfies boundary conditions of periodicity at the domain inlet and outlet, and additional boundary conditions at cubes walls in the flow direction (see Appendix A).

Concerning the walls and the cubes, we consider three different heating configurations.

- Case 1: the cubes surfaces are adiabatic and a constant temperature is fixed at the top and bottom walls ($T(y = H) > T(y = -H)$). With this choice, classical boundary conditions of periodicity for the temperature are used and there is no need to subtract the averaged flux. This configuration allows the validation of the results at the solid wall by comparing with DNS computation in free channels.
- Case 2: the cubes surfaces are adiabatic and a constant incoming heat flux is fixed at the top and bottom walls. Since a heat flux is injected in the system, one must perform the change of variable θ and consider the source term $\Delta T/L$ (see equation 5.2). This configuration also allows the validation of the results at the solid wall by comparing with DNS computation in free channels.
- Case 3: the walls are adiabatic and an incoming heat flux is fixed at the cubes. As previously, due to the injected heat flux, the change of variable is performed. This configuration get closer to heat transfers existing in industrial cases, for which the solid heats.

In the following, the results for Cases 2 and 3 will be presented with the quantities θ_0 and θ_1 . The boundary conditions are summarized in Tab. 5.1.

inlet and outlet	Periodic (z -direction) Non-slip (y -direction) Periodic or Pseudo-periodic (x -direction)
Case 1	$T(-H) = 0; T(+H) = 1; q_w(\text{cubes}) = 0$
Case 2	$q_w(-H) = 1; q_w(+H) = 1; q_w(\text{cubes}) = 0$
Case 3	$q_w(-H) = 0; q_w(+H) = 0; q_w(\text{cubes}) = 1$

Table 5.1: Computational condition.

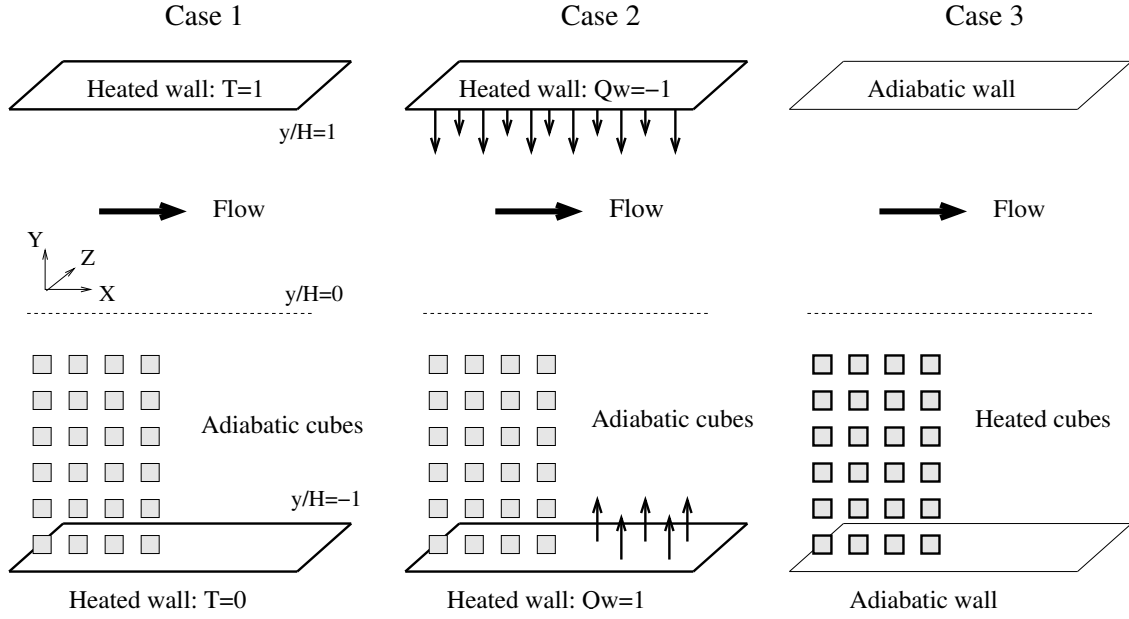


Figure 5.4: Boundary conditions.

5.2.3 Study parameters

For the Navier-Stokes equations, the bulk Reynolds number is fixed at $Re_b = U_b H / \nu = 5500$ to compare our results with those results of Breugem and Boersma (2005). The initial condition for the velocity is a perturbed in the y - and z -directions parabolic profile corresponding to the bulk velocity $1.084U_b$ in the free region and a velocity null in the porous region. The factor 1.084 is obtained from the results of Breugem and Boersma (2005) and corresponds to the ratio between the total bulk velocity in the whole domain and the bulk velocity through the surface $y > 0$. This initial profile imposes a similar total bulk as Breugem and Boersma (2005), once the bulk is distributed between the porous and free regions.

For the heat transfer, the choice of the Prandtl number has been dictated partially by the convergence time of the computation. The convergence time is a limiting factor of the DNS. For this configuration, it corresponds to the time scale of the conductive phenomenon in the y -direction ($(\rho c_p)_f (2H)^2 / k_f$) and can be reduced by increasing k_f . Since the Prandtl number is related to k_f via $Pr = \mu c_p / k_f$, the convergence time imposes the value of the Prandtl number. For this study, we choose the Prandtl number $Pr = 0.1$. Thus, this Prandtl number combined with the Reynolds number gives the Peclet number $Pe^p = Re^p Pr = 1$ in the porous region and $Pe^l = 550$ in the free region.

5.2.4 Numerical method

The governing equations are discretized on a Cartesian mesh constituted of $96 \cdot 10^6$ cells, which size is $H/200$ (see Tab. 5.2). The meshing is identical in the whole domain, nevertheless in the porous region, the interior of the cubes is not discretized. For Prandtl number $Pr > 1$, the spatial resolution is imposed by the temperature and must verify the Batchelor length scale η_0 , which is estimated as $\eta_0 = \eta Pr^{-1/2}$ where η is the Kolmogorov length scale. For heat transfer with Prandtl numbers $Pr < 1$, the spatial resolution is imposed by the velocity, which is the studied case. Thus, we keep the same spatial resolution as the one used by Breugem and Boersma (2005).

For the time advancement, the third-order Runge-Kutta scheme is applied. It has the advantage to be precise and stable. The time increment is $7.6 \cdot 10^{-3} H / U_b$. The momentum convection is computed with a centered spatial discretization scheme, while the heat convection is performed with a non-centered

Reynolds number	$Re_\tau = 390$
Prandtl number	$Pr = 0.1$
Computational volume (x,y,z)	$6\delta \times 4\delta \times 4\delta$
Computational volume (x^+,y^+,z^+)	$1170 \times 780 \times 780$
Spatial resolution $(\Delta x^+, \Delta y^+, \Delta z^+)$	$2 \times 2 \times 2$
Grid numbers	$600 \times 400 \times 400$

Table 5.2: Spatial resolution.

spatial discretization scheme *quick*. The computational conditions are summarized in Tab. 5.3. The time integration is repeated for about $3527 H/U_b$ until the thermal field is judged to be fully developed and then the computation is further continued about $5523 H/U_b$ to obtain the necessary statistics. The number of instantaneous data fields used for the statistics is equal to 3000, spanning on a total time interval of $1996 H/U_b$. The data sampling is started when the statistics variations (velocity, temperature and variance) are observed to be in a steady state. However, there are very low frequency variation on these time histories although their amplitudes are very small. Thus, the statistically steady state is judged with some arbitrariness.

For the computation, we use the Trio_U software which is a Computational Fluid Dynamics code developed by the CEA. The DNS is computed on the JADE computer from the *Centre informatique National de l'Enseignement Supérieur* CINES. The cluster SGI Altix ICE 8200, JADE, is a parallel scalar super-computer with a power of 147 Tflops/s. For more information, we recommend the CINES's website: www.cines.fr.

For one time step advancement, $3.26s$ CPU time is required. The present DNS has been computed on 500 processors (velocity, pressure and temperature).

Mesh	Staggered mesh
Time advancement	third-order Runge-Kutta
Momentum convection	second-ordered central scheme
Heat convection	non-central <i>quick</i> scheme
inlet and outlet	Periodic (z -direction) Non-slip (y -direction) Periodic or Pseudo-periodic (x -direction)

Table 5.3: Computational method.

5.3 Governing equations

In this section, we present the formalism used to analyze the numerical results. The local and instantaneous equations are time-averaged, then volume-averaged. Thus, twice-averaged equations are obtained that are characteristic of turbulent transfers in porous media.

5.3.1 General equations

Navier-Stokes and conductive-convective equations

The flow is incompressible and its thermodynamical properties are assumed constant. The Navier-Stokes

and energy equations governing the flow are:

$$\frac{\partial u_i}{\partial x_i} = 0 \quad (5.5)$$

$$\frac{\partial u_i}{\partial t} + \frac{\partial u_i u_j}{\partial x_j} = -\frac{1}{\rho} \frac{\partial p}{\partial x_i} + \nu \frac{\partial^2 u_i}{\partial x_j^2} \quad (5.6)$$

$$\frac{\partial T}{\partial t} + \frac{\partial u_j T}{\partial x_j} = \frac{\partial}{\partial x_j} \left(\alpha \frac{\partial T}{\partial x_j} \right) \quad (5.7)$$

where α is the thermal diffusivity of the fluid phase.

Statistical averaging

To handle the turbulent characteristics of the flow, the Navier-Stokes equations are statistically averaged. The statistical averaging is defined by:

$$\bar{\psi} = \lim_{p \rightarrow +\infty} \sum_{n=1}^p \psi_n(\mathbf{x}, t) \quad (5.8)$$

where ψ_n is any function of the turbulent field at the location \mathbf{x} and the time t . Using the Reynolds decomposition, the function ψ can be written with the mean field $\bar{\psi}$ and turbulent fluctuations ψ' such that:

$$\psi(\mathbf{x}, t) = \bar{\psi}(\mathbf{x}, t) + \psi'(\mathbf{x}, t) \quad (5.9)$$

The statistical averaging verifies the linearity, the idempotence and the commutation between differentiation and the time operators. Given these properties, the time averaging applied to the Navier-Stokes equations gives:

$$\frac{\partial \bar{u}_i}{\partial x_i} = 0 \quad (5.10)$$

$$\frac{\partial \bar{u}_i}{\partial t} + \frac{\partial}{\partial x_j} (\bar{u}_i \bar{u}_j) = -\frac{1}{\rho} \frac{\partial \bar{p}}{\partial x_i} + \nu \frac{\partial^2 \bar{u}_i}{\partial x_j^2} - \frac{\partial}{\partial x_j} (\overline{u'_i u'_j}) \quad (5.11)$$

$$\frac{\partial \bar{T}}{\partial t} + \frac{\partial}{\partial x_i} (\bar{u}_i \bar{T}) = \frac{\partial}{\partial x_i} \left(\alpha \frac{\partial \bar{T}}{\partial x_i} \right) - \frac{\partial}{\partial x_i} (\overline{u'_i T'}) \quad (5.12)$$

Correlation terms $\overline{u'_i u'_j}$ and $\overline{u'_i T'}$ appear in the momentum and temperature equations. The term $\overline{u'_i u'_j}$ is the Reynolds stress tensor and corresponds to the contribution of the turbulence. The off-diagonal components are shear stresses and play a dominant role in the theory of mean momentum transfer by turbulent motion. The diagonal components are normal stresses and contribute little to the transport of the mean momentum.

The temperature being a passive scalar, the turbulent heat flux $\overline{u'_i T'}$ is seen as an additional diffusion created by the turbulence.

Spatial averaging

The volume averaging operator is applied to the governing equations to look for the mean characteristics of the flow in the porous region. Given the properties of the volume averaging operator (see Section 2.1.2) and the no-slip boundary conditions at the solid walls, the equation of continuity becomes:

$$\frac{\partial \langle \bar{u}_i \rangle}{\partial x_i} = 0 \quad (5.13)$$

The momentum equation takes the following form:

$$\frac{\partial \langle \bar{u}_i \rangle}{\partial t} + \frac{\partial}{\partial x_j} \left(\frac{\langle \bar{u}_i \rangle \langle \bar{u}_j \rangle}{\phi} \right) + \frac{\partial}{\partial x_j} \tau_u^{ij} = -\frac{1}{\rho} \frac{\partial \langle \bar{p} \rangle}{\partial x_i} + \frac{\partial}{\partial x_j} \left(\nu \frac{\partial \langle \bar{u}_i \rangle}{\partial x_j} \right) - \frac{\partial}{\partial x_j} \langle \overline{u'_i u'_j} \rangle + f_i^i \quad (5.14)$$

where f_l^i is a drag force that results from the interaction between the solid and fluid phases:

$$f_l^i = \frac{1}{V} \int_{A_{fs}} \left(\nu \frac{\partial \bar{u}_i}{\partial x_j} - \frac{\bar{p} - \langle \bar{p} \rangle^f(x_0)}{\rho} \delta_{ij} \right) \cdot n_j dS \quad (5.15)$$

τ_u^{ij} corresponds to the momentum dispersion tensor due to the spatial deviation of the velocity field defined by:

$$\tau_u^{ij} = \langle \bar{u}_i \bar{u}_j \rangle - \frac{\langle \bar{u}_i \rangle \langle \bar{u}_j \rangle}{\phi} \quad (5.16)$$

The volume averaging operator applied to the temperature equation gives:

$$\phi \frac{\partial \langle \bar{T} \rangle^f}{\partial t} + \frac{\partial}{\partial x_i} \left(\phi \langle \bar{u}_i \rangle^f \langle \bar{T} \rangle^f \right) + \frac{\partial \tau_{uT}^i}{\partial x_i} = \frac{\partial}{\partial x_i} \left(\alpha \phi \frac{\partial \langle \bar{T} \rangle^f}{\partial x_i} \right) - \frac{\partial}{\partial x_i} \langle \bar{u}_i' \bar{T}' \rangle + T_{or} + \mathcal{P} \quad (5.17)$$

where τ_{uT}^i is the thermal dispersion vector defined by:

$$\tau_{uT}^i = \langle \bar{u}_i \bar{T} \rangle - \phi \langle \bar{u}_i \rangle^f \langle \bar{T} \rangle^f \quad (5.18)$$

The term T_{or} is the tortuosity that traduces the opposition by the solid matrix to the diffusion effect:

$$T_{or} = \frac{\partial}{\partial x_i} \left(\frac{1}{V} \int_{A_{fs}} \alpha \left(T - \langle T \rangle^f(x_0) \right) n_i dS \right) \quad (5.19)$$

The term \mathcal{P} corresponds to the wall heat flux:

$$\mathcal{P} = \frac{1}{V} \int_{A_{fs}} \alpha \frac{\partial \bar{T}}{\partial x_i} n_i dS - \underbrace{\frac{1}{V} \int_{A_{fs}} \frac{\partial \bar{u}_i' \bar{T}'}{\partial x_i} n_i dS}_{=0} \quad (5.20)$$

since $\bar{u}_i' \bar{T}' = 0$ at the fluid-solid interface A_{fs} .

The direct numerical simulation provides the overall terms present in the twice-averaged equations, including f_l^i , τ_u^{ij} , τ_{uT}^i and T_{or} that are characteristic of turbulent transfer in porous media.

5.3.2 Simplified equations

In the studied DNS, the turbulent flow is at steady state and the thermo-physical properties of the fluid (ρ , c_p , ν , k_f) are assumed constant. For the equations of continuity (5.13) and momentum (5.14), the boundary conditions of periodicity in the x - and z -directions imposes that the averaged velocity gradients are constant in these directions. For the equation of energy (5.17), the diffusion, the tortuosity and the dispersion are constant in the x - and z -directions for the boundary conditions considered. Thus, one obtains the following simplified equations:

$$\frac{\partial \langle \bar{u} \rangle}{\partial y} = 0 \quad (5.21)$$

$$\frac{\partial}{\partial y} \left(\frac{\langle \bar{u} \rangle \langle \bar{v} \rangle}{\phi} \right) + \frac{\partial}{\partial y} \tau_u^{yx} = -\frac{1}{\rho} \frac{\partial \langle \bar{p} \rangle}{\partial x} + \frac{\partial}{\partial y} \left(\nu \frac{\partial \langle \bar{u} \rangle}{\partial y} \right) - \frac{\partial}{\partial y} \langle \bar{u}' \bar{v}' \rangle + f_l^y \quad (5.22)$$

$$\langle \bar{u} \rangle \frac{\partial \langle \bar{T} \rangle^f}{\partial x} + \frac{\partial}{\partial y} \left(\phi \langle \bar{v} \rangle^f \langle \bar{T} \rangle^f \right) + \frac{\partial \tau_{uT}^y}{\partial y} = \frac{\partial}{\partial y} \left(\alpha \phi \frac{\partial \langle \bar{T} \rangle^f}{\partial y} \right) - \frac{\partial}{\partial y} \langle \bar{v}' \bar{T}' \rangle + T_{or} + \mathcal{P} \quad (5.23)$$

The energy equations for the three boundary conditions are solved in parallel with a single velocity field solution. Considering Cases 2 and 3, the variable change and the heating configuration impose null averaged temperature gradients in the x - and z -directions. Thus, the energy equation (5.23) becomes:

$$\text{Case 1:} \quad \frac{\partial \tau_{uT}^y}{\partial y} = \frac{\partial}{\partial y} \left(\alpha \phi \frac{\partial \langle \overline{T} \rangle^f}{\partial y} \right) - \frac{\partial}{\partial y} \langle \overline{v'T'} \rangle + T_{or} \quad (5.24)$$

$$\text{Case 2:} \quad \langle \overline{u} \rangle A_0 + \frac{\partial \tau_{u\theta_0}^y}{\partial y} = \frac{\partial}{\partial y} \left(\alpha \phi \frac{\partial \langle \overline{\theta_0} \rangle^f}{\partial y} \right) - \frac{\partial}{\partial y} \langle \overline{v'\theta'_0} \rangle + T_{or} \quad (5.25)$$

$$\text{Case 3:} \quad \langle \overline{u} \rangle A_1 + \frac{\partial \tau_{u\theta_1}^y}{\partial y} = \frac{\partial}{\partial y} \left(\alpha \phi \frac{\partial \langle \overline{\theta_1} \rangle^f}{\partial y} \right) - \frac{\partial}{\partial y} \langle \overline{v'\theta'_1} \rangle + T_{or} + \mathcal{P} \quad (5.26)$$

In order to study the turbulent transfer characteristics at the free-porous interface, the results of the DNS are filtered twice, as the governing equations. First, the statistical quantities are computed (see equations (5.10), (5.11), and (5.12)) for each mesh cell of the whole domain. Furthermore, since the geometry is $2d_p$ -periodic in the x - and z -directions, we can increase the statistics by adding the quantity $\overline{\psi}$ of each periodic cell as:

$$\overline{\psi}_{new}(x, y, z) = \sum_{i=0}^{30} \sum_{k=0}^{20} \overline{\psi}(x + i2d_p, y, z + k2d_p) \quad (5.27)$$

The geometry is thus reduced to a column of cubes in the y -direction.

Then, the volume averaging process is performed applying a spatial filter in the three directions. Finally, one obtains a twice-averaged quantity $\langle \overline{\psi}_{new} \rangle(y)$. The results presented in the next Section correspond to the twice-averaged quantities. Considering the geometry obtained once the statistical filter has been performed, we use a top-hat formed filter in the x - and z -direction, and a quadratic filter (top-hat convoluted twice, see Chapter 1) in the y -direction. The choice of a quadratic filter differs from Breugem and Boersma (2005), who perform the spatial averaging using a triangle shaped filter (top-hat convoluted once). The quadratic filter shows its accuracy for the turbulent viscosity profile and does not change the profiles of the statistic quantities as it will be shown in the following. Furthermore, we remind that the volume averaging operator does not give accurate values at the wall on a half of VER spacing. For a quadratic filter, the zones impacted by the wall effect correspond to $-1 < y/H < -1 + 3d_p = -0.85$ and $1 - 3d_p = 0.85 < y/H < 1$. These zones are delimited by dotted lines in the following figures. On the contrary, Breugem and Boersma (2005) choose to reduce the wall-normal extent of the averaging volume close to the wall ($-1 < y/H < -1 + 2d_p$). This can explain the difference between the Breugem's and our profiles in these zones.

5.4 Results

In this section, we present the averaged results from the DNS performed with Trio_U. For the velocity field, the low-order turbulence statistics and characteristic turbulent structures (velocity, variance, shear stresses, turbulent quantities) are compared with those obtained by Breugem and Boersma (2005). This comparison is a first verification of the relevance of the DNS. An identical work is done for the temperature. However, no similar study exists to validate the results at the free-porous interface. Only, the behavior of the turbulent thermal boundary layer at the top-wall is verified using the knowledge existing for turbulent channel flows.

The results of the present DNS offer a first theoretical basis on turbulent statistics of heat transfer at a free-porous interface.

5.4.1 Statistics of the velocity field

In this paragraph, the results obtained with Trio_U are compared with Breugem's DNS (Breugem and Boersma, 2005). The values of the different Reynolds numbers that characterize both DNS are presented in Table 5.4. The Reynolds numbers are defined by:

$$\begin{aligned}
 Re_b &= U_b H / \nu & \text{with} & \quad U_b = \int_0^H \bar{u} dy, \text{ the bulk flow in the free region} \\
 Re_T &= 2U_T H / \nu & \text{with} & \quad U_T = \frac{1}{2H} \int_{-H}^H \bar{u} dy, \text{ the averaged flow in the whole domain} \\
 Re_{ip} &= U_p H / \nu & \text{with} & \quad U_p = \int_{-H}^0 \bar{u} dy, \text{ the bulk flow in the porous medium} \\
 Re_\tau^t &= u_\tau^t H / \nu & \text{with} & \quad u_\tau^t = \sqrt{-\nu \frac{\partial \bar{u}}{\partial y}(H)}, \text{ the wall shear stress} \\
 Re_\tau^p &= U_\tau^p H / \nu & \text{with} & \quad u_\tau^p = \sqrt{-\nu \frac{\partial \langle \bar{u} \rangle}{\partial y}(0)}, \text{ the porous wall shear stress at } y = 0
 \end{aligned}$$

DNS	ϕ	Re_b	Re_p	Re_T	Re_τ^t	Re_τ^p
Breugem	0.875	5500	502	5963	394	669
Trio_U	0.875	5351	450	5851	390	664
Difference in %	0	2	1	1	2	1

Table 5.4: Characteristic of the Breugem's DNS and Trio_U's DNS.

The values presented in Table 5.4 show a good agreement between the Reynolds number characteristic of Breugem's DNS and our DNS. The small differences could come from the use of the Immersed Boundary Method at cubes used by Breugem and Boersma (2005) that introduces a small penetration velocity through the cubes. This method allows to consider the porous domain as continuous, and thus, the Fast Fourier Transform solver can be used to solve the Poisson equation for the pressure.

5.4.1.1 Velocity profiles

The velocity profiles are presented in Fig. 5.6. In the flow direction (see Fig. 5.6(a)), the profiles obtained by Breugem and Trio_U are very close. The difference between the porous medium and the free region is recovered. In the free region, the profile is skewed with a maximum located above the center of the channel at $y/H = 0.6875$. It results from a skin friction coefficient $C_f = 2(u_\tau/U_b)^2$ larger for the free-porous interface than for the solid top wall. Furthermore, the velocity profile shows an inflexion point ($d^2\bar{u}/dy^2 = 0$) at $y/H = -0.082$. This inflexion point is at the origin of large vortical structures that develop just above the porous wall. These large vortical structures can be associated to instabilities of the Kelvin-Helmholtz type (see Breugem et al. (2005).)

In the normal and cross directions (see Figs. 5.6(b) and 5.6(c)), the averaged velocity must be null at convergence. This result is verified for $\langle \bar{v} \rangle$ but not exactly for $\langle \bar{w} \rangle$, which profile shows small fluctuations in the free region. In our study, we use an identical forcing term in the porous and free regions to impose the periodicity condition. There is no-friction in the free region and the slight time-variations of the forcing term can be at the origin of the observed fluctuations in the $\langle \bar{w} \rangle$ profile. A similar observation can be done for the Breugem's DNS.

Brugem et al. (2005) study the transfer mechanisms at the free-porous interface using a similar analysis as for solid wall and considering the interfacial free-porous zone as a porous wall. They locate the porous wall at $y/H = 0$. Thus, they show that two boundary layers can be distinguished in the free region: one above the permeable wall and one below the solid wall. The border between the two boundary layers corresponds to the maximum of the mean velocity (see Fig. 5.5).

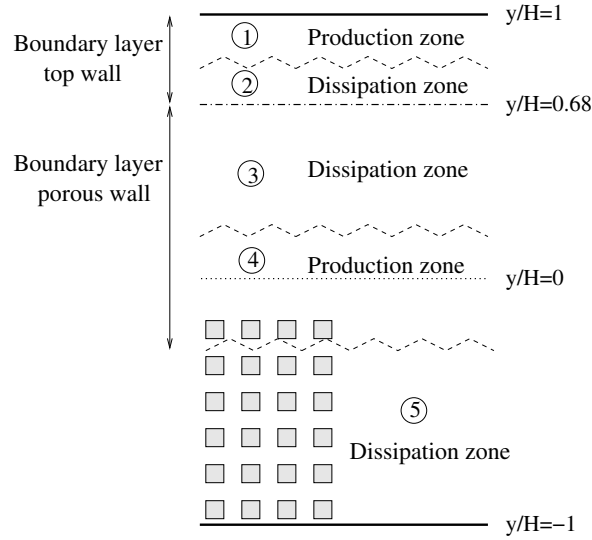


Figure 5.5: Scaling regions for turbulent flow in a free-porous domain.

5.4.1.2 RMS profiles of velocity components

The profiles of the averaged velocity variance are presented in Fig. 5.7. The fluctuations of the three components of the velocity are close for both DNS.

The rms values are low in the porous region, increase to reach a peak at the free-porous interface, then decrease in the free region to reach a smaller peak near the solid wall and decrease again. From this profile description, one can identify two zones of production and three zones of dissipation of fluctuations (see Fig. 5.5). The production of fluctuations is characterized by the peaks at the free-porous interface and at the solid wall. The width and the height of peaks give information on the mechanism at the origin of the fluctuations. Thus, the difference between the peak width shows that the fluctuations are created by two different mechanisms and the size shows that the production at the free-porous interface is stronger than at the solid wall. The zones of dissipation of the fluctuations are located in the porous region and in the free region between the two production zones. In the porous region, the dissipation of the fluctuation is very important and is due to the drag created by the solid matrix. In the free region, two zones of dissipation exist and are related to the two zones of production at the free-porous interface and at the solid wall.

For the dissipation in the free region, Brugem et al. (2005) study the spectra of the rms of the velocity fluctuation and show a very interesting phenomenon. Although the wave number of the fluctuations decrease exponentially, the larger-scale fluctuations decrease more slowly than the small-scale fluctuations. This result confirms the observation of large vortices entering in the upper part of the porous medium.

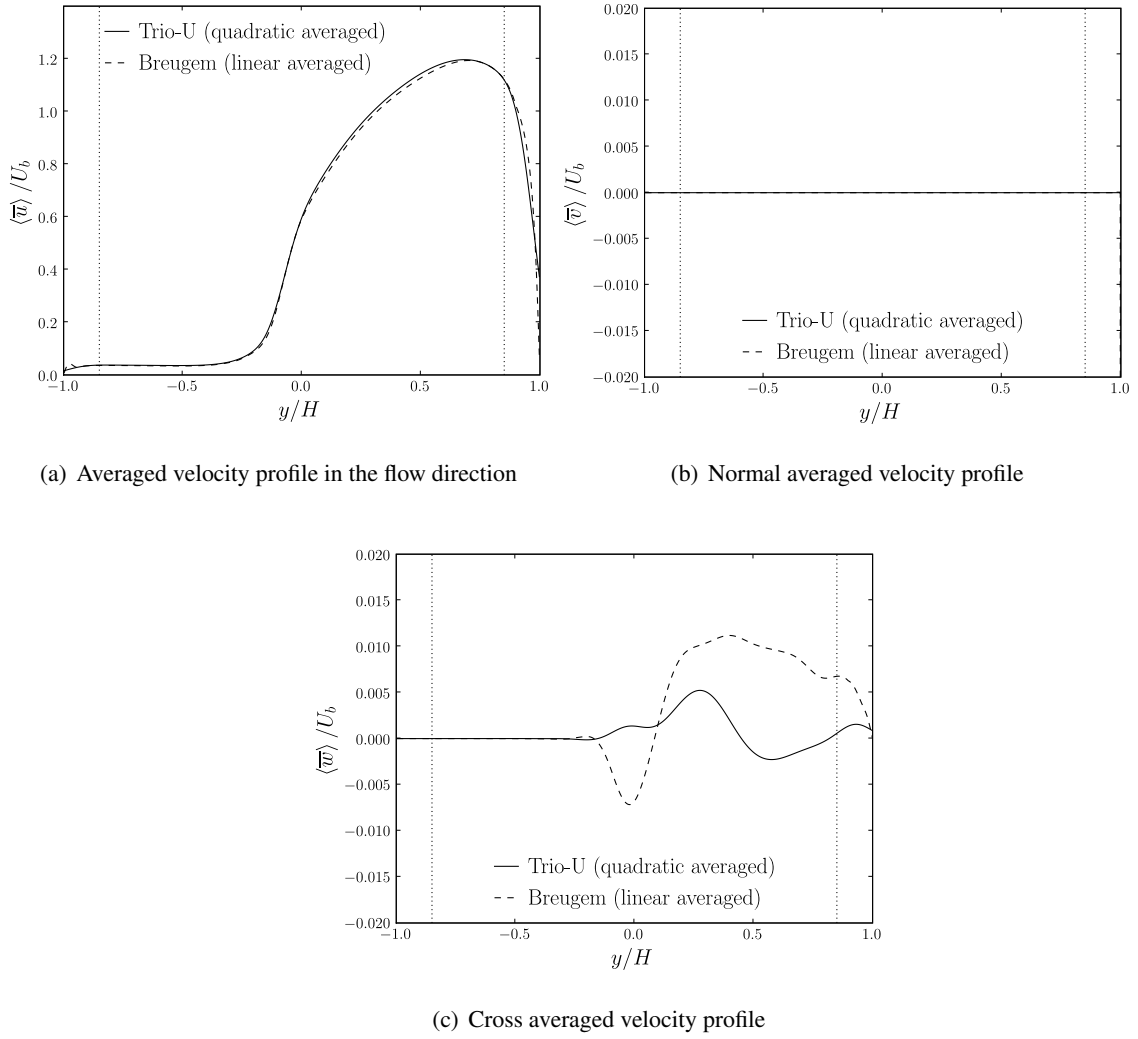


Figure 5.6: Averaged velocity profiles.

5.4.1.3 Shear stress profiles

The total shear stress is defined by:

$$\langle \tau_{xz} \rangle = \nu \frac{\partial \langle \bar{u} \rangle}{\partial y} - \langle \bar{u}' v' \rangle - \langle \bar{u} \bar{v} \rangle \quad (5.28)$$

The right hand terms represent respectively the viscous shear stress ($\nu \frac{\partial \langle \bar{u} \rangle}{\partial y}$), the turbulent shear stress ($\langle \bar{u}' v' \rangle$) and the volume averaged mean shear stress ($\langle \bar{u} \bar{v} \rangle$). The different terms are presented in Fig. 5.8 showing similar profiles for both DNS. The turbulent constraint is negligible in the homogeneous porous region and rises strongly in the interfacial zone to decrease linearly in the free region. The volume averaged viscous and the volume averaged mean shear stresses are negligible in the whole domain. The total shear stress has values of the same order of magnitude as the turbulent shear stress. Thus, one can conclude that the turbulent shear stress contributes the most to the total shear stress.

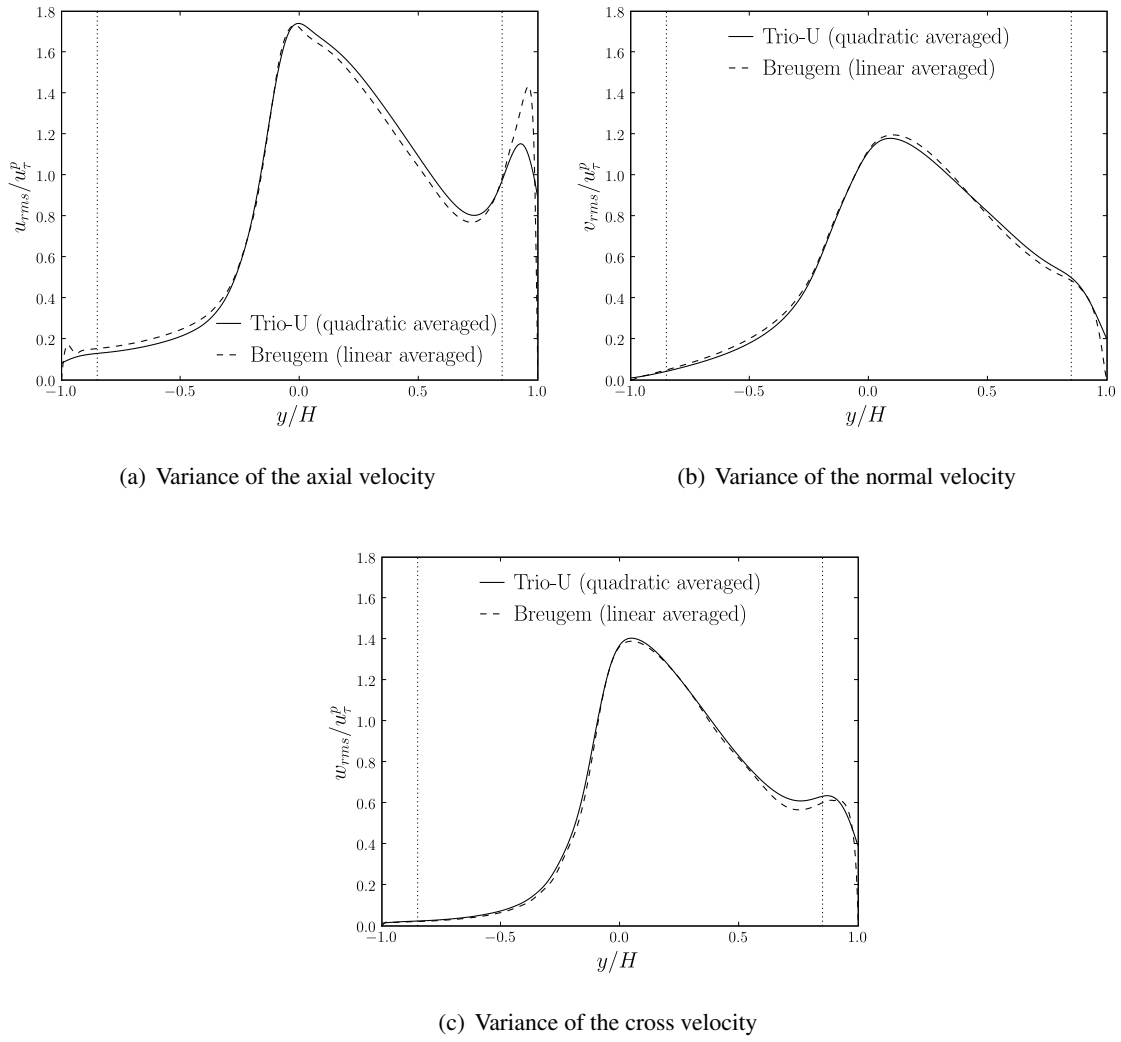


Figure 5.7: Profiles of the averaged velocity variance.

5.4.1.4 Turbulent kinetic energy and dissipation rate profiles

The profiles of the turbulent quantities $\langle k \rangle$ and $\langle \epsilon \rangle$ are presented in Fig. 5.9.

For the volume averaged turbulent kinetic energy (see Fig. 5.9(a)), the profiles obtained by Trio_U and Breugem are identical. This quantity illustrates the intensity of the mixing in the domain. The values are null in the porous medium far from the porous wall, increase to reach a peak around $y = 0$, then decrease in the free region to a minimum around $y = 0.7$, which corresponds to the maximum of the velocity field (border between the two boundary layers). The peak width at $y = 0$ corresponds to large vortical structures (Breugem, 2005). These structures are rapidly destroyed in the porous medium ($-0.5 < y < 0$) due to the friction force created by the solid matrix. In the free region, the vortical structures elongate and eventually disappear.

For the dissipation rate (see Fig. 5.9(b)), the profile cannot be compared because the Breugem's results is not known. However, the behavior is consistent with the physics of turbulent transfer in a free-porous domain. It can be decomposed in four regions:

- In region 1 ($-1 < y/H < -0.5$), the dissipation rate is very low, which corresponds to no-turbulence;

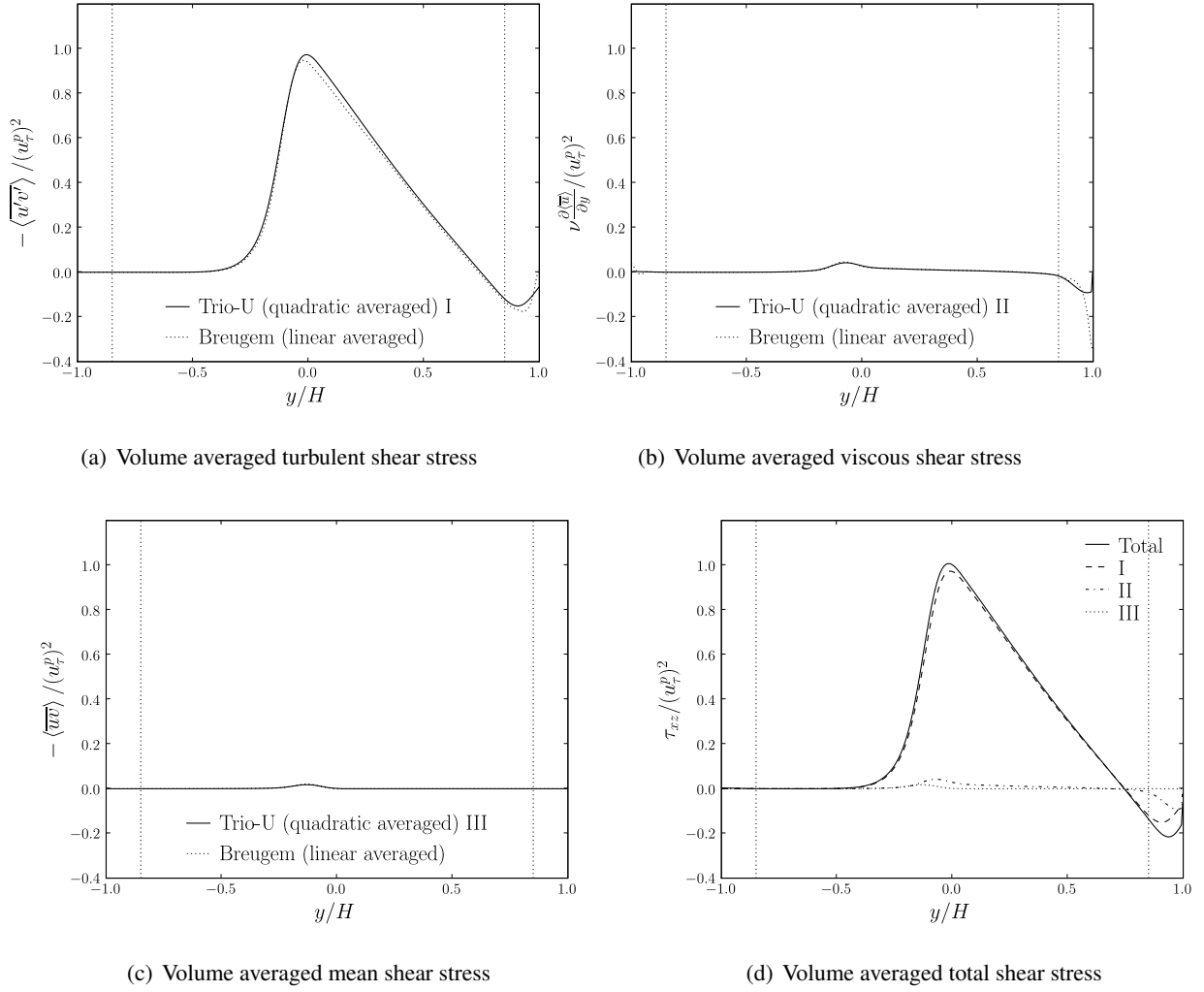


Figure 5.8: Profiles of the volume averaged shear stresses.

- In region 2 ($-0.5 < y/H < 0$), the dissipation rate increases to reach a peak at $y/H = -0.1$; it characterizes the dissipation of the turbulence by the drag due to the presence of the solid matrix;
- Region 3 ($0 < y/H < 0.7$) corresponds to the dissipation of the Kelvin-Helmholtz vortices created by the porous wall;
- Region 4 ($0.7 < y/H < 1.$) corresponds to the dissipation of the turbulent structures coming from the solid wall.

From this profile analysis, one recovers two characteristics of the turbulent flow in a free-porous domain. The impact of the porous region in the dissipation rate compared to the free region and the difference between the porous and solid walls illustrated by the shifted profile in the channel. The shifted profile in the channel is compared to the result of [Moser et al. \(1999\)](#) obtained for $Re_\tau = 360$.

5.4.2 Turbulent viscosity profile

The DNS does not use any model for the Reynolds stresses and solves all the turbulence scales. However, it is important to compute the averaged turbulent viscosity to compare the macroscopic model

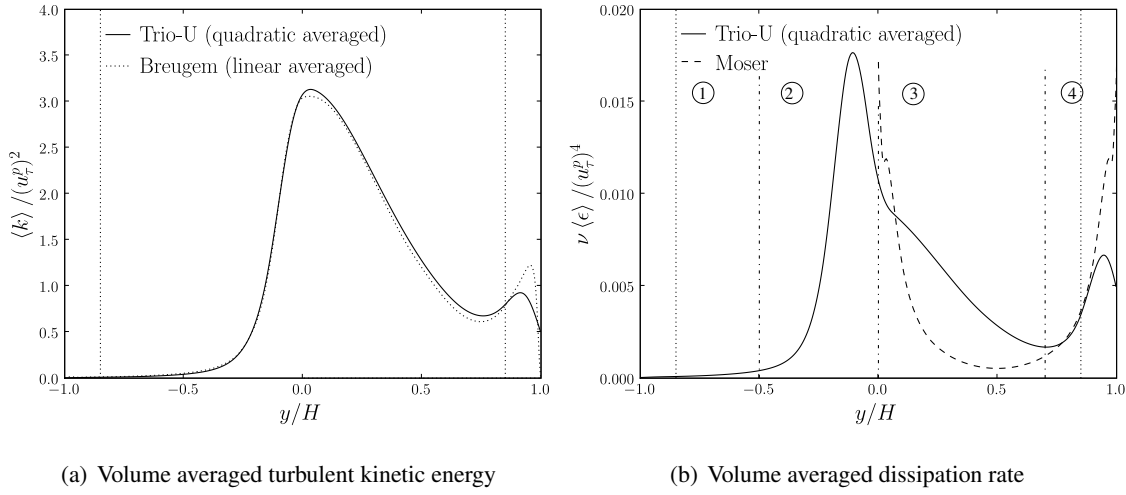


Figure 5.9: Profiles of turbulent quantities.

using this hypothesis. This quantity is obtained with:

$$\nu_{t\phi} = \frac{-\langle u'v' \rangle}{\partial \langle \bar{u} \rangle / \partial y} \quad (5.29)$$

The profiles of the averaged turbulent viscosity are presented in Fig. 5.10. In the relation (5.29), the numerator and the denominator are null for different locations. This is observed in both DNS for $y = 0.7$, $y = -0.5$ and $y = -0.75$.

A difference between the profiles is observed for $-0.5 < y < 0$. This is due to the use of different volume averaging filters. Breugem (2005) uses a triangle shaped function, while we average with a quadratic function. Thus, the observed fluctuations in the Breugem's profile follow the geometry. The order of the filter he uses, is not sufficient.

For $y < -0.5$, the averaged turbulent viscosity is not defined. In this zone, the flow is not disordered by the turbulence, that has been destroyed by the friction force existing in the porous medium. Thus, the axial velocity is homogeneous and the Reynolds stress is null.

The twice averaged quantities (velocity fields, rms velocity fluctuations, shear stresses) and the turbulent characteristics ($\langle k \rangle$, $\nu_{t\phi}$) of the DNS are compared with those of Breugem and Boersma (2005). The profile comparison shows a good agreement validating the computation of the turbulent flow. Furthermore, new quantities are represented ($\langle k \rangle$, $\langle \epsilon \rangle$, $\nu_{t\phi}$) that will be used to build a turbulent macroscopic model in Chapter 6.

5.4.3 Statistics of the temperature field

This Section presents the low-order turbulence statistics and characteristic turbulent structures of the heat transfer for the three studied heating configurations: fixed temperature at walls and adiabatic cubes (Case 1), fixed flux at walls and adiabatic cubes (Case 2) and fixed flux at cubes and adiabatic walls (Case 3). For Case 1, the computed quantity is the temperature T . For Cases 2 and 3, where heat is injected in the system, the computed temperatures are the new variables θ_0 and θ_1 .

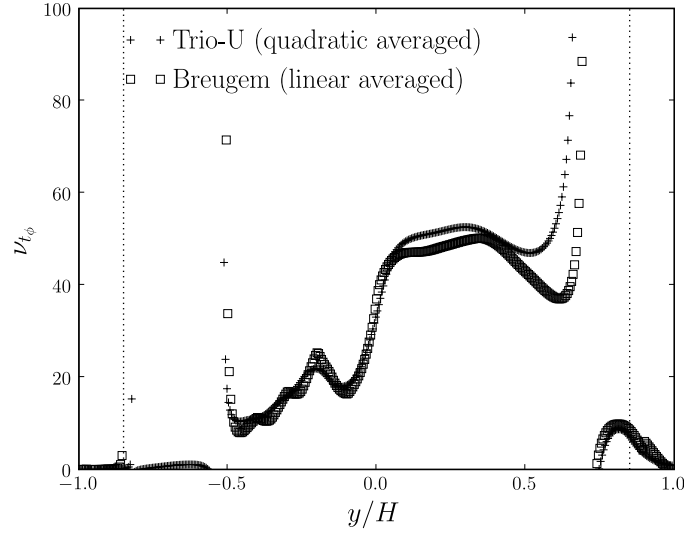


Figure 5.10: Profiles of turbulent quantities.

The quantities are non-dimensionalized by the friction or the difference temperature defined by:

$$\begin{aligned}
 T_\tau^t &= \frac{\alpha \frac{\partial \bar{T}}{\partial y}(H)}{\rho c_p u_\tau^t}, \quad \theta_\tau^t = \frac{q_w}{\rho c_p u_\tau^t} && \text{solid wall friction temperature} \\
 T_\tau^p &= \frac{\alpha \frac{\partial \langle \bar{T} \rangle}{\partial y}(0)}{\rho c_p u_\tau^t}, \quad \theta_\tau^p = \frac{\alpha \frac{\partial \langle \bar{\theta} \rangle}{\partial y}(0)}{\rho c_p u_\tau^t} && \text{porous wall friction temperature} \\
 \Delta T &= [\bar{T}]_{-H}^H, \quad \Delta \theta = [\bar{\theta}]_{-H}^H && \text{temperature difference at walls}
 \end{aligned}$$

5.4.3.1 Verification at the solid wall

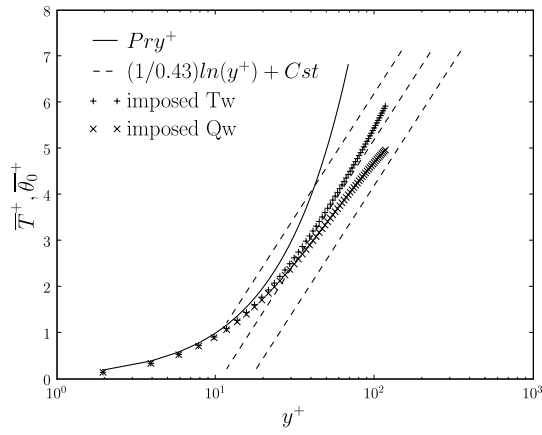
As presented in the introduction, many studies have been performed to understand the turbulent heat transfers in the thermal boundary layer. The obtained results offer theoretical basis on turbulence statistics for different thermal conditions at the solid wall. Thus, we are able to verify the accuracy of our own results in the thermal boundary layer at the upper wall. The temperature and variance profiles for Cases 1 and 2 are presented in Fig. 5.11. The results obtained for Case 3 are not presented because adiabatic wall corresponds to a particular boundary condition.

The dimensionless quantities are presented as a function of y^+ ($= u_\tau y / \nu$) and defined as:

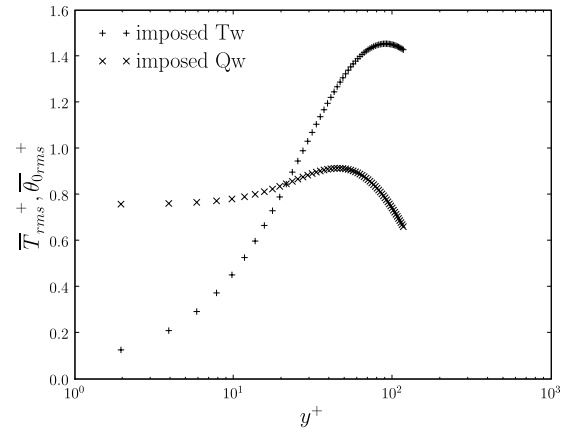
$$\begin{aligned}
 \bar{\psi}^+(x, y, z) &= (\bar{\psi}(x, H, z) - \bar{\psi}(x, y, z)) / \psi_\tau^t \\
 \bar{\psi}_{rms}^+ &= \bar{\psi}_{rms} / \psi_\tau^t, \quad \overline{u'\psi'}^+ = \overline{u'\psi'} / u_\tau^t \psi_\tau^t, \quad \overline{v'\psi'}^+ = \overline{v'\psi'} / u_\tau^t \psi_\tau^t
 \end{aligned}$$

where ψ corresponds to the temperatures T and θ_0 . The results are presented for $y^+ < 120$, thus $0.69 < y/H < 1$. It corresponds to the channel part between the location of the inflection point of the velocity profile and the upper-wall.

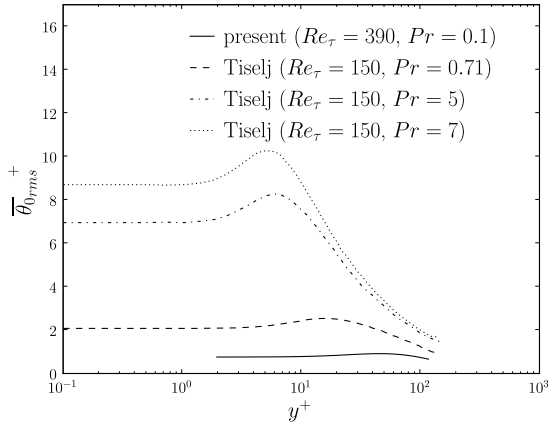
The temperature profiles are presented in Fig. 5.11(a). The profiles follow the relation $\bar{T}^+ = Pr y^+$ in the viscous region ($y^+ < 10$) for the isothermal and isoflux boundary conditions in accordance with the literature (Tiselj et al., 2001b,a; Kawamura et al., 1999, 2000). Distant from the wall ($y^+ > 30$), Kawamura et al. (2000) show the existence of a logarithmic sublayer in $1/0.43 \ln(y^+) + C_{ste}$ for $1 > Pr > 0.2$ and the absence of logarithmic sublayer for $Pr < 0.025$. It shows that the effects of the viscosity become



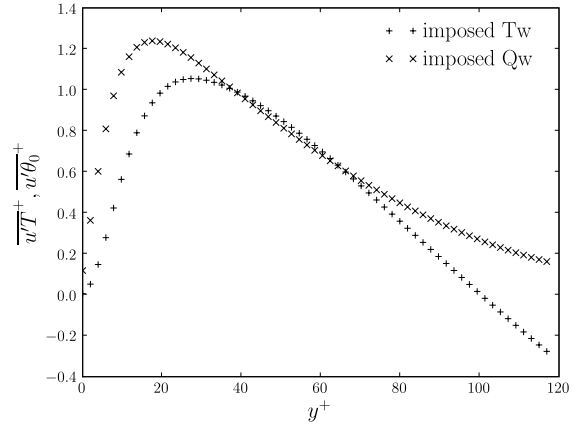
(a) Profiles of mean temperatures



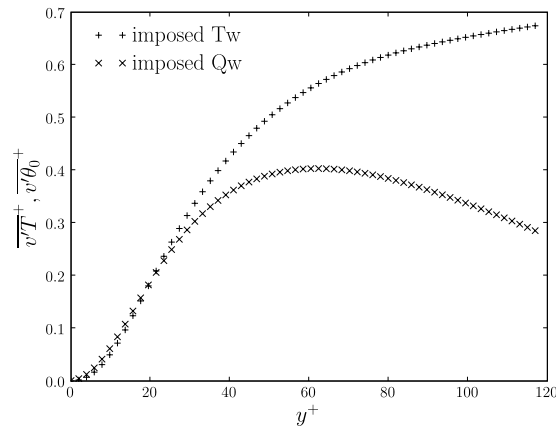
(b) Profiles of rms temperature fluctuation



(c) Comparison of rms profiles for imposed heat flux



(d) Profiles of the turbulent wall axial heat flux



(e) Profiles of the turbulent wall normal heat flux

Figure 5.11: Low-order turbulence statistic profiles at the solid wall for isothermal and isoflux boundary conditions

more important for low Prandtl numbers and move the logarithmic zone at a larger distance from the wall. In our study with $Pr = 0.1$, the profiles does not exhibit a logarithmic sublayer (see Fig. 5.11(a)). This can be due to the effect of the viscosity as presented above and the effect of the porous wall.

The variance profiles are presented in Fig. 5.11(b). For isothermal boundary condition, the temperature fluctuation are null at the wall and increase in the viscous sublayer ($y^+ < 10$), to reach a peak at $y^+ = 87$. Such a behavior can be compared with the results obtained in a channel flow by Debusschere and Rutland (2004) ($Re_\tau = 186$, $Pr = 0.7$) and Nicoud and Poinso (1999) ($Re_\tau = 180$, $Pr = 0.76$). Indeed, they find temperature fluctuations null at walls and that increase to reach a peak at $y^+ \approx 20$. For isoflux boundary conditions, the temperature fluctuations are constant in the viscous sublayer ($y^+ < 10$) and reach a peak at $y^+ = 45$. This result are in accordance, with those of Tiselj et al. (2001b,a) ($Re_\tau = 170$, $Pr = 1$, 5 and $Re_\tau = 150$, $Pr = 0.71$, 5, 7). Especially, Tiselj et al. (2001a) show that the constant value of the temperature fluctuations in the viscous sublayer and the peak location vary with the Prandtl number. They obtained $\bar{T}_{rms}^+ \approx 2$ and a maximum at $y^+ \approx 20$ for $Pr = 0.71$, and $\bar{T}_{rms}^+ \approx 8.7$ and a maximum at $y^+ \approx 7$ for $Pr = 7$ (see Fig. 5.11(c)).

The turbulent flux profiles in the streamwise and normal-wall directions are presented in Figs. 5.11(d) and 5.11(e). The distinct feature is that the thermal wall boundary condition does not affect the turbulent normal heat flux close to the wall (see Fig. 5.11(d)), while it impacts the turbulent axial heat flux in the viscous sublayer (see Fig. 5.11(e)). This feature is coherent with the one observed by Tiselj et al. (2001a) for a low Prandtl number ($Re_\tau = 150$, $Pr = 0.71$).

The study of the thermal boundary layer validates the accuracy of the DNS results. in the near-wall layer. The main features of the low order turbulent statistics are recovered in accordance with the literature (Kawamura et al., 2000; Tiselj et al., 2001b,a; Nicoud and Poinso, 1999; Debusschere and Rutland, 2004)

5.4.3.2 Temperature and RMS profiles

The profiles of the averaged temperatures for the three heating configurations are presented in Fig. 5.12. They can be divided in three domains: the porous and free domains with different temperature gradients and a transition zone making the bond between the two domains.

In order to show the effect of the turbulence in the porous medium, we compare the obtained temperature profiles with temperature profiles obtained without turbulence. In the y -direction, the dispersion can be neglected and the tortuosity approximated by $T_{or} = \alpha_{tor} \phi \partial^2 \langle \bar{T} \rangle^f / \partial y^2$, as we will see in Chapter 6. With these simplifications, the equations (5.24), (5.25), (5.26) reduce to:

$$\text{Case 1:} \quad 0 = (\alpha + \alpha_{tor}) \phi \frac{\partial^2 \langle \bar{T} \rangle^f}{\partial y^2} \quad (5.30)$$

$$\text{Case 2:} \quad \langle \bar{u} \rangle A_0 = (\alpha + \alpha_{tor}) \phi \frac{\partial^2 \langle \bar{\theta}_0 \rangle^f}{\partial y^2} \quad (5.31)$$

$$\text{Case 3:} \quad \langle \bar{u} \rangle A_1 = (\alpha + \alpha_{tor}) \phi \frac{\partial^2 \langle \bar{\theta}_1 \rangle^f}{\partial y^2} + \mathcal{P} \quad (5.32)$$

where $\alpha = 10$ and $\alpha_{tor} = -0.8$. The equations (5.30), (5.31), (5.32) are integrated on the domain and the temperature profile are presented in Fig. 5.12. Comparing the turbulent and laminar profiles in the homogeneous porous medium, one observes that the effect of the turbulence is negligible for $-1 < y/H < -0.5$ and begins to be visible for $y/H > -0.5$.

In the free region, the turbulence dominates the heat transfer. For Case 1, with fixed temperature at wall and adiabatic cubes, the temperature profile presents an inflexion point at $y/H = 0.12$ (see Fig. 5.12(b)).

For Case 2, with fixed flux at wall and adiabatic cubes, the temperature profile presents a minimum at $y/H = 0.44$ (see Fig. ??). These points corresponds to the minimum location of the rms temperature fluctuations (see Fig. 5.13).

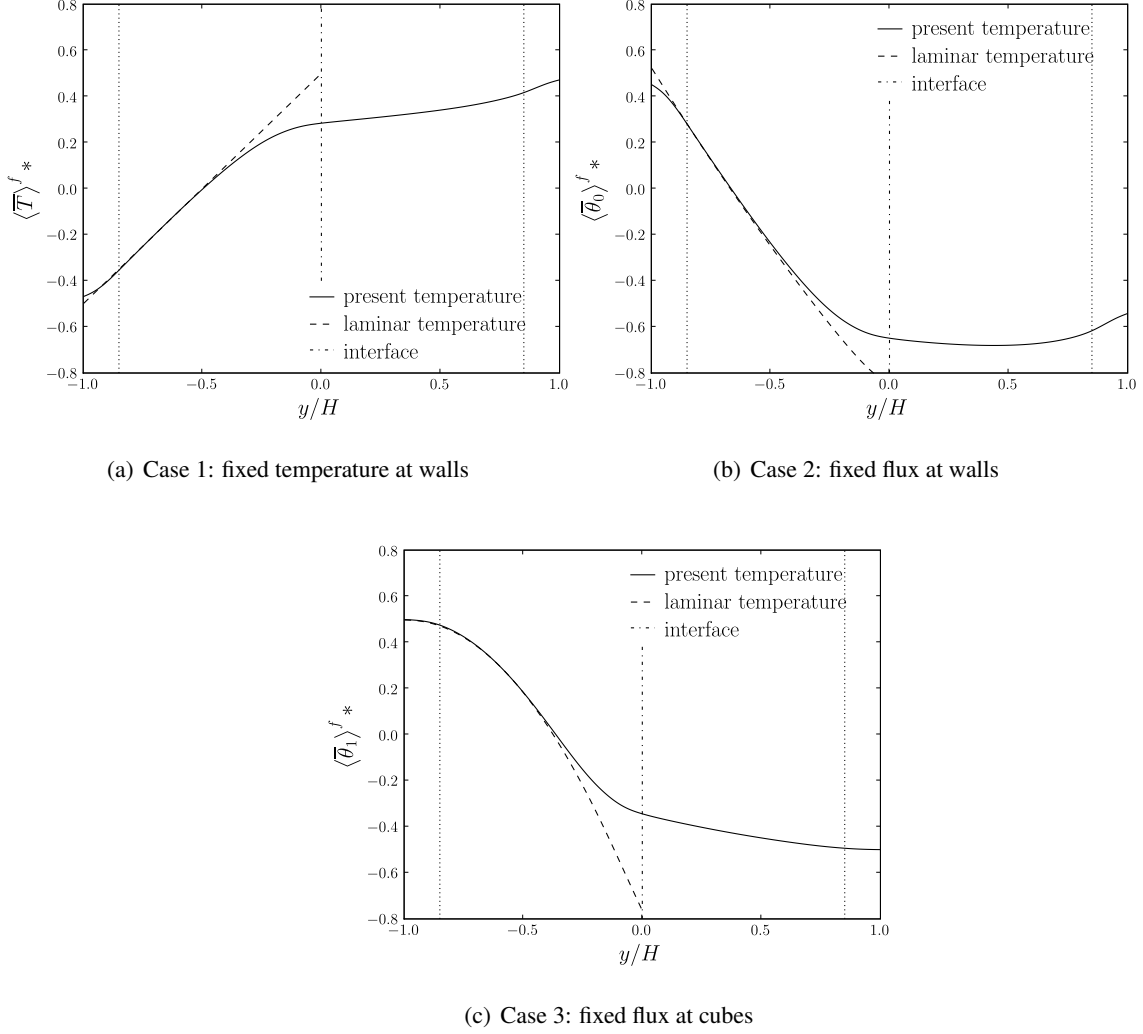


Figure 5.12: Profiles of the volume averaged temperature with $\psi_* = \frac{\langle \psi \rangle^f - (\psi(H) + \psi(-H))/2}{\Delta\psi}$, ψ being T , θ_0 and θ_1 .

The roots mean square temperature fluctuation ψ is defined by:

$$\psi_{rms} = \sqrt{\langle \psi'^2 \rangle^f} \quad (5.33)$$

The profiles of the rms quantities are presented in Fig. 5.13.

For the three heating configurations, the maximum temperature fluctuation is located inside the porous medium ($y/H = -0.38$ for Case 1, $y/H = -0.40$ for Case 2 and $y/H = -0.31$ for Case 3). Furthermore, the rms values are not negligible in the porous medium compared to free region, unlike the rms velocities. These behaviors could be related to the presence of large vortices in the upper-part of the porous medium as found by Breugem et al. (2005). In the free region, the temperature fluctuation behavior depends on the heating configuration. For Case1, the minimum value is located around the inflexion

point of the temperature profile at $y/H = 0.12$. For Case 2, the minimum value is located around the minimum of the temperature profile at $y/H = 0.44$.

At the present time, the profiles of the rms temperature fluctuations are not well understood. A solution for a better understanding of the phenomena, is to decompose the rms temperature fluctuations between its different contributions, (i) the fluctuation of the mean flow and (ii) those of the subfilter scale. This decomposition makes explicit the contributions of the different sources of the fluctuations. This work is not presented here due to a lack of time.

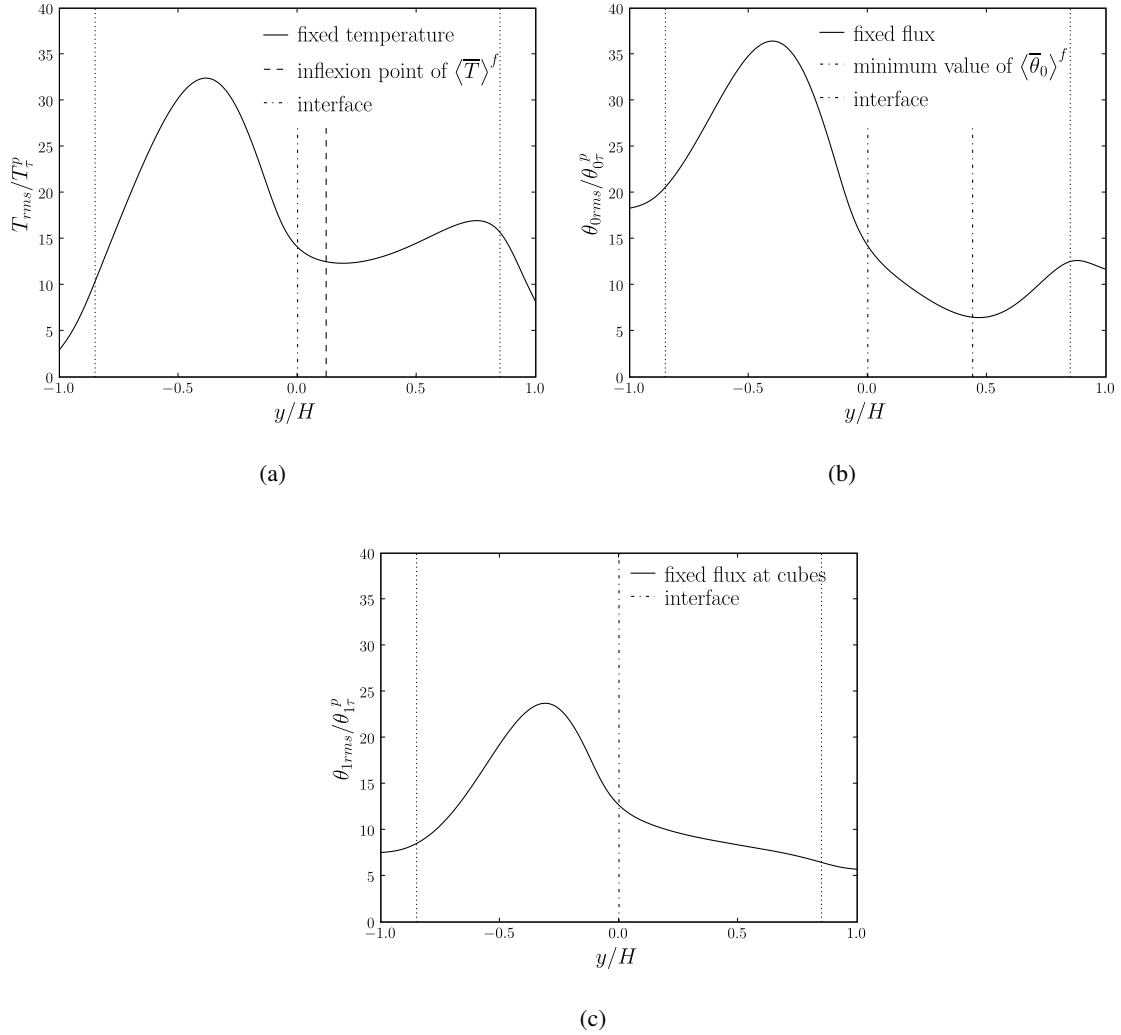


Figure 5.13: Profiles of the RMS temperature fluctuation.

5.4.3.3 Total heat flux profiles

The profiles of different contributions to heat flux in the normal wall direction are presented in Fig. 5.14. For the three heating configurations, the following observations can be done:

- the dispersion is negligible;
- the molecular diffusion dominates the heat transfer in the porous region and is not negligible compared to the turbulent diffusion in the transition zone and in the free region;

- the turbulent diffusion dominates the heat transfer in the free region, it is still important in the upper-part of the porous region and it is negligible for $y/H < -0.5$.

The description of the flux profiles shows two main characteristics of the studied heat transfer. The Peclet numbers ($Pe^p = 1$ in the porous medium and $Pe^l = 550$ in the free region) are not high enough to have a negligible diffusive flux compared to the turbulence flux. The turbulent heat flux is negligible in the lower-part of the porous region, which confirms the disappearance of the turbulence in this zone.

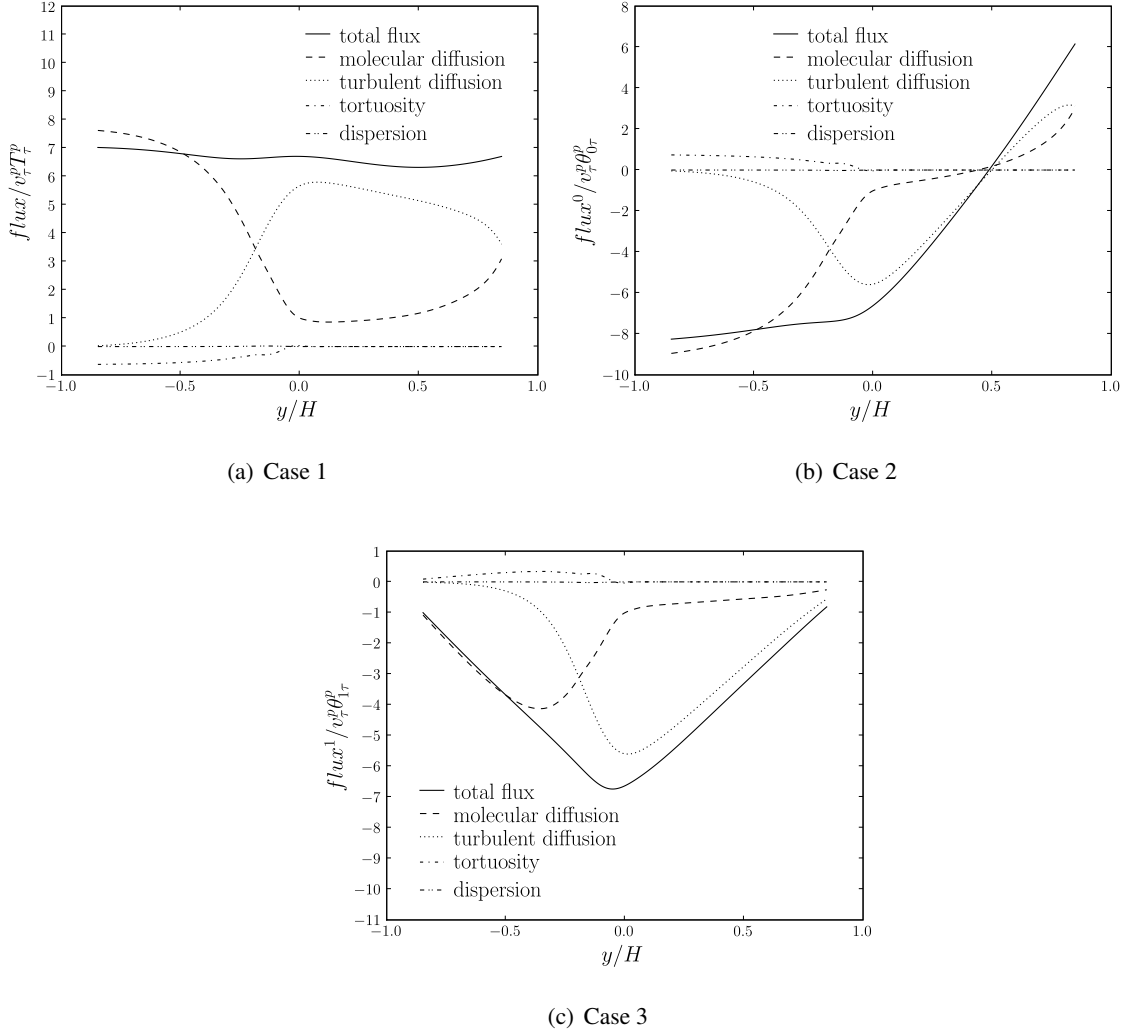


Figure 5.14: Profiles of the heat flux budget.

For fully developed flow and temperature fields, the exact total heat flux in the wall normal direction can be obtained from the integration on $[-H; +H]$ of the averaged energy equations (5.24), (5.25) and (5.26). One obtains:

$$\text{Case 1:} \quad q_y = cste \quad (5.34)$$

$$\text{Case 2:} \quad q_{0y} = A_0 \int_{H^-}^y \langle \bar{u} \rangle (y) dy \quad (5.35)$$

$$\text{Case 3:} \quad q_{1y} = A_1 \int_{H^-}^y \langle \bar{u} \rangle (y) dy - \int_{H^-}^{H^+} \mathcal{P}(y) dy \quad (5.36)$$

The comparison between the present total heat flux and the exact total heat flux are presented in Fig. 5.15. The exact total heat flux are translated to fit the sum of the present total flux at the porous wall $y = 0$. For the three heating configurations, slight differences between the profiles are observed ($\pm 5\%$). It could arise from the lack of periodicity in the z -direction (see Fig. 5.6(c)).

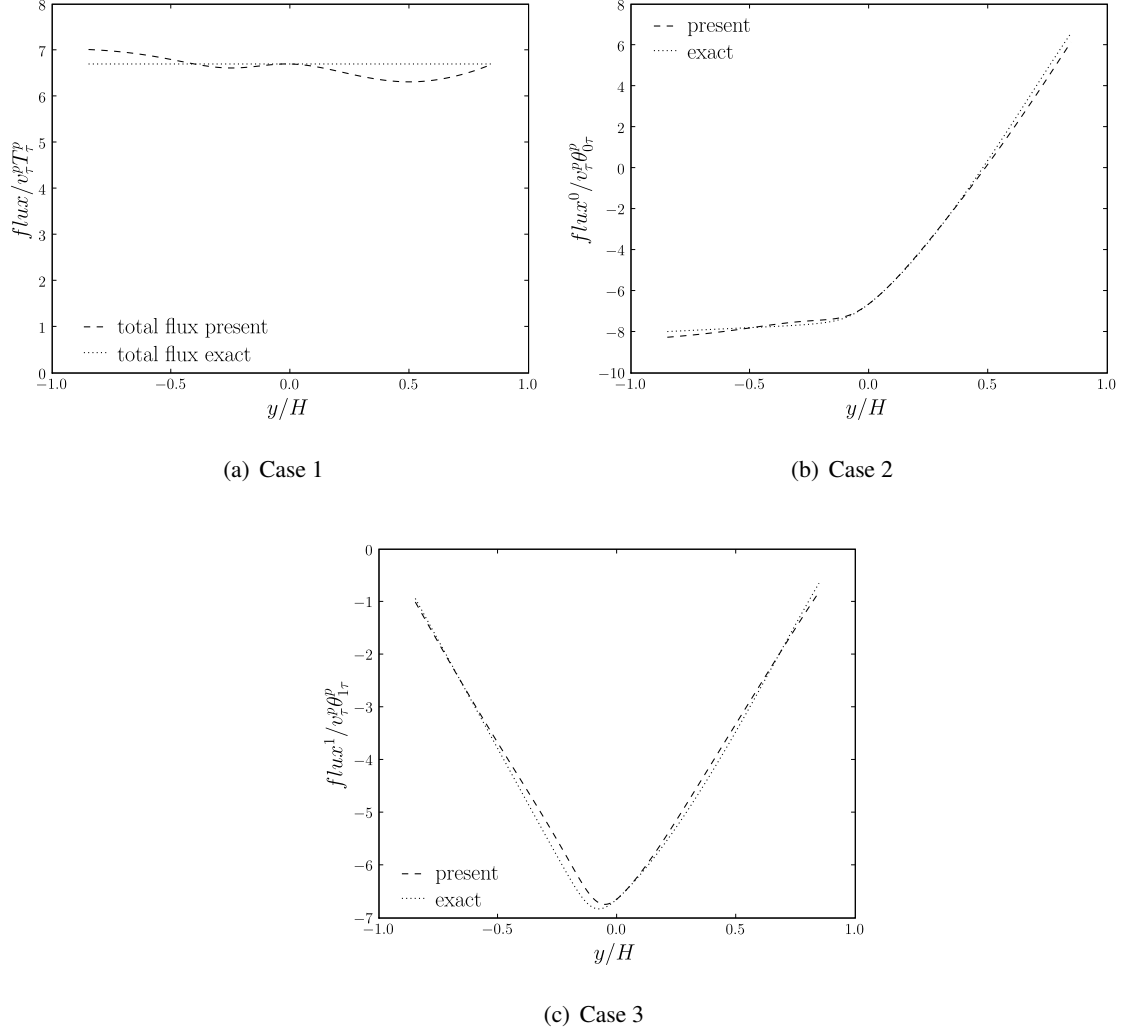


Figure 5.15: Comparison of the total heat flux in the wall normal direction.

5.4.3.4 Turbulent heat flux profiles

The profiles of the streamwise averaged turbulent heat flux are presented in Fig. 5.16. In the porous medium, the behaviors are identical for the three heating configurations (see Fig. 5.16(d)). The values are null at the wall, decrease to a minimum at $y/H = -0.4$ then increase to reach a peak close to the porous interface at $y/H = -0.05$. We notice that the location of the minimum value corresponds approximately to the maximum location of the rms temperature fluctuation (see Fig. 5.13). In the free region, the behaviors are different depending on the applied boundary conditions (see Fig. 5.16(d)). However the profile superimposition in Fig. 5.16(d) shows a noteworthy point at $y/H = 0.7$ that corresponds to the maximum of the velocity field (border between the two boundary layers).

The wall-normal averaged turbulent heat flux are presented in Fig. 5.17. In the porous medium, the

behaviors are identical for the three heating configurations (see Fig. 5.17(d)). The values are null at the wall then decrease to a minimum around $-0.05 < y/H < 0$. In the free region, the behaviors are different depending on the applied boundary conditions as presented in Fig. 5.17(d).

As for the rms temperature fluctuations, the study of the different contributions of the turbulent heat fluxes gives a better understanding of the main contributions at the origin of the profiles. This work is not done in this study due to a lack of time.

Comparing the wall-normal and the streamwise heat fluxes, some observations can be done:

- the values of the wall-normal heat flux are smaller by an order-of-magnitude than the streamwise ones;
- except the extremum location ($-0.05 < y/H < 0$), the form of the wall-normal and streamwise profiles is different.

From these observations, we assume that the wall-normal and streamwise turbulent heat fluxes result from different mechanisms. In order to illustrate this assumption, we study the cross-correlation in the following. The issue is to improve the knowledge of the turbulent heat flux for the RANS simulation of the macroscopic heat transfer in Chapter 6.

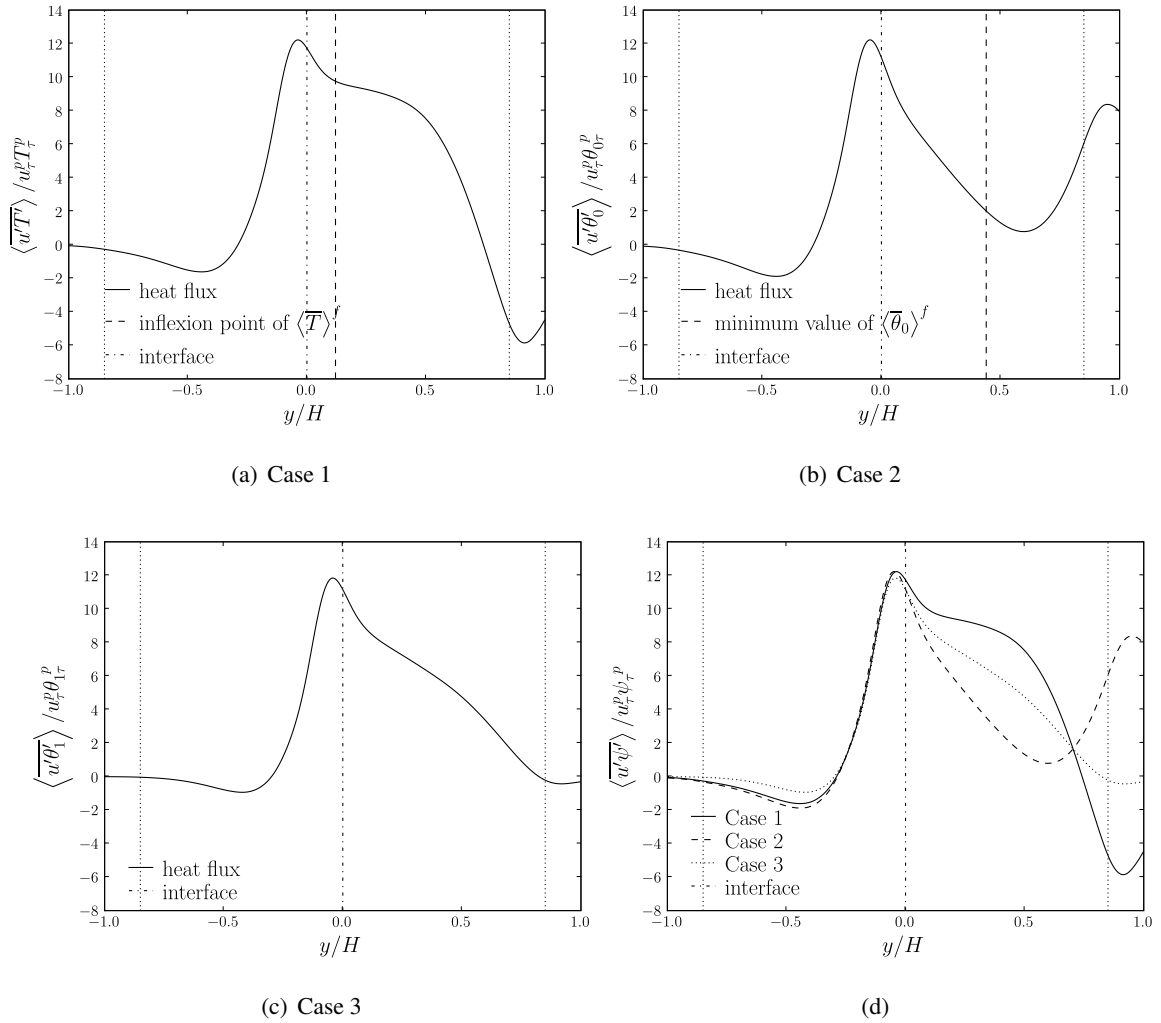


Figure 5.16: Profiles of the streamwise turbulent heat flux.

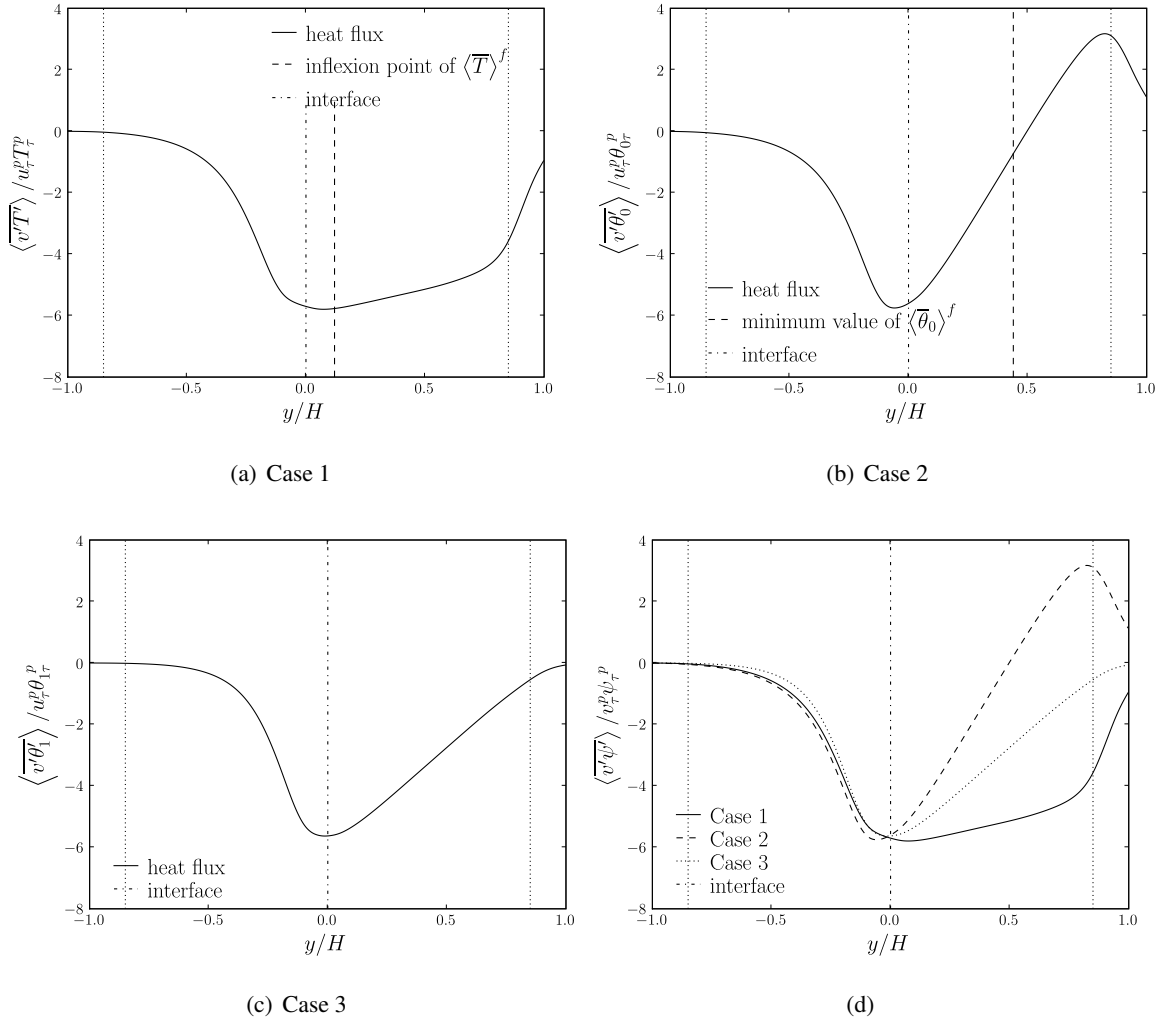


Figure 5.17: Profiles of the wall-normal turbulent heat flux.

5.4.3.5 Cross-correlation profiles

A cross-correlation study is performed by [Kasagi et al. \(1992\)](#) for heat transfer in a turbulent channel. They defined a correlation coefficient $R_{\psi\xi}$ by $R_{\psi\xi} = \overline{\psi'\xi'}/\psi_{rms}\xi_{rms}$ where ψ and ξ are DNS fields (u, v and T). After the computation of the correlation coefficients, they compare the obtained profiles and conclude that the wall-normal turbulent heat flux $\overline{v'T'}$ and the Reynolds shear stress $\overline{u'v'}$ are generated by similar mechanisms in a turbulent channel.

Following this analysis for free-porous domain, we define the correlation coefficients below:

$$R_{u\psi} = \frac{\langle u'\psi' \rangle}{u_{rms}\psi_{rms}}, \quad R_{v\psi} = \frac{\langle v'\psi' \rangle}{v_{rms}\psi_{rms}}, \quad R_{vu} = \frac{\langle v'u' \rangle}{v_{rms}u_{rms}}$$

where ψ corresponds to the temperatures T , θ_0 and θ_1 respectively. The profiles of the cross-correlation coefficients are presented in Fig. 5.18.

For the heating configuration with imposed temperature at walls, the profiles of the cross-correlation R_{uT} , R_{vT} and R_{uv} are presented in Fig. 5.18(a). The comparison between the profiles of R_{vT} and R_{uv} shows an important difference. It reveals a lack of correlation between the averaged turbulent heat flux $\langle v'T' \rangle$ and the averaged Reynolds stress $\langle v'u' \rangle$. On the contrary, the profiles R_{uv} and R_{uT} have a close

main behavior. Thus, the Reynolds shear stress and the turbulent flux $\langle u'T' \rangle$ in the flow direction are generated by similar turbulence mechanisms.

In order to illustrate the similarity, the stresses $\langle u'v' \rangle$ and $\langle u'T' \rangle$ are superposed in Fig. 5.18(b). The Reynolds constraint is scaled following:

$$f_{\langle u'v' \rangle}^f = -\frac{\langle u'v' \rangle^f}{Pr(u_\tau^p)^2} \quad (5.37)$$

The comparison shows an identical decrease between the two constraints at the porous wall in the porous region.

For the two other heating configurations, Case 2 and Case 3, the profiles are presented in Fig. 5.18(c) to (f). It leads to the same observations as for Case 1.

5.4.3.6 Turbulent diffusivity profile

The DNS provides information about the characteristics of the turbulent structures existing in turbulent transfers to create accurate turbulence modeling that can be used for LES or RANS simulations. For this reason, the issue is to express the turbulent correlations as a function of main quantities. In the context of this study, we want to characterize $\langle v'T' \rangle$ to perform a RANS simulation of the turbulent heat transfer in a free-porous domain at the macroscopic scale (see Chapter 6). We propose a turbulence modeling inspired from the one commonly used for free flow. It relates the turbulent heat correlation $\langle v'T' \rangle$ to the gradient of the main temperature via a volume averaged turbulent diffusivity α_{t_ϕ} as:

$$\alpha_{t_\phi} = \frac{\langle v'T' \rangle^f}{\partial \langle T \rangle^f / \partial y} \quad (5.38)$$

The profiles of the macroscopic turbulent diffusivity for the three heating configurations are presented in Fig. 5.19. The three profiles fit in the porous region and are different in the free region. For Case 2, the values diverge due to the intrinsic volume average temperature gradient null for $y/H = 0.44$. However, one observes an identical main behavior for the three cases. The values are negligible for $y/H < -0.5$, then rapidly increase to reach a peak at $y/H = 0.1$ and decrease in the free region.

The identical behavior of the volume averaged turbulent diffusivity for the three heating configurations confirms the relevance of the modeling of the turbulent heat correlation (5.38).

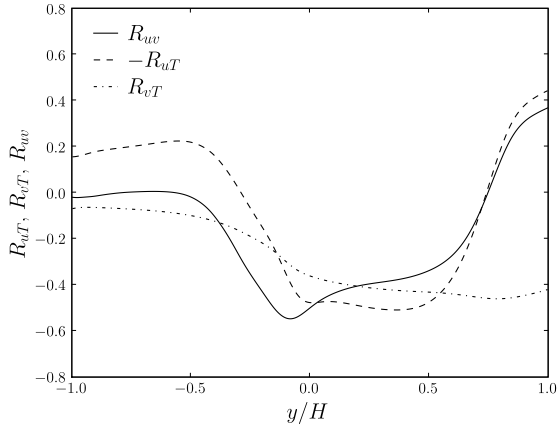
The next step is the closure of α_{t_ϕ} , that we study in more details in Chapter 6. We present here only the main problematic of this step. For the simulation of turbulent free flows via RANS simulations using the $k-\epsilon$ model, the turbulent diffusivity is closed via the turbulent Prandtl model as:

$$\alpha_t = \frac{\nu_t}{Pr_t}, \text{ with } Pr_t = 0.9 \quad (5.39)$$

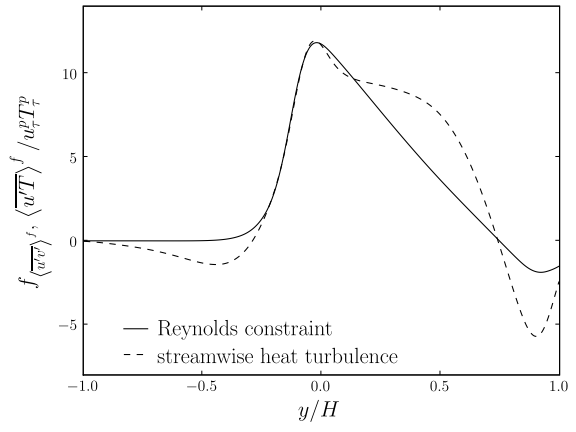
Such a modeling is based on the passive nature of the temperature field, whose turbulence length scale is equal to that of the flow. It verifies the correlation between $\overline{v'T'}$, $\overline{u'T'}$ and $\overline{u'v'}$. For a homogeneous porous medium, [de Lemos and Rocamora \(2002\)](#) assume that the correlation is also valid for the volume averaged quantities and propose the following modeling:

$$\langle \mathbf{v}'T' \rangle^f = \frac{\nu_{t_\phi}}{Pr_t} \nabla \langle T \rangle^f \quad (5.40)$$

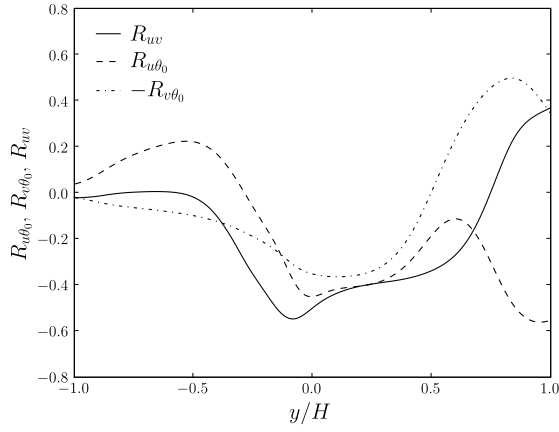
However, we shown that $\langle v'T' \rangle$ and $\langle v'u' \rangle$ result from different mechanisms. Thus, the model (5.40) might not be appropriate for the RANS simulation of turbulent heat transfer in a free-porous domain at the macroscopic scale. In the following chapter, we discuss this problematic and we propose another model to close the volume averaged turbulent diffusivity.



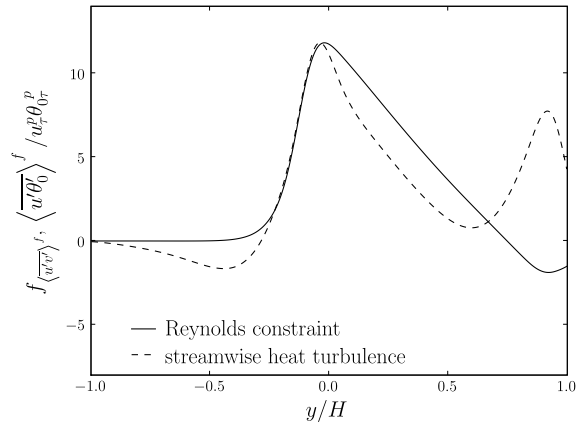
(a) Cross-correlation coefficients-Case 1



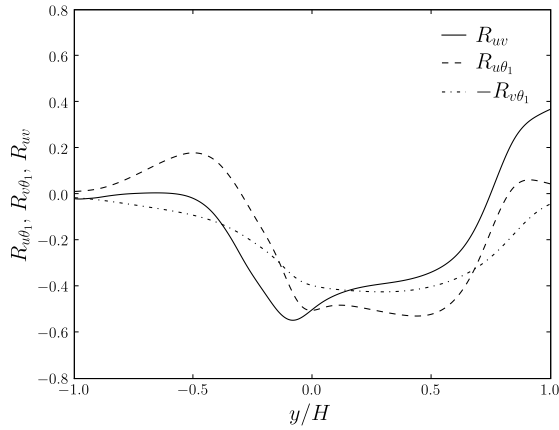
(b) Comparison between $\langle \overline{u'T'} \rangle$ and $\langle \overline{u'v'} \rangle$ -Case 1



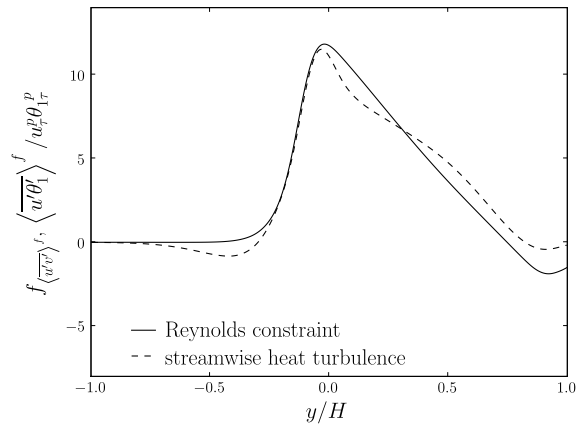
(c) Cross-correlation coefficients-Case 2



(d) Comparison between $\langle \overline{u'\theta'_0} \rangle$ and $\langle \overline{u'v'} \rangle$ -Case 2



(e) Cross-correlation coefficients-Case 3



(f) Comparison between $\langle \overline{u'\theta'_1} \rangle$ and $\langle \overline{u'v'} \rangle$ -Case 3

Figure 5.18: Profiles of the cross-correlations and of the constraints comparison.

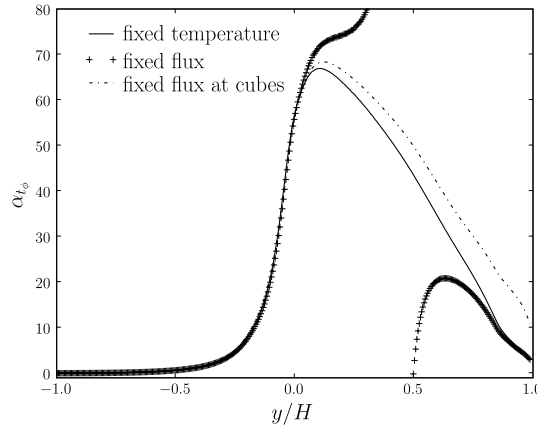


Figure 5.19: Profile of the volume averaged turbulent diffusivity.

5.5 Conclusion

This Chapter presents a direct numerical simulation of turbulent heat transfer in a three-dimensional domain partially filled with a porous medium constituted of cubes. Using the geometry and the spatial discretization of [Breugem and Boersma \(2005\)](#), the simulation is performed at constant friction Reynolds number $Re_\tau = 390$ and Prandtl number $Pr = 0.1$. Furthermore, considering the fluid temperature as a passive scalar, the energy equations for three heating boundary conditions are solved in parallel with a single velocity field solution. The results of the DNS are statistical quantities, that we spatially average on the whole domain.

For the flow, the twice averaged quantities (velocity fields, rms of velocity fluctuations, shear stresses) and the turbulent characteristics (averaged turbulent kinetic energy and averaged turbulent viscosity) are compared with the results of [Breugem and Boersma \(2005\)](#). The profile comparison shows a good agreement validating the DNS computation of the turbulent flow. Thus, we recover the observations of [Breugem and Boersma \(2005\)](#) that the turbulent structures are created at the porous wall and elongate in the free channel, while they are rapidly destroyed in the porous medium by the solid matrix.

For the temperature, no comparison can be done with previous studies. However using the results existing for turbulent channel flows, we validate the thermal boundary layer at the top wall in the viscous zone and show the impact of the porous wall in the logarithmic zone. We present the twice averaged quantities (temperature field, rms temperature fluctuations, cross correlation, heat flux balance) and the turbulent heat characteristics (averaged turbulent diffusivity) for the three heating configurations. Thus, we show that the turbulent heat flux in the wall normal direction $\langle v'T' \rangle$ and the Reynolds constraint $\langle u'v' \rangle$ are created by different mechanisms. This information is very important for the modeling of the turbulent heat correlations in the context of RANS simulations and will be used in the next chapter. Indeed, the issue of Chapter 5 is to simulate a macroscopic turbulent heat transfer at a free-porous interface with a $k-\epsilon$ model for the flow and a thermal model for the temperature. The macroscopic results obtained with the model will be compared to the DNS profiles considered as results of reference.

Chapter 6

Turbulent heat transfer at the free-porous interface for a Poiseuille flow

In Chapters 2 and 3, we studied the jump conditions that must be applied at a free-porous interface for laminar heat transfer. However, as presented in the introduction, the heat transfer is turbulent in a core of a nuclear reactor. In Chapter 5, we have presented a direct numerical simulation of turbulent heat transfer in a free-porous domain that gives access to local quantities. In this chapter, we study the coupling at the interface between the macroscopic turbulent heat transfer model used in the homogeneous porous region and the standard turbulent heat transfer model of the free region. As for laminar studies, we use the multi-scale method based on two up-scaling steps and three levels of description of the interface. At last, the macroscopic profiles are compared with the results of reference given by the DNS.

6.1 Introduction

The study of laminar heat transfer at a free-porous interface relies on the description scale of the interface. For turbulent heat transfer, the modeling depends also on the description of the turbulence. In order to introduce the different modeling issues, we present first the turbulent models and for each one the associated model of the interface.

Direct numerical simulation

The direct numerical simulation of turbulent heat transfer at a free-porous interface captures the turbulence without the use of any modeling and describes the fine structure of the porous medium. Such a computation corresponds to a *numerical experimentation* that gives access to local quantities, and thus can be used as a simulation of reference. The DNS presented in Chapter 5 is realized in this purpose.

At this scale of description of the turbulence, [Breugem and Boersma \(2005\)](#) propose a modeling for the momentum transfer at the free-porous interface. It consists in applying a spatial average on the Navier-Stokes equations, with a size for the representative elementary volume smaller than the length scale of the turbulent structure. This constraint imposes a filter size different in the porous and free regions to solve each scale of the turbulence. This approach called *DNS with continuum* gives correct profiles comparing to the results of reference but requires a large amount of discretization cells numbers (10^7 for the DNS with continuum instead of 10^8 grid nodes for the DNS with cubes).

Another approach consists in substituting the interfacial zone by an appropriate boundary condition at the free-porous interface, that features the impact of the porous medium on the free region. Using such an approach, [Hahn et al. \(2002\)](#) propose a boundary condition inspired from [Beavers and Joseph \(1967\)](#) and obtain good results for laminar transfers. However, the approach fails for turbulent heat transfers comparing to experimental results ([Zagni and Smith, 1976](#); [Zippe and Graf, 1983](#); [Kong and Schetz,](#)

1982). Furthermore, as for the laminar case, the value of the jump coefficient α is not known and can have a large impact on the results.

For turbulent heat transfer, there is no study that proposes a modeling of heat transfer at the free-porous interface. Nevertheless, [Stalio and Nobile \(2003\)](#) study the influence of rough walls on the heat flux for turbulent flows. Representing the rough wall by riblets, they perform direct numerical simulation for different riblet geometry.

Large eddy simulation

Large eddy simulations (LES) of the turbulence introduce a first level of modeling. The turbulent structures of the transfer, whose sizes are larger than a cut-off scale are explicitly computed as for a DNS. For the smallest turbulent structures, their impact on the larger scales are modeled with sub-filter models. LES is used to study transfer at a free-porous interface for weather prediction ([Shaw and Schumann, 1992](#); [Finnigan, 2000](#); [Watanabe, 2004](#)). In such cases, an identical filter is used to average the turbulence and the porous medium. However, as noted in the introduction, for homogeneous porous media the size of the representative elementary volume is larger than the length scale of the turbulence. Thus, this approach is not able to capture the turbulence inside the core of a nuclear reactor.

Reynolds-averaged Navier-Stokes modeling

As presented in the introduction, this approach relies on statistical averaging, which leads to turbulent correlation terms. We present here, the closure associated to the k - ϵ model where the Reynolds constraint is modeled similarly to the molecular shear stress constraint with a turbulent viscosity. This closure will be used in the remainder of the chapter.

This turbulence modeling can be used with a fine description of the porous medium as done by [Prinos et al. \(2003\)](#) to study turbulent flow at a free-porous interface. The computational cost associated to such a method is low ($\approx 10^4$ mesh cells for Reynolds numbers in 7.10^3 and 2.10^3) allowing various simulations with different geometries and parameters. We remind that the k - ϵ model suffers a lack of generality, especially in recirculation zones. However, knowing the limit of the modeling, the results obtained using the k - ϵ model at the pore scale can be considered as reference to study transfers at the free-porous interface.

For a macroscopic description of the interface, the domain is composed of two homogeneous regions separated with a surface of discontinuity. The turbulence in the homogeneous porous medium is characterized with a macroscopic k - ϵ model, while in the free region a standard model is used. The issue is to couple the two models at the free-porous interface.

For momentum transfer, the first boundary conditions used are the continuity of the turbulent quantities k , ϵ and their first gradients, and a jump condition for the shear stress ([Lee and Howell, 1987](#); [de Lemos and Pedras, 2000](#)). Then de Lemos et al. ([de Lemos, 2005](#); [de Lemos and Silva, 2006](#); [de Lemos, 2009](#)) propose to introduce a jump condition for the diffusive flux of the turbulent kinetic energy k . On the contrary, [Chandesris and Jamet \(2009b\)](#) follow another approach. They close the macroscopic modeling of the interface by determining the position where the jump conditions vanish. In their case, it corresponds to the center of gravity of the surface excess value of the friction force.

For turbulent heat transfer, [Kuznetsov et al. \(2002\)](#); [Kuznetsov and Xiong, 2003](#); [Kuznetsov, 2004](#)) propose a modeling based on the assumption of turbulent transfer in the clear fluid, while it remains laminar in the porous region. Thus they perform studies that couple a standard k - ϵ model with a turbulent Prandtl in the free region and laminar model in the porous region. However, there exists no study using this scale of description that couples a macroscopic thermal turbulent model in the porous region with a standard thermal turbulent model in the free region. The literature proposes thermal turbulent models for each region separately only. For free regions, the turbulent heat correlation is commonly closed with a first gradient closure related to the turbulent quantities via the turbulent Prandtl model. For homogeneous porous region, the authors follow the models existing in free regions. Thus, [Hsu and Cheng \(1988\)](#) model the averaged turbulent heat correlation by an averaged temperature gradient with

a macroscopic turbulent diffusivity. Then, de Lemos et al. (de Lemos and Rocamora, 2002; de Lemos and Braga, 2003; Braga and de Lemos, 2006) use a macroscopic turbulent Prandtl model that relates the averaged turbulent heat flux to the averaged turbulent quantities.

The issue of this chapter is to investigate the modeling of turbulent heat transfer at a free porous interface at low numerical cost for the interface and turbulence description. Thus, we choose the approach combining a macroscopic turbulent Prandtl model in the homogeneous porous region, a standard turbulent Prandtl model in the free region and boundary conditions at the interface. For the determination of the boundary conditions at the free-porous interface, we use the multi-scale method developed in Chapters 2 and 3 for laminar heat transfer. This method allows to derive the boundary conditions from the local governing equations performing two up-scaling steps and using three levels of description of the interface. For the good understanding of the modeling process, we present the developments for the momentum, turbulent quantities and thermal equations.

The first up-scaling step changes the scale of description from microscopic to mesoscopic using the method presented in Chapter 1. At this scale of description, the transfer equations are valid in the whole domain including the transition zone. The smoothing process makes appear additional non-closed terms related to the turbulence. These quantities are closed introducing new turbulent model characteristic of the mesoscopic scale and valid in the whole domain.

The second up-scaling step changes the scale of description from mesoscopic to macroscopic. At this scale of description, the continuous modeling of the interface is replaced by equivalent closed jump conditions. To derive the boundary conditions from the mesoscopic description, the generic analysis is used, which allows to express the boundary conditions at the free-porous interface as a function of surface excess quantities. The relations obtained are complex and involve unknown terms. In order to close the boundary conditions, we use the knowledge acquired for laminar transfer in Chapters 2 and 3. Thus we are able to propose a closed macroscopic model to characterize the turbulent heat transfer at a free-porous interface. This model is assessed by comparison with the DNS reference results.

In this chapter, the jump conditions that must be applied to couple a macroscopic heat transfer turbulent model in a porous region and a standard heat transfer turbulent model in a free region, are derived using the multi-scale approach presented above. Section 5.2 presents the first up-scaling step and Section 5.3 presents the second up-scaling step. In Section 5.4, the obtained macroscopic model is compared with the results of reference given by the DNS in Chapter 5. The macroscopic turbulent Prandtl model gives accurate results in the free region, but does not capture the correct physics in the porous region. Thus, another model for the macroscopic turbulent flux is proposed that improves the characterization of the turbulence decrease in the porous medium.

6.2 First up-scaling step

6.2.1 Governing equations at the microscopic scale

At the microscopic scale transfers are governed by the Navier-Stokes equations and the energy conservation equation. In the context of the turbulence modeling with the RANS approach, the statistical averaging is applied to the governing equations. The flow being incompressible, it comes at steady state:

$$\frac{\partial \bar{u}_i}{\partial x_i} = 0 \quad (6.1)$$

$$\frac{\partial}{\partial x_j} (\bar{u}_i \bar{u}_j) = -\frac{1}{\rho} \frac{\partial \bar{p}}{\partial x_j} + \nu \frac{\partial^2 \bar{u}_i}{\partial x_j^2} - \frac{\partial}{\partial x_j} (\overline{u'_i u'_j}) \quad (6.2)$$

$$\frac{\partial}{\partial x_i} (\bar{u}_i \bar{T}) = \frac{\partial}{\partial x_i} \left(\alpha \frac{\partial \bar{T}}{\partial x_i} \right) - \frac{\partial}{\partial x_i} (\overline{u'_i T'}) \quad (6.3)$$

The equations (6.2) and (6.3) are not closed due to the turbulent momentum correlation $\overline{u'_i u'_j}$ and the turbulent heat correlation $\overline{u'_i T'}$.

To close the momentum equation (6.2), the Reynolds constraint $\overline{u'_i u'_j}$ is modeled introducing a turbulent viscosity ν_t :

$$\overline{u'_i u'_j} = -\nu_t \left(\frac{\partial \bar{u}_i}{\partial x_j} + \frac{\partial \bar{u}_j}{\partial x_i} \right) + \frac{2}{3} k \delta_{ij} \quad (6.4)$$

and the standard k - ϵ turbulent modeling:

$$\nu_t = C_\mu \frac{k^2}{\epsilon} \quad (6.5)$$

$$\frac{\partial}{\partial x_i} (\bar{u}_i k) = \frac{\partial}{\partial x_i} \left[\left(\nu + \frac{\nu_t}{\sigma_k} \right) \frac{\partial k}{\partial x_i} \right] + P - \epsilon \quad (6.6)$$

$$\frac{\partial}{\partial x_i} (\bar{u}_i \epsilon) = \frac{\partial}{\partial x_i} \left[\left(\nu + \frac{\nu_t}{\sigma_\epsilon} \right) \frac{\partial \epsilon}{\partial x_i} \right] + (c_1 P - c_2 \epsilon) \frac{\epsilon}{k} \quad (6.7)$$

where P is the turbulent production due to the averaged velocity gradients and defined by:

$$P_k = \nu_t \left(\frac{\partial \bar{u}_i}{\partial x_j} + \frac{\partial \bar{u}_j}{\partial x_i} \right) \frac{\partial \bar{u}_i}{\partial x_j} \quad (6.8)$$

Using the turbulent viscosity hypothesis, the momentum equation becomes:

$$\frac{\partial}{\partial x_j} (\bar{u}_i \bar{u}_j) = -\frac{\partial}{\partial x_j} \left(\bar{p} + \frac{2}{3} k \right) + \frac{\partial}{\partial x_j} \left((\nu + \nu_t) \left(\frac{\partial \bar{u}_i}{\partial x_j} + \frac{\partial \bar{u}_j}{\partial x_i} \right) \right) \quad (6.9)$$

Thus, the momentum transfer is described at the microscopic scale with the standard k - ϵ turbulent model. For the constant associated to this modeling, one uses the values recommended by [Launder and Spalding \(1972\)](#):

$$C_\mu = 0.09, \quad c_1 = 1.44, \quad c_2 = 1.92, \quad \sigma_k = 1.00, \quad \sigma_\epsilon = 1.3 \quad (6.10)$$

In order to close the energy equation (6.3), the turbulent correlation $\overline{u'_j T'}$ is modeled with the closure assumption of the first gradient:

$$-\overline{u'_j T'} = \alpha_t \frac{\partial \bar{T}}{\partial x_j} \quad (6.11)$$

where α_t is a thermal turbulent diffusivity. This quantity is closed using the turbulent Prandtl model, that relates the turbulent thermal diffusivity to the turbulent viscosity ν_t via a turbulent Prandtl number:

$$\alpha_t = \frac{\nu_t}{Pr_t}, \text{ with } Pr_t \approx 0.9 \quad (6.12)$$

This model is based on the consideration that, the temperature being a passive scalar, its turbulent length scale corresponds to the momentum one.

Thus, the energy equation can be rewritten as follows:

$$\frac{\partial}{\partial x_i} (\bar{u}_i \bar{T}) = \frac{\partial}{\partial x_i} \left((\alpha + \alpha_t) \frac{\partial \bar{T}}{\partial x_i} \right) \quad (6.13)$$

At the microscopic scale, the turbulence is described using the k - ϵ model for the momentum transfer and the turbulent Prandtl model for the heat transfer. Thus, the governing equations are closed and we can perform the first up-scaling step.

6.2.2 Governing equations at the mesoscopic scale

6.2.2.1 Continuity and momentum equations

The modeling at the mesoscopic scale is obtained applying the volume averaging operator to the local governing equations (6.1) and (6.9). Using the permutation rule between the integral and the derivation operators presented in Chapter 1, it comes:

$$\frac{\partial \langle \bar{u}_i \rangle}{\partial x_i} = 0 \quad (6.14)$$

$$\frac{\partial}{\partial x_j} \left(\frac{\langle \bar{u}_i \rangle \langle \bar{u}_j \rangle}{\phi} \right) + \frac{\partial \tau_u^{ij}}{\partial x_j} = -\frac{1}{\rho} \frac{\partial \langle \bar{p} \rangle}{\partial x_i} + \frac{\partial}{\partial x_j} \left(\nu \frac{\partial \langle \bar{u}_i \rangle}{\partial x_j} \right) + \frac{\partial}{\partial x_j} \left\langle \nu_t \left(\frac{\partial \bar{u}_i}{\partial x_j} + \frac{\partial \bar{u}_j}{\partial x_i} \right) \right\rangle + f_l^i \quad (6.15)$$

where τ_u^{ij} is the momentum dispersion tensor and f_l^i the volume force applied to the fluid phase by the solid phase. As seen in Chapter 5, they are defined by:

$$\tau_u^{ij} = \langle \bar{u}_i \bar{u}_j \rangle - \frac{\langle \bar{u}_i \rangle \langle \bar{u}_j \rangle}{\phi} \quad (6.16)$$

$$f_l^i = \frac{1}{V} \int_{A_i} \left(\nu \frac{\partial \bar{u}_i}{\partial x_j} - \frac{\bar{p}}{\rho} \delta_{ij} \right) \cdot n_j dS \quad (6.17)$$

The equation (6.15) is obtained using the non-slip condition at the fluid-solid interface A_i for the spatial deviation of the velocity. This condition leads to the turbulent viscosity ν_t null at the wall via a turbulent diffusion $\bar{u}_i' \bar{u}_j'$.

In order to model the averaged turbulent Reynolds tensor, one uses the idea proposed by Pedras and de Lemos (2001) for a homogeneous porous medium. They define a macroscopic turbulent viscosity $\nu_{t\phi}$ such that:

$$\left\langle \nu_t \left(\frac{\partial \bar{u}_i}{\partial x_j} + \frac{\partial \bar{u}_j}{\partial x_i} \right) \right\rangle = \nu_{t\phi} \left\langle \left(\frac{\partial \bar{u}_i}{\partial x_j} + \frac{\partial \bar{u}_j}{\partial x_i} \right) \right\rangle = \nu_{t\phi} \left(\frac{\partial \langle \bar{u}_i \rangle}{\partial x_j} + \frac{\partial \langle \bar{u}_j \rangle}{\partial x_i} \right) \quad (6.18)$$

using the non-slip coefficient at the fluid-solid interface.

To model the macroscopic turbulent viscosity $\nu_{t\phi}$, Pedras and de Lemos (2001) propose the following definition inspired from the k - ϵ model:

$$\nu_{t\phi} = C_\mu \frac{(\langle k \rangle^f)^2}{\langle \epsilon \rangle^f} \quad (6.19)$$

This assumption has not been verified by Pedras and de Lemos (2001). But it seems reasonable for turbulent heat transfer in a fluid-porous domain. Indeed, using the DNS presented in Chapter 5, we compare $\nu_{t\phi}^{\text{DNS}}$ and $\nu_{t\phi}^{\text{model}}$ defined by:

$$\nu_{t\phi}^{\text{DNS}} = \frac{\langle \bar{u}_i' \bar{u}_j' \rangle}{\left(\frac{\partial \langle \bar{u}_i \rangle}{\partial x_j} + \frac{\partial \langle \bar{u}_j \rangle}{\partial x_i} \right)}, \quad \nu_{t\phi}^{\text{model}} = C_\mu \frac{(\langle k \rangle^f)^2}{\langle \epsilon \rangle^f} \quad (6.20)$$

where $\bar{u}_i' \bar{u}_j'$, $\frac{\partial \bar{u}_i}{\partial x_j}$, k and ϵ are computed from the DNS data. The comparison between $\nu_{t\phi}^{\text{DNS}}$ and $\nu_{t\phi}^{\text{model}}$ is presented in Fig. 6.1. The order of magnitude is verified. Thus, the definition (6.19) gives a correct approximation of the mesoscopic turbulent viscosity in a free-porous domain.

The governing momentum equation at the mesoscopic scale is:

$$\frac{\partial}{\partial x_j} \left(\frac{\langle \bar{u}_i \rangle \langle \bar{u}_j \rangle}{\phi} \right) + \frac{\partial \tau_u^{ij}}{\partial x_j} = -\frac{1}{\rho} \frac{\partial \langle \bar{p} \rangle}{\partial x_i} + \frac{\partial}{\partial x_j} \left(\nu \frac{\partial \langle \bar{u}_i \rangle}{\partial x_j} \right) + \frac{\partial}{\partial x_j} \nu_{t\phi} \left(\frac{\partial \langle \bar{u}_i \rangle}{\partial x_j} + \frac{\partial \langle \bar{u}_j \rangle}{\partial x_i} \right) + f_l^i \quad (6.21)$$

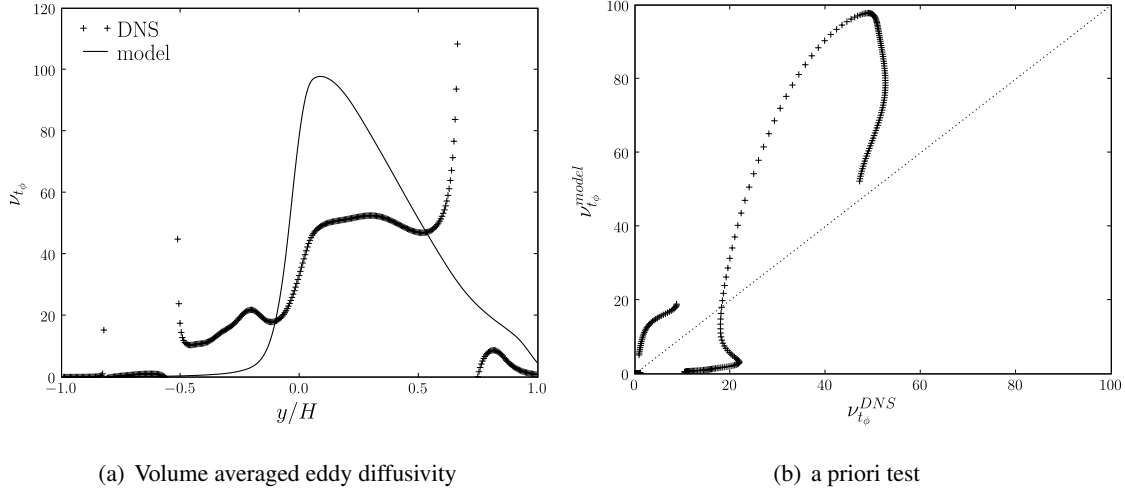


Figure 6.1: Profiles of volume averaged eddy diffusivity.

The equation (6.21) is not closed due to terms characteristic of the local scale in τ_u^{ij} and f_l^i . Thus to close (6.21), the momentum dispersion tensor τ_u^{ij} and the volume force f_l^i must be modeled. The closure relations are proposed in Section 6.2.3.

6.2.2.2 Kinetic energy and dissipation rate equations

The mesoscopic equations of the kinetic energy $\langle k \rangle$ and the dissipation rate $\langle \epsilon \rangle$ are obtained applying the volume averaging operator to the local equations (6.6) and (6.7). Using the permutation rule between the integral and derivation operators presented in Chapter 1, it comes:

$$\frac{\partial}{\partial x_i} \left(\frac{\langle \bar{u}_i \rangle \langle k \rangle}{\phi} \right) + \frac{\partial \tau_k^i}{\partial x_i} = \frac{\partial}{\partial x_i} \left[\left(\nu + \frac{\nu_{t\phi}}{\tilde{\sigma}_k} \right) \frac{\partial \langle k \rangle}{\partial x_i} \right] + \langle P \rangle - \langle \epsilon \rangle \quad (6.22)$$

$$\frac{\partial}{\partial x_i} \left(\frac{\langle \bar{u}_i \rangle \langle \epsilon \rangle}{\phi} \right) + \frac{\partial \tau_\epsilon^i}{\partial x_i} = \frac{\partial}{\partial x_i} \left[\left(\nu + \frac{\nu_{t\phi}}{\tilde{\sigma}_\epsilon} \right) \frac{\partial \langle \epsilon \rangle}{\partial x_i} \right] + \left\langle (c_1 P - c_2 \epsilon) \frac{\epsilon}{k} \right\rangle + f_\epsilon \quad (6.23)$$

where τ_k and τ_ϵ are the sub-filter vectors associated to the transport of k and ϵ respectively. They are defined as follows:

$$\tau_k = \langle \bar{u}_i k \rangle - \frac{\langle \bar{u}_i \rangle \langle k \rangle}{\phi} \quad (6.24)$$

$$\tau_\epsilon^i = \langle \bar{u}_i \epsilon \rangle - \frac{\langle \bar{u}_i \rangle \langle \epsilon \rangle}{\phi} \quad (6.25)$$

$\tilde{\sigma}_k$ and $\tilde{\sigma}_\epsilon$ are macroscopic turbulent Prandtl numbers. They are introduced because the microscopic turbulent viscosity ν_t is not constant inside the representative elementary volume. They are defined such that:

$$\left\langle \frac{\nu_t}{\sigma_k} \frac{\partial k}{\partial x_i} \right\rangle = \frac{\nu_{t\phi}}{\tilde{\sigma}_k} \left\langle \frac{\partial k}{\partial x_i} \right\rangle \quad (6.26)$$

$$\left\langle \frac{\nu_t}{\sigma_\epsilon} \frac{\partial \epsilon}{\partial x_i} \right\rangle = \frac{\nu_{t\phi}}{\tilde{\sigma}_\epsilon} \left\langle \frac{\partial \epsilon}{\partial x_i} \right\rangle \quad (6.27)$$

and are supposed constant. The macroscopic turbulent Prandtl numbers are not computed and the local turbulent Prandtl numbers σ_k and σ_ϵ are used instead.

Furthermore, the equations (6.22) and (6.23) are obtained using the non-slip condition at the wall for k and its gradient. This condition is not verified for ϵ and the commutation between the integral and derivation operators creates additional terms brought together in f_ϵ^i :

$$f_\epsilon^i = \frac{1}{V} \int_{A_i} \nu \frac{\partial \epsilon}{\partial x_i} n_i dS + \frac{\partial}{\partial x_i} \left(\left(\nu + \frac{\nu_{t_\phi}}{\tilde{\sigma}_\epsilon} \right) \frac{1}{V} \int_{A_i} \epsilon n_i dS \right) \quad (6.28)$$

Then, following Nakayama and Kuwahara (1999), the production terms $\langle P \rangle$ and $\langle (c_1 P - c_2 \epsilon) \frac{\epsilon}{k} \rangle$ are separated into two contributions: a mesoscopic production term coming from the mesoscopic velocity gradient, and a sub-filter production term:

$$\langle P \rangle = \left\langle \nu_t \left(\frac{\partial \bar{u}_i}{\partial x_j} + \frac{\partial \bar{u}_j}{\partial x_i} \right) \frac{\partial \bar{u}_i}{\partial x_j} \right\rangle = \nu_{t_\phi} \left(\frac{\partial \langle \bar{u}_i \rangle}{\partial x_j} + \frac{\partial \langle \bar{u}_j \rangle}{\partial x_i} \right) \frac{\partial \langle \bar{u}_i \rangle}{\partial x_j} + P_k \quad (6.29)$$

$$\left\langle (c_1 P_k - c_2 \epsilon) \frac{\epsilon}{k} \right\rangle = \left\langle \left(c_1 \nu_t \left(\frac{\partial \bar{u}_i}{\partial x_j} + \frac{\partial \bar{u}_j}{\partial x_i} \right) \frac{\partial \bar{u}_i}{\partial x_j} - c_2 \epsilon \right) \frac{\epsilon}{k} \right\rangle \quad (6.30)$$

$$= \left(c_1 \nu_{t_\phi} \left(\frac{\partial \langle \bar{u}_i \rangle}{\partial x_j} + \frac{\partial \langle \bar{u}_j \rangle}{\partial x_i} \right) \frac{\partial \langle \bar{u}_i \rangle}{\partial x_j} - c_2 \langle \epsilon \rangle \right) \frac{\langle \epsilon \rangle}{\langle k \rangle} + S_\epsilon \quad (6.31)$$

where P_k and S_ϵ are the sub-filter production terms.

The equations for $\langle k \rangle$ and $\langle \epsilon \rangle$ become:

$$\frac{\partial}{\partial x_i} \left(\frac{\langle u_i \rangle \langle k \rangle}{\phi} \right) + \frac{\partial \tau_k^i}{\partial x_i} = \frac{\partial}{\partial x_i} \left[\left(\nu + \frac{\nu_t}{\tilde{\sigma}_k} \right) \frac{\partial \langle k \rangle}{\partial x_i} \right] + \nu_{t_\phi} \left(\frac{\partial \langle \bar{u}_i \rangle}{\partial x_j} + \frac{\partial \langle \bar{u}_j \rangle}{\partial x_i} \right) \frac{\partial \langle \bar{u}_i \rangle}{\partial x_j} + P_k - \langle \epsilon \rangle \quad (6.32)$$

$$\frac{\partial}{\partial x_i} \left(\frac{\langle u_i \rangle \langle \epsilon \rangle}{\phi} \right) + \frac{\partial \tau_\epsilon^i}{\partial x_i} = \frac{\partial}{\partial x_i} \left[\left(\nu + \frac{\nu_t}{\tilde{\sigma}_\epsilon} \right) \frac{\partial \langle \epsilon \rangle}{\partial x_i} \right] + \left(c_1 \nu_{t_\phi} \left(\frac{\partial \langle \bar{u}_i \rangle}{\partial x_j} + \frac{\partial \langle \bar{u}_j \rangle}{\partial x_i} \right) \frac{\partial \langle \bar{u}_i \rangle}{\partial x_j} - c_2 \langle \epsilon \rangle \right) \frac{\langle \epsilon \rangle}{\langle k \rangle} + P_\epsilon \quad (6.33)$$

where P_ϵ is the sum of the sub-filter production S_ϵ and the additional term f_ϵ coming from the commutation:

$$P_\epsilon = S_\epsilon + f_\epsilon \quad (6.34)$$

To close (6.32) and (6.33), the sub-filter production terms P_k and P_ϵ , the subfilter dispersion vectors τ_k^i and τ_ϵ^i must be modeled. The closure relations are proposed in Section 6.2.3.

6.2.2.3 Energy conservation equation

The mesoscopic modeling of the energy equation is obtained applying the volume averaging operator on the equation (6.13). Using the permutation rule between the integral and derivation operators presented in Chapter 1, it comes:

$$\frac{\partial}{\partial x_i} \left(\phi \langle \bar{u}_i \rangle^f \langle \bar{T} \rangle^f \right) + \frac{\partial \tau_{uT}^i}{\partial x_i} = \frac{\partial}{\partial x_i} \left(\alpha \phi \frac{\partial \langle \bar{T} \rangle^f}{\partial x_i} + \phi \left\langle \alpha_t \frac{\partial \bar{T}}{\partial x_i} \right\rangle^f \right) + T_{or} + \mathcal{P} \quad (6.35)$$

where τ_{uT}^i is the dispersive vector, T_{or} the tortuosity and \mathcal{P} the wall heat flux. As seen in the previous Chapter, there are defined by:

$$\tau_{uT}^i = \langle \bar{u}_i \bar{T} \rangle - \phi \langle \bar{u}_i \rangle^f \langle \bar{T} \rangle^f \quad (6.36)$$

$$T_{or} = \frac{\partial}{\partial x_i} \left(\frac{1}{V} \int_{A_i} \alpha \left(\bar{T} - \langle \bar{T} \rangle^f(x_0) \right) n_i dS \right) \quad (6.37)$$

$$\mathcal{P} = \frac{1}{V} \int_{A_i} \alpha \frac{\partial \bar{T}}{\partial x_i} n_i dS + \underbrace{\frac{1}{V} \int_{A_i} \alpha_t \frac{\partial \bar{T}}{\partial x_i} n_i dS}_{=0} \quad (6.38)$$

since $\overline{u'T'} = 0$ at the fluid-solid interface A_i .

de Lemos and Rocamora (2002) propose a model for the averaged turbulent heat flux based on two considerations. First, they consider a constant turbulent Prandtl number model, second they use the passive characteristic of the temperature to assume that the modeling process between $\langle \nu_t \partial \langle \overline{T} \rangle^f / \partial x_i \rangle$ and $\langle \nu_t \left(\frac{\partial \overline{u}_i}{\partial x_j} + \frac{\partial \overline{u}_j}{\partial x_i} \right) \rangle$ are identical. Thus, by similarity with the relation (6.18), they write:

$$\frac{1}{Pr_t} \left\langle \nu_t \frac{\partial \langle \overline{T} \rangle^f}{\partial x_i} \right\rangle = \frac{\nu_{t_\phi}}{Pr_t} \frac{\partial \langle \overline{T} \rangle^f}{\partial x_i} \quad (6.39)$$

This assumption is very strong and might be inappropriate at a free-porous interface. We prefer to follow another approach and define a mesoscopic turbulent thermal diffusivity α_{t_ϕ} such that:

$$\left\langle \alpha_t \frac{\partial \overline{T}}{\partial x_i} \right\rangle^f = \alpha_{t_\phi} \frac{\partial \langle \overline{T} \rangle^f}{\partial x_i} \quad (6.40)$$

This first modeling step consists in relating the averaged turbulent heat flux to the averaged temperature gradient as presented in Section 5.4.3.6:

$$\left\langle \overline{u'_i T'} \right\rangle^f = \alpha_{t_\phi} \frac{\partial \langle \overline{T} \rangle^f}{\partial x_i} \quad (6.41)$$

The validity of this model in the y -direction is verified in Section 5.4.3.6 and using the DNS data one can compute a mesoscopic turbulent diffusivity of reference $\alpha_{t_\phi}^{\text{DNS}}$ given by (see Fig. 5.19 in Chapter 5):

$$\alpha_{t_\phi}^{\text{DNS}} = \frac{\langle \overline{v' T'} \rangle^f}{\partial \langle \overline{T} \rangle^f / \partial y} \quad (6.42)$$

This model is not closed and requires the closure of α_{t_ϕ} in function of averaged quantities characteristic of the flow. In the second modeling step, we propose a closure for the mesoscopic turbulent diffusivity inspired from the turbulent Prandtl model for free flow, that relates α_{t_ϕ} to ν_{t_ϕ} such that:

$$\alpha_{t_\phi} = \frac{\nu_{t_\phi}}{Pr_{t_\phi}}, \text{ with } Pr_{t_\phi} = 0.9 \quad (6.43)$$

This closure relies on the assumption that the length scale of the averaged turbulence is identical for the flow and the heat transfer. This assumption is strong especially at a free-porous interface. For a first verification, a modeled mesoscopic turbulent diffusivity is computed using the DNS data such that:

$$\alpha_{t_\phi}^{\text{model}} = C_\mu \frac{(\langle k \rangle^f)^2}{\langle \epsilon \rangle^2} \frac{1}{Pr_{t_\phi}} \quad (6.44)$$

The comparison between $\alpha_{t_\phi}^{\text{model}}$ and the $\alpha_{t_\phi}^{\text{DNS}}$ of reference is presented in Fig. 6.2. The order of magnitude is verified. Thus, the closure (6.43) gives a correct approximation of the mesoscopic turbulent diffusivity of reference in a free-porous domain.

The mesoscopic equation for $\langle T \rangle^f$ becomes:

$$\frac{\partial}{\partial x_i} \left(\phi \langle \overline{u}_i \rangle^f \langle \overline{T} \rangle^f \right) + \frac{\partial \tau_{uT}^i}{\partial x_i} = \frac{\partial}{\partial x_i} \left(\phi (\alpha + \alpha_{t_\phi}) \frac{\partial \langle \overline{T} \rangle^f}{\partial x_i} \right) + T_{or} + \mathcal{P} \quad (6.45)$$

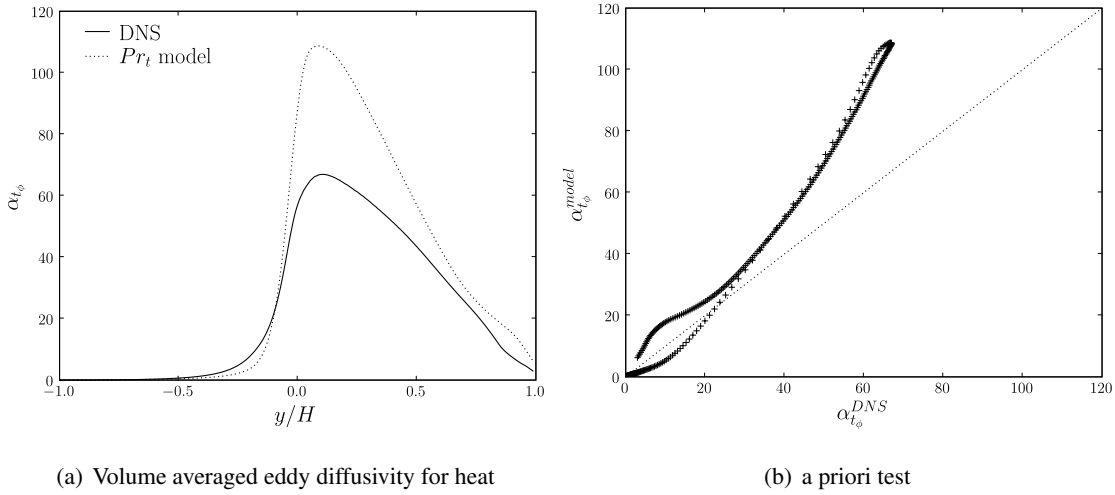


Figure 6.2: Profiles of volume averaged eddy diffusivity.

This equation is not closed due to τ_{uT}^i and T_{or} that involve local terms characteristic of the microscopic scale. In order to close the equation (6.45), the dispersion term τ_{uT}^i and the tortuosity term T_{or} must be modeled. We recall that \mathcal{P} is known and corresponds to the averaged flux at cubes.

The turbulent model derived at the mesoscopic scale using the volume averaging operator is presented in the system (6.46). The closure of the model requires the modeling of height terms: τ_u^{ij} , τ_k^i , τ_ϵ , τ_{uT}^i , f_l^i , T_{or} , P_k and P_ϵ . The closure relations used in the homogeneous region and the transition zone are discussed in the following.

$$\frac{\partial \langle \bar{u}_i \rangle}{\partial x_i} = 0 \quad (6.46a)$$

$$\frac{\partial}{\partial x_j} \left(\frac{\langle \bar{u}_i \rangle \langle \bar{u}_j \rangle}{\phi} \right) + \frac{\partial \tau_u^{ij}}{\partial x_j} = -\frac{1}{\rho} \frac{\partial \langle \bar{p} \rangle}{\partial x_i} + \frac{\partial}{\partial x_j} \left(\nu \frac{\partial \langle \bar{u}_i \rangle}{\partial x_j} \right) + \frac{\partial}{\partial x_j} \nu_{t\phi} \left(\frac{\partial \langle \bar{u}_i \rangle}{\partial x_j} + \frac{\partial \langle \bar{u}_j \rangle}{\partial x_i} \right) + f_l^i \quad (6.46b)$$

$$\frac{\partial}{\partial x_i} \left(\frac{\langle u_i \rangle \langle k \rangle}{\phi} \right) + \frac{\partial \tau_k^i}{\partial x_i} = \frac{\partial}{\partial x_i} \left[\left(\nu + \frac{\nu_t}{\tilde{\sigma}_k} \right) \frac{\partial \langle k \rangle}{\partial x_i} \right] + \nu_{t\phi} \left(\frac{\partial \langle \bar{u}_i \rangle}{\partial x_j} + \frac{\partial \langle \bar{u}_j \rangle}{\partial x_i} \right) \frac{\partial \langle \bar{u}_i \rangle}{\partial x_j} + P_k - \langle \epsilon \rangle \quad (6.46c)$$

$$\frac{\partial}{\partial x_i} \left(\frac{\langle u_i \rangle \langle \epsilon \rangle}{\phi} \right) + \frac{\partial \tau_\epsilon^i}{\partial x_i} = \frac{\partial}{\partial x_i} \left[\left(\nu + \frac{\nu_t}{\tilde{\sigma}_\epsilon} \right) \frac{\partial \langle \epsilon \rangle}{\partial x_i} \right] + \left(c_1 \nu_{t\phi} \left(\frac{\partial \langle \bar{u}_i \rangle}{\partial x_j} + \frac{\partial \langle \bar{u}_j \rangle}{\partial x_i} \right) \frac{\partial \langle \bar{u}_i \rangle}{\partial x_j} - c_2 \langle \epsilon \rangle \right) \frac{\langle \epsilon \rangle}{\langle k \rangle} + P_\epsilon \quad (6.46d)$$

$$\frac{\partial}{\partial x_i} \left(\phi \langle \bar{u}_i \rangle^f \langle \bar{T} \rangle^f \right) + \frac{\partial \tau_{uT}^i}{\partial x_i} = \frac{\partial}{\partial x_i} \left(\phi (\alpha + \alpha_{t\phi}) \frac{\partial \langle \bar{T} \rangle^f}{\partial x_i} \right) + T_{or} + \mathcal{P} \quad (6.46e)$$

$$\text{with} \quad \nu_{t\phi} = C_\mu \frac{(\langle k \rangle^f)^2}{\langle \epsilon \rangle^f}, \quad \alpha_{t\phi} = \frac{\nu_{t\phi}}{Pr_{t\phi}} \quad (6.46f)$$

6.2.3 Closed mesoscopic equations

At the mesoscopic scale, the averaged turbulent model is valid in the whole domain, *i.e* in the homogeneous regions and in the transition zone. However this model is not closed due to the presence of local quantities in the terms of friction, sub-filter dispersion and sub-filter production. To characterize the transfer at the mesoscopic scale and perform the second up-scaling step, these terms must be closed. For the momentum, the kinetic energy and the dissipation rate equations ((6.46b), (6.46c) and (6.46d)) we use the closure relations proposed by Chandesris and Jamet (2009b). Six terms remain that we do not characterize in the transition zone. However this information is not necessary to perform the second up-scaling step, as we will see in Section 6.3.

For the heat transfer, the averaged mesoscopic model (6.46e) is similar to the non-closed mesoscopic equation obtained for laminar studies. Thus, to close the equation (6.46e), we use the method performed for laminar transfer in Chapters 2 and 3.

6.2.3.1 Momentum transfer and turbulent quantities

The closure at the mesoscopic scale is done by Chandesris and Jamet (2009b). We present here the main results.

In the free region, the porosity is constant $\phi = 1$ and there is no solid. The friction term f_l^i present in the equation (6.46b) is null. Furthermore, the terms of sub-filter production P_k and P_ϵ are also null because their expression ((6.31) and (6.29)) involve solid quantities only. Another simplification can be done in the free region, if the filter size is smaller than the scale of variation of the averaged quantities. In this case, the averaged quantities are equivalent to the local quantities ($\langle \bar{u} \rangle \approx \bar{u}$, $\langle k \rangle \approx k$ and $\langle \epsilon \rangle \approx \epsilon$) and the sub-filter dispersions τ_u^{ij} , τ_k^i and τ_ϵ^i are null.

Thus, the equations (6.46b), (6.31) and (6.29) are identical to the equations of the standard turbulent k - ϵ model (6.6), (6.7) and the associated momentum equation (6.2).

In the homogeneous porous region, closure relations must be specified for the friction term f_l^i , for the production terms P_k and P_ϵ , and for the sub-filter dispersion terms τ_u^{ij} , τ_k^i and τ_ϵ^i .

The sub-filter dispersion terms are almost constant in the homogeneous porous region, and their divergence in the equations (6.46b), (6.46c) and (6.46d) is neglected. Thus, the influence of the sub-filter dispersion terms is not considered in the closed mesoscopic model.

For the friction term f_l^i and the production terms P_k and P_ϵ , their closure relation depend directly on the geometry of the porous medium. Concerning the friction term f_l^i , different correlations exist depending different communities. In the community of natural porous medium, the friction term is modeled with the Darcy-Forchheimer law:

$$f_l^i = -\nu \mathcal{K}^{-1} (1 + \mathcal{F}) \langle \bar{u}_i \rangle \quad (6.47)$$

where \mathcal{K} is the permeability and \mathcal{F} the Forchheimer coefficient.

For the sub-filter production terms P_k and P_ϵ , we use the correlations proposed by Nakayama and Kuwahara (1999) for porous media made of cubes:

$$P_k = \epsilon_\infty \quad (6.48a)$$

$$P_\epsilon = c_2 \frac{\epsilon_\infty^2}{k_\infty} \quad (6.48b)$$

$$\epsilon_\infty = 39 \phi^2 (1 - \phi)^{5/2} \frac{\langle \bar{u} \rangle^3}{d_p} \quad (6.48c)$$

$$k_\infty = 3.7 (1 - \phi) \phi^{3/2} \langle \bar{u} \rangle^2 \quad (6.48d)$$

In the homogeneous porous region, the equations (6.46b), (6.46c) and (6.46d) are closed when the terms f_l^i , P_k and P_ϵ are computed for the studied porous medium and for the Reynolds numbers considered.

In the transition zone, the closure of the equations (6.46b), (6.46c) and (6.46d), requires the determination of six terms f_l^i , P_k , P_ϵ , τ_u^{ij} , τ_k^i and τ_ϵ .

These quantities vary continuously in the transition zone and the divergence of the dispersive terms is not null. Thus, the correlations giving f_l^i , P_k and P_ϵ in the homogeneous porous region are not valid. In the transition zone, the quantities f_l^i , P_k , P_ϵ , τ_u^{ij} , τ_k^i and τ_ϵ are not known and the equations (6.46b), (6.46c) and (6.46d) are not closed. However the issue is to propose a modeling at the macroscopic scale and we do not need to characterize precisely these terms in the transition zone. Indeed at the macroscopic scale, the continuous interface is substituted by a surface of discontinuity and the value of these terms is not used directly. We model only the impact of their variation on the homogeneous regions with jump conditions at the interface.

We notice that the quantities f_l^i , P_k , P_ϵ , τ_u^{ij} , τ_k^i and τ_ϵ can be computed with the data given by the DNS. However, this degree of information is not necessary to derive a closed macroscopic k - ϵ model as we will see in Section 6.3. Of course it could bring some improvements. Nevertheless it is not the issue of this chapter, that is to present a macroscopic model for the turbulent heat transfer at a free-porous interface. Thus, for the remainder of the study, we assume that the terms f_l^i , P_k , P_ϵ , τ_u^{ij} , τ_k^i and τ_ϵ vary continuously in the transition zone, without specifying these variations.

6.2.3.2 Heat transfer

In order to close the heat transfer equation (6.46e), closure relations for the thermal dispersion τ_{uT}^i and the turbulent tortuosity T_{or} must be proposed. Using the method performed in Chapters 2 and 3, a closed model is derived in the homogeneous porous region and we assume its validity in the whole domain including the transition zone. The relation of the effective transfer coefficients are determined comparing the closed and the non-closed model.

In the free region, the porosity is constant $\phi = 1$ and there is no solid. The turbulent tortuosity T_{or} and the injected heat \mathcal{P} are null. Furthermore, the filter size is supposed to be smaller than the scale of variation of the averaged quantities. The averaged quantities are equivalent to the local quantities ($\langle \bar{u} \rangle \approx \bar{u}$, $\langle \bar{T} \rangle \approx \bar{T}$) and the thermal dispersion tensor τ_{uT}^i is null.

Thus, in the free region, the temperature equation (6.46e) is identical to the local turbulent Prandtl model (6.13).

In the homogeneous porous region, we close the dispersion vector τ_{uT}^i and the turbulent tortuosity T_{or} using the closure relation for the spatial deviation temperature. Drouin et al. (2010) present the full closure below:

$$\tilde{\bar{T}} = b_i \frac{\partial \langle \bar{T} \rangle^f}{\partial x_i} + s \mathcal{P} \quad (6.49)$$

where b_i and s are the vector and scalar fields mapping $\nabla \langle T_f \rangle^f$ and \mathcal{P} onto $\tilde{\bar{T}}$. The closure relation (6.49) is injected in the open terms τ_{uT}^i and T_{or} . Considering the length scale separation, one obtains the following closed relations:

$$-\tau_{uT}^i = D_{ij}^p \frac{\partial \langle \bar{T} \rangle^f}{\partial x_i} + D_i^a \mathcal{P} \quad (6.50)$$

$$T_{or} = \frac{\partial}{\partial x_i} \left(\phi \alpha_{ij}^{or} \frac{\partial \langle \bar{T} \rangle^f}{\partial x_i} \right) + \frac{\partial}{\partial x_i} (T_i^a \mathcal{P}) \quad (6.51)$$

where the coefficients correspond to:

- a passive dispersive tensor:

$$D_{ij}^p = - \left\langle b_j \tilde{u}_i \right\rangle \quad (6.52)$$

- an active dispersive vector:

$$D_i^a = - \left\langle s \tilde{u}_i \right\rangle \quad (6.53)$$

- a passive tortuosity tensor:

$$\alpha_{ij}^{or} = \frac{\alpha}{V} \int_{A_i} b_j n_i dS \quad (6.54)$$

- an active tortuosity vector:

$$T_i^a = \frac{\alpha}{V} \int_{A_i} s n_i dS \quad (6.55)$$

Using these writings in (6.45), the following closed turbulent temperature model is derived:

$$\frac{\partial}{\partial x_i} \left(\phi \langle \bar{u}_i \rangle^f \langle \bar{T} \rangle^f \right) = \frac{\partial}{\partial x_i} \left([\phi(\alpha + \alpha_{t\phi} + \alpha_{ij}^{or}) + D_{ij}^p] \frac{\partial \langle \bar{T} \rangle^f}{\partial x_i} \right) + \frac{\partial}{\partial x_i} ((D_i^a + T_i^a) \mathcal{P}) + \mathcal{P} \quad (6.56)$$

The analytical relation of the effective coefficients D_{ij}^p , D_i^a , α_{ij}^{or} and T_i^a are determined comparing the non-closed relations ((6.36), (6.37) and the closed ones ((6.50), (6.51). It results the following system:

$$D_{ij}^p \frac{\partial \langle \bar{T} \rangle^f}{\partial x_i} + D_i^a \mathcal{P} = \langle \bar{u}_i \bar{T} \rangle - \phi \langle \bar{u}_i \rangle^f \langle \bar{T} \rangle^f \quad (6.57)$$

$$\frac{\partial}{\partial x_i} \left(\phi \alpha_{ij}^{or} \frac{\partial \langle \bar{T} \rangle^f}{\partial x_i} \right) + \frac{\partial}{\partial x_i} (T_i^a \mathcal{P}) = \frac{\partial}{\partial x_i} \left(\frac{1}{V} \int_{A_i} \alpha (\bar{T} - \langle \bar{T} \rangle^f(x_0)) n_i dS \right) \quad (6.58)$$

The computation of the effective coefficients requires two numerical simulations to obtain two temperatures fields and solve a system composed of four unknowns and four equations.

In the transition zone, as for the homogeneous porous medium, the dispersion τ_{uT}^i and the turbulent tortuosity T_{or} must be closed. In the transition zone, the length scale separation is not valid and the commutation between the integral and derivation operator is not possible. Nevertheless, to close the mesoscopic equation (6.46e), we assume that the closed mesoscopic equation (6.56) is valid in the transition zone. The effective coefficients are determined comparing the closed and non-closed models, that leads to the relations (6.57) and (6.58).

The closed mesoscopic equation (6.56) involves all the phenomena and requires the determination of four effective transfer coefficient D_{ij}^p , D_i^a , α_{ij}^{or} and T_i^a . However in the context of our study, simplifications can be done that reduce the number of effective transfer coefficient as we will see in the following.

6.2.4 1D problem

Once the statistical and the volume averages are applied, the turbulent flow is 1D at the mesoscopic scale. Such a turbulent flow allows some simplifications on the mesoscopic temperature field.

Governing equations at the mesoscopic scale

From the continuity equation and the non slip condition at the upper-wall, the velocity is null in the y -direction $\langle \bar{v} \rangle = 0$. At the mesoscopic scale the system reduces to:

$$0 = \underbrace{-\frac{1}{\rho} \frac{\partial \langle \bar{p} \rangle}{\partial x}}_{f_p} + \underbrace{\frac{\partial}{\partial y} \left((\nu + \nu_{t_\phi}) \frac{\partial \langle \bar{u} \rangle}{\partial y} \right)}_{f_v} + \underbrace{\phi \nu \frac{1 + \mathcal{F}}{\mathcal{K}} \langle \bar{u} \rangle}_{f_t^i} \quad (6.59a)$$

$$0 = \underbrace{\frac{\partial}{\partial y} \left[\left(\nu + \frac{\nu_{t_\phi}}{\tilde{\sigma}_k} \right) \frac{\partial \langle k \rangle}{\partial y} \right]}_{\text{diff}_k} + \underbrace{\nu_{t_\phi} \left(\frac{\partial \langle \bar{u} \rangle}{\partial y} \right)^2}_{\text{prodM}_k} + \underbrace{P_k}_{\text{prod}_k} - \underbrace{\langle \epsilon \rangle}_{\text{diss}_k} \quad (6.59b)$$

$$0 = \underbrace{\frac{\partial}{\partial y} \left[\left(\nu + \frac{\nu_{t_\phi}}{\tilde{\sigma}_\epsilon} \right) \frac{\partial \langle \epsilon \rangle}{\partial y} \right]}_{\text{diff}_\epsilon} + \underbrace{c_1 \nu_{t_\phi} \left(\frac{\partial \langle \bar{u} \rangle}{\partial y} \right)^2 \frac{\langle \epsilon \rangle}{\langle k \rangle}}_{\text{prodM}_\epsilon} - \underbrace{c_2 \frac{\langle \epsilon \rangle^2}{\langle k \rangle}}_{\text{diss}_\epsilon} + \underbrace{P_\epsilon}_{\text{prod}_\epsilon} \quad (6.59c)$$

$$\phi \langle \bar{u} \rangle^f \frac{\partial \langle \bar{T} \rangle^f}{\partial x} = \frac{\partial}{\partial y} \left(\phi (\alpha + \alpha_{t_\phi} + \alpha_{or}) \frac{\partial \langle \bar{T} \rangle^f}{\partial y} \right) + \mathcal{P} \quad (6.59d)$$

$$\text{with} \quad \nu_{t_\phi} = C_\mu \frac{(\langle k \rangle^f)^2}{\langle \epsilon \rangle^f} \quad \alpha_{t_\phi} = \frac{\nu_{t_\phi}}{Pr_{t_\phi}} \quad (6.59e)$$

where \bar{u} is the velocity in the x -direction and α_{or} is the component of the diagonal tortuosity tensor in the y -direction.

To lighten the writing of the problem, we have assumed that the sub-filter dispersive terms are considered in the variation of f_t^i , P_k and P_ϵ . The terms of porosity ϕ , permeability \mathcal{K} , Forchheimer coefficient \mathcal{F} , the source terms P_k and P_ϵ , and the diffusivities α_{t_ϕ} and α_{or} are function of the y coordinate. Furthermore, the pressure gradient is zero in the y -direction, and thus, the pressure gradient $\partial \langle \bar{p} \rangle / \partial x$ is constant.

For the turbulent temperature equation, simplifications have been done based on three considerations:

- the averaged temperature gradient is null or constant in the x -direction and the effective transfer coefficients are functions of the y coordinate, thus the diffuse flux is constant in the x -direction;
- the averaged flow is 1D in the x -direction and there is no averaged velocity in the y -direction, thus, the dispersion is negligible in the y -direction:

$$\tau_{uT} = \langle \bar{u} \bar{T} \rangle - \phi \langle \bar{u} \rangle^f \langle \bar{T} \rangle^f = 0 \quad (6.60)$$

that leads to $D_{yy}^p = D_y^a = 0$. This results has been verified.

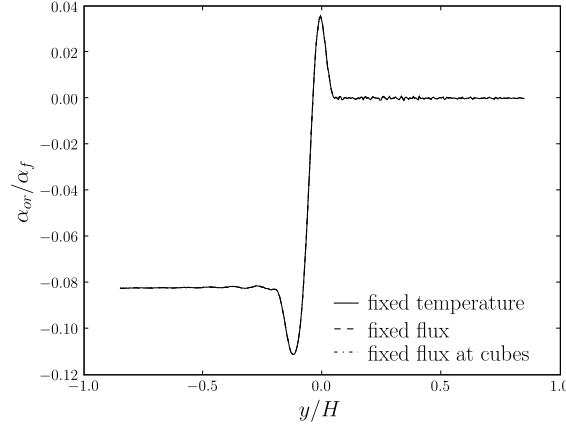
- the tortuosity reduces to:

$$T_{or} = \frac{\partial}{\partial y} \left(\phi \alpha_{or} \frac{\partial \langle \bar{T} \rangle^f}{\partial y} \right) \quad (6.61)$$

For $\mathcal{P} = 0$, the result is obvious, and for $\mathcal{P} = cste$, the coefficient T_i^a in the relation (6.51) is constant in the homogeneous porous medium, thus, the active part of the tortuosity is null. The tortuosity coefficients α_{or} , computed from the DNS data for the three thermal configurations, are presented in Fig. 6.3

We notice that, unlike the momentum and turbulent quantities, the mesoscopic model for the heat transfer is closed, and the effective coefficients α , α_{t_ϕ} and α_{or} are known in the whole domain including the transition zone.

In the following, we perform the second up-scaling step to derive a closed model at the macroscopic scale.


 Figure 6.3: Profiles of the tortuosity coefficients α_{or} computed from the DNS data.

6.3 Second up-scaling step

At the mesoscopic scale, the transfer is modeled by equations valid in the whole domain, *i.e* in the homogeneous porous and free regions and in the transition zone. At the macroscopic scale, the domain is composed of two homogeneous regions (porous and free) separated by a surface of discontinuity. The issue of this section is to study the boundary conditions that must be applied at the free-porous interface for the different physical quantities. First, we present the results obtained by [Chandesris and Jamet \(2009b\)](#) for the physical quantities related to the k - ϵ model (velocity, turbulent kinetic energy, dissipation rate). Then, we study the jump conditions required for the macroscopic modeling of the turbulent heat transfer.

6.3.1 Jump conditions for the velocity and the turbulent quantities

For the momentum equation, three forces are involved: the viscous force f_v , the pressure force f_p and the friction force f_l^i . At the mesoscopic scale, the porosity ϕ , the permeability \mathcal{K} and the Forchheimer's coefficient \mathcal{F} vary continuously in the transition zone. At the macroscopic scale, these quantities are discontinuous at the interface. Thus, by construction, the friction and pressure forces are not correctly described by the macroscopic model in the transition zone. Thus, as for the laminar study, we define the surface excess quantity to consider the difference between the two descriptions. The surface excess quantities of the friction and pressure forces are defined by:

$$(f_l^i)^{ex} = \nu \int_{H^-}^{y_m} \left(\phi \frac{1 + \mathcal{F}(\langle \bar{u} \rangle)}{\mathcal{K}} \langle \bar{u} \rangle - \phi^p \frac{1 + \mathcal{F}^p(\bar{u}_m)}{\mathcal{K}^p} \bar{u}_m \right) dy + \nu \int_{y_m}^{H^+} \phi \frac{1 + \mathcal{F}(\langle \bar{u} \rangle)}{\mathcal{K}} \langle \bar{u} \rangle dy \quad (6.62)$$

$$(f_p)^{ex} = \left(\int_{H^-}^{y_m} (\phi - \phi^p) dy + \int_{y_m}^{H^+} (\phi - \phi^l) dy \right) \frac{1}{\rho} \frac{d \langle \bar{p} \rangle^f}{dx} = \frac{(\phi)^{ex}}{\rho} \frac{d \langle \bar{p} \rangle^f}{dx} \quad (6.63)$$

where \bar{u}_m is the velocity at the macroscopic scale, \mathcal{K}^p is the permeability in the homogeneous porous region, \mathcal{F}^p is the Forchheimer's term in the homogeneous porous region and y_m is the interface location.

For the viscous force, one obtains after integration:

$$(f_v)^{ex} = \left[(\nu + \nu_{t_\phi}) \frac{\partial \langle \bar{u} \rangle}{\partial y} (H^+) - (\nu + \nu_{t_\phi}) \frac{\partial \bar{u}_m^l}{\partial y} (H^+) \right] - \left[(\nu + \nu_{t_\phi}) \frac{\partial \langle \bar{u} \rangle}{\partial y} (H^-) - (\nu + \nu_{t_\phi}) \frac{\partial \bar{u}_m^p}{\partial y} (H^-) \right] - \left[(\nu + \nu_{t_\phi}) \frac{\partial \bar{u}_m^l}{\partial y} (y_m) - (\nu + \nu_{t_\phi}) \frac{\partial \bar{u}_m^p}{\partial y} (y_m) \right] \quad (6.64)$$

As for laminar studies, the macroscopic and mesoscopic quantities are identical in the homogeneous regions. Thus, the first term of the right hand side of the equality is null. Adding the viscous, pressure and friction forces, one obtains the jump condition that must be applied to the velocity gradient at the free-porous interface:

$$(\nu + \nu_{t_\phi}) \frac{\partial \bar{u}_m^l}{\partial y} (y_m) - (\nu + \nu_{t_\phi}) \frac{\partial \bar{u}_m^p}{\partial y} (y_m) = (f_l^i)^{ex} + (f_p)^{ex} \quad (6.65)$$

The excess value of the pressure force is closed because it is related to the excess value of the porosity that is known. The friction excess value $(f_l^i)^{ex}$ is not closed due to the presence of mesoscopic terms that are not known at the macroscopic scale. In order to close this excess quantity, we locate the interface y_m at the center of gravity of $(f_l^i)^{ex}$, leading to the following closure relation:

$$(f_l^i)^{ex} (y_{f_l^i}) = 0 \quad (6.66)$$

Using the DNS results of [Breugem and Boersma \(2005\)](#), [Chandesris and Jamet \(2009b\)](#) shows that the center of gravities of $(f_l^i)^{ex}$ and $(f_p)^{ex}$ are approximately identical and correspond for the studied geometry to:

$$y_{f_l^i} \approx y_\phi = -0.075 \quad (6.67)$$

Thus, for an interface location such that $y_m = -0.075$, there is no excess value and the jump condition for the gradient velocity reduces to the continuity:

$$(\nu + \nu_{t_\phi}) \frac{\partial \bar{u}_m^l}{\partial y} (y_m) - (\nu + \nu_{t_\phi}) \frac{\partial \bar{u}_m^p}{\partial y} (y_m) = 0 \quad (6.68)$$

The equation of the kinetic energy (6.59b) expresses the balance between four quantities: a diffusion term (diff_k), a production term at the macroscopic scale (prodM_k), a sub-filter production term (prod_k) and a dissipation term (diss_k). As for the momentum balance, excess values are defined and a jump condition for the kinetic energy is expressed:

$$\left(\nu + \frac{\nu_t}{\tilde{\sigma}_k} \right) \frac{\partial k_m^l}{\partial y} (y_m) - \left(\nu + \frac{\nu_t}{\tilde{\sigma}_k} \right) \frac{\partial k_m^p}{\partial y} (y_m) = -(\text{prodM}_k)^{ex} - (\text{prod}_k)^{ex} + (\text{diss}_k)^{ex} \quad (6.69)$$

The structure of the transport equation of the dissipation rate is identical to the turbulent kinetic energy one. Thus, the jump condition of the dissipation rate applied at the free-porous interface is the following:

$$\left(\nu + \frac{\nu_t}{\tilde{\sigma}_\epsilon} \right) \frac{\partial \epsilon_m^l}{\partial y} (y_m) - \left(\nu + \frac{\nu_t}{\tilde{\sigma}_\epsilon} \right) \frac{\partial \epsilon_m^p}{\partial y} (y_m) = -(\text{prodM}_\epsilon)^{ex} - (\text{prod}_\epsilon)^{ex} + (\text{diss}_\epsilon)^{ex} \quad (6.70)$$

The jump conditions of the macroscopic turbulent kinetic energy and dissipation rate are not closed because the excess values involve unknown mesoscopic terms.

In order to close these excess values, the method the asymptotic expansion can be proposed. However, to simplify the study, we assume that the sum of the excess values is negligible when the interface location corresponds to $y_m = -0.075$. Thus for this particular interface location, the diffusive flux of the turbulent kinetic energy k_m and the dissipation rate ϵ_m are continuous. This assumption is very strong, but has given good results as shown by [Chandesris and Jamet \(2009b\)](#).

6.3.2 Jump conditions for the heat transfer

We remind that for the studied case the mesoscopic and macroscopic temperature fields can be simplified. However, in order to be exhaustive, we use the full equation (6.56) to derive the jump conditions at the free-porous interface with conservation principles. Then, the macroscopic model is simplified in the context of our study leading to closed jump conditions.

At the macroscopic scale, the heat transfer is described using the following equations:

In the porous region ($H^- < y < y_m$)

$$\frac{\partial}{\partial x_i} \left(\bar{u}_{i,m}^p \bar{T}_m^p \right) = \frac{\partial}{\partial x_i} \left([\phi^p (\alpha^p + \alpha_{t_\phi}^p + \alpha_{ij}^{or,p}) + D_{ij}^{p,p}] \frac{\partial \bar{T}_m^p}{\partial x_i} \right) + \frac{\partial}{\partial x_i} \left((D_i^{a,p} + T_i^{a,p}) \mathcal{P}_m^{i,p} \right) + \mathcal{P}_m^{i,p} \quad (6.71)$$

In the free region ($y_m < y < H^+$)

$$\frac{\partial}{\partial x_i} \left(\bar{u}_{i,m}^l \bar{T}_m^l \right) = \frac{\partial}{\partial x_i} \left([\phi^l (\alpha^l + \alpha_{t_\phi}^l) + D_{ij}^{p,l}] \frac{\partial \bar{T}_m^l}{\partial x_i} \right) \quad (6.72)$$

As for laminar heat transfer, the energy balance involves the heat flux and the injected heat. At the mesoscopic scale, the effective coefficients and the heat source vary continuously in the transition zone, while they are discontinuous at the macroscopic scale. Thus, the heat flux and the heat source are not correctly described by the macroscopic model in the transition zone. The difference between the modeling can be reflected through the corresponding excess values:

$$\left(\frac{\partial \langle \bar{q}_i \rangle^f}{\partial x_i} \right)^{ex} = \int_{H^-}^{y_m} \left(\frac{\partial \langle \bar{q}_i \rangle^f}{\partial x_i} - \frac{\partial \bar{q}_{i,m}^p}{\partial x_i} \right) dy + \int_{y_m}^{H^+} \left(\frac{\partial \langle \bar{q}_i \rangle^f}{\partial x_i} - \frac{\partial \bar{q}_{i,m}^l}{\partial x_i} \right) dy \quad (6.73)$$

$$(\mathcal{P})^{ex} = \int_{H^-}^{y_m} (\mathcal{P} - \mathcal{P}_m^{i,p}) dy + \int_{y_m}^{H^+} (\mathcal{P}) dy \quad (6.74)$$

where the mesoscopic total heat flux $\langle \bar{q}_i \rangle^f$ is defined by:

$$\langle \bar{q}_i \rangle^f = [\phi(\alpha + \alpha_{t_\phi} + \alpha_{ij}^{or}) + D_{ij}^p] \frac{\partial \langle \bar{T} \rangle^f}{\partial x_i} + (D_i^a + T_i^a) \mathcal{P} - \langle \bar{u}_i \rangle \langle \bar{T} \rangle \quad (6.75)$$

This definition is used for the macroscopic total heat flux in the homogeneous porous and free regions.

As for laminar heat transfer, the macroscopic and mesoscopic models are equivalent in the homogeneous regions. Thus, the heat flux in the y -direction reduces to:

$$\left(\frac{\partial \langle \bar{q}_y \rangle^f}{\partial x_y} \right)^{ex} = \left(\frac{\partial \langle \bar{q}_y \rangle^f}{\partial y} (H^+) - \frac{\partial \bar{q}_{y,m}^l}{\partial y} (H^+) \right) - \left(\frac{\partial \langle \bar{q}_y \rangle^f}{\partial y} (H^-) - \frac{\partial \bar{q}_{y,m}^p}{\partial y} (H^-) \right) - \left(\frac{\partial \bar{q}_{y,m}^l}{\partial y} (y_m) - \frac{\partial \bar{q}_{y,m}^p}{\partial y} (y_m) \right) \quad (6.76)$$

which reduces to:

$$\left(\frac{\partial \langle \bar{q}_y \rangle^f}{\partial x_y} \right)^{ex} = \frac{\partial \bar{q}_{y,m}^l}{\partial y} (y_m) - \frac{\partial \bar{q}_{y,m}^p}{\partial y} (y_m) \quad (6.77)$$

Adding the relations (6.73), (6.74) and (6.77), one obtains the jump condition for the heat flux in the y -direction:

$$\bar{q}_{y,m}^l (y_m) - \bar{q}_{y,m}^p (y_m) = - \left(\frac{\partial \langle \bar{q}_x \rangle^f}{\partial x} \right)^{ex} - \left(\frac{\partial \langle \bar{q}_z \rangle^f}{\partial z} \right)^{ex} - (\mathcal{P})^{ex} \quad (6.78)$$

The temperature jump condition is determined from the conservation of the conductive heat flux in the y -direction and takes the following form:

$$\bar{T}_m^l(y_m) - \bar{T}_m^p(y_m) = \left(\frac{\langle \bar{q}_{y,c} \rangle^f}{\phi(\alpha + \alpha_{t_\phi} + \alpha_{yy}^{or}) + D_{yy}^p} \right)^{ex} \quad (6.79)$$

These jump conditions are not closed because the excess values involve mesoscopic terms that are not known at the macroscopic scale. A solution to close the excess values is to use the method of the matched asymptotic expansions. However, in the context of our study where the fields are 1D, simplifications can be done: the surface excess quantities of the flux gradient reduces to convective excess quantity in the x -direction and there is no dispersion in the y -direction. Thus, the jump conditions can be rewritten such that:

$$\bar{q}_{y,m}^l(y_m) - \bar{q}_{y,m}^p(y_m) = - \left(\phi \langle \bar{u} \rangle \frac{\partial \langle \bar{T} \rangle^f}{\partial x} \right)^{ex} - (\mathcal{P})^{ex} \quad (6.80)$$

$$\bar{T}_m^l(y_m) - \bar{T}_m^p(y_m) = \left(\frac{\langle \bar{q}_{y,c} \rangle^f}{\phi(\alpha + \alpha_{t_\phi} + \alpha_{yy}^{or})} \right)^{ex} \quad (6.81)$$

The jump condition for the heat flux involves two surface excess quantities coming from the convection and the injected heat. The excess quantity of the injected heat is closed knowing its profile in the transition zone. On the contrary, the excess value of the convective term is not closed because it involves mesoscopic terms that are not known at the macroscopic scale. However, in the following section we study heat transfer, and it is shown that this term is zero or negligible. Thus, the jump conditions is closed.

The jump condition for the temperature involves the surface excess quantity of the conductive flux times to a resistivity. This surface excess is not closed, due to the mesoscopic terms $\langle \bar{q}_{y,c} \rangle^f$, that is not known at the macroscopic scale. However, we use the results obtained in Chapters 2 and 3 showing that the temperature jump has no impact on the macroscopic closure. Thus, we close the temperature jump condition using the continuity at the free-porous interface.

$$\bar{q}_{y,m}^l(y_m) - \bar{q}_{y,m}^p(y_m) = - (\mathcal{P})^{ex} \quad (6.82)$$

$$\bar{T}_m^l(y_m) - \bar{T}_m^p(y_m) = 0 \quad (6.83)$$

6.4 Results

The momentum transfer is described using the standard k - ϵ model. Considering the low bulk Reynolds number ($Re_b = 5500$), this might not be appropriate. However, [Chandesris and Jamet \(2009b\)](#) show that the standard k - ϵ model is able to give accurate results. At the upper-wall, the application of a standard wall function requires the location of the first computational node in the logarithmic zone ($y^+ > 30$). Since the Reynolds number is moderate, it implies that the size of the first computational cell is large. Then, in order to have a maximum of precision in the rest of the domain, the mesh is refined far from the upper wall. The total number of cells used in the y -direction is 80.

In the following we present the results obtained by [Chandesris and Jamet \(2009c\)](#) for the momentum transfer. Then using the resulting macroscopic velocity profile, we compute the heat transfer at the macroscopic scale. The macroscopic results are compared with the profiles of the DNS presented in Chapter 5.

6.4.1 Results for the momentum transfer

The macroscopic profiles of velocity, turbulent quantities and turbulent viscosity are compared to the results of reference obtained with the DNS (see Chapter 5) in Fig. 6.4. The different quantities

are illustrated under a no-dimensional form obtained with the characteristic quantities of the associated simulation. The characteristic quantities of the DNS and the macroscopic k - ϵ model (porosity, Darcy, Reynolds number) are presented in Tab. 6.1. We remind the definitions of the Reynolds numbers below:

$$\begin{aligned}
 Re_b &= U_b H / \nu & \text{with} & & U_b &= \int_0^1 U dy, \text{ the bulk flow in the free region} \\
 Re_T &= 2U_T H / \nu & \text{with} & & U_T &= \frac{1}{2H} \int_{-H}^H U dy, \text{ the averaged flow in the whole domain} \\
 Re_{ip} &= U_{ip} H / \nu & \text{with} & & U_{ip} &= \int_{-1}^0 U dy, \text{ the bulk flow in the porous medium} \\
 Re_\tau^t &= u_\tau^t H / \nu & \text{with} & & u_\tau^t &= \left(-\nu \frac{\partial \bar{u}}{\partial y}(y=H) \right)^{1/2}, \text{ the wall shear stress} \\
 Re_\tau^p &= U_\tau^p H / \nu & \text{with} & & u_\tau^p &= \left(-\nu \frac{\partial \langle \bar{u} \rangle}{\partial y}(y=0) \right)^{1/2}, \text{ the porous wall shear stress } y=0
 \end{aligned}$$

	ϕ	Da	Re_b	Re_{ip}	Re_T	Re_τ^t	Re_τ^p
DNS (Trio-U)	0.875	$3.4 \cdot 10^{-4}$	5351	450	5851	390	664
macroscopic k - ϵ model	0.875	$3.4 \cdot 10^{-4}$	5500	535	6066	421	680
Ecart en %	0	0	3	15	3	7	2

Table 6.1: Characteristic of the DNS (Trio-U) and the macroscopic k - ϵ model.

The velocity profile \bar{u}_m is in good agreement with the DNS result as presented in Fig. 6.4(a). The choice of the standard k - ϵ model appears to be sufficient to capture the main physical features of the flow. In the channel, the skewness of the profile is recovered. This skewness is created by the friction velocity higher at the porous wall than at the upper wall. As a consequence, the position of the maximum of velocity is located above the center of the channel.

In the transition zone, the velocity profile is well captured. This result supports the hypothesis done to estimate the location of the center of gravity of $(f_f)^{ex}$.

In the homogeneous porous region, the pressure gradient is imposed to have $Re_b = 5500$.

The profiles of the turbulent quantities k_m and ϵ_m are presented in Figs. 6.4(b) and 6.4(c).

For the turbulent kinetic energy k_m , the main behavior and the order of magnitude are recovered. The profile increases from $y/H \approx 0.5$ to reach a peak at the porous wall where large-scale vortical structures are created. Then, the profile decreases linearly in the channel featuring the disappearance of the turbulence by elongation of the streaky structures.

The profile is shifted in the direction of the porous medium, which induces a weaker value of the gradient of k_m in the channel. This result comes from the lack of accuracy of the boundary condition at the free-porous interface. The assumption of the continuity of the diffuse flux of k_m at the free-porous interface located at $y_m = -0.075$, is not appropriate. However as we will see on the profile of the macroscopic turbulent viscosity, this error modeling has a low impact.

For the turbulent dissipation ϵ_m , the values are recovered in the homogeneous regions far from the porous wall. At the porous wall, the macroscopic profile has higher values and does not capture the decrease of the DNS profile inside the free region. The difference between the two behaviors is explained by the fact that the macroscopic model is not build to model correctly the transfer close to the free-porous interface, but to capture the good profile in the homogeneous regions.

Furthermore, we notice that the location of the macroscopic peak is close from the one of the DNS profile. That validates the use of the continuity for the diffuse flux of ϵ_m at the free-porous interface located at $y_m = -0.08$.

The profile of the macroscopic turbulent viscosity $\nu_{t\phi m}$ is presented in Fig. 6.4(b). Compared to the DNS result, the behavior and the order of magnitude are well recovered.

In the homogeneous porous region, the values are weak for $y_m/H < 0.5$, then increase linearly to the porous wall. It corresponds to the destruction of the turbulent structures by the friction force of the porous matrix.

In the free region, the values follow a parabolic profile that reaches a maximum for $y_m/H \approx 0.3$. It reflects, the creation of the turbulent structures at the porous wall, then their destruction in the upper part of the channel due to the friction force created by the solid wall.

The shear stress constraints profiles are presented in Figs. 6.4(e) and 6.4(f).

For the viscous shear stress, the macroscopic profile fits the DNS results including the zone close to the free-porous interface where the peak location and the values are recovered. Thus, the gradient of the macroscopic velocity profile is well captured by the standard $k-\epsilon$ model.

For the turbulent shear stress, the macroscopic profile fits the DNS results except at the free-porous interface. The peak locations between the macroscopic and DNS profiles are close. Thus, we conclude that the macroscopic modeling of the volume averaged Reynolds shear stress is correct in the homogeneous regions :

$$\langle \overline{u'v'} \rangle = \nu_{t_m} \frac{\partial \bar{u}_m}{\partial y} \quad (6.84)$$

and that the boundary conditions of continuity for the diffuse flux of the velocity and the turbulent quantity are a good approximation to close the macroscopic model at the free-porous interface.

6.4.2 Results for heat transfer

In this section, we present the results obtained with the macroscopic temperature model for the three heating configurations studied in the DNS (see Chapter 5). At the macroscopic scale, the turbulent thermal diffusivity can be closed by the macroscopic turbulent Prandtl model:

$$\alpha_{t_m} = \frac{\nu_{t_m}}{Pr_t}, \text{ with } Pr_t = 0.9 \quad (6.85)$$

where ν_{t_m} is computed with values from the macroscopic $k-\epsilon$ simulation. The macroscopic turbulent diffusivity α_{t_m} is compared to the mesoscopic turbulent diffusivity of reference in Fig. 6.5. The comparison shows that α_{t_m} does not capture properly the decrease of the turbulent diffusivity in the porous medium. This difference is at the origin of wrong macroscopic temperature and heat flux profiles as we will see in the following. Thus, the turbulent Prandtl model (6.85) is not accurate at the macroscopic scale. In order to have a better approximation of the thermal turbulence at the porous interface, we propose another closure for the macroscopic turbulent diffusivity:

$$\alpha_{t_m}^1 = \frac{\nu_{t_m} k_m}{2(u_\tau^p)^2} \quad (6.86)$$

This new closure is obtained increasing the weighting of the turbulent kinetic energy to use its exponential profile in the porous region (see Fig. 6.4(b)). Furthermore, it is constructed to be homogeneous to a viscosity. However, the physic of such a relation is not currently understood.

The profile of the macroscopic turbulent diffusivity $\alpha_{t_m}^1$ is presented in Fig. 6.5. It shows a good capture the physics at the porous wall, *i.e* the decrease in the porous medium and the peak location of the

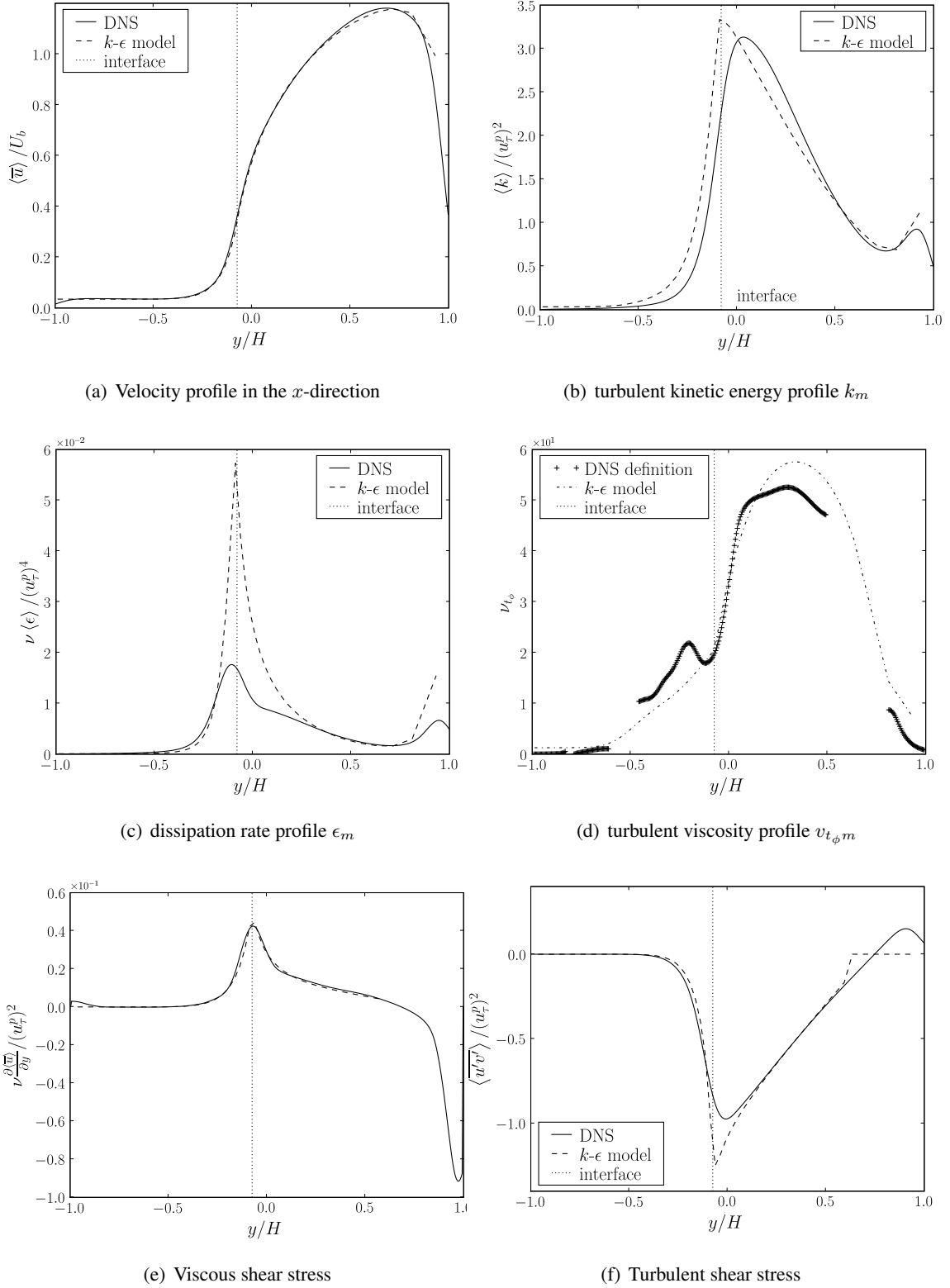


Figure 6.4: Profiles of velocity, turbulent quantities, turbulent viscosity and shear stress constraints.

maximum turbulent thermal diffusivity.

The results obtained with the new closure (6.86) are presented in the following more extensively for the three heating configurations.

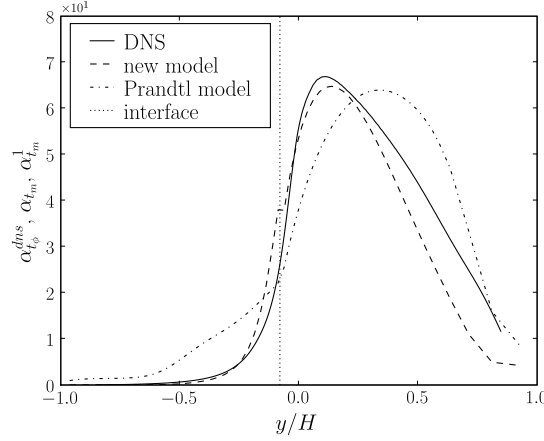


Figure 6.5: Profiles of turbulent thermal diffusivity.

Heating configuration with imposed temperatures at walls

For boundary conditions with imposed temperature at walls, there is no temperature gradient in the x -direction. In such a case, the macroscopic model takes the following form:

- in the homogeneous porous region:

$$0 = \frac{\partial}{\partial y} \left[\phi_p (\alpha + \alpha_{or}^p + \alpha_{t_m}) \frac{\partial T_m^p}{\partial y} \right] \quad (6.87)$$

- in the free region:

$$0 = \frac{\partial}{\partial y} \left[\phi_l (\alpha + \alpha_{or}^l + \alpha_{t_m}) \frac{\partial T_m^l}{\partial y} \right] \quad (6.88)$$

- at the free-porous interface:

$$T_m^l(y_m) - T_m^p(y_m) = 0 \quad (6.89)$$

$$q_{ym}^l(y_m) - q_{ym}^p(y_m) = 0 \quad (6.90)$$

The profiles of the different quantities (temperature, tortuosity, diffuse heat flux, turbulent heat flux, diffuse heat flux) obtained with this macroscopic model are presented in Fig. 6.6.

The temperature profiles are presented in Fig. 6.6(a) and both models give good results. Nevertheless, the macroscopic profile obtained with the new modeling is closer to the result of reference. Thus, the new model seems to be more appropriate to characterize the turbulent heat transfer at the free-porous interface. This is verified increasing the order of comparison by comparing the heat flux.

The profiles of the molecular heat flux are presented in Fig. 6.6(c). The two macroscopic profiles have the correct order of magnitude. Nevertheless only the new model profile fits the DNS values at the porous wall for $-0.5 < y < 0.5$. The same observations can be done for the tortuosity profiles presented in Fig. 6.6(b).

The profiles of the turbulent heat flux are presented in Fig. 6.6(d). The macroscopic turbulent Prandtl model overestimates the turbulent heat flux in the whole domain, while the new model captures the main behaviors.

The energy balance for the new model is presented in Fig. 6.6(e). It shows, that the energy transfer between the different fluxes is well recovered.

All these observations about the heat flux validate the new model. We comment further that the macroscopic values are not correct at the upper-wall, which shows the shortage of the wall functions used at the upper-wall.

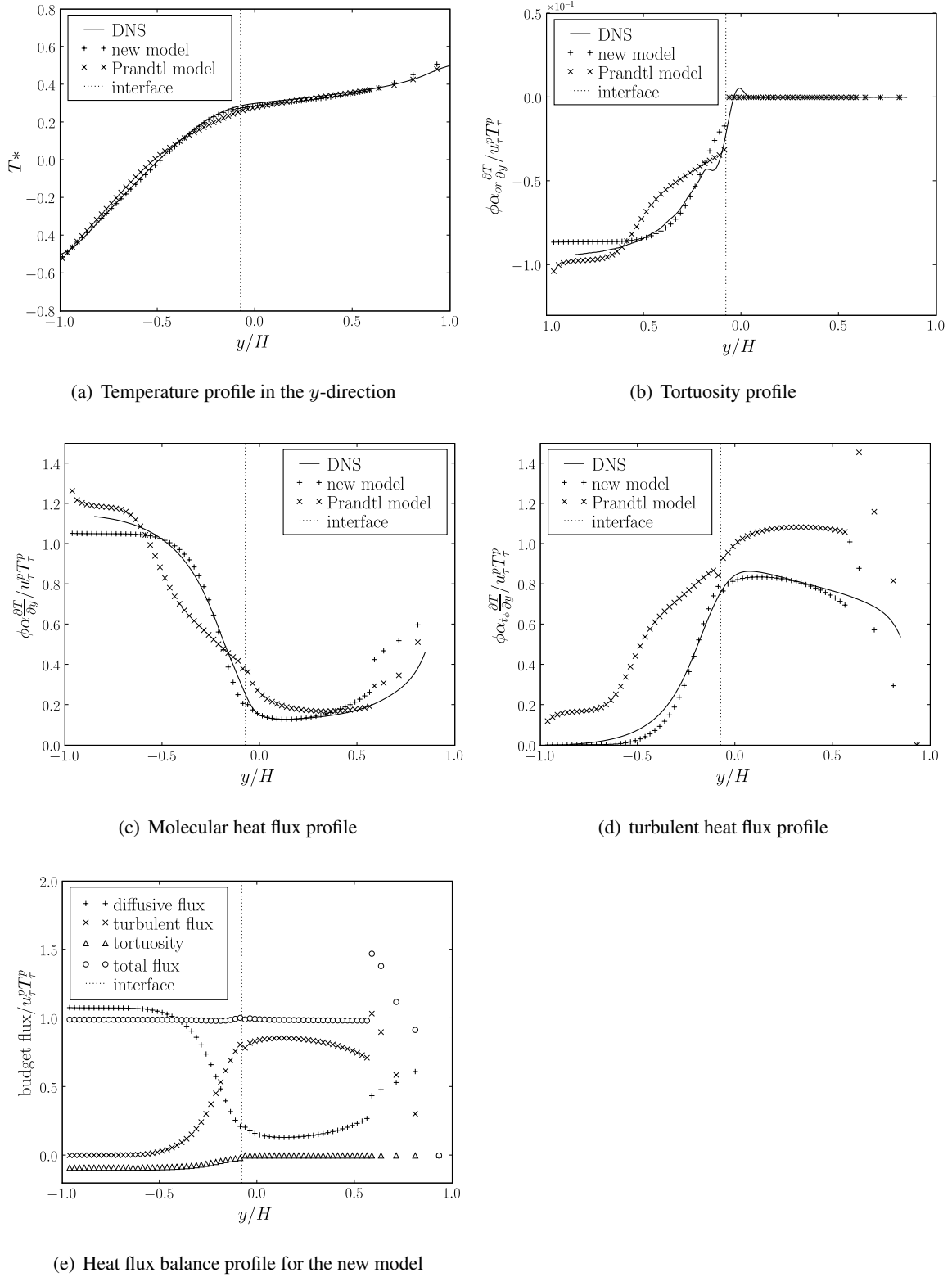


Figure 6.6: Profiles of temperature and heat flux.

Heating configuration with imposed flux at walls

For boundary conditions with imposed flux at walls, the DNS gives the quantity θ_0 issue from the variable change $T_0 = \theta_0 - A_0 x$ (see Chapter 5), where A_0 corresponds to the flux increase on the domain and is

computed performing an energy balance. Such a variable change makes appear a source term $(\rho c_p)uA_0$ in the local equation (see Appendix A equation (A.17)). Performing on the equation (A.17) the previous developments, one obtains the following macroscopic model for θ_0 :

- in the homogeneous porous region:

$$(\rho C_p)u_m^p A_0 = \frac{\partial}{\partial y} \left[\phi_p(\alpha + \alpha_{or}^p + \alpha_{tm}) \frac{\partial \theta_{0m}^p}{\partial y} \right] \quad (6.91)$$

- in the free region:

$$(\rho C_p)u_m^l A_0 = \frac{\partial}{\partial y} \left[\phi_l(\alpha + \alpha_{or}^l + \alpha_{tm}) \frac{\partial \theta_{0m}^l}{\partial y} \right] \quad (6.92)$$

- at the free-porous interface:

$$\theta_{0m}^l(y_m) - \theta_{0m}^p(y_m) = 0 \quad (6.93)$$

$$q_{\theta ym}^l(y_m) - q_{\theta ym}^p(y_m) = -(\rho c_p)A_0 (\langle \bar{u} \rangle)^{(ex)} \quad (6.94)$$

The jump condition on the heat flux is not closed because the surface excess quantity involves the mesoscopic velocity that is not known at the macroscopic scale. In order to determine the impact of a such a jump condition, we determine the surface excess of the velocity for the macroscopic model used in this study. Knowing the averaged velocity $\langle \bar{u} \rangle$ from the DNS results and the macroscopic field u_m obtained for the macroscopic model closed with boundary conditions of continuity at the interface $y_m = -0.075$, we obtained

$$(\langle u \rangle)^{(ex)}(y_m = -0.075) = \int_{-H}^{+H} (\langle u \rangle - u_m) dy = -0.0047 \quad (6.95)$$

The jump condition for the heat flux at the free-porous interface corresponds to 0.47 percent of the energy injected in the domain. Thus, the use of boundary condition of continuity for the heat flux is an accurate approximation.

The different quantities obtained for this closed macroscopic model are presented in Fig. 6.7.

The temperature profiles are presented in Fig. 6.7(a). Unlike the previous heating configuration, the profiles obtained with the macroscopic models are distant from the solution of reference. None of them captures the correct temperature gradient in the porous medium. Nevertheless, the profile issue from α_{tm}^1 is closer to the DNS profile.

The molecular and turbulent fluxes are presented in Figs. 6.7(c) and 6.7(d). The two macroscopic models give flux profiles with correct orders of magnitude. Nevertheless the macroscopic turbulent Prandtl model profiles are distant from the DNS result in the porous medium, while the α_{tm}^1 modeling captures the main behavior.

For the turbulent heat flux, the difference between the new model and DNS profile is of the same order of magnitude as the one observes for the previous heating configuration. For the molecular flux and the tortuosity (see Fig. 6.7(b)), the difference has increased in the porous medium. This difference is at the origin of the error observed for the temperature profile.

Heating configuration with imposed flux at cubes

For boundary conditions with imposed flux at the cube walls, the DNS gives the quantity θ_1 coming from the change of variable $T_1 = \theta_1 - A_1 x$ (see Chapter 5). This heating configuration is similar to the previous one and the form of the macroscopic model is identical to the equations (6.91) to (6.94) with an additional thermal source in the porous medium. This thermal source appears in the jump condition of the total heat flux in addition to the excess value of the velocity. As for the previous heating configuration, the term $(\rho c_p)A_1 (\langle \bar{u} \rangle)^{(ex)}$ is negligible compared to the total heat flux injected in the domain. Thus the macroscopic model takes the following form:

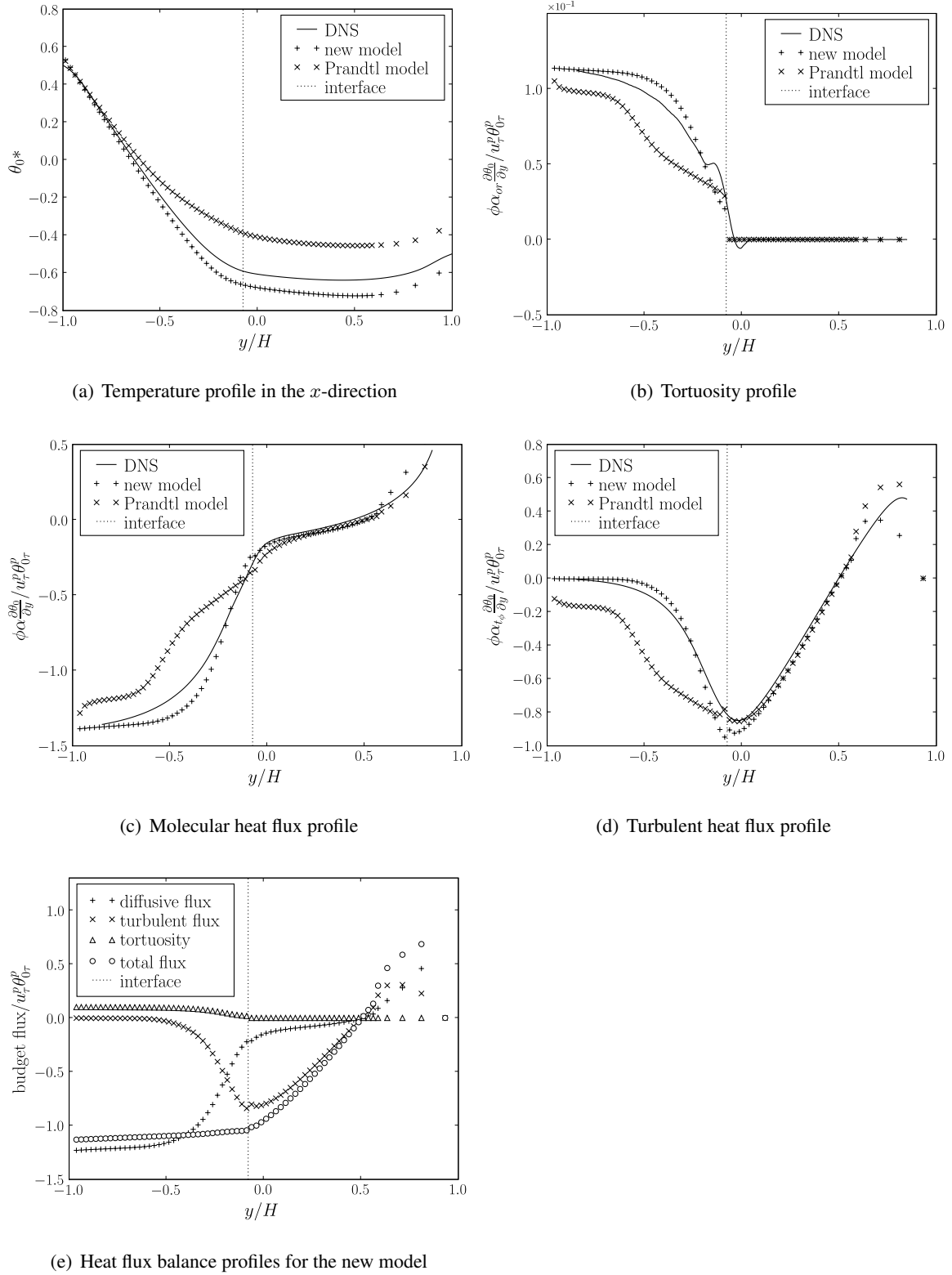


Figure 6.7: Profiles of temperature and heat flux.

- in the homogeneous porous region:

$$(\rho C_p) u_m^p A_1 = \frac{\partial}{\partial y} \left[\phi_p (\alpha + \alpha_{or}^p + \alpha_{tm}) \frac{\partial \theta_{1m}^p}{\partial y} \right] \quad (6.96)$$

- in the free region:

$$(\rho C_p) u_m^l A_1 = \frac{\partial}{\partial y} \left[\phi_l (\alpha + \alpha_{or}^l + \alpha_{tm}) \frac{\partial \theta_{1m}^l}{\partial y} \right] \quad (6.97)$$

- at the free-porous interface:

$$\theta_{1m}^l(y_m) - \theta_{1m}^p(y_m) = 0 \quad (6.98)$$

$$q_{\theta ym}^l(y_m) - q_{\theta ym}^p(y_m) = -(\mathcal{P})^{(ex)} \quad (6.99)$$

The jump condition for the heat flux is closed knowing the profile of the injected heat in the transition zone.

The quantities computed with this closed macroscopic model are presented in Fig. 6.8.

The observations about the obtained results are similar to those done for the previous heating configuration. The macroscopic temperature profiles are distant from the DNS profile (see Fig. 6.8(a)). The flux study shows that the new model α_{tm}^1 captures the main behavior in the whole domain unlike the macroscopic turbulent Prandtl model. The error existing for the temperature profile issue from the new modeling comes from the tortuosity and the molecular flux.

The quantities (temperature, heat flux, turbulent thermal diffusivity) obtained with two macroscopic models are compared with the results of the DNS. The comparison shows that the macroscopic turbulent Prandtl model gives the good order of magnitude and the correct heat flux profiles in the free region. However it does not capture the physic in the homogeneous porous region. Considering the difference existing between the macroscopic turbulent thermal diffusivity and the DNS one, we conclude that the system is not sensitive to the turbulence modeling in the free region. On the contrary, it is sensitive in the homogeneous porous region and the approximate model is not able to give accurate results. Thus, we propose improvements for the macroscopic turbulent Prandtl model, that increase the weighting of the turbulent kinetic energy. This new model has the asset to characterize a better diffusivity in the homogeneous porous region. As a consequence, the behaviors of the heat flux profiles (tortuosity, molecular flux and turbulent heat flux) are better recovered.

However we notice the sensitivity of the temperature to the value of turbulent diffusivity in the porous medium. This quantity is underestimated in the porous region for $y/H < -0.2$ corresponding to a lack of mixing in this zone (see Fig. 6.9). We observe, that the consequences of this lack of mixing on the temperature field depend on the type of the boundary conditions used. For boundary conditions with imposed temperature (Dirichlet-type), the impact is not much noticeable (see Fig. 6.6(a)). On the contrary, for boundary conditions with imposed flux (Neumann-type), the consequence on the temperature is important: the temperature is underestimated in the transition zone and in the free region (see Figs. 6.7(a) and 6.8(a)).

6.5 Conclusion

In this chapter, we study the jump conditions that must be applied at a free porous interface for a turbulent heat flow above a porous medium.

First, a $k-\epsilon$ model with turbulent Prandtl model is derived at the mesoscopic scale using the volume averaging operator. This model is valid in the whole domain including the transition zone. It corresponds to a macroscopic $k-\epsilon$ model with a macroscopic turbulent Prandtl model in the homogeneous porous region and degenerates to the standard model in the free region.

Second, the jump conditions that must be applied at the discontinuous interface are derived from the mesoscopic scale using conservation methods. For the momentum and turbulent equations, the jump conditions are not closed, because they involve surface excess quantities with unknown mesoscopic terms. In order to close these jump conditions we use the work of [Chandesris and Jamet \(2009b\)](#), that closes the macroscopic model for a fixed interface location: the center of gravity of the surface excess

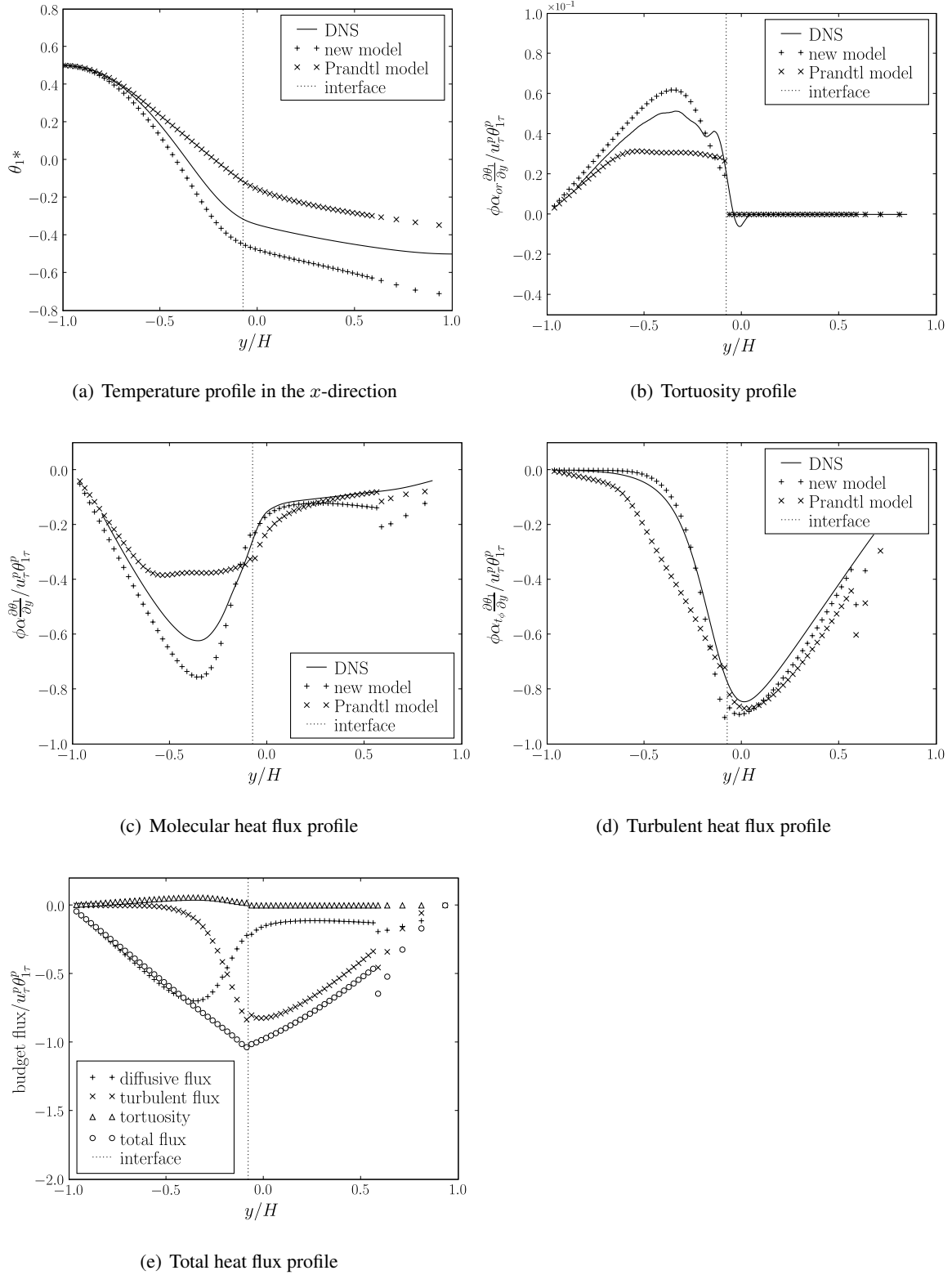


Figure 6.8: Profiles of temperature and heat flux.

quantity of the friction force. For this particular interface location, the continuity for the diffuse flux of the velocity is verified and assuming also the continuity for the diffuse flux of k and ϵ , the macroscopic model gives accurate fields in the homogeneous regions. For the turbulent heat transfer, the jump conditions are

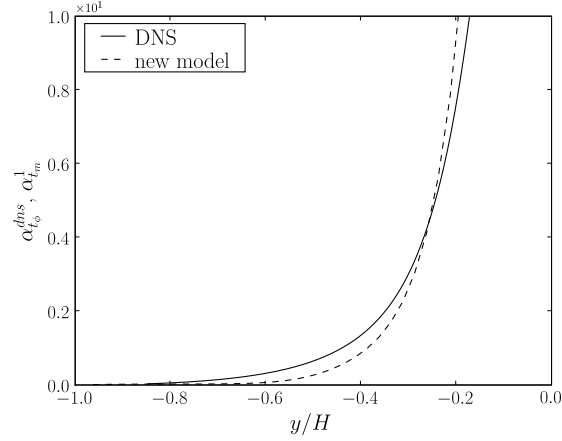


Figure 6.9: Zoom of the turbulent thermal diffusivity profiles.

closed considering the studied temperature field. They correspond to the continuity of the temperature and to a jump condition with the surface excess quantity of the injected power for the heat flux. The determination of this surface excess value at the interface is obtained knowing the profile of the injected power in the transition zone.

The macroscopic model is compared to the simulation of reference given by the DNS in Chapter 5. As expected, it gives good results for the momentum transfer, where the different quantities (velocity, turbulent kinetic energy, turbulent viscosity and the shear stress constraints) are well captured. On the contrary, the comparison for heat transfer shows the weakness of the macroscopic turbulent Prandtl model to characterize the heat transfer at the porous wall. We propose another model for the macroscopic thermal diffusivity:

$$\alpha_{t_m} = \frac{\nu_{t_m} k_m}{2(u_\tau^p)^2} \quad (6.100)$$

This model reproduces a turbulence decrease in the porous medium closer to the physics of reference. Its accuracy is verified for the heating configurations with imposed temperature at the wall, but its limits are revealed for heating configuration with constant flux. Such results show the sensitivity of the system to the modeling of the turbulence decrease in the homogeneous porous region.

The results obtained in this chapter can be improved in different ways. The jump conditions obtained for the momentum and turbulent quantities are not general. A study with the method of the matched asymptotic expansions would verify the assumption of continuity and would give approximate solutions of the mesoscopic problem at different orders. Thus, the dependence between the jump conditions and the interface location would be explained. For the heat transfer, the improvements rely on a better modeling of the macroscopic thermal diffusivity in the homogeneous porous region. This information is the key of the good characterization of the transfer at the interface. However the mechanism of the turbulence decrease in the porous medium is complex and difficult to understand.

Chapter 7

Conclusion

The main objective of this work is to study the heat transfers at the interface between a porous medium and a free region using a multi-scale approach. In this Chapter we recapitulate the main results and discuss different issues.

7.1 Main conclusions

In a free-porous domain, the exact description of the solid matrix can be complex and the computation of the transfers at the local scale may require a large amount of degrees of freedom. The multi-scale approach allows to lower down the fine description of the porous medium introducing a macroscopic scale of description. At the macroscopic scale, the domain is characterized by homogeneous models for the porous and free media connected by boundary conditions at the free-porous interface. The main modeling issue relies on the definition of appropriate boundary conditions at the free-porous interface. Considering this issue, questions arise:

- the form of the boundary conditions that must apply at the interface: Are the physical quantities continuous or discontinuous at the free-porous interface?
- the value of the jump parameters related to these jump conditions: Are these jump parameters intrinsic quantities? How to determine them?
- the location of the surface of discontinuity.

These questions are studied by [Chandesris and Jamet \(2006, 2007, 2009c,b,a\)](#) for momentum transfer. They succeed in making explicit the physics that exists at the free-porous interface using a multi-scale approach based on three levels of descriptions of the interface (microscopic, mesoscopic and macroscopic) and two up-scaling steps. With this approach, they derive the jump conditions that must be applied at the macroscopic interface from the momentum equations at the microscopic scale. The main issues are related to the second up-scaling step (mesoscopic/macroscopic) and they are similar to those existing for the interfacial study in two-phase flows. Thus, it is suitable to transpose the methods used for two-phases flows (generic analysis and method of matched asymptotic expansions) to the study of the free-porous interface.

The multi-scale approach applied to heat transfers

Applying this multi-scale approach to the study of heat transfer at a free-porous interface, new questions arise. First, questions are related to the first up-scaling step (microscopic/mesoscopic), which consists in obtaining continuous equations that are valid in the whole domain including the transition zone. The continuous equations are derived from the local equations at the microscopic scale using the volume

averaging operator and involve non-closed terms. In order to close these terms a modeling step must be achieved for which questions arise:

- the form of the closed mesoscopic equations: How to model the non-closed terms characteristic of the porous description-type? Are the usual models available in the literature valid in the transition zone?
- the determination of the effective coefficients: How to determine the effective coefficients in the transition zone?

For the laminar momentum transfer, these questions are easily answered. Indeed, only one non-closed term exists that is modeled through a permeability coefficient known in the transition zone. For the heat transfer, there are four non-closed terms (tortuosity for the fluid phase, tortuosity for the solid phase, heat transfer coupling and dispersion) that require complex modelings involving numerous effective transfer coefficients.

In order to answer the question regarding the form of the closed model, the different approaches existing in the literature for homogeneous porous media are presented: the heuristic, mixed and volume averaging methods. However, these approaches cannot be used directly at the free-porous interface. Indeed, the volume averaging method relies on the strong hypothesis of length scale separation that is not valid at the interface. And the mixed method postulates the form of the closed model instead of formally proving it as for the volume averaging method. In Chapter 2, we propose another method built on the advantages of the mixed and volume averaging methods. Thus, the form of the closed model is derived using the volume averaging method and the effective coefficients are determined by identification as for the mixed method. This new method allows to characterize the heat transfer at the free-porous interface through continuous equations.

Results for laminar heat transfers

The laminar heat transfers are studied analytically for flows normal to the interface. For this configuration, there is no jump condition for the flow and the averaged velocity is constant in the whole domain. The determination of the jump conditions for the heat transfer via the second up-scaling step does not present any major difficulty and small adjustments of the method were enough.

At local thermal equilibrium, jump condition for the temperature and a jump condition for the total heat flux are obtained. As for the momentum transfer, the method of matched asymptotic expansions shows that:

- the jump conditions depend on a 1 order phenomenon in ε ;
- the value of the jump parameter can be related to intrinsic values of the interface and can be directly computed for a given interface location.

Furthermore, from these results, the apparent interface can be determined. The apparent interface is defined as the location of the interface for which the boundary conditions of continuity are sufficient. It appears that the location of the apparent interface depends only of intrinsic properties of the interface and illustrate it through an example on a complex geometry.

At local thermal non-equilibrium, both fluid and solid temperatures must be considered. The main difficulty is to couple the two-temperature model of the homogeneous porous region with the one-temperature model of the free region. To proceed we introduce a new equivalent writing of the modeling with an identical number of equations in both regions. Thanks to this formalism, both methods providing boundary conditions can be used. One obtains three jump relations as boundary conditions at the fluid-porous

interface: a temperature jump and a heat flux jump for the fluid phase and a heat flux jump for the solid phase. As for transfer at local thermal equilibrium, the relation given the apparent interface is determined analytically. The obtained relation is complex due to the number of involved phenomena, nevertheless it can be discussed. When a phenomenon dominates the others, simplifications can be done that makes explicit the location of the apparent interface. Otherwise, the apparent interface is not known directly and the resolution of the macroscopic model at order 1 is needed.

Results for turbulent heat transfers

For the study of turbulent heat transfers at a free-porous interface, we face a lack of information in the literature. In order to gain insight in the influence of the free-porous interface in the turbulent transfers, a direct numerical simulation is performed. Using the geometry proposed by [Breugem and Boersma \(2005\)](#), we compute a flow field that is in good agreement with Breugem's results and three temperature fields resulting in three different thermal boundary conditions ($Re_\tau = 390$, $Pr = 0.1$). As [Breugem and Boersma \(2005\)](#), the results obtained for the momentum transfer shows that the turbulent structures at the free-porous interface are different compared to the turbulence near the solid wall. At the free-porous interface, the turbulence is dominated by large vortical structures responsible for exchange of momentum in the channel that does not exist at the solid wall. This difference between the porous and solid wall is also observed for the temperature fields. Furthermore, three characteristics of the heat transfer in a free-porous domain are found:

- the wall-normal turbulent heat flux can be modeled with an averaged temperature gradient via a turbulent diffusivity;
- the wall-normal turbulent heat flux and the Reynolds shear stress are not correlated;
- the temperature fluctuations are different from the velocity ones.

The first two characteristics give information about the turbulent heat flux modeling and can be used for RANS simulations. From the characteristics, one can predict that the turbulent Prandtl model will not be accurate in a free-porous medium. The third characteristic is not expected. It reflects that the turbulence of the temperature field does not follow the turbulence of the flow. We did not succeed in clarifying this point due to a lack of time.

The next step is to determine a RANS modeling of the turbulent heat transfer at the macroscopic scale using the DNS as a simulation of reference. The momentum transfer is computed following the work done by [Chandesris2009a](#). They obtain accurate results with a $k-\epsilon$ model using boundary conditions of continuity for a particular interface location. For the heat transfer, the issue to determine (i) the closure for the turbulent diffusivity and (ii) the jump conditions that must be applied at the free-porous interface, whose location is fixed by the momentum transfer. It turns out that using the knowledge acquired from the laminar study and appropriate simplifications, the determination of the jump conditions becomes very easy. One obtains the temperature continuity and a jump condition for the heat flux corresponding to the excess value of the injected heat flux. The difficulty arises in the closure of the turbulent diffusivity. Indeed, the turbulent Prandtl modeling is not accurate enough to capture correctly the turbulent heat transfer in the porous medium. Thus, we propose another closure for the turbulent diffusivity increasing the weighting of the averaged kinetic energy. This new model is able to capture the turbulence decrease in the porous medium and the resulting macroscopic model gives the correct flux in the domain including the interface.

7.2 Discussion and outlooks

This study allows a better understanding of the heat transfer mechanisms at a free-porous interface. The models used to characterize the heat transfer are complex due to the number of effective trans-

fer coefficients involved. However, only the total heat flux conservation plays an important part in the boundary conditions that must be applied at the free-porous interface. Such a result considerably simplifies the determination of the boundary conditions. Thus, using boundary conditions of continuity for the temperature, only the heat flux jump parameters must be computed to close the macroscopic model. For heating configurations, for which the solid heat source dominates the heat transfer, the macroscopic problem is easily solved for any interface location knowing the solid heat source in the transition zone.

With the analytical method, one can determine the boundary conditions of the heat transfer for any free-porous interface location. The computation of such boundary conditions requires a two-steps resolution. This computation can be avoid if the apparent interface exists. However, the apparent interface location for the heat transfer can be different to the momentum transfer one. In such a case, a solution is to use the resolution path presented below: the continuity of the temperature and a jump condition for the total heat flux computed to the apparent interface of the momentum transfer.

Furthermore, it must be noted that the determination of order 1 jump condition has an interest depending on the value of the ε parameter. If the size of the transition zone is large compared to the domain length (ε large), thus the order 1 brings an important correction. Otherwise, the zeroth order solution is sufficient to capture the correct order of magnitude.

This work can be extended to heat transfers for turbulent flows normal to the free-porous interface. For this configuration, new problems arise. Indeed, the macroscopic model in the homogeneous porous medium does not easily degenerate into the standard model used in the free region. It is due to slip-streams in the free region, that require additional modelings especially for the dispersive phenomenon. Once this work done, one can close the study with heat transfer for non one-dimensional turbulent flows. This configuration is a first step in the understanding of the physics existing in a nuclear reactor. Indeed, the presence of solid structures in the upper part of the nuclear reactor is at the origin of recirculating flows from the upper plenum to the fuel zone.

Furthermore, another example of extension could be the study of geometries closer to industrial uses. Indeed the present work, an academic geometry is used to allow the clarification of the physics existing at the free-porous interface through analytical developments. With more practical geometries, one could give information for the industrial models commonly built on empirical considerations.

Appendix A

Boundary conditions of pseudo-periodicity

This appendix presents the boundary condition of pseudo-periodicity. This boundary condition is used in Chapter 2 to compute an infinite homogeneous porous medium, and in Chapter 5 to compute turbulent heat transfer for a flow tangent at the interface. Especially, we use this configuration to introduce the pseudo-periodicity.

A.1 The variable change

We study heat transfer for a flow tangent to a free-porous interface. To compute such a configuration, boundary conditions must be applied at the domain (inlet/outlet) as presented in Fig. A.1.

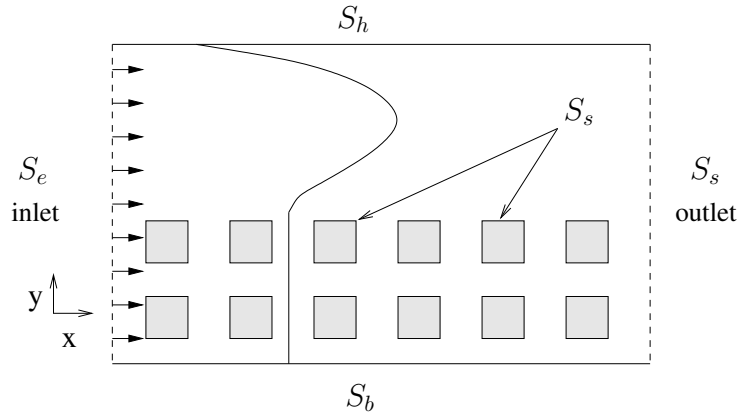


Figure A.1: Geometrical configuration.

For the velocity, using the boundary conditions of periodicity at the inlet/outlet is obvious. For the temperature T , the choice of the boundary conditions at the inlet/outlet depends from the energy balance. If there is no source of energy inside of the domain, boundary conditions of periodicity for the temperature are enough. If not, boundary conditions of periodicity for the temperature are not accurate because the calcul is not able to converge. For a constant increase at the steady state, boundary conditions of pseudo-periodicity are a good solution. It consists in performing a variable change and to compute the new variable θ with boundary conditions of periodicity:

$$\theta(x, y) = T(x, y) - \frac{\Delta T}{L}x \quad (\text{A.1})$$

where ΔT is the temperature increase on the domain of size L .

Preforming this change of variable, a source term appears in the microscopic equations as we will show in the following.

A.2 Determination of the source term

In order to determine the value of the source term A , an energy balance is performed on the whole domain. The local governing equation of the fluid phase are integrated on whole fluid volume of the domain and using the Stokes theorem one can obtain:

$$(\rho c_p)_f \nabla \cdot (\mathbf{v}_f T_f) = \nabla \cdot (k_f \nabla T_f) \quad (\text{A.2})$$

$$\int_{\partial V_f} (\rho c_p)_f T_f \mathbf{v} \cdot \mathbf{n} dS = \int_{\partial V_f} k_f \mathbf{n} \cdot \nabla T_f dS \quad (\text{A.3})$$

that can be rewritten as follows:

$$\begin{aligned} \int_{S_e} -(\rho c_p)_f T_f(0; y) v_x(0; y) dy + \int_{S_s} (\rho c_p)_f T_f(L; y) v_x(L; y) dy = \\ \int_{S_e} -k_f \frac{\partial T_f}{\partial x}(0; y) dy + \int_{S_s} -k_f \frac{\partial T_f}{\partial x}(L; y) dy + \int_{S_b} -k_f \frac{\partial T_f}{\partial y}(x; -H) dx \\ + \int_{S_h} k_f \frac{\partial T_f}{\partial y}(x; H) dx + \int_{S_s} k_f \mathbf{n} \cdot \nabla T_f dS \end{aligned} \quad (\text{A.4})$$

By construction, the increase of the temperature is constant and the velocity is periodic which gives:

$$T_f(L; y) = T_f(0; y) + AL \quad (\text{A.5})$$

$$\frac{\partial T_f}{\partial x}(-H; y) = \frac{\partial T_f}{\partial x}(L; y) \quad (\text{A.6})$$

$$v_x(0; y) = v_x(L; y) \quad (\text{A.7})$$

Thus, the equation (A.4) reduces to:

$$\int_{S_s} (\rho c_p)_f AL v_x(L; y) dy = \int_{S_b} -k_f \frac{\partial T_f}{\partial y}(x; 0) dx + \int_{S_h} k_f \frac{\partial T_f}{\partial y}(x; H) dx + \int_{S_s} k_f \mathbf{n} \cdot \nabla T_f dS \quad (\text{A.8})$$

Perfoming the energy balance for the solid phase, the local governing equation are integrated on the volume and using the Stokes theorem we obtain:

$$0 = \nabla \cdot (k_s \nabla T_s) + S_s \quad (\text{A.9})$$

$$0 = \int_{\partial V_s} -k_s \mathbf{n} \cdot \nabla T_s + \int_{V_s} S_s dV \quad (\text{A.10})$$

$$(\text{A.11})$$

With the continuity of the heat flux at the fluid-solid interface, the energy balance for the solid (A.10) can be rewritten as follows:

$$\int_{\partial V_s} k_s \mathbf{n} \cdot \nabla T_f = \int_{V_s} S_s dV \quad (\text{A.12})$$

Thus, the equation (A.8) becomes:

$$(\rho c_p)_f AL \int_{-H}^H v_x(0; y) dy = \int_0^L q^b dx - \int_0^L q^h dx + \int_{V_s} S_s dV \quad (\text{A.13})$$

that gives the source term A

$$A = \frac{(q^b - q^h)L + \int_{V_s} S_s dV}{(\rho c_p)_f L \int_{-H}^H v_x(0; y) dy} \quad (\text{A.14})$$

A.3 Implementation in Trio-U

Local governing equations

From the local governing equations for the temperatures T_f and T_s (see (A.2) et (A.9)), we introduce the following variable change $T_f = \theta_f + Ax$ et $T_s = \theta_s + Ax$, leading to:

$$(\rho c_p)_f \nabla \cdot (\mathbf{v}_f(\theta_f + Ax)) = \nabla \cdot (k_f \nabla(\theta_f + Ax)) \quad (\text{A.15})$$

$$0 = \nabla \cdot (k_s \nabla(\theta_s + Ax) + S_s) \quad (\text{A.16})$$

As the source term A is constant, the system reduces to:

$$(\rho c_p)_f \nabla \cdot (\mathbf{v}_f(\theta_f)) + (\rho c_p)_f \mathbf{v}_f A \cdot \mathbf{e}_x = \nabla \cdot (k_f \nabla(\theta_f)) \quad (\text{A.17})$$

$$0 = \nabla \cdot (k_s \nabla(\theta_s)) + S_s \quad (\text{A.18})$$

Thus, the quantity $(\rho c_p)_f \mathbf{v}_f A \cdot \mathbf{e}_x$ is the additional term that must be implemented in Trio-U.

Conditions at the fluid-solid surface

At the fluid-solid interface, there is the continuity of the temperature and heat flux such that:

$$T_f = T_s \quad (\text{A.19})$$

$$k_f \mathbf{n}_{fs} \cdot \nabla T_f = k_s \mathbf{n}_{fs} \cdot \nabla T_s \quad (\text{A.20})$$

Using the variable change $T_f = \theta_f + Ax$ et $T_s = \theta_s + Ax$ in Eqs. (A.19) et (A.20), one obtains:

$$\theta_f = \theta_s \quad (\text{A.21})$$

$$k_f \mathbf{n}_{fs} \cdot \nabla \theta_f = k_s \mathbf{n}_{fs} \cdot \nabla \theta_s + (k_s - k_f) A \mathbf{n}_{fs} \cdot \mathbf{e}_x \quad (\text{A.22})$$

Thus, the quantity $(k_s - k_f) A \mathbf{n}_{fs} \cdot \mathbf{e}_x$ is the additional term created by the variable change and must be added in the code. In Trio-U, the continuity of the heat flux at the fluid-solid interface is computed as follows:

$$k_f \frac{\theta_f - \theta_i}{\Delta x/2} = h(\theta_f - \theta_s) + \text{Cte}^1 \quad (\text{A.23})$$

$$k_s \frac{\theta_i - \theta_s}{\Delta x/2} = h(\theta_f - \theta_s) + \text{Cte}^2 \quad (\text{A.24})$$

where Cte^1 and Cte^2 are constant that must be determined, Δx the length of the cell, θ_i the temperature at the interface and h the transfer coefficient. Using the relation (A.22) with the temperature at the interface θ_i , one obtains:

$$\theta_i = \frac{k_f \theta_f + k_s \theta_s}{k_f + k_s} + \frac{k_f - k_s}{k_f + k_s} A \frac{\Delta x}{2} \quad (\text{A.25})$$

Injecting θ_i in the relations (A.23) and (A.24), the constantes Cte^1 and Cte^2 are determined:

$$\text{Cte}^1 = -k_f \frac{k_f - k_s}{k_f + k_s} A \quad (\text{A.26})$$

$$\text{Cte}^2 = k_s \frac{k_s - k_f}{k_f + k_s} A \quad (\text{A.27})$$

Furthermore h is computed by the code with:

$$h(\theta_f - \theta_s) = \lambda_f \nabla \theta_f = \lambda_s \nabla \theta_s, \text{ thus } h = \frac{\lambda_f \lambda_s}{\lambda_f + \lambda_s} \frac{2}{\Delta x} \quad (\text{A.28})$$

Bibliography

- Abe, H., Kawamura, H., and Matsuo, Y. (2004). Surface heat-flux fluctuations in a turbulent channel flow up to $Re=1020$ with $Pr=0.025$ and 0.71 . *Int. J. Heat Fluid Flows*, 25:404–419.
- Aguilar-Madera, C.J. Valdés-Parada, F. G. B. and Ochoa-Tapia, J. A. (2011). One-domain approach for heat transfer between a porous medium and a fluid. *Int. J. Heat Mass Transfer*.
- Alazmi, B. and Vafai, K. (2001). Analysis of fluid flow and heat transfer interfacial conditions between a porous medium and a fluid layer. *Int. J. Heat Mass Transfer*, 44(9):1735–1749.
- Allaire, G. (1989). Prolongement de la pression et homogénéisation des équations de Stokes dans un milieu poreux connexe. *C. R. Acad. Sci. Paris, Série I*, t. 309:717–722.
- Antohe, B. V. and Lage, J. L. (1997). A general two-equation macroscopic turbulence model for incompressible flow in porous media. *Int. J. Heat Mass Transfer*, 40:3013–3024.
- Beavers, G. and Joseph, D. (1967). Boundary conditions at a naturally permeable wall. *J. Fluid Mech.*, 30:197–207.
- Braga, E. J. and de Lemos, M. J. S. (2006). Simulation of turbulent natural convection in a porous cylindrical annulus using a macroscopic two-equation model. *Int. J. Heat Mass Transfer*, 49(23-24):4340–4351.
- Breugem, W.-P. (2005). *The influence of wall permeability on laminar and turbulent flows: Theory and simulations*. PhD thesis, Technische Universiteit Delft.
- Breugem, W.-P., Boersma, B., and Uittenbogaard, R. (2005). The influence of wall permeability on turbulent channel flow. *J. Fluid Mech.*, 562:35–72.
- Breugem, W.-P. and Boersma, B. J. (2005). Direct numerical simulations of turbulent flow over a permeable wall using a direct and a continuum approach. *Phys. Fluids*, 17:025103.
- Carbonell, R. G. and Whitaker, S. (1984). *Fundamentals of transport phenomena in porous media*. Martinus Nijhoff.
- Chandesris, M. and Jamet, D. (2006). Boundary conditions at a planar fluid-porous interface for a Poiseuille flow. *Int. J. Heat Mass Transfer*, 49(13-14):2137–2150.
- Chandesris, M. and Jamet, D. (2007). Boundary conditions at a fluid-porous interface: An a priori estimation of the stress jump coefficients. *Int. J. Heat Mass Transfer*, 50(17-18):3422–3436.
- Chandesris, M. and Jamet, D. (2009a). Boundary conditions for turbulent flows through hybrid fluid-porous domains. In *4th International Conference on Applications of Porous Media, ICAPM 2009, Istanbul, Turkey, August 10-12*.
- Chandesris, M. and Jamet, D. (2009b). Derivation of jump conditions for the turbulence $k-\epsilon$ model at a fluid / porous interface. *Int. J. Heat Fluid Flow*, 30:306–318.
- Chandesris, M. and Jamet, D. (2009c). Jump conditions and surface-excess quantities at a fluid/porous interface: a multi-scale approach. *Transp. Porous Media*, 78:419–438.
- Chandesris, M., Serre, G., and Sagaut, P. (2006). A macroscopic turbulence model for flow in porous media suited for channel, pipe and rod bundle flows. *Int. J. Heat Mass Transfer*, 49:2739–2750.

- de Lemos, M. J. S. (2005). Turbulent kinetic energy distribution across the interface between a porous and a clear region. *Int. Comm. Heat Mass Transfer*, 32:107–115.
- de Lemos, M. J. S. (2009). Turbulent flow around fluid-porous interfaces computed with a diffusion-jump model for k and epsilon transport equations. *Transp. Porous Med.*, 78:331–346.
- de Lemos, M. J. S. and Braga, E. (2003). Modeling of turbulent natural convection in porous media. *Int. Comm. Heat Mass Transfer*, 30(5):615–624.
- de Lemos, M. J. S. and Pedras, M. H. J. (2000). Simulation of turbulent flow through hybrid porous medium - clear fluid domains. In *Proc. of the ASME Heat Transfer Division*, volume 5, pages 113–122.
- de Lemos, M. J. S. and Pedras, M. H. J. (2001a). Alternative transport equations for turbulent kinetic energy for flow in porous media. In *Proc. of NHTC'01, 35th National Heat Transfer Conference, Anaheim CA*, pages 1255–1262.
- de Lemos, M. J. S. and Pedras, M. H. J. (2001b). Recent mathematical models for turbulent flow in saturated rigid porous media. *J. Fluids Eng.*, 123:935–940.
- de Lemos, M. J. S. and Rocamora, F. D. J. (2002). Turbulent transport modeling for heated flow in rigid porous media. In *Proc. of the 12th Int. Heat Transfer Conf.*, pages 791–796.
- de Lemos, M. J. S. and Silva, R. A. (2006). Turbulent flow over a layer of a highly permeable medium simulated with a diffusion-jump model for the interface. *Int. J. Heat Mass Transfer*, 49(3-4):546–556.
- Debusschere, B. and Rutland, C. (2004). Turbulent scalar transport mechanisms in plane channel and couette flows. *Int. J. Heat Mass Transfer*, 47:1771–1781.
- d'Hueppe, A., Chandesris, M., Jamet, D., and Goyeau, B. (2010). Boundary conditions at a fluid-porous interface for a convective heat transfer problem: analysis of the jump relations. *Int. J. Heat Mass Transfer*, submitted.
- Drouin, M., Grégoire, O., Simonin, O., and Chanoine, A. (2010). Macroscopic modeling of thermal dispersion for turbulent flows in channels. *International Journal of Heat and Mass Transfer*, 53:2206 – 2217.
- Duman, T. and Shavit, U. (2009). An apparent interface location as a tool to solve the porous interface flow problem. *Transp. Porous Med.*, 78:509–524.
- Edwards, D. A., Brenner, H., and Wasan, D. T. (1991). *Interfacial Transport Processes and Rheology*. Butterworth-Heinemann.
- Emmerich, H. (2003). *The Diffuse Interface Approach in Materials Science*. Springer.
- Finnigan, J. (2000). Turbulence in plant canopies. *Annu. Rev. Fluid Mech.*, 32:519–571.
- Fried, J. J. and Combarous, M. A. (1971). Dispersion in porous media. *Advances in Hydro. Science*, 7:169–282.
- Getachew, D., Minkowycz, W., and Lage, J. (2000). A modified form of the $k - \epsilon$ model for turbulent flows of an incompressible fluid in porous media. *Int. J. Heat Mass Transfer*, 43:2909–2915.
- Ghisalberti, M. and Nepf, H. M. (2009). Shallow flows over a permeable medium: The hydrodynamics of submerged aquatic canopies. *Transp. Porous Med.*, 78:385–402.
- Goyeau, B., Lhuillier, D., Gobin, D., and Velarde, M. G. (2003). Momentum transport at a fluid-porous interface. *Int. J. Heat Mass Transfer*, 46:4071–4081.
- Gray, W. (1975). A derivation of the fluid equations for multi-phase transport. *Chem. Eng. Sci.*, 30:229–233.
- Gray, W. G. and Lee, P. C. Y. (1977). On the theorems for local volume averaging of multiphase systems. *Int. J. Multiphase Flow*, 3:333–340.
- Hahn, S., Je, J., and Choi, H. (2002). Direct numerical simulation of turbulent channel flow with permeable walls. *J. Fluid Mech.*, 450:259–285.

BIBLIOGRAPHY

- Han, N. W., Bhakta, J., and Carbonell, R. G. (1985). Longitudinal and lateral dispersion in packed beds: effect of a column length and particule size distribution. *AIChE J.*, 31:277–288.
- Hirata, S. C., Goyeau, B., and Gobin, D. (2009). Stability of thermosolutal natural convection in superposed fluid and porous layers. *Transp. Porous Med.*, 78:525–536.
- Hsu, C. T. and Cheng, P. (1988). Closure schemes of the macroscopic energy equation for convective heat transfer in porous media. *Int. Comm. Heat Mass Transfer*, 15:689–703.
- Jamet, D. and Chandesris, M. (2009). On the intrinsic nature of jump coefficients at the interface between a porous medium and a free fluid region. *Int. J. Heat Mass Transfer*, 52(1-2):289–300.
- Kasagi, N., Tomita, Y., and Kuroda, A. (1992). Direct numerical simulation of passive scalar field in a turbulent channel flow. *Journal of heat transfer-Transactions of the ASME*, 114:598–606.
- Kaviany, M. (1995). *Principles of Heat Transfer in Porous Media*. Springer-Verlag, New York, second edition.
- Kawamura, H., Abe, H., and Matsuo, Y. (1999). DNS of turbulent heat transfer in channel flow with respect to reynolds and prandtl number effects. *Int. J. Heat Fluid Flow*, 20:196–207.
- Kawamura, H., Abe, H., and Shingai, K. (2000). DNS of turbulence and heat transport in a channel flow with different reynolds and prandtl numbers and boundary conditions. In *3rd Int. Symp. on Turbulence, Heat and Mass Transfer*.
- Kim, J. and Moin, P. (1989). *Transport of passive scalars in a turbulent channel flow*. Springer-Verlag, Berlin.
- Koch, D. L. and Brady, J. F. (1985). Dispersion in fixed beds. *J. Fluid Mech.*, 154:399–427.
- Koch, D. L. and Brady, J. F. (1987a). A non local description of advection diffusion with application to dispersion in porous media. *J. Fluid Mech.*, 180:387–403.
- Koch, D. L. and Brady, J. F. (1987b). The symmetry properties of the effective diffusivity tensor in anisotropic porous-media. *Physics of Fluids*, 30:642–650.
- Koch, D. L., Cox, R. G., Brenner, H., and Brady, J. F. (1989). The effect of order of dispersion in porous media. *J. Fluid Mech.*, 200:173–188.
- Kong, F. Y. and Schetz, J. A. (1982). Turbulent boundary layer over porous surfaces with different surface geometries. In *AIAA 20th Aerospace Sciences Meeting, January 11-14, Orlando, Florida*, pages AIAA–82–0030.
- Kozuka, M., Seki, Y., and Kawamura, H. (2009). DNS of turbulent heat transfer in a channel flow with high spatial resolution. *Int. J. Heat Fluid Flows*, 30:514–524.
- Kuwahara, F. and Nakayama, A. (1999). Numerical determination of thermal dispersion coefficients using a periodic porous structure. *J. Heat Transfer*, 121:160–163.
- Kuwahara, F., Nakayama, A., and Koyama, H. (1996). A numerical study of thermal dispersion in porous media. *J. Heat Transfer*, 118:756–761.
- Kuwahara, F., Shirota, M., and Nakayama, A. (2001). A numerical study of interfacial convective heat transfer coefficient in two-energy equation model for convection in porous media. *Int. J. Heat Mass Transfer*, 44:1153–1159.
- Kuznetsov, A. and Xiong, M. (2003). Development of an engineering approach to computations of turbulent flows in composite porous/fluid domains. *Int. J. Therm. Sci.*, 42:913–919.
- Kuznetsov, A. V. (2004). Numerical modeling of turbulent flow in a composite porous/fluid duct utilizing a two-layer $k - \varepsilon$ model to account for interface roughness. *Int. J. Therm. Sci.*, 43:1047–1056.
- Kuznetsov, A. V., Cheng, L., and Xiong, M. (2002). Effects of thermal dispersion and turbulence in forced convection in a composite parallel-plate channel: Investigation of constant wall temperature cases. *Num. Heat Transfer, Part A*, 42:365–383.

- Larson, R. E. and Higdon, J. J. L. (1986). Microscopic flow near the surface of a two-dimensional porous media. Part 1. Axial flow. *J. Fluid Mech.*, 166:449–472.
- Larson, R. E. and Higdon, J. J. L. (1987). Microscopic flow near the surface of a two-dimensional porous media. Part 2. Transverse flow. *J. Fluid Mech.*, 178:119–136.
- Launder, B. E. and Spalding, D. B. (1972). *Mathematical Models of Turbulence*. Academic Press, London.
- Lee, K. and Howell, J. R. (1987). Forced convective and radiative transfer within a highly porous layer exposed to a turbulent external flow field. In *Proc. of the 1987 ASME-JSME Thermal Engineering Joint Conf.*, volume 2, pages 377–386.
- Matheron, G. (1967). *Eléments pour une théorie des milieux poreux*. Masson.
- Mikelic, A. (2000). *Filtration in Porous Media and Industrial Application*, volume 1734, chapter Homogenization theory and applications to filtration through porous media, pages 127–214. Springer.
- Moser, R. D., Kim, J., and Mansour, N. N. (1999). Direct numerical simulation of turbulent channel flow up to $Re_\tau = 590$. *Phys. Fluids*, 11(4):943–945.
- Na, Y., Papavassiliou, D., and Hanratty, T. (1999). Use of direct numerical simulation to study the effect of prandtl number on temperature fields. *Int. J. Heat Fluid Flow*, 20:187–195.
- Nakayama, A. and Kuwahara, F. (1999). A macroscopic turbulence model for flow in a porous medium. *J. Fluids Eng.*, 121:427–433.
- Nicoud, F. and Poinot, T. (1999). Dns of a channel flow with variable properties. *Turbulence and Shear Flow Phenomena*, 697.
- Nield, D. A. (2001). Alternative models of turbulence in a porous medium, and related matters. *J. Fluids Eng.*, 123:928–931.
- Nield, D. A. (2009). The beavers-joseph boundary condition and related matters: A historical and critical note. *Transp. Porous Med.*, 78:537–540.
- Ochoa-Tapia, J. A. and Whitaker, S. (1995a). Momentum transfer at the boundary between a porous medium and a homogeneous fluid – I. Theoretical development. *Int. J. Heat Mass Transfer*, 38(14):2635–2646.
- Ochoa-Tapia, J. A. and Whitaker, S. (1995b). Momentum transfer at the boundary between a porous medium and a homogeneous fluid - II. Comparison with experiment. *Int. J. Heat Mass Transfer*, 38(14):2647–2655.
- Ochoa-Tapia, J. A. and Whitaker, S. (1997). Heat transfer at the boundary between a porous medium and a homogeneous fluid. *Int. J. Heat Mass Transfer*, 40(11):2691–2707.
- Pedras, M. and de Lemos, M. (2000). On the definition of turbulent kinetic energy for flow in porous media. *Int. Comm. Heat Mass Transfer*, 27(2):211–220.
- Pedras, M. and de Lemos, M. (2001). On the mathematical description and simulation of turbulent flow in a porous medium formed by an array of elliptic rods. *J. Fluids Eng.*, 123:941–947.
- Pinson, F., Gregoire, O., Quintard, M., Prat, M., and Simonin, O. (2007). Modeling of turbulent heat transfer and thermal dispersion for flows in flat plate heat exchangers. *Int. J. Heat Mass Transfer*, 50:1500–1515.
- Pinson, F., Grégoire, O., and Simonin, O. (2006). $k - \epsilon$ macro-scale modeling of turbulence based on a two scale analysis in porous media. *Int. J. Heat Fluid Flow*, 27:955–966.
- Pokrajac, D. and Manes, C. (2009). Velocity measurements of a free-surface turbulent flow penetrating a porous medium composed of uniform-size spheres. *Transp. Porous Med.*, 78:367–383.
- Prat, M. (1989). On the boundary conditions at the macroscopic level. *Transp. Porous Media*, 4:259–280.
- Prat, M. (1990). Modelling of heat transfer by conduction in a transition region between a porous medium and an external fluid. *Transp. Porous Media*, 5:71–95.

BIBLIOGRAPHY

- Prat, M. (1992). Some refinements concerning the boundary conditions at the macroscopic level. *Transp. Porous Media*, 7:147–161.
- Prinos, P., Sofiadis, D., and Keramaris, E. (2003). Turbulent flow over and within a porous bed. *J. Hydraulic Eng.*, pages 720–733.
- Quintard, M., Kaviany, M., and Whitaker, S. (1997). Two-medium treatment of heat transfer in porous media: numerical results for effective properties. *Adv. Water Resour.*, 20:77–94.
- Quintard, M. and Whitaker, S. (1993). One- and two-equation models for transient diffusion processes in two-phase systems. *Advances in Heat Transfer*, 23:369–464.
- Quintard, M. and Whitaker, S. (1994). Transport in ordered and disordered porous media - II. Generalized volume averaging. *Transp. Porous Media*, 14:179–206.
- Renard, P. and de Marsily, G. (1997). Calculating equivalent permeability: a review. *Advances in Water Resources*, 20:253–278.
- Rocamora, J. F. D. and de Lemos (2000). Analysis of convective heat transfer for turbulent flow in saturated porous media. *Int. Comm. Heat Mass Transfer*, 27, No 6:825–834.
- Saffman, P. G. (1971). On the boundary condition at the surface of a porous medium. *Stud. Appl. Math.*, L(2):93–101.
- Sahraoui, M. and Kaviany, M. (1992). Slip and no-slip velocity boundary conditions at interface of porous, plain media. *Int. J. Heat Mass Transfer*, 35(4):927–943.
- Sahraoui, M. and Kaviany, M. (1994). Slip and no-slip temperature boundary conditions at interface of porous, plain media: convection. *Int. J. Heat Mass Transfer*, 37(6):1029–1044.
- Saleh, S., Thovert, J., and Adler, P. (1993). Flow along porous media by partial image velocimetry. *AIChE Journal*, 39(11):1765–1776.
- Sanchez-Palencia, E. (1974). Comportement local et macroscopique d'un type de milieux hétérogènes. *Int. J. Eng. Sci.*, 12:331–351.
- Shavit, U. (2009). Special issue on "transport phenomena at the interface between fluid and porous domains" a preface. *Transp. Porous Med.*, 78:327–330.
- Shaw, R. and Schumann, U. (1992). Large-eddy simulation of turbulent flow above and within a forest. *Boundary-Layer Meteorology*, 61:47–64.
- Stalio, E. and Nobile, E. (2003). Direct numerical simulation of heat transfer over riblets. *Int. J. Heat Fluid Flow*, 24:356–371.
- Tennekes, H. and Lumley, J. (1972). *A First Course in Turbulence*. MIT Press.
- Tiselj, I., Bergant, R., Mavko, B., Basjic, I., and Hestroni, G. (2001a). Dns of turbulent heat transfer in channel flow with heat conduction in the solid wall. *J. Heat Transfer*, 123:849–857.
- Tiselj, I., Pogrebnyak, E., Li, C., Mosyak, A., and Hestroni, G. (2001b). Effect of wall boundary condition on scalar transfer in a fully developed turbulent flume. *Phys. Fluids*, 4(13):1028.
- Valdés-Parada, F., Alvarez-Ramirez, J., Goyeau, B., and Ochoa-Tapia, J. A. (2009a). Computation of jump coefficients for momentum transfer between a porous medium and a fluid using a closed generalized transfer equation. *Transp. Porous Med.*, 78:439–457.
- Valdés-Parada, F., Alvarez-Ramirez, J., Goyeau, B., and Ochoa-Tapia, J. A. (2009b). Jump condition for diffusive and convective mass transfer between a porous medium and a fluid involving adsorption and chemical reaction. *Transp. Porous Med.*, 78:459–476.

- Valdés-Parada, F. J., Goyeau, B., and Ochoa-Tapia, J. A. (2006). Diffusive mass transfer between a microporous medium and an homogeneous fluid: Jump boundary conditions. *Chem. Eng. Sci.*, 61(5):1692–1704.
- Valdés-Parada, F. J., Goyeau, B., and Ochoa-Tapia, J. A. (2007a). Jump momentum boundary condition at a fluid-porous dividing surface: Derivation of the closure problem. *Chem. Eng. Sci.*, 62:4025–4039.
- Valdés-Parada, F. J., Ochoa-Tapia, J., and Alvarez-Ramirez, J. (2007b). Diffusive mass transport in the fluid-porous medium inter-region: Closure problem solution for the one-domain approach. *Chem. Eng. Sci.*, 62:6054–6068.
- Wakao, N. and Kaguei, S. (1982). *Heat and mass transfer in packed beds*. Gordon and Breach.
- Watanabe, T. (2004). Large-eddy simulation of coherent turbulence structures associated with scalar ramps over plant canopies. *Boundary-Layer Meteorology*, 112:307–341.
- Whitaker, S. (1967). Diffusion and dispersion in porous media. *AIChE Journal*, 13(3):420–427.
- Whitaker, S. (1969). Advances in theory of fluid motion in porous media. *Ind. Eng. Chem.*, 61:14–28.
- Whitaker, S. (1999). *The method of volume averaging*. Kluwer academic publishers.
- Zagni, A. and Smith, K. (1976). Channel flow over permeable beds of graded spheres. *Journal of Hydraulics Division*, 102(HY2):207–222.
- Zeytounian, R. K. (1986). *Les modèles Asymptotiques de la mécanique des fluides I, Lecture Notes in Physics*. Springer-Verlag, Berlin.
- Zippe, H. and Graf, W. (1983). Turbulent boundary-layer flow over permeable and non-permeable rough surfaces. *Journal of Hydraulic Research*, 21(1):51–65.
- Zwillinger, D. (1989). *Handbook of differential equations*. Academic Press, Boston.

Abstract

This work deals with the study of heat transfer between a porous medium and a free medium, using multi scale approaches. First, we derive the boundary conditions that must be applied at a free-porous interface for laminar heat transfer at local thermal equilibrium and, then, at local thermal non-equilibrium. For turbulent heat transfer, a direct numerical simulation is performed supplying a better understanding of the physic at the free-porous interface. Then, we determine a turbulent model with associated jump conditions. These studies answer fundamental questions regarding the physical meaning of the jump conditions, the values of the jump parameters and the location of the interface for heat transfer.

Keywords

Heat transfer, interface, boundary conditions, porous media, volume averaging method, multi-scale, excess quantity, turbulence.

Résumé

Ce travail porte sur l'étude du transfert de chaleur entre un milieu poreux et un milieu libre en utilisant une approche multi-échelle. Dans un premier temps, nous dérivons les conditions limites à imposer à une interface libre-poreux dans le cas des transferts de chaleur à l'équilibre thermique local puis dans le cas du déséquilibre thermique local. Pour les transferts de chaleur turbulent, une simulation numérique directe est réalisée afin d'apporter une meilleure compréhension de la physique existant à l'interface libre-poreux. Puis, nous déterminons un modèle turbulent avec des conditions de saut. Ces études répondent à des questions fondamentales liées à la compréhension physique des conditions de saut, des valeurs des paramètres des saut et de la position de l'interface dans le cadre des transferts de chaleur.

Mots-clés

Transfert de chaleur, interface, condition limites, milieu poreux, prise de moyenne volumique, multi-échelles, grandeur en excès, turbulence.